frontiers | Research Topics

Mathematical modeling and computational predictions in oncoimmunology

Edited by
Vladimir A. Kuznetsov, Heiko Enderling and Mark Chaplain

Published in
Frontiers in Immunology
Frontiers in Oncology

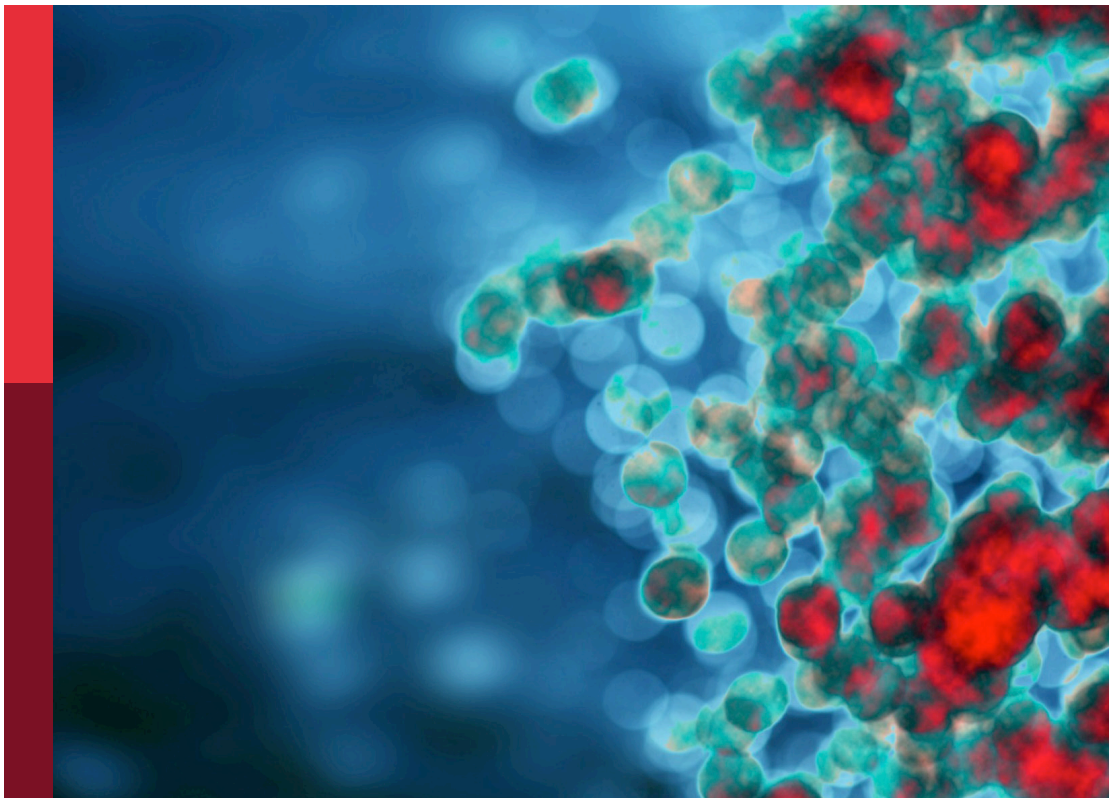

ISSN 1664-8714
ISBN 978-2-8325-5006-9
DOI 10.3389/978-2-8325-5006-9

About Frontiers

Frontiers is more than just an open access publisher of scholarly articles: it is a pioneering approach to the world of academia, radically improving the way scholarly research is managed. The grand vision of Frontiers is a world where all people have an equal opportunity to seek, share and generate knowledge. Frontiers provides immediate and permanent online open access to all its publications, but this alone is not enough to realize our grand goals.

Frontiers journal series

The Frontiers journal series is a multi-tier and interdisciplinary set of open-access, online journals, promising a paradigm shift from the current review, selection and dissemination processes in academic publishing. All Frontiers journals are driven by researchers for researchers; therefore, they constitute a service to the scholarly community. At the same time, the *Frontiers journal series* operates on a revolutionary invention, the tiered publishing system, initially addressing specific communities of scholars, and gradually climbing up to broader public understanding, thus serving the interests of the lay society, too.

Dedication to quality

Each Frontiers article is a landmark of the highest quality, thanks to genuinely collaborative interactions between authors and review editors, who include some of the world's best academicians. Research must be certified by peers before entering a stream of knowledge that may eventually reach the public - and shape society; therefore, Frontiers only applies the most rigorous and unbiased reviews. Frontiers revolutionizes research publishing by freely delivering the most outstanding research, evaluated with no bias from both the academic and social point of view. By applying the most advanced information technologies, Frontiers is catapulting scholarly publishing into a new generation.

What are Frontiers Research Topics?

Frontiers Research Topics are very popular trademarks of the *Frontiers journals series*: they are collections of at least ten articles, all centered on a particular subject. With their unique mix of varied contributions from Original Research to Review Articles, Frontiers Research Topics unify the most influential researchers, the latest key findings and historical advances in a hot research area.

Find out more on how to host your own Frontiers Research Topic or contribute to one as an author by contacting the Frontiers editorial office: frontiersin.org/about/contact

Mathematical modeling and computational predictions in oncoimmunology

Topic editors

Vladimir A. Kuznetsov — Upstate Medical University, United States
Heiko Enderling — University of Texas MD Anderson Cancer Center, United States
Mark Chaplain — University of St Andrews, United Kingdom

Citation

Kuznetsov, V. A., Enderling, H., Chaplain, M., eds. (2024). *Mathematical modeling and computational predictions in oncoimmunology*. Lausanne: Frontiers Media SA. doi: 10.3389/978-2-8325-5006-9

Topic editor Vladimir Kuznetsov is employed by AptaMatrix, Inc. All other Topic Editors declare no competing interests with regards to the Research Topic subject.

Table of contents

frontiers | Frontiers in Immunology

TYPE Editorial
PUBLISHED 30 May 2024
DOI 10.3389/fimmu.2024.1432372

OPEN ACCESS

EDITED AND REVIEWED BY
Peter Brossart,
University of Bonn, Germany

*CORRESPONDENCE
Vladimir A. Kuznetsov
kuznetsv@upstate.edu
Heiko Enderling
henderling@mdanderson.org
Mark Chaplain
majc@st-andrews.ac.uk

RECEIVED 14 May 2024
ACCEPTED 23 May 2024
PUBLISHED 30 May 2024

CITATION
Kuznetsov VA, Enderling H and Chaplain M (2024) Editorial: Mathematical modeling and computational predictions in oncoimmunology.
Front. Immunol. 15:1432372.
doi: 10.3389/fimmu.2024.1432372

Editorial: Mathematical modeling and computational predictions in oncoimmunology

Vladimir A. Kuznetsov[1,2]*, Heiko Enderling[3]* and Mark Chaplain[4]*

[1]Urology, Upstate Medical University, Syracuse, NY, United States, [2]Biochemistry and Molecular Biology, Upstate Medical University, Syracuse, NY, United States, [3]Department of Radiation Oncology, University of Texas MD Anderson Cancer Center, Houston, TX, United States, [4]School of Mathematics and Statistics, University of St Andrews, St Andrews, United Kingdom

KEYWORDS

oncoimmunology, mathematical modeling, nonlinear dynamics, computational prediction, immune response, immunotherapy

Editorial on the Research Topic
Mathematical modeling and computational predictions in oncoimmunology

The immune system can recognize and kill malignant cells. Anti-cancer immune mechanisms are realized as multiscale, nonlinear cellular and molecular processes. Many factors determine the outcome of immune system-tumor interactions, including cancer-associated antigens, immune cells, and host organisms. In the context of such complexity and non-linear dynamics, deep data-driven theory and mathematical modeling enables an increase in our understanding of mechanisms controlling these processes, defining reliable biomarkers, and potentially improving the capability of immune and combined therapies.

Here we review and summarize the contributions to the Research Topic "*Mathematical modeling and computational predictions in oncoimmunology*."

The review by Metzcar et al. deals with the overview of a mechanistic learning approach that combines mechanistic mathematical modeling with data-driven machine learning. The authors reviewed the perspective of this approach and discussed how mechanistic learning may advance mathematical oncology. The four categories of mechanistic learning (sequential, parallel, extrinsic, intrinsic) are presented with examples from oncology research such as longitudinal tumor response predictions and time-to-event analyses.

Boklund et al. develop a mathematical model of myeloproliferative neoplasm (MPN) progression and treatment of MPN with JAK1/2 inhibitor ruxolitinib. A system of ordinary differential equations (ODUs) describes and models the dynamics of the interaction between healthy cells, malignant cells, and inflammatory cytokines produced by the immune system. By fitting the model to data, the authors show that the proposed mechanisms of ruxolitinib action are compatible with the disease dynamics. The model analysis and data fitting enable computational predictions and uncertainty quantification of the future course of the disease for individual patients based on longitudinal measurements of the MPN load.

In their article, Ledzewicz and Schättler develop a model of the tumor treatment effects when traditional chemo- and radiotherapies are combined with immunotherapy. Based on the classical Stepanova (1980) and Kuznetsov (1994) papers, a dynamical system model of the low-

dimensional cellular immune response against cancer antigen(s) is formulated. It is shown that the system's dynamics is dependent upon the values of its parameters, and encompasses the 3E's (elimination, equilibrium, escape) of tumor antigen(s)-immune system interactions. Using numerical analysis, optimal control strategies for implementing immunotherapy, chemotherapy, and radiotherapy are formulated to reverse the tumor 'escape' scenario.

Castorina et al. analyze the Gompertz population growth law to evaluate radiation and immunotherapy effects on tumor mass dynamics in individual patients. Using time course data, they show that the Gompertz law can describe therapy effects with two effective parameters. Their macroscopic approach quantifies the treatment/interaction effect between the immune system, radiotherapy, and tumor progression. This result permits quantitative tumor mass kinetics data analyses, which give useful indications for disease progression and assess the potential efficacy of radiotherapy and immunotherapy combinations.

Adhikarla et al. validate the previously reported mathematical model against experimental data where the timing of the CAR-T cell therapy is varied keeping the targeted alpha particle therapy (TAT) dosage and timing constant. Model parameters are elucidated from the experimental data to optimize the timing of CAR-T cell therapy post-TAT by maximizing progression-free survival. The effect of fractionated dosing of both TRT and CAR-T cell therapies on the survival metrics is also studied. In addition, multiple dosing strategies for TRT and CAR-T cell therapies are tested to analyze whether the splitting and scheduling of the doses result in improved tumor control or survival.

To assess the combined effects of anti-PD-1 and anti-FGFR3 small molecule inhibitors (SMI) on tumor growth and the immune response, Bergman et al. build agent-based models (ABM) that capture key aspects of tumor heterogeneity and CD8+ T cell phenotypes, their spatial interactions, and their response to therapeutics. The model quantifies how tumor antigenicity and FGFR3 activating mutations impact the disease process and response to anti-PD-1 antibodies and anti-FGFR3 SMI. The modeling results indicate the need to quantify FGFR3 signaling, and the fitness advantage conferred on bladder cancer cells harboring this mutation.

Yosef and Bunimovich-Medrazitsky present a theoretical investigation of non-muscle invasive bladder cancer (NMIBC) growth and its continuous treatment with Mitomycin-C (MMC). Based on biological data analysis and using ordinary differential equations (ODEs) the authors describe the cells and drug molecule dynamics of tumor-immune cell interactions during MMC treatment. Several hypothetical scenarios for NMIBC depict the evolution of tumors for small, medium, and large tumors. The results offer the possibility to improve MMC chemotherapy for NMIBC patients and explain some of the mysteries of NMIBC chemotherapy.

West et al. present a multiscale mathematical model that captures the phenotypic, vascular, microenvironmental, and spatial heterogeneity that shapes acid-mediated invasion and immune escape over a biologically realistic time scale. The model explores several immune escape mechanisms such as i) acid inactivation of immune cells, ii) competition for glucose, and iii) inhibitory immune checkpoint receptor expression (PD-L1). This model helps to decompose the key constraints on evolutionary costs and benefits of three key phenotypic axes on tumor invasion and treatment: acid resistance, glycolysis, and PD-L1 expression. The benefits of concomitant anti-PD-L1 and buffer treatments are promising treatments to limit the adverse effects of immune escape.

Lems et al. extend an existing mathematical model and embed it in multi-scale spatial simulations to describe the effects of immunosuppression and spatial heterogeneity on the crosstalk between EMT and IFNγ-induced PD-L1 expression. This analysis demonstrates that the relation between PD-L1 expression and EMT status is highly complex, and depends on the forms of immunosuppression established by the tumor as well as on spatial heterogeneity concerning cytokines influencing these pathways. These results may contribute to the development of therapeutic strategies for effectively combating metastatic dissemination, as well as immune evasion.

Conclusion

The collected articles demonstrate that mathematical modeling and computational simulation contribute to oncoimmunology by consolidating experimental, theoretical, and clinical facts into quantitatively/qualitatively predictive and hypothesis-driven frameworks. Moreover, the modeling allows the prediction and validation of specific mechanisms and key parameters of the studied complex systems *in vitro* and *in vivo*. By computational analysis of independent data identifying molecular and cellular mechanisms and interaction parameters, mathematical models can be useful tools to stratify immunotherapy responses and personalize outcomes for cancer patients.

Author contributions

VK: Writing – review & editing, Writing – original draft. HE: Writing – review & editing, Writing – original draft. MC: Writing – review & editing, Writing – original draft.

Conflict of interest

The authors declare that the research was conducted in the absence of any commercial or financial relationships that could be construed as a potential conflict of interest.

Publisher's note

frontiers | Frontiers in Immunology

TYPE Original Research
PUBLISHED 10 August 2023
DOI 10.3389/fimmu.2023.1219669

OPEN ACCESS

EDITED BY
Heiko Enderling,
Moffitt Cancer Center, United States

REVIEWED BY
Morgan Craig,
University of Montreal, Canada
Marta Canel,
University of Edinburgh, United Kingdom

*CORRESPONDENCE
Joost B. Beltman
j.b.beltman@lacdr.leidenuniv.nl

RECEIVED 09 May 2023
ACCEPTED 30 June 2023
PUBLISHED 10 August 2023

CITATION
Lems CM, Burger GA and Beltman JB (2023) Tumor-mediated immunosuppression and cytokine spreading affects the relation between EMT and PD-L1 status.
Front. Immunol. 14:1219669.
doi: 10.3389/fimmu.2023.1219669

Tumor-mediated immunosuppression and cytokine spreading affects the relation between EMT and PD-L1 status

Carlijn M. Lems, Gerhard A. Burger and Joost B. Beltman*

Division of Drug Discovery and Safety, Leiden Academic Centre for Drug Research, Leiden University, Leiden, Netherlands

Epithelial-mesenchymal transition (EMT) and immune resistance mediated by Programmed Death-Ligand 1 (PD-L1) upregulation are established drivers of tumor progression. Their bi-directional crosstalk has been proposed to facilitate tumor immunoevasion, yet the impact of immunosuppression and spatial heterogeneity on the interplay between these processes remains to be characterized. Here we study the role of these factors using mathematical and spatial models. We first designed models incorporating immunosuppressive effects on T cells mediated *via* PD-L1 and the EMT-inducing cytokine Transforming Growth Factor beta (TGFβ). Our models predict that PD-L1-mediated immunosuppression merely reduces the difference in PD-L1 levels between EMT states, while TGFβ-mediated suppression also causes PD-L1 expression to correlate negatively with TGFβ within each EMT phenotype. We subsequently embedded the models in multi-scale spatial simulations to explicitly describe heterogeneity in cytokine levels and intratumoral heterogeneity. Our multi-scale models show that Interferon gamma (IFNγ)-induced partial EMT of a tumor cell subpopulation can provide some, albeit limited protection to bystander tumor cells. Moreover, our simulations show that the true relationship between EMT status and PD-L1 expression may be hidden at the population level, highlighting the importance of studying EMT and PD-L1 status at the single-cell level. Our findings deepen the understanding of the interactions between EMT and the immune response, which is crucial for developing novel diagnostics and therapeutics for cancer patients.

KEYWORDS

epithelial-mesenchymal transition (EMT), PD-L1, immunoevasion, ordinary differential equations, cellular Potts model

1 Introduction

Activating invasion and metastasis, and avoiding immune destruction are core hallmarks of cancer, i.e., acquired capabilities that are crucial for the formation of malignant tumors (1). A comprehensive understanding of the interplay between these hallmarks is imperative for developing novel diagnostic and therapeutic approaches. Still, few studies to date have focused on the interaction between metastatic dissemination and immunoevasion, and hence its biological basis remains in large part unexplored.

Epithelial-mesenchymal transition (EMT), a process during which cells transition from an adhesive epithelial to a motile mesenchymal phenotype (2), is of critical importance for invasion and metastasis (reviewed in (3–5)). This phenomenon is increasingly referred to as epithelial-mesenchymal plasticity (EMP), because emerging evidence suggests that this transition is often incomplete, resulting in the manifestation of intermediate epithelial/mesenchymal (E/M) phenotypes (6). Such partial EMT programs in particular are associated with enhanced metastatic dissemination as well as therapy resistance (7, and reviewed in (8)). Moreover, EMT has been proposed to facilitate tumor immune escape (reviewed in 9).

A well-established mechanism through which cancer cells acquire immune resistance involves co-opting immune checkpoint pathways (10). Under normal physiological conditions, these pathways are pivotal for modulating the immune response and maintaining self-tolerance. As a case in point, tumor cells often upregulate the immune checkpoint protein Programmed Death-Ligand 1 (PD-L1) (11), either in response to inflammatory cytokines, such as Interferon gamma (IFNγ), or through constitutive oncogenic signaling (10). Interaction of PD-L1 with its receptor Programmed Death-1 (PD-1) on the membrane of T cells suppresses the survival, proliferation, and effector functions of these cells, including their cytokine release (12).

The literature reports numerous links between immunoevasion mediated by PD-L1 and EMT (reviewed in 13). One mechanism proposedly underlying the crosstalk between EMT and PD-L1-mediated immune resistance is that PD-L1 is post-transcriptionally regulated by the microRNA-200 (miR-200)–Zinc Finger E-Box Binding Homeobox 1 (ZEB1) axis (14–16), which is part of the 'core' EMT regulatory machinery (6). The binding of miR-200 to PD-L1 mRNA inhibits translation of the checkpoint ligand, and such binding can generally promote degradation of the miRNA–mRNA complex (17, 18). To investigate this mechanism, we recently presented a mathematical model connecting a model for the core EMT network to a model for IFNγ-induced PD-L1 expression (19), considering mutual inhibitory feedback between miR-200 and PD-L1. Model analysis showed that this interaction gives rise to tristability in PD-L1 levels, with a mesenchymal state corresponding with high PD-L1 expression, an epithelial state with low PD-L1 expression, and an E/M state with intermediate (albeit still relatively low) PD-L1 expression. Stimulation with IFNγ further amplifies the difference in PD-L1 expression between the stable EMT states. Furthermore, the bi-directional crosstalk between miR-200 and PD-L1 reduces the amount of inducing signal required to undergo EMT in the presence of IFNγ.

Despite displaying interesting dynamics relevant for tumor progression, our prior model of EMT–PD-L1 dynamics (19) did not take into account several mechanisms and factors affecting EMT and PD-L1 expression. First, an important missing mechanism was the negative feedback of PD-L1 on the IFNγ secretion of T cells, which results from the PD-L1–PD-1 interaction (20). Second, our prior model did not explicitly describe Transforming Growth Factor beta (TGFβ) as an EMT-inducing signal, and as a central player in tumor immune evasion (reviewed in 21). Of particular relevance here is the ability of TGFβ to inhibit IFNγ release both directly and indirectly by inhibiting T cell proliferation and differentiation. Third, our regulatory EMT–PD-L1 network model did not consider the potential role of spatial effects, such as the spatiotemporal and potentially localized spreading of cytokines within the tumor microenvironment (TME). Fourth, the model described the behavior of an average tumor cell and therefore did not account for intratumoral heterogeneity, which was recently demonstrated to contribute to resistance to PD-(L)1 blockade (22).

In the present study, we extended the model presented by Burger et al. (19) to explore the role of immunosuppression through PD-L1 or TGFβ, and of intratumoral heterogeneity on the crosstalk between EMT and PD-L1 expression. Analysis of our models with immunosuppression shows that negative feedback of PD-L1 on IFNγ only decreases the difference in PD-L1 expression between EMT phenotypes, whereas TGFβ-mediated IFNγ inhibition gives rise to a negative correlation between TGFβ and PD-L1 levels within EMT phenotypes. By subsequently embedding the above networks in multi-scale cell-based spatial simulations with cytokine spreading and intratumoral heterogeneity, we show that partial EMT of a tumor cell subset induced by IFNγ offers bystander tumor cells limited protection from IFNγ. Moreover, we demonstrate that a study at the cell population level may hide the underlying relation between PD-L1 expression and EMT status. Overall, our analysis illustrates how tumor-mediated immunosuppression and cytokine spreading can affect the complex relationship between EMT and PD-L1 status.

2 Results

2.1 PD-L1-mediated IFNγ inhibition limits PD-L1 primarily for mesenchymal cells

Within our previously modeled PD-L1–EMT network (Figure 1A, black, solid arrows), we did not consider the influence of immunosuppression. One way through which such suppression is expected to take place is the inhibition of IFNγ production following the interaction of tumor-expressed PD-L1 with T cell-expressed PD-1 (20). To study how this negative feedback of PD-L1 on IFNγ production affects the relationship between EMT and IFNγ-induced PD-L1 expression, we extended the model of

10.3389/fimmu.2023.1219669

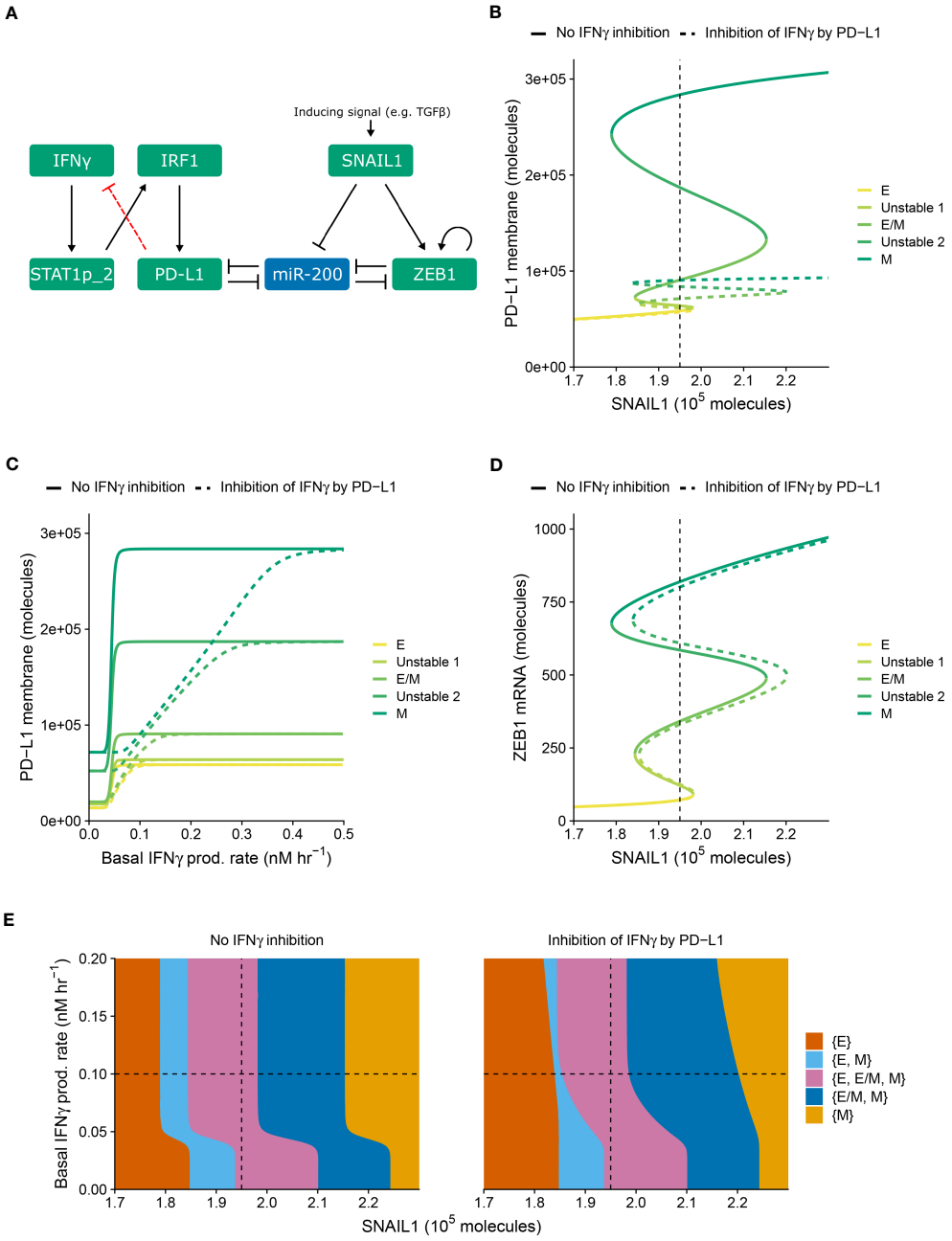

FIGURE 1
PD-L1-mediated IFNγ inhibition only quantitatively affects PD-L1 expression and EMT. **(A)** Schematic depiction of the EMT–PD-L1 regulatory network (black, solid arrows) extended with negative feedback of PD-L1 on IFNγ (red, dashed arrow). **(B–D)** Bifurcation **(B, D)** and continuation **(C)** diagrams illustrating how, in the absence (solid lines) and presence (dashed lines) of PD-L1-mediated IFNγ inhibition, the steady-state expression of PD-L1 on the membrane **(B)** and ZEB1 mRNA **(D)** depend on SNAIL1, considering a fixed basal IFNγ production rate of 0.1 nM h^{-1}, and the steady-state expression of PD-L1 on the membrane depends on the basal IFNγ production rate, considering a fixed SNAIL1 level of 1.95×10^5 molecules **(C)**. Colors represent the different stable equilibria (representing E, E/M, and M phenotypes) and unstable equilibria (indicated in legend). **(E)** Phase diagram showing how the presence of stable equilibria (colored regions, indicated in legend) depends on the basal IFNγ production rate and SNAIL1 in the absence (left) and presence (right) of PD-L1-mediated IFNγ inhibition. Vertical dashed lines in **(B, D, E)** show the SNAIL1 level used in **(C)**, while horizontal dashed lines in **(E)** show the basal IFNγ production rate used in **(B, D)**.

Burger et al. (19) with this regulation (Figure 1A, red, dashed arrow).

We examined the behavior of the modified network (i.e., with PD-L1-mediated IFNγ inhibition) for various levels of SNAIL1 (considered to be activated via, e.g., TGFβ) and baseline IFNγ production rates (Figure 1). The model with inhibition displays similar tristability in PD-L1 expression on the cell membrane as the model without inhibition (Figure 1B), resulting from several saddle-node bifurcations. In both models, mesenchymal cells have the highest PD-L1 level and epithelial cells the lowest. Notably, the negative feedback loop does not cause additional bifurcation points, hence the qualitative behavior of the two models is the same.

However, the feedback does decrease PD-L1 expression for all EMT phenotypes, thereby reducing the absolute and relative differences in PD-L1 expression between phenotypes. The inhibition affects the equilibrium PD-L1 level for all phenotypes when the IFNγ production rate is low, but only the mesenchymal phenotype for intermediate IFNγ production rates (Figure 1C). At high IFNγ production rates, the feedback has no effect on PD-L1 expression for any phenotype because the IFNγ level is still sufficiently high to closely approach the maximal transcription rate of PD-L1.

We subsequently investigated the impact of PD-L1-mediated IFNγ inhibition on ZEB1 expression and EMT phenotype stability. The inhibition causes a rightward shift of the upper part of the bifurcation diagram of ZEB1 as dependent on SNAIL1 input signal (Figure 1D), because a reduced PD-L1 expression leads to an increased amount of miR-200, in turn affecting EMT. To further characterize this effect, we created a phase diagram showing how the stability of EMT phenotypes depends on SNAIL1 levels and baseline IFNγ production rates (Figure 1E). Compared to the model without IFNγ inhibition, in the presence of such inhibition the IFNγ-induced leftward shift occurs for higher IFNγ production rates and is no longer parallel for the different bifurcation points. These bifurcation point shifts remain similar upon adjustment of the model parameters implementing the negative feedback, i.e., a sensitivity analysis (Figure S1, left panels). In conclusion, our model predicts that negative feedback of PD-L1 on IFNγ has a quantitative, but not qualitative, effect on the relationship between EMT and PD-L1 expression.

2.2 TGFβ-mediated IFNγ inhibition causes PD-L1 expression to correlate negatively with TGFβ within EMT phenotypes

Apart from PD-L1-mediated IFNγ inhibition leading to immunosuppression, such suppression can also be invoked by TGFβ. In order to separately study the impact of this alternative inhibition on the crosstalk between EMT and IFNγ-induced PD-L1 expression, we explicitly described TGFβ in our model as a driver of SNAIL1 expression (Figure 2A). Moreover, we extended this model with the inhibition of IFNγ production by TGFβ, in a similar manner as for PD-L1-mediated IFNγ production.

Using this modified model (i.e., with TGFβ-mediated IFNγ inhibition), we studied how the system responds to different levels of TGFβ and baseline IFNγ production rates (Figure 2). As was the case for PD-L1-mediated IFNγ inhibition, the model extension with TGFβ-mediated IFNγ inhibition does not affect the tristability of PD-L1 expression on the membrane (Figure 2B). However, TGFβ-mediated IFNγ inhibition leads to a complicated relation between PD-L1 expression and TGFβ. Specifically, PD-L1 levels tend to correlate negatively with TGFβ within each EMT phenotype, especially for low IFNγ production rates. Across EMT phenotypes, there is still a primarily positive correlation between TGFβ and PD-L1 expression

Next, we investigated the influence of TGFβ-mediated IFNγ inhibition on ZEB1 and the stability of EMT phenotypes. In the bifurcation diagram of ZEB1, as dependent on the TGFβ concentration (Figure 2C), it causes a rightward shift of the bifurcation point separating the {E/M, M} and {M} states compared with the model without inhibition. Consequently, the total range of TGFβ for which the hybrid E/M phenotype can (co-) exist is strongly increased. This is reminiscent of the influence of other proteins such as OVOL on the core EMT regulatory network (23, 24), although contrary to OVOL expression, TGFβ-mediated IFNγ inhibition does not lead to a range in which the hybrid E/M phenotype is the only possible phenotype. The increase occurs for a range of IFNγ production rates, as visualized in a phase diagram depicting the various stability regimes (Figure 2D). Interestingly, upon increasing the IFNγ production rate, the same bifurcation point undergoes a leftward shift, leading to a part of the curve gradually splitting off and eventually disappearing (Figure S2). This phenomenon also occurs for the bifurcation point separating the {E, E/M, M} and {E/M, M} states (Figure S2). Nevertheless, this only occurs for very limited ranges of IFNγ production rates. Importantly, also this model extension exhibits good robustness with respect to changes in inhibition-related parameter values (Figure S1, right panels). Moreover, when we combined both PD-L1- and TGFβ-mediated IFNγ inhibition, the effects observed for the separate inhibition mechanisms were retained (Figure S3). In summary, TGFβ-mediated IFNγ inhibition mainly results in a negative correlation between TGFβ and PD-L1 expression within EMT phenotypes, yet a positive correlation across phenotypes.

2.3 IFNγ-induced partial EMT of a tumor cell subset can provide limited protection to bystander tumor cells

In practice, the outcome of the crosstalk between EMT and IFNγ-induced PD-L1 expression is likely to also depend on the (an) isotropy of the TME with regard to the involved cytokines IFNγ and TGFβ. Therefore, we embedded our models describing IFNγ inhibition by either PD-L1 or TGFβ, or without such IFNγ inhibition, in multi-scale spatial simulations using the cellular Potts model (CPM) (25, 26). These 2D simulations comprise tumor cells, IFNγ-secreting $CD8^+$ T cells, and a partial differential equation (PDE) layer describing the spatiotemporal spreading of IFNγ. The production and cellular uptake rates of IFNγ were derived from the literature (see Methods for details). Our simulations additionally include a static TGFβ field that is either uniform or has a gradient with the highest concentrations at the tumor edge. The latter mimics the accumulation of TGFβ at the invasive front which has been experimentally observed (27, 28).

Discussion is ongoing concerning how far $CD8^+$ T cell-derived IFNγ can spread within the TME. Specifically, mathematical simulations predict cytokine gradients in dense, cytokine-consuming environments to range between one and a few cell diameters (29). However, these predictions are contradicted by experimental findings showing that IFNγ produced by activated $CD8^+$ T cells diffuses substantially from the site of tumor cell-T cell interaction (30, 31). Since both extremes are likely relevant and can depend on tumor-secreted factors such as galectins (32), we investigated two extreme spreading scenarios by modifying

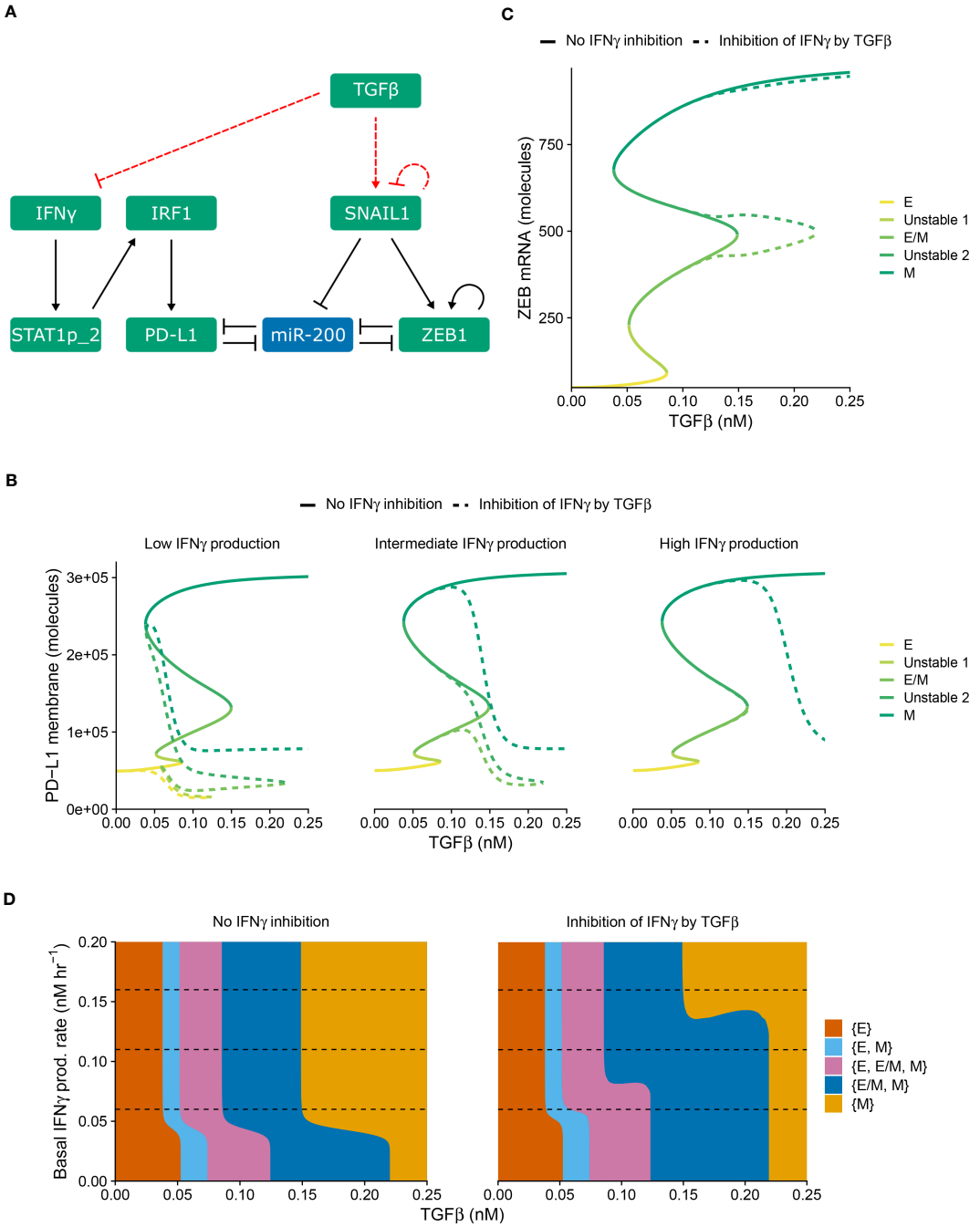

FIGURE 2
TGFβ-mediated IFNγ inhibition causes PD-L1 expression to correlate negatively with TGFβ within each EMT phenotype. **(A)** Schematic depiction of the EMT–PD-L1 regulatory network (black, solid arrows) extended with TGFβ-mediated IFNγ inhibition and SNAIL1 stimulation (red, dashed arrows). **(B, C)** Bifurcation diagrams illustrating how, in the absence (solid lines) and presence (dashed lines) of TGFβ-mediated IFNγ inhibition, the steady-state expression of PD-L1 on the membrane **(B)** and ZEB1 mRNA **(C)** depend on TGFβ, considering fixed basal IFNγ production rates of 0.06 nM h^{-1} (**B**, left), 0.11 nM h^{-1} (**B**, middle, and **C**), and 0.16 nM h^{-1} (**B**, right). Colors represent the different stable equilibria (representing E, E/M, and M phenotypes) and unstable equilibria (indicated in legend). **(D)** Phase diagram showing how the presence of stable equilibria (colored regions, indicated in legend) depends on the basal IFNγ production rate and TGFβ concentration in the absence (left) and presence (right) of TGFβ-mediated IFNγ inhibition. Horizontal dashed lines in **(D)** show the basal IFNγ production rates used in **(B, C)**.

the rate of cellular uptake of IFNγ. For these short- and long-range spreading scenarios, the IFNγ concentration in molecules $cell^{-1}$ decreases by a factor of 2.7 within one and six cell layers, respectively.

We first employed our multi-scale models to study a long-range IFNγ spreading scenario within a T cell-infiltrated tumor embedded in a uniform TGFβ field (Figure 3A and Video S1). We considered tumor cells to be either homogeneous or heterogeneous with regard

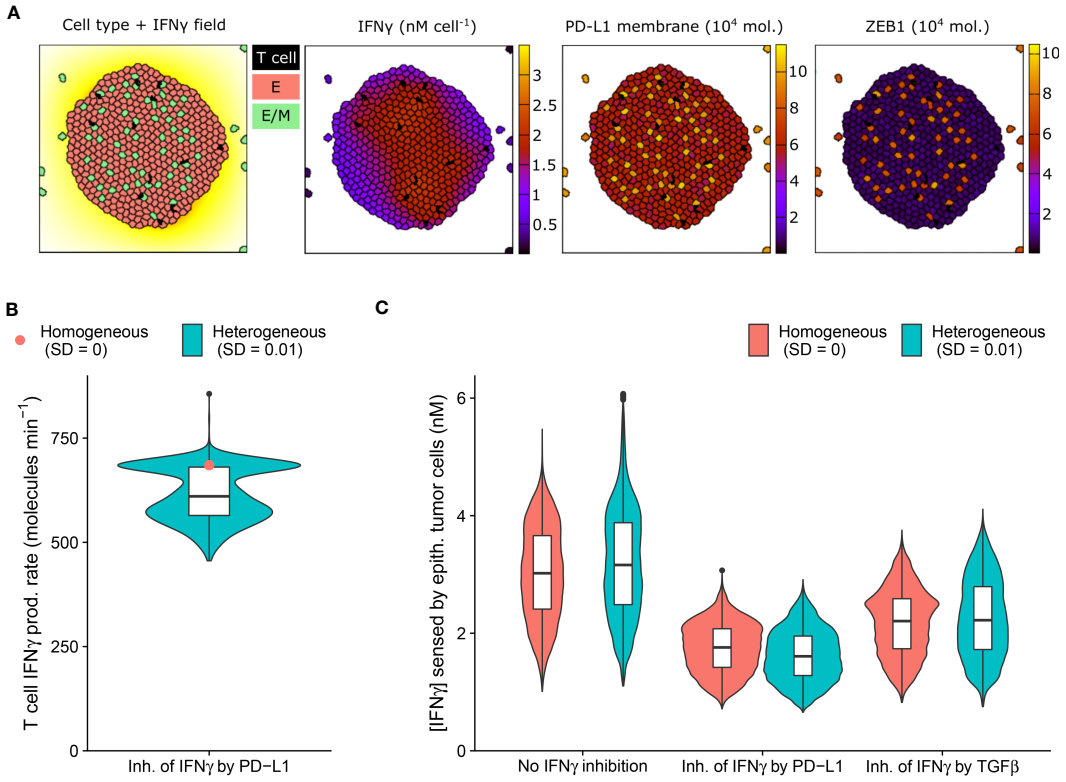

FIGURE 3
An IFNγ-induced hybrid tumor subset can provide limited protection to bystander epithelial tumor cells. **(A)** Still images of a CPM simulation of IFNγ-secreting T cells within a tumor with long-range IFNγ spreading, intratumoral heterogeneity, and PD-L1-mediated IFNγ inhibition. Left color scheme: lattice sites are colored according to IFNγ level; T cells are black, and epithelial (E) and hybrid (E/M) tumor cells are red and green, respectively. Other color schemes: T cells are black, and tumor cells are colored according to IFNγ (middle-left), PD-L1 (middle-right), and ZEB1 (right) levels. Elapsed simulation time is 2410 minutes. **(B, C)** Violin and box plots showing the IFNγ production rate of T cells **(B)** and the IFNγ concentration sensed by epithelial tumor cells **(C)**. In **(B)**, results are shown for a tumor with negative feedback of PD-L1 on IFNγ, and in **(C)** for tumors without IFNγ inhibition (left), inhibition of IFNγ by PD-L1 (middle) or by TGFβ (right). Colors denote heterogeneous (blue) or homogeneous tumors (red; only median is shown in **(B)**). Plots are based on data 2100-2410 minutes after initialization and 5 simulations per condition.

to their model parameter values (see Methods), with the latter scenario likely being the most realistic for human cancers. We simulated limited heterogeneity so that no epithelial tumor cells spontaneously underwent EMT in the absence of IFNγ. Under this condition, cells also did not undergo a complete transition to a mesenchymal state in the presence of IFNγ.

IFNγ has a dual role in cancer immunity (reviewed in 33) and is implicated in tumor immune surveillance through the induction of tumor cell cycle arrest, senescence, and death. The presence of intratumoral heterogeneity makes it plausible that a subset of tumor cells is resistant to the antitumorigenic effects of IFNγ, yet is sensitive to other IFNγ-driven responses, including partial or full EMT. Because these transitions could in turn affect PD-L1 expression, inhibiting further IFNγ production, bystander tumor cells might indirectly be protected by EMT of a tumor subpopulation. We therefore investigated this potential impact of EMT triggered in a tumor subpopulation on bystander tumor cells.

As anticipated, our model predicts the entire tumor to be exposed to IFNγ due to the substantial IFNγ spreading (Figure 3A). Notably, the tumor cell subset that converts to an intermediate E/M state in response to IFNγ (12%) has a higher PD-L1 expression than cells remaining epithelial. In tumors with PD-L1-mediated inhibition of IFNγ secretion by neighboring T cells, this increased PD-L1 level gives rise to a clear subset of T cells with a low IFNγ production rate (Figure 3B). Consequently, epithelial tumor cells have on average a 7.0% lower IFNγ exposure in heterogeneous versus homogeneous tumors with PD-L1-mediated IFNγ inhibition (Figure 3C). Note that this small difference in sensed IFNγ by tumor cells between the homogeneous and heterogeneous scenario does not occur for tumors without IFNγ inhibition or with TGFβ-mediated IFNγ inhibition. In the scenario without IFNγ inhibition, the epithelial subpopulation is even exposed to a slightly higher (5.6%) IFNγ concentration in heterogeneous compared to homogeneous tumors. This is because several hybrid cells escape the tumor (Figure 3A), thereby no longer inhibiting IFNγ production of intratumoral T cells, and causing the remaining epithelial cells to reside close to the IFNγ-rich tumor center. This implies that the true effect of E/M hybrid cells on IFNγ reduction caused by the inhibition of IFNγ by PD-L1 is in fact larger than the net 7.0%. In summary, our spatial simulations provide

evidence for a potential protective effect provided by a small subpopulation of hybrid tumor cells towards the remainder of the tumor population owing to PD-L1-mediated immunosuppression.

2.4 Population-level responses may hide the relationship between PD-L1 expression and EMT status

In all investigated ODE models with or without immunosuppression, we found a clear relation between EMT and PD-L1 status, predicting PD-L1 to be lowest for epithelial cells, intermediate for hybrid E/M cells, and highest for mesenchymal cells. However, it is unclear whether this relation can be uncovered in experimental data when studying tumor cells at population level. Therefore, we investigated the relation between EMT status, ZEB1, and PD-L1 within spatial simulations implementing scenarios with short-range IFNγ spreading at the invasive front of a tumor. Note that we utilized scenarios without intratumoral heterogeneity in order to prevent this source of heterogeneity from detecting relationships between markers. Because TGFβ accumulation may occur at the invasive front in carcinomas (27, 28), we simulated tumors with either a homogeneous TGFβ field or a TGFβ gradient (Figure 4A and Videos S2, S3), in the absence or presence of IFNγ inhibition (either by PD-L1 or by TGFβ).

Within tumors with homogeneously distributed TGFβ or with a TGFβ gradient, the overall relationship between PD-L1 membrane and ZEB1 expression is as expected, with a higher PD-L1 expression being accompanied by a higher ZEB1 expression (Figures 4B–D). For instance, for tumors with a TGFβ gradient, those without IFNγ inhibition have both the highest PD-L1 and ZEB1 levels. However, between these two TGFβ tumor types, the relationship between PD-L1 and ZEB1 expression is not as straightforward. Specifically, when there is no IFNγ inhibition or PD-L1-mediated IFNγ inhibition, tumors obtain a similar level of PD-L1 expression regardless of the shape of the TGFβ field (Figure 4B; blue and orange), whereas tumors with a TGFβ gradient reach a much higher ZEB1 expression (Figure 4C; blue and orange). Moreover, in the case of IFNγ inhibition by TGFβ, tumors with a TGFβ gradient obtain a considerably lower PD-L1 (Figure 4B; green) but a similar ZEB1 level compared to those with a uniform TGFβ field (Figure 4C; green).

We subsequently examined the temporal relationship between PD-L1 membrane expression and EMT status on a single-cell level. For all tumors that are isotropic with regard to TGFβ, our models predict that the number of hybrid cells continues to increase over time (Figure 4E). This coincides with an increase in ZEB1 (Figure 4C), yet PD-L1 levels approximately reach a steady state (Figure 4B). This also applies to tumors with a TGFβ gradient and IFNγ inhibition by TGFβ (Figures 4B, C, E), although in that case the number of hybrid cells reaches a steady state. There is a minor continued increase in the number of fully mesenchymal cells in this setting (Figure 4E). Only in tumors with a TGFβ gradient and no immunosuppression or PD-L1-mediated IFNγ inhibition, PD-L1 expression continues to increase over time (Figure 4B). To conclude, an increase in the number of hybrid E/M or mesenchymal cells coincides with an increase in EMT marker ZEB1 in all studied scenarios, yet PD-L1 expression does not always keep increasing along with ZEB1. For individual tumor cells, however, we do observe the expected positive correlation between PD-L1 and ZEB1 expression in each scenario (Figure S4). This relation is most evident at high IFNγ levels (i.e., the top edge in each panel) in tumors with a TGFβ gradient. This implies that studying tumors at a population level may conceal the relationship between PD-L1 membrane expression and EMT status.

3 Discussion and conclusion

In the current study, we created mathematical and spatial models of the crosstalk between EMT and IFNγ-induced PD-L1 expression and showed that immunosuppression and heterogeneity across tumor cells and space lead to a highly complex relationship between EMT status and PD-L1 expression in cancer. Adding immunosuppression in the form of a negative feedback loop from PD-L1 on IFNγ affects this relationship only quantitatively, diminishing the differences in PD-L1 levels between the EMT phenotypes. The effect of immunosuppression through inhibition of IFNγ by TGFβ, on the other hand, results in a negative correlation between PD-L1 expression and TGFβ within each EMT phenotype. When combining PD-L1- and TGFβ-mediated IFNγ inhibition (through the multiplication of the two shifted Hill functions involved), the observed effects are consistent with those of each inhibition mechanism individually. Note that a different type of interaction between these inhibitions, such as synergism or antagonism (34), could potentially affect this outcome. Embedding the above model versions in spatial simulations of immune-infiltrated tumors, we demonstrated that IFNγ-induced partial EMT of a tumor cell subpopulation can provide limited protection to bystander tumor cells by limiting their exposure to IFNγ. Lastly, we showed that studying EMT status and PD-L1 expression at a population level may conceal their relationship. Our findings contribute to a more comprehensive understanding of the interaction between EMT and the immune response, which is essential for developing novel diagnostic and therapeutic options for cancer patients.

An interesting prediction from our models is that even though IFNγ-induced EMT gives rise to a continuous increase in average ZEB1 expression over time (Figure 4C), average PD-L1 expression may reach a steady state (Figure 4B). A potential underlying reason is that local fluctuations in IFNγ cause fluctuating PD-L1 levels that may conceal the relation between PD-L1 and ZEB1 expression (Figure S4). In addition, the EMT-induced upregulation of PD-L1 is relatively small compared to the initial IFNγ-induced PD-L1 upregulation. Moreover, note that our models (including the model on which our extensions are based, i.e. Burger et al. (19)) predict hybrid E/M cells to have only slightly increased (Figure 1B) or even lower (Figure 2B) PD-L1 expression compared to epithelial cells, especially in the absence of IFNγ. This is contradicted by a recent mathematical model presented by Sahoo et al. (35), which predicts an almost equal (high) level of PD-L1 for the hybrid and mesenchymal phenotypes. The model-predicted difference in PD-

10.3389/fimmu.2023.1219669

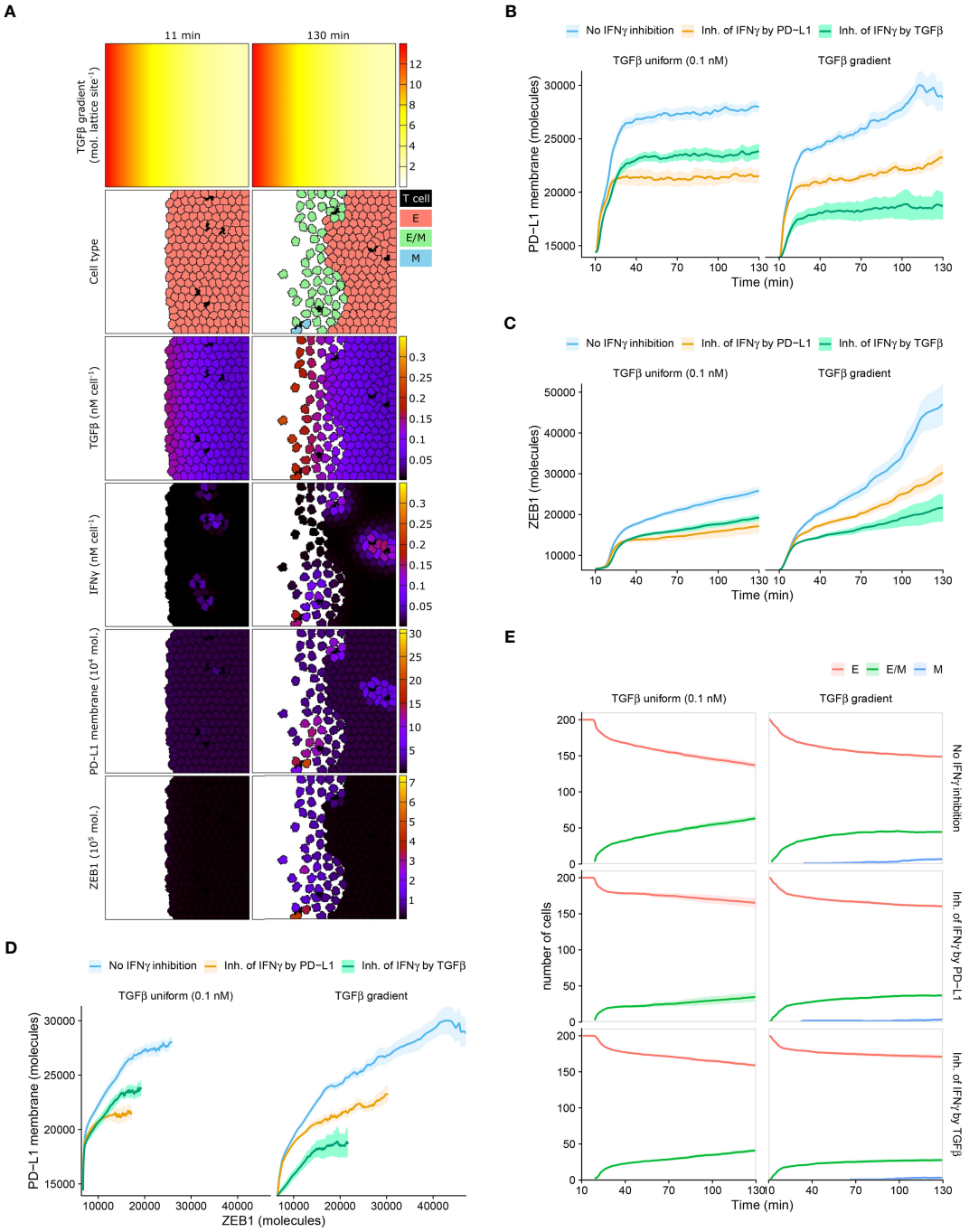

FIGURE 4
Mean PD-L1 expression need not correlate with EMT status. **(A)** Still images of a CPM simulation of IFNγ-secreting T cells at a tumor invasive front with short-range IFNγ spreading, a TGFβ gradient, and no IFNγ inhibition. Top color scheme: lattice sites are colored according to TGFβ level. Second color scheme from the top: T cells are black, and epithelial (E), hybrid (E/M), and mesenchymal (M) tumor cells are red, green, and blue, respectively. Other color schemes: T cells are black, and tumor cells are colored according to (from top to bottom) TGFβ, IFNγ, PD-L1, and ZEB1 levels. Elapsed simulation time in minutes is displayed above the stills. **(B, C)** Average (bold line) and standard error of the mean (SEM; ribbon) of PD-L1 membrane **(B)** and ZEB1 **(C)** expression of tumor cells over time. **(D)** Average (bold line) and SEM (ribbon) of PD-L1 membrane expression as a function of ZEB1 expression over time. **(E)** Average (bold line) and SEM (ribbon) of the number of tumor cells per EMT phenotype (indicated in legend) over time. Plots in **(B–E)** are based on 10 simulations per condition, and results are shown for tumors with a uniform TGFβ field (left panels) or a TGFβ gradient (right panels). The absence or mode of IFNγ inhibition is indicated in the legend.

L1 expression between the hybrid E/M and epithelial states suggests that it is necessary to perform temporal experiments at a single-cell level to accurately capture the relationship between PD-L1 expression and EMT status (similar to Figure S4). Thus, future research should further characterize this difference, including its context and cell-line specificity.

The complexity of the relationship between PD-L1 expression and EMT status, and the influence of immunosuppression and

spatial distribution of cytokines IFNγ and TGFβ, have relevant diagnostic implications. Both PD-L1 and EMT scores have been proposed as biomarkers for selecting patients responding to PD-1/PD-L1 blockade therapy (36, 37). However, the numerous mechanisms and factors affecting the expression of PD-L1 and EMT regulators, such as ZEB1, complicate their use as selective biomarkers (6, 38, 39). Regarding PD-L1, our model indeed predicts that a low expression may be attributed to a lack of an active immune response (initial PD-L1 level in Figure 4B). Alternatively, the PD-L1 level could have been high initially, suppressing the immune response and consequently decreasing the expression of PD-L1. Therefore, using PD-L1 as a predictive biomarker may prevent the treatment of a subset of patients who, despite their low to moderate PD-L1 expression, have a high probability of responding. For ZEB1 as a biomarker, a major difficulty lies in the fact that its absolute expression may depend on the shape of the TGFβ field (Figure 4C), as our simulations predict. Moreover, since diverse signaling pathways regulate ZEB1 activity (40), a ZEB1^{high} tumor status is not necessarily associated with an ongoing immune response.

Furthermore, our findings support the hypothesis that T cell suppression by a hybrid E/M subpopulation in tumors with considerable IFNγ spreading may contribute to collective immunoevasion by decreasing the overall IFNγ level, albeit only slightly (Figure 3C). Several processes may play a role in this limited protection provided by hybrid E/M cells to other tumor cells in our simulations. First, the small effect size may partly be attributed to the aforementioned minor difference in PD-L1 expression between hybrid E/M and epithelial cells. Second, in our simulations, a substantial number of hybrid cells escape the tumor on account of their increased motility (Figure 3A). Note that this is in contrast with experimental observations and mathematical modeling predictions in breast carcinoma where hybrid cancer stem cells (CSCs) were found to typically reside in the tumor interior (41, 42). This distribution originated from differential EMT-inducing signals in the interior and outer regions of the tumor. Nevertheless, these findings do not exclude the possibility that hybrid (or fully mesenchymal cells) escape the tumor, as this was not specifically investigated. For example, the mathematical model of Bocci et al. (42) did not consider migration of hybrid or mesenchymal CSCs. Third, in our models we consider the IFNγ production by T cells to increase instantly upon detaching from a hybrid tumor cell. In reality, the slightly increased PD-L1 level of hybrid cells compared to epithelial cells may contribute to a sustained state of T cell exhaustion (20), resulting in long-term impaired IFNγ secretion. For these reasons, the protective effect of the hybrid tumor subset over the remainder of the tumor population may be larger than predicted here. Even if this is not the case in reality, only a minor IFNγ reduction may already be highly relevant, e.g., if it lowers the IFNγ level beyond a certain efficacy threshold of the cytopathic and cytostatic effects of IFNγ (33). If so, therapeutically targeting the hybrid subpopulation may increase the overall IFNγ concentration beyond said threshold, enhancing, e.g., the IFNγ-mediated killing of bystander epithelial tumor cells. In the future, it would therefore be useful to expand our models with the dynamics of tumor growth and T cell-mediated killing, to evaluate the importance of the predicted decrease in IFNγ. As an example of a similar approach, Benchaib et al. (43) describe tumor growth dynamics and IFNγ-induced dormancy in their mathematical model of the interaction between cancer and immune cells in the lymph node. Their simulations predict three possible outcomes that coincide with the main phases of the immunoediting process, namely tumor elimination, equilibrium, and evasion.

In our multi-scale spatial simulations, we make two more assumptions regarding T cells that would likely affect our model predictions quantitatively. First, we consider the ratio of T cells to tumor cells to be 1:40. Although this ratio represents a realistic scenario, lower ratios have been observed in some tumors, for example in glioblastoma (44). Naturally, in such tumors with very limited T cell infiltration (immunologically cold tumors), the effects predicted by our models will be less pronounced. Second, we consider T cells not to consume IFNγ. However, given that IFNγ has been shown to increase the abundance of the T cell population (45) as well as their migration and cytotoxicity (46), T cells likely take up IFNγ to a certain extent. Still, given the low T cell:tumor cell ratio, we expect that this additional consumption has only a minor effect on intratumoral IFNγ concentrations. Moreover, to our knowledge, there is no evidence indicating that T cells preferentially consume large quantities of IFNγ relative to tumor cells.

We propose that one promising therapeutic strategy for combating not only tumor immunoevasion but also cancer metastasis involves interfering with the pathways that control the interplay between EMT and PD-L1. Increasing efforts already focus on searching for opportunities to therapeutically interfere with EMT in cancer (reviewed in 47). Potential therapeutic candidates include upstream signaling pathways, such as the TGFβ signaling pathway, and molecular drivers of EMT. Blocking TGFβ signaling may also hinder its T cell-suppressive effects and is therefore an especially interesting approach. Nevertheless, our model-based analysis suggests that IFNγ is a more prominent driver of PD-L1 expression than EMT-driven PD-L1 expression *via* miR-200, which is consistent with our recent bioinformatic analysis of cancer patient data from the Cancer Genome Atlas (39). As such, we expect combination therapies of agents targeting EMT and the PD-1–PD-L1 interaction to be most effective for enhancing the antitumor immune response. Consistent with this, co-administration of TGFβ-blocking and anti-PD-L1 antibodies provoked antitumor immunity and tumor regression in metastatic urothelial cancer by facilitating T cell infiltration (48). We conclude that there is ample potential for therapeutic exploitation of the EMT–PD-L1 axis.

Our multi-scale models have three important limitations. A first limitation is that we markedly accelerated the EMT and PD-L1 regulatory network dynamics relative to their true cellular and spatial dynamics to reduce computation time. As a consequence, PD-L1 expression in our simulations was established on a time scale of seconds instead of hours, and a full EMT transition required minutes instead of days (cf. Figures 1D–F in 19). For the long-range IFNγ spreading scenario, this merely implies that in practice more time is needed for a subpopulation of hybrid cells to emerge and suppress the immune response. In actual tumors with short-range IFNγ spreading, however, the brief T cell-tumor cell interactions in

our simulations might be insufficient to induce PD-L1 expression, let alone an EMT. Still, $CD8^+$ T cells normally form conjugates with antigen-expressing tumor cells that can last minutes to hours (49), presumably exposing tumor cells to IFNγ for a sufficient period to induce PD-L1 expression and consequently trigger EMT.

A second limitation of our simulations is that we modeled the difference in motility between the EMT phenotypes only based on cell surface interactions, and we did not differentiate between the migratory behavior of cells in a partial EMT or mesenchymal state. Future efforts should focus on the implementation of a more sophisticated cancer invasion model, such as the cellular Potts-based model recently presented by Pramanik et al. (50), to better characterize how different modes of cell migration contribute to cancer metastasis as a consequence of EMT–PD-L1 crosstalk.

Lastly, a third limitation of our work is that we considered $CD8^+$ T cells to be the only source of IFNγ in our models, even though it is well established that other immune cells in the TME can also secrete this cytokine. Examples include $CD4^+$ T cells, natural killer (NK) cells, and NK T cells (51). A recent study even found the production of IFNγ by $CD4^+$ chimeric antigen receptor (CAR) T cells to be considerably higher than that of $CD8^+$ CAR T cells in a model of B-cell malignancy (52). Since these additional cellular components could potentially affect how our simulations replicate tumor biology, it would be worth including them (and the effects of additionally produced IFNγ) in future model versions. This also applies to the cellular sources of TGFβ, which include tumor cells, regulatory T cells, fibroblasts, and macrophages (21). We currently described this cytokine with a static field (either uniformly distributed or with a gradient) but it could instead be modeled dynamically. Note that such an effort would benefit from additional experiments to obtain reliable production and cellular uptake rates.

In conclusion, we extended an existing mathematical model and embedded it in multi-scale spatial simulations to describe the effects of immunosuppression and spatial heterogeneity on the crosstalk between EMT and IFNγ-induced PD-L1 expression. Our analysis demonstrates that the relation between PD-L1 expression and EMT status is highly complex, and depends on the forms of immunosuppression established by the tumor as well as on spatial heterogeneity concerning cytokines influencing these pathways. Experimental validation of the hypotheses presented here based on temporal, single-cell measurements will be required to shed further light on the relationship between PD-L1 expression and EMT status. Ultimately, these insights may contribute to the development of novel therapeutic strategies for effectively combating metastatic dissemination as well as immunoevasion.

4 Materials and methods

4.1 ODE models

4.1.1 IFNγ–PD-L1–EMT model

The IFNγ–PD-L1–EMT model (19) uses appropriate miRNA–mRNA dynamics from the theoretical framework by Lu et al. (53) (see Supplementary Information) to combine the simplified TCS model (24) with a model for IFNγ-induced PD-L1 expression, which is based on an extension of a published JAK–STAT model (54). See Supplementary Information for the model definition and used parameters.

4.1.2 Negative feedback of PD-L1 on IFNγ

Even though the negative feedback of membrane-bound PD-L1 on the production of IFNγ is not mediated by direct transcriptional regulation, for simplicity, we used a shifted Hill function to model this regulation. The shifted Hill function for activation and inhibition of A by B is defined as

$$H^S(B, \lambda_{BA}) = H^-(B) + \lambda_{BA} H^+(B), \tag{1}$$

$$H^-(B) = \frac{1}{1 + (\frac{B}{B_A^0})^{n_{BA}}}, \tag{2}$$

$$H^+(B) = 1 - H^-(B), \tag{3}$$

where the weight factor λ_{BA} represents the fold change in the production rate of A due to B, with $\lambda_{BA} > 1$ for activation and $\lambda_{BA} < 1$ for inhibition. The Hill coefficient n_{BA} represents the cooperativity of the interaction, while the threshold B_A^0 is the concentration of B at which the value of H^- equals 0.5. The IFNγ–PD-L1–EMT model uses the concentration of IFNγ (in nM) as input. Here, we model the IFNγ (I) concentration with the following ordinary differential equation (ODE):

$$\frac{dI}{dt} = g_I H^S(P_M, \lambda_{P_M,I}) - k_I I\,. \tag{4}$$

The meaning of parameters and their utilized values are provided in Table 1. We chose the basal production and degradation rate of IFNγ arbitrarily and varied the former to simulate different levels of IFNγ exposure. Note that upon embedding our ODE models into multi-scale spatial simulations (see below), we utilized IFNγ production and cellular uptake rates from the literature. To our knowledge, there are no experimental data available in which both IFNγ secreted by T cells and the tumor cell membrane PD-L1 expression are measured. For simplicity, we chose the value 0.1 for $\lambda_{P_M,I}$ to allow for a considerable inhibitory effect, and the value 2 for $n_{P_M,I}$. $P_M{}_I^0$ was loosely based on the half-functional rule defined in Huang et al. (55), which states that a regulatory link should have an approximately equal chance of being functional or not functional. Note that we performed a sensitivity analysis to study the impact of these parameter values on the model predictions (Figure S1, left panels).

4.1.3 TGFβ–SNAIL1 model

For the TGFβ–SNAIL1 submodel, we adapted the TGFβ–miR-200 and SNAIL1–miR-34 modules of the revised CBS model (56, see Supplementary Information; originally published by 57). Our key modifications are the exclusion of the autocrine TGFβ–miR-200 feedback loop and the double-negative SNAIL1–miR-34 feedback loop. Because we later implement the ODE models in multi-scale models wherein tumor cells respond to extra-cellular TGFβ, our revised submodel did not need to describe TGFβ mRNA. Instead, we consider the protein TGFβ to be produced at a constant

TABLE 1 Parameters used for the model extensions representing the immunosuppressive effects of PD-L1 and TGFβ.

		Prod. rate g		Degr. rate k		
IFNγ	I	g_I	0-0.5 nM h^{-1}	k_I	1 h^{-1}	
	Threshold B_A^0		Hill coefficient n_{BA}		Max. fold change λ_{BA}	
Inh. I by P_M	$P_{M_I}^0$	6×10^4 mol.	$n_{P_M,I}$	2	$\lambda_{P_M,I}$	0.1
Inh. I by T	T_I^0	0.1 nM	$n_{T,I}$	2	$\lambda_{T,I}$	0.1

The top panel shows the production and degradation rate of IFNγ; the bottom panel shows parameters for the shifted Hill functions of the interactions. The parameter values were not directly obtained from the literature but were selected in this study. The production rate of IFNγ was varied to simulate different IFNγ levels.

rate and to be degraded linearly, which is effectively identical to having a fixed TGFβ concentration as input. The revised TGFβ–SNAIL1 submodel consists of the following ODEs for TGFβ (T), SNAIL1 mRNA (m_S), and SNAIL1 protein (S):

$$\frac{dT}{dt} = g_T - k_T T, \tag{5}$$

$$\frac{dm_S}{dt} = g0_{m_S} + g_{m_S} H^+(T) H^-(S) - k_{m_S} m_S, \tag{6}$$

$$\frac{dS}{dt} = g_S m_S - k_S S\,. \tag{7}$$

All initial conditions (i.e., the initial concentrations of T, m_S, and S) are set to 0. At the beginning of a simulation, the levels of TGFβ and SNAIL1 mRNA swiftly become positive because of their baseline production rates, which in turn triggers the production of SNAIL1 protein. Parameter meanings and utilized values are provided in Table 2. Note that, for consistency, we use g and k to denote production and degradation rates. As with IFNγ, we use arbitrary values for the production and degradation rate of TGFβ and vary the former to simulate different TGFβ exposure levels.

To create our extended model, we connected the TGFβ–SNAIL1 submodel to the central IFNγ–PD-L1–EMT model (see Figure 2A). Note that we converted the output SNAIL1 concentration, which was in nM in Zhang et al. (56) into number of molecules in order to use SNAIL1 as input in the IFNγ–PD-L1–EMT model. For consistency, we converted SNAIL1 mRNA to number of molecules as well. As in Jolly et al. (24) and Burger et al. (19), we use a cell volume of 10000 μm^3, such that 1 nM amounts to approximately 6020 molecules ($6.02 \times 10^{23} \cdot 10^{-9} \cdot 10000 \times (10^{-5})^3$). To properly convert units, we thus multiplied model parameters $g0_{m_S}$, g_{m_S}, and J_{m_S1} with 6020. In addition, we matched the range of TGFβ within which bifurcations occur to that of the CBS model by modifying parameters $g0_{m_S}$, g_{m_s}, and J_{m_S0}.

4.1.4 Inhibition of IFNγ by TGFβ

Modeling the individual components of pathways involved in the TGFβ-mediated inhibition of IFNγ secretion is a complex task. As for PD-L1-mediated IFNγ inhibition, we also used a shifted Hill function to model this regulation in a phenomenological manner. In this case, we model the IFNγ concentration (I) with the following ODE:

$$\frac{dI}{dt} = g_I H^S(T, \lambda_{T,I}) - k_I I. \tag{8}$$

Parameter meanings and utilized values are provided in Table 1. In the absence of experimental data on the relationship between extracellular TGFβ and T cell IFNγ release, in selecting the shifted Hill function parameter values we took into account the same

TABLE 2 Variables and parameters used for the TGFβ–SNAIL1 module.

		Prod. rate g		Degr. rate k	
TGFβ protein	T	g_T	0-0.3 nM h^{-1}	k_T	1 h^{-1}
SNAIL1 mRNA	m_S	$g0_{m_S}$	1500 molecules h^{-1}	k_{m_s}	0.09 h^{-1}
		g_{m_S}	600 molecules h^{-1}		
SNAIL1 protein	S	g_S	17 h^{-1}	k_S	1.66 h^{-1}
	Threshold B_A^0		Hill coefficient n_{BA}		
Act. m_S by T	J_{m_S0}	0.1 nM	n_{nt}	2	
Inh. m_S by S	J_{m_S1}	4.0334×10^6 molecules	n_{ns}	1	

The top panel shows variable names and production and degradation rates; the bottom panel shows parameters for the Hill functions of the interactions. Parameter values were either taken from the revised CBS model by Zhang et al. (56) or modified (shade). $g0_{m_s}$ is the baseline production rate of SNAIL1 mRNA. The production rate of TGFβ was varied to simulate different TGFβ levels.

considerations as for the negative feedback of PD-L1 on IFNγ. We again conducted a sensitivity analysis to examine the effects of these parameter values on our model predictions (Figure S1, right panels).

4.1.5 Combined IFNγ inhibition model

In our combined model with two forms of IFNγ inhibition, we model the dynamics of IFNγ with the following ODE:

$$\frac{dI}{dt} = g_I H^S(P_M, \lambda_{P_M,I}) H^S(T, \lambda_{T,I}) - k_I I. \quad (9)$$

Note that an interesting alternative to the utilized product term of the two individual shifted Hill functions would be a combination Hill function (34), which allows for the modeling of synergistic or antagonistic effects.

4.2 Multi-scale models

We embedded our ODE models with separate PD-L1- or TGFβ-mediated IFNγ inhibition in multi-scale models of T cell-infiltrated tumors using the cellular Potts model (CPM) framework (25, 26), which was previously used for simulating EMT (58) and T cell-tumor cell interactions (59–62). The CPM is a lattice-based technique wherein cells consist of a collection of lattice sites that are assigned a specific 'spin' value to indicate their belonging to a particular cell. The models enable cellular movement through minimization of the Hamiltonian (H), a global energy function defined as

$$H = H_{sort} + H_l + H_{Act}\,. \quad (10)$$

The term H_{sort} describes cell surface interactions and a cell area or volume constraint that considers deviations from a target cell area or volume. As we employed two-dimensional simulations, the term 'area' applies here. H_{sort} is calculated with the following equation:

$$H_{sort} = \sum_{\substack{(i,j)(i',j') \\ neighbors}} J(\tau(\sigma(i,j)), \tau(\sigma(i',j')))(1 - \delta_{\sigma(i,j),\sigma(i',j')}) + \varsigma_a \sum_{spin} \sum_{types} (a(\sigma) - A_{\tau(\sigma)})^2, \quad (11)$$

where (i,j) and (i',j') are neighboring lattice sites with respective x coordinates i and i' and y coordinates j and j', $J(\tau, \tau')$ represents the surface energy between cells of types τ and τ', σ represents the spin of a cell, $\delta_{\sigma,\sigma'}$ denotes the Kronecker delta, ς_a represents a weighting term for the cell area constraint, $a(\sigma)$ is the current area of a cell, and $A_{\tau(\sigma)}$ is the target area of cells with type τ. We distinguished between epithelial (E), hybrid E/M (H), and mesenchymal (M) tumor cells based on ZEB1 mRNA expression (mZ) as calculated with the ODE model. Cells transitioned as follows: E to H: $mZ \geq$ 235 molecules; H to E: $mZ \leq$ 145 molecules; H to M: $mZ \geq$ 715 molecules; and M to E: $mZ \leq$ 370 molecules. These cut-off values correspond roughly to the average expression level during each transition as predicted by our ODE models. Cells could not directly transition from a mesenchymal to a hybrid phenotype. To mimic the 'invasion' of hybrid and mesenchymal tumor cells, we set their surface energies with medium (*med*) lower than those with tumor cells. Conversely, we set $J_{E,med}$ higher than $J_{E,E}$ to reflect the adhesive properties of epithelial tumor cells. To prevent the migration of T cells (*Tcell*) out of the tumor, we set $J_{Tcell,med}$ higher than their surface energies with tumor cells.

The Hamiltonian of our models additionally included the term H_l that represents the surface area constraint of cells and is calculated with the function (63)

$$H_l = \varsigma_l \sum_{\sigma} (l(\sigma) - L_{\tau(\sigma)})^2, \quad (12)$$

where ς_l represents the weight of the perimeter constraint, $l(\sigma)$ is the actual perimeter of a cell, calculated as the number of boundary interfaces with neighboring lattice sites of a different spin, and $L_{\tau(\sigma)}$ represents the target perimeter for cells with type τ. In order to promote the emergence of roundish cells, we set L_τ to the ratio of the perimeter of a circle to its area ($2\sqrt{\pi A_\tau}$), with the area corresponding to the target area of a cell of type τ (following 59). Additionally, we set $\varsigma_{l_{Tcell}} < \varsigma_{l_M} < \varsigma_{l_H} < \varsigma_{l_E}$, causing T cells to deform most easily and epithelial tumor cells to most strongly retain a roundish shape.

Lastly, the active migration of T cells was driven by the term H_{Act} that describes the Act model wherein actin dynamics cause cell protrusions that in turn drive cell motility (64). H_{Act} is calculated with

$$H_{Act} = \frac{\varsigma_{Act}}{Max_{Act}} (GM_{Act}(u) - GM_{Act}(v)), \quad (13)$$

where ς_{Act} is a weighting term of the Act model, and Max_{Act} is the maximum actin activity value, which is assigned to lattice sites that are newly incorporated by a cell. The actin activity Act of a lattice site decreases with 1 after each Monte Carlo step until it reaches 0. $GM_{Act}(u)$ and $GM_{Act}(v)$ represent the geometric mean actin activities around sites u and v, respectively. The geometric mean activity around site u is calculated with

$$GM_{Act}(u) = \left(\prod_{y \epsilon V(u)} Act(y) \right)^{1/|V(u)|}, \quad (14)$$

where $|V(u)|$ is the second-order Moore neighborhood of site u. This implements a positive feedback mechanism that favors updates from site u into a neighboring site v with a lower actin activity. We only applied H_{Act} to T cells and employed parameters for amoeboid cells (64). The resulting average migration speed was approximately 7 μm min^{-1}, which is consistent with values previously measured in TC-1, EL4, and EG7 tumors (65, 66). To prevent T cells from breaking due to actin protrusion dynamics, we employed the connectivity constraint described by Merks et al. (67). Tumor cells only moved passively *via* cell surface interactions based on H_{sort} and H_l.

The simulation space comprised a square area representing the TME within which T cells and tumor cells were restricted to move. We derived the production rate of IFNγ by T cells and its rate of cellular uptake from the literature (see Supplementary Information). T cells were considered to continuously produce IFNγ. Because T cells were almost always in contact with tumor cells during our simulations, this

is expected to closely resemble reality in which T cells may primarily produce IFNγ during periods of cognate antigen recognition. We simulated two different extents of IFNγ spreading by modifying the cellular uptake rate of IFNγ (see Supplementary Information). Simulations either had a uniform TGFβ field or a TGFβ gradient (see Supplementary Information). To enable all tumor cells to respond to extracellular TGFβ, we included the TGFβ–SNAIL1 submodel in the ODE models without IFNγ inhibition or with PD-L1-mediated IFNγ inhibition. The space had a scale of 2 μm per lattice site and was 700 × 700 μm and 400 × 400 μm in size for long-range and short-range IFNγ spreading simulations, respectively. To mimic the typically low T cell: tumor cell ratios observed within tumors (68), we simulated T cells and tumor cells at a 1:40 ratio. In long-range and short-range IFNγ spreading simulations, T cells were initiated randomly within respectively a circular tumor comprising 480 tumor cells or the middle-outer cell layers of an invasive front comprising 200 tumor cells. T cells were frozen in motion and not secreting IFNγ for the initial 10 minutes to allow tumor cell ODE dynamics to reach a steady state.

Simulations had a temporal scale of 0.6 seconds per Monte Carlo step, and output was generated every 10-minute and 1-minute interval for long-range and short-range IFNγ spreading simulations, respectively. ODE dynamics were accelerated 1800 times relative to CPM and PDE dynamics in order to make simulations less time-consuming and thus computationally feasible. CPM simulation parameters are provided in Table 3. In some of our simulations, we implemented intratumoral heterogeneity (see Supplementary Information).

4.3 Simulation and analysis

We used COPASI (COmplex PAthway SImulator) (RRID: SCR_014260) for ODE model simulations (72). For CPM simulations, we used the Morpheus framework (RRID: SCR_014975) (73). We performed analysis in R (R Project for Statistical Computing, RRID:SCR_01905) (74) with RStudio (RStudio, RRID:SCR_000432) (75) and the tidyverse (76) packages.

TABLE 3 Cellular Potts simulation parameters.

Parameter	Value	Description	Ref.
$J_{\sigma,\sigma'}$	$J_{E,E}$ = 2; $J_{E,H}$ = 5; $J_{E,M}$ = 5; $J_{H,H}$ = 14; $J_{H,M}$ = 14; $J_{M,M}$ = 14; $J_{E,Tcell}$ = 0.5; $J_{H,Tcell}$ = 0.5; $J_{M,Tcell}$ = 0.5; $J_{Tcell,Tcell}$ = 0.5; $J_{E,med}$ = 3; $J_{H,med}$ = 1; $J_{M,med}$ = 1; $J_{Tcell,med,low}$ = 2; $J_{Tcell,med,high}$ = 15	Surface energies between cell types: $J_{Tcell,med,low}$ for TGFβ gradient simulations, $J_{Tcell,med,high}$ for other simulations	–
A_τ	A_{tum} = 452 μm^2	Target area for a cell of type τ	(30, 59)
	A_{Tcell} = 140 μm^2		
L_τ	$2\sqrt{\pi A_\tau}$	Target perimeter for a cell of type τ	(59)
ς_a	$\varsigma_{a,tum}$ = 1	Strength of cell area constraint	(59)
	$\varsigma_{a,Tcell}$ = 1		
$*\varsigma_l$	$\varsigma_{l,E}$ = 0.25	Strength of cell perimeter constraint	(59)
	$\varsigma_{l,H}$ = 0.2		
	$\varsigma_{l,M}$ = 0.15		
	$\varsigma_{l,Tcell}$ = 0.1		
ς_{Act}	$\varsigma_{Act,Tcell}$ = 20	Strength of actin protrusion dynamics	(64)
Max_{Act}	20	Actin activity value assigned to lattice sites newly occupied by T cells	(64)
g_I	1200 molecules min^{-1}	Basal production rate of IFNγ by T cells	(69)
$*k_I$	$k_{I,Tcell}$ = 0 min^{-1}	Uptake rate of IFNγ: $k_{I,short}$ for short-range IFNγ spreading simulations, $k_{I,long}$ for long-range IFNγ spreading simulations	(68, 70)
	$k_{I,tum,short}$ = 2100 min^{-1}		
	$k_{I,med,short}$ = 420 min^{-1}		
	$k_{I,tum,long}$ = 0.021 min^{-1}		
	$k_{I,med,long}$ = 0.0042 min^{-1}		
D_I	5430 μm^2 min^{-1}	Diffusion coefficient of IFNγ	(71)

The values of starred (*) parameters were based on the cited references but slightly modified. *E* = epithelial tumor cell; *H* = hybrid tumor cell; *M* = mesenchymal tumor cell; *tum* = all tumor cells independent of EMT phenotype; *Tcell* = T cell; *med* = medium.

Data availability statement

Data and code to run model simulations (including COPASI and Morpheus files) and generate all figures are available at https://doi.org/10.5281/zenodo.8114632 (77), further inquiries can be directed to the corresponding author.

Author contributions

CL, GB, and JB conceptualized and designed the study. CL performed the research; GB and JB supervised the research. CL drafted the manuscript; GB and JB critically revised the manuscript. All authors read and approved the final manuscript.

Funding

This work was supported by a Vidi grant from the Netherlands Organization for Scientific Research (NWO; grant 864.12.013 to JB).

Conflict of interest

The authors declare that the research was conducted in the absence of any commercial or financial relationships that could be construed as a potential conflict of interest.

Publisher's note

Supplementary material

The Supplementary Material for this article can be found online at: https://www.frontiersin.org/articles/10.3389/fimmu.2023.1219669/full#supplementary-material

References

1. Hanahan D. Hallmarks of cancer: new dimensions. *Cancer Discovery* (2022) 12:31–46. doi: 10.1158/2159-8290.CD-21-1059

2. Yang J, Antin P, Berx G, Blanpain C, Brabletz T, Bronner M, et al. Guidelines and definitions for research on epithelial-mesenchymal transition. *Nat Rev Mol Cell Biol* (2020) 21:341–52. doi: 10.1038/s41580-020-0237-9

3. Derynck R, Weinberg RA. EMT and cancer: more than meets the eye. *Dev Cell* (2019) 49:313–6. doi: 10.1016/j.devcel.2019.04.026

4. Williams ED, Gao D, Redfern A, Thompson EW. Controversies around epithelial-mesenchymal plasticity in cancer metastasis. *Nat Rev Cancer* (2019) 19:716–32. doi: 10.1038/s41568-019-0213-x

5. Lu W, Kang Y. Epithelial-mesenchymal plasticity in cancer progression and metastasis. *Dev Cell* (2019) 49:361–74. doi: 10.1016/j.devcel.2019.04.010

6. Nieto MA, Huang RYJ, Jackson RA, Thiery JP. EMT: 2016. *Cell* (2016) 166:21–45. doi: 10.1016/j.cell.2016.06.028

7. Lüönd F, Sugiyama N, Bill R, Bornes L, Hager C, Tang F, et al. Distinct contributions of partial and full EMT to breast cancer malignancy. *Dev Cell* (2021) 56:3203–3221.e11. doi: 10.1016/j.devcel.2021.11.006

8. Jolly MK, Somarelli JA, Sheth M, Biddle A, Tripathi SC, Armstrong AJ, et al. Hybrid epithelial/mesenchymal phenotypes promote metastasis and therapy resistance across carcinomas. *Pharmacol Ther* (2018) 194:161–84. doi: 10.1016/j.pharmthera.2018.09.007

9. Terry S, Savagner P, Ortiz-Cuaran S, Mahjoubi L, Saintigny P, Thiery JP, et al. New insights into the role of EMT in tumor immune escape. *Mol Oncol* (2017) 11:824–46. doi: 10.1002/1878-0261.12093

10. Pardoll DM. The blockade of immune checkpoints in cancer immunotherapy. *Nat Rev Cancer* (2012) 12:252–64. doi: 10.1038/nrc3239

11. Okazaki T, Honjo T. The PD-1-PD-L pathway in immunological tolerance. *Trends Immunol* (2006) 27:195–201. doi: 10.1016/j.it.2006.02.001

12. Zitvogel L, Kroemer G. Targeting PD-1/PD-L1 interactions for cancer immunotherapy. *OncoImmunology* (2012) 1:1223–5. doi: 10.4161/onci.21335

13. Jiang Y, Zhan H. Communication between EMT and PD-L1 signaling: New insights into tumor immune evasion. *Cancer Lett* (2020) 468:72–81. doi: 10.1016/j.canlet.2019.10.013

14. Chen L, Gibbons DL, Goswami S, Cortez MA, Ahn YH, Byers LA, et al. Metastasis is regulated *via* microRNA-200/ZEB1 axis control of tumour cell PD-L1 expression and intratumoral immunosuppression. *Nat Commun* (2014) 5:5241. doi: 10.1038/ncomms6241

15. Noman MZ, Janji B, Abdou A, Hasmim M, Terry S, Tan TZ, et al. The immune checkpoint ligand PD-L1 is upregulated in EMT-activated human breast cancer cells by a mechanism involving ZEB-1 and miR-200. *OncoImmunology* (2017) 6:e1263412. doi: 10.1080/2162402X.2016.1263412

16. Martinez-Ciarpaglini C, Oltra S, Roselló S, Roda D, Mongort C, Carrasco F, et al. Low miR200c expression in tumor budding of invasive front predicts worse survival in patients with localized colon cancer and is related to PD-L1 overexpression. *Modern Pathol* (2019) 32:306–13. doi: 10.1038/s41379-018-0124-5

17. Baccarini A, Chauhan H, Gardner TJ, Jayaprakash AD, Sachidanandam R, Brown BD. Kinetic analysis reveals the fate of a microRNA following target regulation in mammalian cells. *Curr Biol* (2011) 21:369–76. doi: 10.1016/j.cub.2011.01.067

18. Kim CK, Pak TR. miRNA degradation in the mammalian brain. *Am J Physiol Cell Physiol* (2020) 319:C624–9. doi: 10.1152/ajpcell.00303.2020

19. Burger GA, Nesenberend DN, Lems CM, Hille SC, Beltman JB. Bidirectional crosstalk between epithelial-mesenchymal plasticity and IFNγ-induced PD-L1 expression promotes tumour progression. *R Soc Open Sci* (2022) 9:220186. doi: 10.1098/RSOS.220186

20. Jiang Y, Li Y, Zhu B. T-cell exhaustion in the tumor microenvironment. *Cell Death Dis* (2015) 6:e1792. doi: 10.1038/cddis.2015.162

21. Batlle E, Massague J. Transforming growth factor- ′ β Signaling in immunity and cancer. *Immunity* (2019) 50 539:924–40. doi: 10.1016/j.immuni.2019.03.024

22. Williams JB, Li S, Higgs EF, Cabanov A, Wang X, Huang H, et al. Tumor heterogeneity and clonal cooperation influence the immune selection of IFN-γ-signaling mutant cancer cells. *Nat Commun* (2020) 11:1–14. doi: 10.1038/s41467-020-14290-4

23. Jia D, Jolly MK, Boareto M, Parsana P, Mooney SM, Pienta KJ, et al. OVOL guides the epithelial-hybrid-mesenchymal transition. *Oncotarget* (2015) 6:15436–48. doi: 10.18632/ONCOTARGET

24. Jolly MK, Tripathi SC, Jia D, Mooney SM, Celiktas M, Hanash SM, et al. Stability of the hybrid epithelial/mesenchymal phenotype. *Oncotarget* (2016) 7:27067–84. doi: 10.18632/oncotarget.8166

25. Graner F, Glazier JA. Simulation of biological cell sorting using a two-dimensional extended Potts model. *Phys Rev Lett* (1992) 69:2013–6. doi: 10.1103/PhysRevLett.69.2013

26. Glazier JA, Graner F. Simulation of the differential adhesion driven rearrangement of biological cells. *Phys Rev E* (1993) 47:2128–54. doi: 10.1103/PhysRevE.47.2128

27. Yang L, Huang J, Ren X, Gorska AE, Chytil A, Aakre M, et al. Abrogation of TGF beta signaling in mammary carcinomas recruits Gr-1+CD11b+ myeloid cells that promote metastasis. *Cancer Cell* (2008) 13:23–35. doi: 10.1016/J.CCR.2007.12.004

28. Dalal BI, Keown PA, Greenbergt AH. Immunocytochemical localization of secreted transforming growth factor-1 to the advancing edges of primary tumors and to lymph node metastases of human mammary carcinoma. *Am J Pathol* (1993) 143:381–9.

29. Thurley K, Gerecht D, Friedmann E, Höfer T. Three-dimensional gradients of cytokine signaling between T cells. *PloS Comput Biol* (2015) 11:1–22. doi: 10.1371/journal.pcbi.1004206

30. Hoekstra ME, Bornes L, Dijkgraaf FE, Philips D, Pardieck IN, Toebes M, et al. Long-distance modulation of bystander tumor cells by CD8+ T-cell-secreted IFN-γ. *Nat Cancer* (2020) 1:291–301. doi: 10.1038/s43018-020-0036-4

31. Thibaut R, Bost P, Milo I, Cazaux M, Lemaître F, Garcia Z, et al. Bystander IFN-γ activity promotes widespread and sustained cytokine signaling altering the tumor microenvironment. *Nat Cancer* (2020) 1:302–14. doi: 10.1038/s43018-020-0038-2

32. Hoekstra ME, Vijver SV, Schumacher TN. Modulation of the tumor microenvironment by CD8+ T cell-derived cytokines. *Curr Opin Immunol* (2021) 69:65–71. doi: 10.1016/j.coi.2021.03.016

33. Castro F, Cardoso AP, Goncalves RM, Serre K, Oliveira MJ. Interferon-gamma at the crossroads of tumor immune surveillance or evasion. *Front Immunol* (2018) 9:847. doi: 10.3389/fimmu.2018.00847

34. Chakraborty A, Jusko WJ. Pharmacodynamic interaction of recombinant human interleukin-10 and prednisolone using *in vitro* whole blood lymphocyte proliferation. *J Pharm Sci* (2002) 91:1334–42. doi: 10.1002/jps.3000

35. Sahoo S, Nayak SP, Hari K, Purkait P, Mandal S, Kishore A, et al. Immunosuppressive traits of the hybrid epithelial/mesenchymal phenotype. *Front Immunol* (2021) 12:797261. doi: 10.3389/fimmu.2021.797261

36. Ren D, Hua Y, Yu B, Ye X, He Z, Li C, et al. Predictive biomarkers and mechanisms underlying resistance to PD1/PD-L1 blockade cancer immunotherapy. *Mol Cancer* (2020) 19:19. doi: 10.1186/s12943-020-1144-6

37. Chen L, Heymach JV, Qin FXF, Gibbons DL. The mutually regulatory loop of epithelial- mesenchymal transition and immunosuppression in cancer progression. *OncoImmunology* (2015) 4:e1002731. doi: 10.1080/2162402X.2014.1002731

38. Patel SP, Kurzrock R. PD-L1 expression as a predictive biomarker in cancer immunotherapy. *Mol Cancer Ther* (2015) 14:847–56. doi: 10.1158/1535-7163.MCT-14-0983

39. Bruns IB, Beltman JB. Quantifying the contribution of transcription factor activity, mutations and microRNAs to CD274 expression in cancer patients. *Sci Rep* (2022) 12:1–15. doi: 10.1038/s41598-022-08356-0

40. Perez-Oquendo M, Gibbons DL. Regulation of ZEB1 function and molecular associations in tumor progression and metastasis. *Cancers* (2022) 14:1864. doi: 10.3390/cancers14081864

41. Liu S, Cong Y, Wang D, Sun Y, Deng L, Liu Y, et al. Breast cancer stem cells transition between epithelial and mesenchymal states reflective of their normal counterparts. *Stem Cell Rep* (2014) 2:78–91. doi: 10.1016/J.STEMCR.2013.11.009

42. Bocci F, Gearhart-Serna L, Boareto M, Ribeiro M, Ben-Jacob E, Devi GR, et al. Toward understanding cancer stem cell heterogeneity in the tumor microenvironment. *Proc Natl Acad Sci* (2019) 116:148–57. doi: 10.1073/pnas.1815345116

43. Benchaib MA, Bouchnita A, Volpert V, Makhoute A. Mathematical modeling reveals that the administration of EGF can promote the elimination of lymph node metastases by PD-1/PD-L1 blockade. *Front Bioengineering Biotechnol* (2019) 7:104. doi: 10.3389/fbioe.2019.00104

44. Jenner AL, Smalley M, Goldman D, Goins WF, Cobbs CS, Puchalski RB, et al. Agent-based computational modeling of glioblastoma predicts that stromal density is central to oncolytic virus efficacy. *iScience* (2022) 25:104395. doi: 10.1016/j.isci.2022.104395

45. Whitmire JK, Tan JT, Whitton JL. Interferon-γ acts directly on CD8+ T cells to increase their abundance during virus infection. *J Exp Med* (2005) 201:1053–9. doi: 10.1084/jem.20041463

46. Bhat P, Leggatt G, Waterhouse N, Frazer IH. Interferon-γ derived from cytotoxic lymphocytes directly enhances their motility and cytotoxicity. *Cell Death Dis* (2017) 8:e2836. doi: 10.1038/CDDIS.2017.67

47. Jonckheere S, Adams J, Groote DD, Campbell K, Berx G, Goossens S. Epithelial-mesenchymal transition (EMT) as a therapeutic target. *Cells Tissues Organs* (2021) 211:1–26. doi: 10.1159/000512218

48. Mariathasan S, Turley SJ, Nickles D, Castiglioni A, Yuen K, Wang Y, et al. TGFβ attenuates tumour response to PD-L1 blockade by contributing to exclusion of T cells. *Nature* (2018) 554:544–8. doi: 10.1038/nature25501

49. Weigelin B, den Boer AT, Wagena E, Broen K, Dolstra H, de Boer RJ, et al. Cytotoxic T cells are able to efficiently eliminate cancer cells by additive cytotoxicity. *Nat Commun* (2021) 12:5217. doi: 10.1038/s41467-021-25282-3

50. Pramanik D, Jolly MK, Bhat R. Matrix adhesion and remodeling diversifies modes of cancer invasion across spatial scales. *J Theor Biol* (2021) 524:110733. doi: 10.1016/j.jtbi.2021.110733

51. Burke JD, Young HA. IFN-γ: A cytokine at the right time, is in the right place. *Semin Immunol* (2019) 43:101280. doi: 10.1016/j.smim.2019.05.002

52. Boulch M, Cazaux M, Cuffel A, Guerin MV, Garcia Z, Alonso R, et al. Tumor-intrinsic sensitivity to the pro-apoptotic effects of IFN-γ is a major determinant of CD4+ CAR T-cell antitumor activity. *Nat Cancer* (2023). doi: 10.1038/s43018-023-00570-7

53. Lu M, Jolly MK, Gomoto R, Huang B, Onuchic JN, Ben-Jacob E. Tristability in cancer-associated microRNA-TF chimera toggle switch. *J Phys Chem B* (2013) 117:13164–74. doi: 10.1021/jp403156m

54. Quaiser T, Dittrich A, Schaper F, Mönnigmann M. A simple work flow for biologically inspired model reduction - application to early JAK-STAT signaling. *BMC Syst Biol* (2011) 5:30. doi: 10.1186/1752-0509-5-30

55. Huang B, Lu M, Jia D, Ben-Jacob E, Levine H, Onuchic JN. Interrogating the topological robustness of gene regulatory circuits by randomization. *PloS Comput Biol* (2017) 13:1–21. doi: 10.1371/journal.pcbi.1005456

56. Zhang J, Tian XJ, Zhang H, Teng Y, Li R, Bai F, et al. TGF-β-induced epithelial-to-mesenchymal transition proceeds through stepwise activation of multiple feedback loops. *Sci Signaling* (2014) 7:ra91. doi: 10.1126/scisignal.2005304

57. Tian XJ, Zhang H, Xing J. Coupled reversible and irreversible bistable switches underlying TGFβ-induced epithelial to mesenchymal transition. *Biophys J* (2013) 105:1079–89. doi: 10.1016/j.bpj.2013.07.011

58. Neagu A, Mironov V, Kosztin I, Barz B, Neagu M, Moreno-Rodriguez RA, et al. Computational modeling of epithelial-mesenchymal transformations. *BioSystems* (2010) 100:23–30. doi: 10.1016/j.biosystems.2009.12.004

59. Beck RJ, Bijker DI, Beltman JB. Heterogeneous, delayed-onset killing by multiple-hitting T cells: Stochastic simulations to assess methods for analysis of imaging data. *PloS Comput Biol* (2020) 16:e1007972. doi: 10.1371/journal.pcbi.1007972

60. Gadhamsetty S, Marée AF, Beltman JB, de Boer RJ. A general functional response of cytotoxic T lymphocyte-mediated killing of target cells. *Biophys J* (2014) 106:1780–91. doi: 10.1016/j.bpj.2014.01.048

61. Gadhamsetty S, Marée AF, de Boer RJ, Beltman JB. Tissue dimensionality influences the functional response of cytotoxic T lymphocyte-mediated killing of targets. *Front Immunol* (2017) 7:668. doi: 10.3389/fimmu.2016.00668

62. Gadhamsetty S, Marée AF, Beltman JB, de Boer RJ. A sigmoid functional response emerges when cytotoxic T lymphocytes start killing fresh target cells. *Biophys J* (2017) 112:1221–35. doi: 10.1016/j.bpj.2017.02.008

63. Ouchi NB, Glazier JA, Rieu JP, Upadhyaya A, Sawada Y. Improving the realism of the cellular Potts model in simulations of biological cells. *Physica A: Stat Mechanics its Appl* (2003) 329:451–8. doi: 10.1016/S0378-4371(03)00574-0

64. Niculescu I, Textor J, de Boer RJ. Crawling and gliding: a computational model for shape-driven cell migration. *PloS Comput Biol* (2015) 11:e1004280. doi: 10.1371/journal.pcbi.1004280

65. Mrass P, Takano H, Lai GN, Daxini S, Lasaro MO, Iparraguirre A, et al. Random migration precedes stable target cell interactions of tumor-infiltrating T cells. *J Exp Med* (2006) 203:2749–61. doi: 10.1084/jem.20060710

66. Boissonnas A, Fetler L, Zeelenberg IS, Hugues S, Amigorena S. *In vivo* imaging of cytotoxic T cell infiltration and elimination of a solid tumor. *J Exp Med* (2007) 204:345–56. doi: 10.1084/jem.20061890

67. Merks RM, Brodsky SV, Goligorksy MS, Newman SA, Glazier JA. Cell elongation is key to in silico replication of *in vitro* vasculogenesis and subsequent remodeling. *Dev Biol* (2006) 289:44–54. doi: 10.1016/j.ydbio.2005.10.003

68. Beck RJ, Slagter M, Beltman JB. Contact-dependent killing by cytotoxic T lymphocytes is insufficient for EL4 tumor regression *in vivo*. *Cancer Res* (2019) 79:3406–16. doi: 10.1158/0008-5472.CAN-18-3147

69. Han Q, Bagheri N, Bradshaw EM, Hafler DA, Lauffenburger DA, Love JC. Polyfunctional responses by human T cells result from sequential release of cytokines. *Proc Natl Acad Sci United States America* (2012) 109:1607–12. doi: 10.1073/pnas.1117194109

70. Anderson P, Yip YK, Vilcek J. Human interferon-γ is internalized and degraded by cultured fibroblasts. *J Biol Chem* (1983) 258:6497–502. doi: 10.1016/s0021-9258(18)32439-6

71. Ross AE, Pompano RR. Diffusion of cytokines in live lymph node tissue using microfluidic integrated optical imaging. *Analytica Chimica Acta* (2018) 1000:205–13. doi: 10.1016/j.aca.2017.11.048

72. Hoops S, Sahle S, Gauges R, Lee C, Pahle J, Simus N, et al. COPASI–a complex pathway simulator. *Bioinformatics* (2006) 22:3067–74. doi: 10.1093/bioinformatics/btl485

73. Starruß J, De Back W, Brusch L, Deutsch A. Morpheus: A user-friendly modeling environment for multiscale and multicellular systems biology. *Bioinformatics* (2014) 30:1331–2. doi: 10.1093/bioinformatics/btt772

74. R Core Team. *R: A language and environment for statistical computing*. Vienna, Austria: R Foundation for Statistical Computing (2022).

75. RStudio Team. *RStudio: Integrated Development Environment for R*. Boston, MA: RStudio, PBC. (2020).

76. Wickham H, Averick M, Bryan J, Chang W, McGowan LD, Francois R, et al. Welcome to the tidyverse. *J of Open Source Software* (2019) 4:1686. doi: 10.21105/joss.01686

77. Lems CM, Burger GA, Beltman JB. *lacdr-tox/lems-emt-pdl1-models-figures*. (2023). doi: 10.5281/zenodo.8114632.

frontiers | Frontiers in Immunology

TYPE Brief Research Report
PUBLISHED 19 January 2024
DOI 10.3389/fimmu.2023.1303814

OPEN ACCESS

EDITED BY
Heiko Enderling,
University of Texas MD Anderson Cancer Center, United States

REVIEWED BY
Scott Christley,
University of Texas Southwestern Medical Center, United States
Urszula Foryś,
University of Warsaw, Poland

*CORRESPONDENCE
Urszula Ledzewicz
urszula.ledzewicz@p.lodz.pl

RECEIVED 28 September 2023
ACCEPTED 26 December 2023
PUBLISHED 19 January 2024

CITATION
Ledzewicz U and Schättler H (2024) Optimal dosage protocols for mathematical models of synergy of chemo- and immunotherapy. *Front. Immunol.* 14:1303814. doi: 10.3389/fimmu.2023.1303814

Optimal dosage protocols for mathematical models of synergy of chemo- and immunotherapy

Urszula Ledzewicz[1,2]* and Heinz Schättler[3]

[1]Institute of Mathematics, Lodz University of Technology, Lodz, Poland, [2]Department of Mathematics and Statistics, Southern Illinois University Edwardsville, Edwardsville, IL, United States, [3]Department of Electrical and Systems Engineering, Washington University, St. Louis, MO, United States

The release of tumor antigens during traditional cancer treatments such as radio- or chemotherapy leads to a stimulation of the immune response which provides synergistic effects these treatments have when combined with immunotherapies. A low-dimensional mathematical model is formulated which, depending on the values of its parameters, encompasses the 3 E's (elimination, equilibrium, escape) of tumor immune system interactions. For the escape situation, optimal control problems are formulated which aim to revert the process to the equilibrium scenario. Some numerical results are included.

KEYWORDS

mathematical model, immunotherapy, chemotherapy, synergy, optimal control

1 Introduction

The release of tumor antigen during traditional cancer treatments, such as radio- (1) or chemotherapy (2), can lead to a stimulation of the innate immune response which, in some cases, is able to trigger protective antitumor immunity with possibly long-lasting effects (3, 4). For example, a well-documented abscopal effect of radiation therapy (i.e., the reduction of tumor metastases in areas well outside the field of radiation) is hypothesized of being immune mediated (5–8). These stimulatory effects are the basis for an observed synergy some of these therapies have with immunotherapy, e.g., check-point blockades.

Mathematical models of tumor growth and treatment have a long history going back to the 1980s with research unabatedly continuing (e.g., see (9)). Probably the earliest works on tumor-immune interactions are Stepanova's paper (10) and (11) by Kuznetsov et al. while mathematical models including immunotherapies are more recent [e.g (12–20)]. Capturing all aspects of tumor-immune interactions in a mathematical model is difficult as the competitive interactions between tumor cells and the immune system are complex, to say the least, and still are the topic of intense medical research. While large-scale, agent-based, PDE, or hybrid models are more precise, they suffer from the inabilities to determine a large number of parameters.

In this paper, we consider a *qualitative*, low-dimensional mathematical model (21). Rather than analyzing the dynamical system for a specific set of parameters, the aim of a qualitative analysis is to understand the totality of all the possibilities the model allows for. Especially for nonlinear models this is an important aspect in pointing out both mathematical limitations and complexities of the underlying dynamics. Motivated by the papers (10, 11, 22, 23) here we consider a model for tumor immune system interactions which in addition to tumor volume and immunocompetent cell densities includes as a third separate variable tumor antigen. This model retains the main aspects of tumor immune system interactions called the three E's of *cancer immunoediting* (24, 25). These are (i) *elimination*: the immune system is able to completely eradicate the tumor; (ii) *equilibrium*: adaptive immunity is able to maintain cancer in a benign state (tumor dormancy) (26), and (iii) *tumor escape*: tumor growth overcomes or evades the actions of the immune system (27). From a practical (therapeutical) point of view, the first case will never be seen while therapy will not be able to save the patient in the last. Only when it is possible to influence the dynamics (that is, tumor growth) through treatment which will lead to positive changes on a permanent basis, i.e., even after treatment has been stopped, a cure is possible. This requires that the system can be reverted back to the equilibrium situation.

Optimal control problems are optimization problems in time in which the full range of possibilities to influence the dynamics of a system, i.e., without *a priori* restrictions on these structures, is considered. This is very different from a "best in class" argument sometimes wrongly also called optimal control in many publications where only a limited number of possibilities is considered, often by mere simulations. Typically in optimal control problems the aim is to transfer the state of a dynamical system from a given initial point into a desired set of terminal states. This is accomplished by minimizing some suitably chosen criterion subject to the dynamics of the system and other constraints that need to be satisfied. Solutions then are functions of time which describe the best actions relative to the chosen criterion. Historically, there has been great success in applying optimal control to engineering problems (moon landing, autopilots on airplanes) and economics (portfolio optimization) while medical applications with its uncertainties in the dynamics—these are generally based on *ad-hoc* modeling premises, not like in physics on first principles—and usually a large parameter uncertainty in the model lack similar success stories. Nevertheless, the scheduling of therapeutic agents over time has all the characteristics of an optimal control problem (28) and there is an increasing bulk of literature in which optimal control is applied to medical problems, e.g., see (19, 29–33). The aim is to minimize some objective related to tumor burden and quality of life of the patient while the underlying system follows the processes of tumor development and treatment interactions. While direct clinical applications are a mere possibility for the future in our opinion, currently the use of optimal control techniques lies more in understanding the dynamics of mathematical models proposed to study medical processes (which contributes to a validation of these models) while solutions to optimal control problems can be helpful in identifying realistic therapy protocols that possibly can be explored in medical trials and practice (28, 31). The contributions of our paper lie in this direction. We formulate an optimal control problem for a qualitative mathematical model of tumor immune system interactions which considers the transfer of the state of the system from a malignant initial condition (corresponding to a tumor escape situation) into a benign state (corresponding to the equilibrium scenario) and show how geometric properties of the dynamics help in formulating and understanding the proper goal of treatment. We discuss the complexities of obtaining optimal controls in this case and highlight some numerical results.

2 Methods

A low-dimensional, qualitative model for tumor immune system interactions under chemo- and immunotherapy is formulated as a dynamical system and analyzed mathematically. For the medically relevant scenario of tumor escape (malignant), optimal control problems are formulated whose solutions would revert the system to the equilibrium case (benign).

2.1 Mathematical model

We consider the following dynamics (21) for tumor immune system interactions based on classical papers by Stepanova (10) and Kuznetsov et al. (11):

$$\dot{x} = \xi x\left(1 - \frac{x}{x_\infty}\right) - \theta xy - \alpha xu, \tag{1}$$

$$\dot{y} = a(1 - bx)yz + \gamma - \delta y - \kappa yu + \nu yv, \tag{2}$$

$$\dot{z} = \sigma x + \psi xu - \mu z, \tag{3}$$

State variables are the *tumor volume* x, the *immunocompetent cell density* y, and *tumor antigen* z. The variable y is a non-dimensional, order of magnitude quantity which is related to various types of T-cells activated during the immune reaction and summarily represents the actions of the immune system. The variables u and v represent time-varying dose rates $u = u(t)$ at which chemotherapy is given and a time-varying immune boost $v = v(t)$. For simplicity, drug dose rates and concentrations are identified. (It is well-known how to deal with the required changes if standard pharmacokinetic models are included (34). All Greek letters and a and b are parameters which for the time under consideration are assumed constant. The meaning of variables and parameters is given in Table 1.

Most of the terms in the equations are standard. Log-linear terms of the Skipper model (35) are used to formulate the damage done to the tumor through the concentrations of the agents and a logistic growth model is used for the tumor volume. This is merely for sake of specificity and analogous results hold qualitatively, for example, for a Gompertzian growth function. Equations 1, 2 follow

TABLE 1 Variables and parameters.

variable	interpretation	parameter	interpretation
x	tumor volume	ξ	tumor growth rate
x_∞	tumor carrying capacity	θ	tumor-immune interaction
y	immunocompetent cell density	a	tumor antigen stimulated proliferation rate
		b	inverse threshold for tumor suppression
		γ	rate of influx into y from primary organs
		δ	death rate of T-cells
z	tumor antigen	σ	intrinsic immunogenicity of the tumor
		μ	elimination of antigen by the immune system
u	concentration of a cytotoxic agent	α	chemotherapeutic killing parameter on x
		κ	chemotherapeutic killing parameter on y
		ψ	therapy induced boost to immunogenicity
v	concentration of an immunotherapeutic agent	ν	immune boost

the classical papers by Stepanova (10) and Kuznetsov (11) and have been taken over with only small changes. Equation 3 extends these earlier 2-dimensional models to include a direct link between tumor antigen z and the immuno-competent cell density y. This has led to the modified term $a(1-bx)yz$ used in Equation 2. In (10) this term instead was taken of the form $a(1-bx)y^2$ with the justification that tumor antigen would be proportional to the tumor volume thus generating the factor y^2 in the interaction term as tumor antigen is not considered separately in that model. In (2) we have therefore replaced one the factors y with z restoring a direct link between these two variables. Equation 3 is based on a similar equation in (36) and models the evolution of tumor antigen. It is assumed that the tumor produces antigen z at rate σ which results in an intrinsic (i.e., not therapy induced) immunogenicity of the tumor. Antigen is cleared by the immune system at rate μ which leads to the creation of immune effector cells which generate a stimulating effect onto the proliferation of lymphocytes and thus a positive influx into the compartment determining the immunocompetent cell density y. This effect is represented by the term ayz in Equation 2. The term ψxu models the immuno-stimulatory aspect of therapy assuming that the tumor produces antigen at a dose dependent rate ψu with ψ modeling the therapy induced immunogenicity of the tumor.

2.2 The three E's of immuno-editing

Depending on the value of the parameters, the dynamical Equations 1–3 properly replicate the full variety of medically realistic scenarios. In order not to be confusing with the *medical notion* of *equilibrium*, we use the terminology *stationary point* for the states which are obtained as solutions when the derivatives in Equations 1–3 are set to zero. There always exists a tumor-free stationary point given by $w_0 = (0, \frac{\gamma}{\delta}, 0)$. It is stable if $\xi\delta < \theta\gamma$ and unstable if $\xi\delta > \theta\gamma$. Intuitively, stability means that solutions of the dynamics which start near w_0 converge to w_0 in time. The relevant term is a difference between products of tumor stimulating parameters (the tumor growth rate ξ and natural death rate δ of immune cells) and tumor inhibiting parameters (the influx γ stimulating the immune system and the effectiveness θ of the immune system fighting the tumor). Stationary points with positive tumor volumes x_* are zeros of a cubic polynomial $Q = Q(x)$ computed by eliminating y_* and z_* from the equations $\dot{y} = 0$ and $\dot{z} = 0$. Given the logistic growth model used in Equation 1, only zeros in the range $0 < x_* < x_\infty$ are viable solutions for the tumor volume.

The three E's of immuno-editing correspond to the following scenarios:

2.2.1 Elimination

This situation arises if the tumor-free stationary point is stable and no stationary points with positive tumor volumes exist. All solutions of the dynamics converge to the tumor-free stationary point, i.e., the actions of the immune system are eliminating the tumor. While this is not a relevant scenario medically—in fact, it will never be observed—it nevertheless is part of the complete picture of tumor immune system interactions.

2.2.2 Equilibrium

This situation arises once the tumor-free stationary point becomes unstable and there exists a stationary point with small tumor volume x_* (and generally up-regulated y_*) which is stable. We call this stationary point 'benign'. There are two different scenarios mathematically which correspond to the medical notion of equilibrium: In the simpler one, the benign stationary point is the only stationary point with positive tumor volume and all trajectories converge to it. In the second case, called the *bi-stable scenario*, there exist three stationary points with positive tumor volumes labelled $0 < x_{*,b} < x_{*,u} < x_{*,m} < x_\infty$. We call the stationary point with lowest tumor volumes, $x_{*,b}$, *benign* and the one with highest tumor volume, $x_{*,m}$, *malignant*. This is merely terminology, but it is somewhat justified by the fact that typically the tumor volume $x_{*,b}$ is small with high $y_{*,b}$ while $x_{*,m}$ is high (close to carrying capacity) with low $y_{*,m}$. Both the benign and malignant stationary points are stable and we call their regions of attraction (i.e., the set of all initial conditions (x_0,y_0,z_0) from which the solution of the dynamics converges to the respective equilibrium point) the benign, respectively malignant regions. The third stationary point $x_{*,u}$ is unstable and there exists a surface (its 2-

dimensional stable manifold) that passes through it which separates the benign from the malignant region, the so-called *stability boundary*. (For 2-dimensional systems the terminology separatrix is common (37)). Depending on where the initial condition for the system lies, as time evolves, for the system without any outside interventions the state will converge either to the benign stationary point— and this also corresponds to the medical equilibrium scenario—or it will converge to the malignant stationary point in which case tumor escape occurs. In a rather precise mathematical sense, the bifurcations (changes in stability) which arise as the values for parameters change characterise the transitions from the medical state of equilibrium to the one of tumor escape.

2.2.3 Escape

In addition to the situation just described, it is also possible that there exists just one viable equilibrium point which, however, has high tumor volume x_* and low y_*, i.e., is malignant. In this case, unless somehow by means outside of the modeling done here a change in the values of the parameters can be achieved, after the termination of any treatment the state of the system will always converge to the malignant equilibrium point and it is not possible to revert to the medical condition of equilibrium. In this case, a cure is elusive.

We illustrate the role of the stability boundary in the bi-stable scenario through a 2-dimensional representation in Figure 1. Formally, we have dropped Equation 3 and replaced z in Equation 2 by the equilibrium relation $\mu z = \sigma x$. This thus is not directly related to Equations 1–3, but is merely intended to give an illustration of the underlying geometric scenario. Mathematically it will look the same, but not quite as clearly visible, in a higher-dimensional setting. Figure 1 faithfully represents the dynamics in the bi-stable case when both a stable benign and malignant stationary point exist. Obviously, whether or not this is the case depends on the parameter values, but it will hold true for an open set, i.e., for a whole range of values. We note that the same feature is present in the original models by Stepanova (10) and Kuznetsov (11), but also in a more recent in spirit similar 2-dimensional model by Bekker et al. (37) (where a slightly simplified dynamics has been used). In that paper the effects of various immunotherapies on shifting the stability boundary are considered for the model. All these low-dimensional mathematical models clearly point out the stability boundary as the defining structure for tumor immune system dynamics. Such a stability boundary only exists in the bistable scenario and for therapy is the only relevant case.

2.3 Formulation of treatment as an optimal control problem in the bi-stable scenario

From a practical point of view, only if the current state of the system (initial condition) is malignant the question of treatment arises. Treatment then should aim to move the state into the benign region, possibly in an efficient way or, in other words, one simply wants to minimize the use of agents to limit side-effects. If 'tumor escape' can be reversed to the 'equilibrium' condition through therapy by moving the state of the system into the benign region,

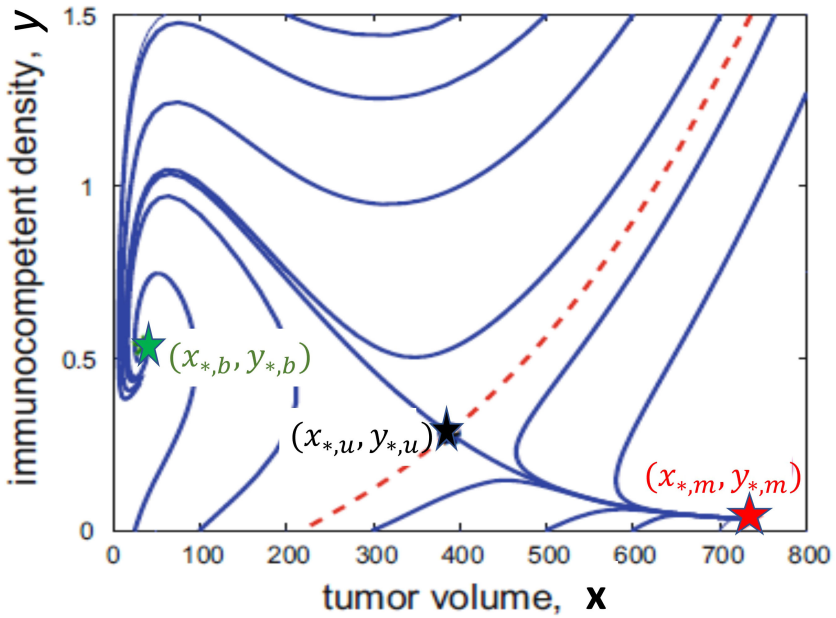

FIGURE 1
A 2-dimensional illustration of the bi-stable scenario showing the benign stationary point $(x_{*,b}, y_{*,b})$ in green, the saddle point $(x_{*,u}, y_{*,u})$ in black and the malignant stationary point $(x_{*,m}, y_{*,m})$ in red. The dashed red curve is the stability boundary which separates trajectories which converge to the benign stationary point (above the red curve) from those which converge to the malignant stationary point (below the red curve).

then—but this assumes that parameter values will not change—after therapy is halted convergence to the benign equilibrium point will occur.

Formulating the problem as an optimal control problem can help with singling out reasonable therapy protocols obtained by minimizing some criterion. For the problem considered here, the initial condition is the present state of the system, desired terminal states are in principle all points in the benign region, the dynamics is given by Equations 1–3, and other constraints that need to be considered are related to the side effects of therapy. Optimal controls then give the protocols on how to administer the therapeutic agents in time which are 'best' relative to the chosen criterion. Formulating this criterion is a relevant step in this process. If the objective function does not properly represent the overall goal of therapy results may simply not give beneficial suggestions for therapy protocols. When formulating this criterion to be minimized, the following aspects thus must be taken into account:

(1) *Minimizing the objective must induce the system to move into the benign region*. For this aim, the geometric shape of the boundary between the benign and malignant regions matters, but there exist many ways to realize such an objective. Here we use a penalty term of the form $V_x x(T) + V_y y(T) + V_z z(T)$ evaluated at the terminal point $w(T)$ where $\vec{V} = (V_x, V_y, V_z)$ is a suitable vector oriented to point from the benign into the malignant region (as we shall minimize the objective). Generally, one wants to minimize the tumor volume, but it also is the aim to up-regulate the immunocompetent cell density. Thus V_x should be positive while V_y may be allowed to be negative.

(2) Side effects of the therapies have not been included in the modeling. Hence these must now be incorporated indirectly by including penalty terms into the objective which limit the overall amounts of drugs given. The total amount of drugs given are measured by the so-called AUC ('area under the curve') in pharmacology. This quantity is given by the integral over the dose rate of the drugs: $\int_0^T u(t)dt$ and $\int_0^T v(t)dt$. Alternatively, *a priori* constraints on these amounts could be fixed and then the question would be how to best administer these amounts in time. In the literature often quadratic terms are used for the controls for mathematical expediency, but they have no pharmacological meaning.

(3) Mathematically, the existence of a solution needs to guaranteed.

All these considerations led us to formulate the following objective:

$$J = J(u,v) = V_x x(T) + V_y y(T) + V_z z(T) + \int_0^T (Au(t) + Bv(t) + C)dt\,. \tag{4}$$

The objective Equation 4 is a weighted average of 'good' and 'bad' terms with the components of the vector $\vec{V}$ and the coefficients A, B and C weights. These are *variables of choice* which need to be chosen to strike a balance between the benefit at the terminal time T and the overall side effects. As it is standard in engineering approaches, these coefficients should be calibrated to fine-tune the response of the system.

3 Results

Understanding the geometric properties of the stability boundary gives relevant insights into the possible behavior of *ad-hoc* chosen therapy protocols. Given a malignant initial condition, it is a more than reasonable strategy to apply chemo- and/or immunotherapy for some time τ, probably chosen by medical guidelines. The time of administration, however, may be crucial. The example in Figure 2 highlights this importance as it shows that the timing of therapy can make a crucial difference and that what might overall constitute a 'good' strategy is anything from obvious. The graphs in the figure show the course of two trajectories in (x,y)-space (not their evolution in time) when both chemo- and immunotherapy are applied for time τ and then therapy is stopped. The specific numerical values are irrelevant as we merely want to illustrate a general phenomenon which always exists in the bistable scenario, simply caused by the presence of a stability boundary. The initial segment under therapy is shown as the magenta curve, the subsequent trajectories without treatment are shown in red and green, respectively. For the red portion, $\tau = 0.72$ and this was not sufficient to move the state of the system into the benign region so that convergence to the malignant stationary point occurs. On the other hand, increasing the time just to $\tau = 0.73$ the benign region is reached and subsequently the trajectory converges to the benign stationary point, i.e., the medical condition called equilibrium has been achieved. At the time when therapy is stopped, the states lie close to the stability boundary, but on opposite sides. For a while both trajectories still trace the stability boundary and in each case the tumor volume increases for some time and so does the immunocompetent cell density making it rather impossible to decide whether the course of action was successful or not. Separation of the trajectories only occurs when the state gets close to the unstable saddle point $w_{*,u}$ where the instability of the saddle becomes dominant and forces the trajectories to converge to one of the stable stationary points. Only at that time the separation between benign or malignant behavior becomes noticeable. If the state is in the benign region, eventually the reaction of the immune system will be strong enough to control the tumor. This clearly points to the importance of transferring the state of the system well into the benign region. Such an objective is easily incorporated in an optimal control framework, but it requires some knowledge about the geometry of the stability boundary.

Considering treatment as an optimal control problem avoids such fallacies as the solutions can be forced to transfer the state well into the benign region. For the problem formulated here a theoretical analysis based on necessary conditions for optimality [e.g., see (38–41)] singles out the following types of therapy protocols as optimal (42, 43): (a) drug administration schedules which alternate between maximum dose-rates and rest-periods, so-called *bang-bang* controls in optimal control (43) and (b) specific

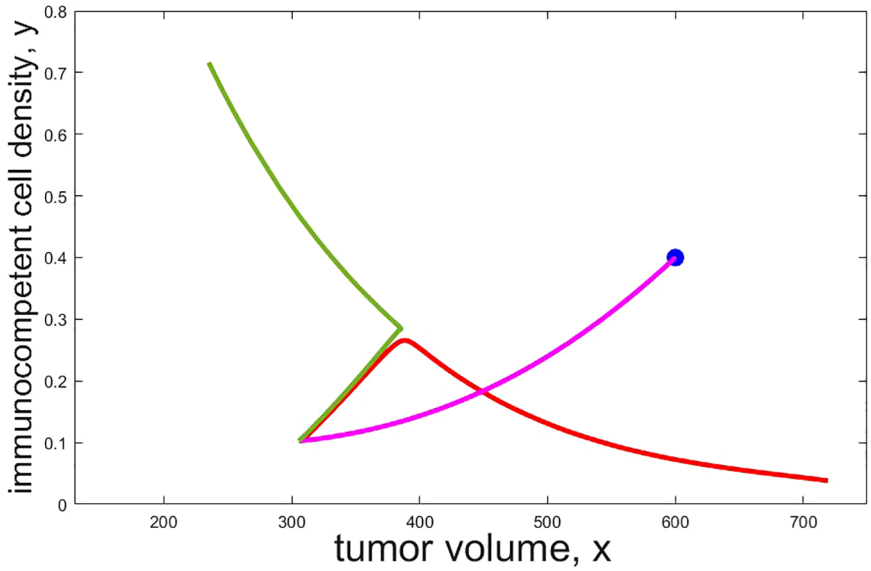

FIGURE 2
Projections of trajectories which administer both chemo and immunotherapy ($u \equiv 1$ and $v \equiv 1$) from the initial condition (x_0,y_0,z_0) = (600,0.40,400) (shown as a blue dot) for time τ and then turn off therapy. The initial segment under therapy is shown by a magenta curve, the subsequent trajectories are shown in red (τ = 0.72), respectively green (τ = 0.73). After therapy is stopped both trajectories still show virtually the same behavior for some time (that is, tumor volume and immuno competent sell density evolve the same way in time) before a separation occurs. Only then the red trajectory converges to the malignant stationary point while the green one converges to the benign one. As this simulation demonstrates, a small change in the administration time of the agents can make a big difference and this may not be recognizable for quite some time from the time history of the states.

intermittent administrations with particular time-varying dosage protocols at reduced rates. These rates are determined by mathematical formulas for what in optimal control theory are called *singular* controls. Such protocols can be ruled as being not optimal for immunotherapy based on a mathematical analysis of the problem with tools of geometric optimal control theory (Legendre-Clesch condition (38, 39, 41).

Figure 3 shows a numerically computed candidate bang-bang solution for the problem with a fixed terminal time T. The panel shows the controls u and v and a projection of the corresponding trajectory into (x,y)-space. Segments of the curves which correspond to immunotherapy only ($u = 0$ and $v = 1$) are shown as a magenta curve and segments of the curves which correspond to chemotherapy only ($u = 1$ and $v = 0$) are shown as a blue curve. The segment of the curve where both chemo- and immunotherapy are at full dose ($u = 1$ and $v = 1$) is shown as a brown curve and the segment of the curve where none of chemo- or immunotherapy is active ($u = 0$ and $v = 0$) is shown as a black curve. As before, this is merely an episodal illustration.

Unfortunately, and contrary to what seems to be claimed in some publications, there are no "fool-proof" numerical algorithms (not to mention software) which safely compute optimal controls for a mathematical problem of the type considered here. The Hamiltonian function for the control problem is not convex in the control and this precludes the use of simple two-point boundary algorithms. Discretization methods are notoriously unreliable when it comes to locating optimal singular controls often arbitrarily declaring that optimal solutions have been found simply when the value of the objective changes by little. The extremal shown in Figure 3 was painstakingly computed solving the very sensitive two-point boundary for bang-bang controls using our own code verifying that the result was an extremal. In line with the theoretical results, immunotherapy follows a bang-bang control and here is active at the beginning to be terminated at the second switching time t_2 = 0.630. The more potent chemotherapy is activated almost immediately at the first switching time t_1 = 0.055 and both therapies are on at full dose until the second switching time. The bulk of the reduction in tumor volume occurs during this time-interval. Chemotherapy is terminated at the third switching time t_3 = 1.195 and then only reactivated briefly at the fourth switching time t_4 = 2.4580 close to the end of the therapy horizon. During the long no treatment phase $[t_3, t_4]$ the tumor volume first increases slightly, but then, as the immunocompetent density increases, starts to decrease again. This behavior is typical for the evolution of a trajectory in a benign region. Therapy then concludes with a brief segment of maximum dose chemotherapy after the prolonged no treatment phase $[t_3, t_4]$. While there are no claims made that the parameter values underlying this calculation are medically realistic (they were simply used from various sources to illustrate the structure of possible solutions) and the switching times are merely given to convey some sense of the timing for this particular example, both the controls and trajectories follow reasonable patterns.

The graph in Figure 3 represents a situation when chemotherapy is significantly more effective than immunotherapy—this was reflected in the numerical values chosen for this particular

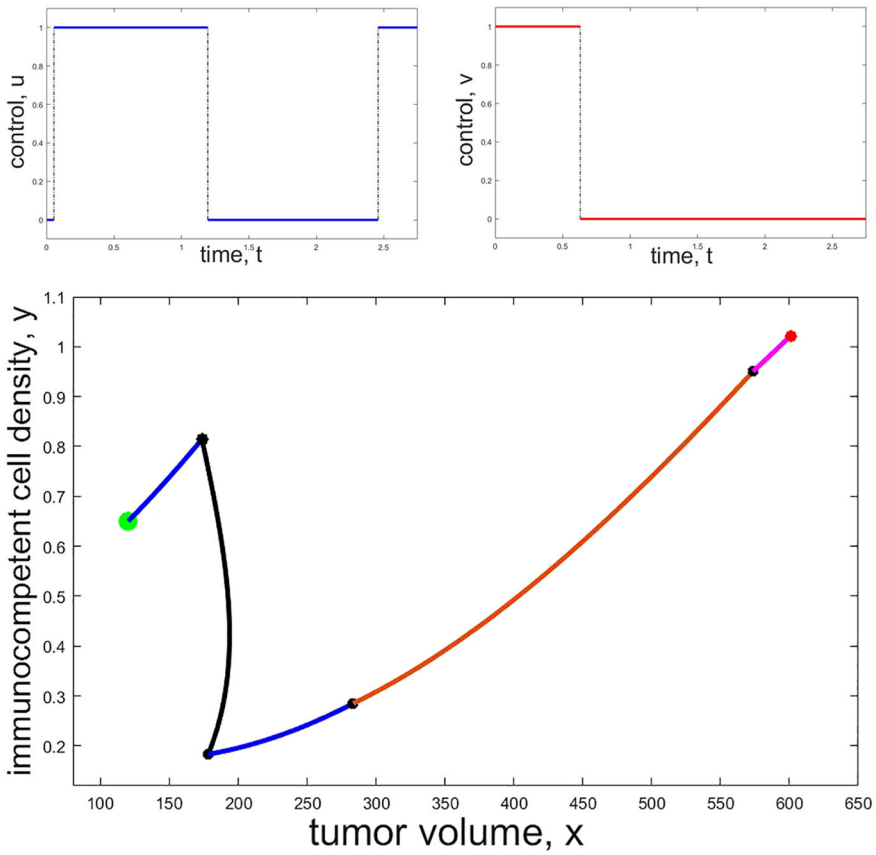

FIGURE 3
Example of a numerically computed candidate bang-bang trajectory: The top row shows the controls u (left, blue) and v (right, red) as functions of time while the bottom panel shows the projection of the corresponding trajectory into (x,y)-space. The initial point is marked with a red and the terminal point with a green dot. Black dots show the states on the trajectory where a change in the controls occurs. Initially only immunotherapy is given (magenta segment), then both chemo- and immunotherapy are active at the same time (brown segment) while immunotherapy is stopped and only chemotherapy is given along the blue segments. No drugs are administered along the black segment.

computation—and is only meant to be representative for such a scenario. Depending on the severity of side effects (represented in the weights of the objective) and the efficacy of the particular agents, different distributions of the administration of the agents will arise. Various examples of locally optimal bang-bang controls for a related optimal control problem are given in (42). Based on our numerical computations, bang-bang controls (administrations of the agents at full dose with rest periods) are the commonly observed optimal protocols for these types of problems.

4 Discussion

We formulated a 3-dimensional model for tumor-immune system interactions which in an attempt to more closely model the synergies traditional treatments might have with immunotherapies includes a separate equation for tumor antigen. For a mathematical model of tumor-immune interactions to be credible, it is in our opinion a necessary condition that it encompasses, within its range of parameters, the full spectrum of medically known tumor immune system interactions: elimination, equilibrium and tumor escape. This holds for Equations 1–3. Including tumor antigen as a separate state variable is an attempt to model synergistic effects which traditional treatments (chemotherapy considered here) have when combined with immunotherapies.

We reiterate that the model is qualitatively, not quantitative. The aim is to obtain information about the behavior of the dynamics overall, not about some particular situation. For the latter, a rather precise knowledge of the parameter values is required (which simply lies beyond our possibilities). Our emphasis here was on how understanding the behavior of the dynamics can help in the search for optimal dosage protocols. The optimal control problem allows to explore possible therapy protocols *in silico* suggesting what could be 'good' administration protocols relative to some chosen mathematical criterion. Unfortunately, there does not exist off-the-shelf software to solve such optimal control problems reliably and computing optimal controls. As there is great freedom in formulating this objective, there exists the danger of using inadequate criteria for mathematical expediency leading to not only not beneficial but possibly harmful outcomes. Thus we emphasize the need for an a posteriori analysis of the feasibility of the computed therapy protocols. In particular, as

side effects of the therapies are only included indirectly while minimizing the objective, the feasibility of the computed strategies from this point of view needs to be checked. It is believed that solutions to these optimal control problems can aid in formulating realistic therapy protocols that can be explored in medical trials and practice.

Data availability statement

The original contributions presented in the study are included in the article/supplementary material. Further inquiries can be directed to the corresponding author.

Author contributions

UL: Conceptualization, Supervision, Writing – original draft, Writing – review & editing. HS: Conceptualization, Software, Writing – original draft, Writing – review & editing.

Funding

The author(s) declare that no financial support was received for the research, authorship, and/or publication of this article.

Conflict of interest

The authors declare that the research was conducted in the absence of any commercial or financial relationships that could be construed as a potential conflict of interest.

Publisher's note

All claims expressed in this article are solely those of the authors and do not necessarily represent those of their affiliated organizations, or those of the publisher, the editors and the reviewers. Any product that may be evaluated in this article, or claim that may be made by its manufacturer, is not guaranteed or endorsed by the publisher.

References

1. Apetoh L, Ghiringhelli F, Tesniere A, Obeid M, Ortiz C, Criollo A, et al. Toll-like receptor 4-dependent contribution of the immune system to anticancer chemotherapy and radiotherapy. *Nat Med* (2007) 13):1050–9. doi: 10.1038/nm1622

2. Wielkie K, Hahnfeldt P. Modeling the dichotomy of the immune response to cancer:cytotoxic effects and tumor-promoting inflammation. *Bull Math Biol* (2017) 79:1436–48. doi: 10.1007/s11538-017-0291-4

3. Hagemann T, Balkwill F, Lawrence T. Inflammation and cancer: a double-edged sword. *Can Cell* (2007) 12:300–1. doi: 10.1016/j.ccr.2007.10.005

4. Tang C, Wang X, Soh H, Seyedin S, Cortez MA, Krishnan S, et al. Combining radiation and immunotherapy: a new systemic therapy for solid tumors? *Cancer Immunol Res* (2014) 2:831–8. doi: 10.1158/23266066.CIR-14-0069

5. Filatenkov A, Baker J, Mueller A, Kenkel J, Ahn G, Dutt S, et al. Ablative tumor radiation can change the tumor immune cell microenvironment to induce durable complete remissions. *Clin Can Res* (2015) 21:3727–39. doi: 10.1158/1078-0432.CCR-14-2824

6. Golden EB, Demaria S, Schiff P, Chachoua A, Formenti S. An abscopal response to radiation and ipilimumab in a patient with metastatic nonsmall cell lung cancer. *Can Immunol Res* (2013) 1:365–72. doi: 10.1158/2326-6066.CIR-13-0115

7. Poleszczuk JT, Enderling H. The optimal radiation dose to induce robust systemic anti-tumor immunity. *Int J Mol Sci* (2018) 19(11):3377. doi: 10.3390/ijms19113377

8. Poleszczuk JT, Luddy KA, Prokopiou S, Robertson-Tessi M, Moros E, Fishman M, et al. Abscopal benefits of localized radiotherapy depend on activated T-cell trafficking and distribution between metastatic lesions. *Cancer Res* (2016) 76(5):1009–18. doi: 10.1158/0008-5472.CAN-15-1423

9. Enderling H, Chaplain MAJ. Mathematical modeling of tumor growth and treatment. *Curr Pharm Design* (2014) 20(30):4934–40. doi: 10.2174/1381612819666131125150434

10. Stepanova NV. Course of the immune reaction during the development of a Malignant tumour. *Biophys* (1980) 24:917–23.

11. Kuznetsov VA, Makalkin IA, Taylor MA, Perelson AS. Nonlinear dynamics of immunogenic tumors: parameter estimation and global bifurcation analysis. *Bul Math Biol* (1994) 56:295–321. doi: 10.1007/BF02460644

12. Bellomo N, Preziosi L. Modelling and mathematical problems related to tumor evolution and its interaction with the immune system. *Math Comp Model* (2000) 32:413–52. doi: 10.1016/S0895-7177(00)00143-6

13. Bodnar M, Forys U. A model of immune system with time-dependent immune reactivity. *Nonlin Anal: Theory Methods Appl* (2009) 70(2):1049–58. doi: 10.1016/j.na.2008.01.031

14. Kogan Y, Fory U, Shukron O, Kronik N, Agur Z. Cellular immunotherapy for high grade gliomas: mathematical analysis deriving efficacious infusion rates based on patient requirements. *SIAM J Appl Math* (2010) 70(6):1953–76. doi: 10.1137/08073740X

15. Lai X, Friedman A. Combination therapy of cancer with cancer vaccine and immune checkpoint inhibitors: A mathematical model. *PloS One* (2017) 12(5): e0178479. doi: 10.1371/journal.pone.0178479

16. Lai X, Stiff A, Duggan M, Wesolowski R, Carson W.E.III, Friedman A. Modeling combination therapy for breast cancer with BET and immune checkpoint inhibitors. *Proc Natl Acad Sci USA* (2018) 115(21):5534–9. doi: 10.1073/pnas.1721559115

17. d'Onofrio A. A general framework for modelling tumor-immune system competition and immunotherapy: Mathematical analysis and biomedial inferences. *Physica D* (2005) 208:202–35. doi: 10.1016/j.physd.2005.06.032

18. d'Onofrio A. Metamodeling tumor-immune system interaction, tumor evasion and immunotherapy. *Math Comp Model* (2008) 47:614–37. doi: 10.1016/j.mcm.2007.02.032

19. de Pillis LG, Radunskaya A. A mathematical tumor model with immune resistance and drug therapy: an optimal control approach. *J Theo Med* (2001) 3:79–100. doi: 10.1080/10273660108833067

20. de Pillis LG, Radunskaya A, Wiseman CL. A validated mathematical model of cellmediated immune response to tumor growth. *Canc Res* (2005) 65:7950–8. doi: 10.1158/0008-5472.CAN-05-0564

21. Ledzewicz U, Schättler H. On modeling the synergy of Cancer immunotherapy with radiotherapy. *Commun Nonlin Sci Num Simul* (2023) 118. doi: 10.1016/j.cnsns.2022.106987

22. Ledzewicz U, Naghnaeian M, Schättler H. Optimal response to chemotherapy for a mathematical model of tumor-immune dynamics. *J Math Biol* (2012) 64:557–77. doi: 10.1007/s00285-011-0424-6

23. de Vladar HP, González JA. Dynamic response of cancer under the influence of immunological activity and therapy. *J Theor Biol* (2004) 227:335–48. doi: 10.1016/j.jtbi.2003.11.012

24. Dunn GP, Old LJ, Schreiber RD. The three E's of cancer immunoediting. *Ann Rev Immunol* (2004) 22:329–60. doi: 10.1146/annurev.immunol.22.012703.104803

25. Dunn GP, Bruce AT, Ikeda H, Old LJ, Schreiber RD. Cancer immunoediting: From immunosurveillance to tumor escape. *Nat Immunol* (2002) 3:991–8. doi: 10.1038/ni1102-991

26. Koebel CM, Vermi W, Swann J, Zerafa N, Rodig S, Old L, et al. Adaptive immunity maintains occult cancer in an equilibrium state. *Nature* (2007) 450:903–7. doi: 10.1038/nature06309

27. Swann JB, Smyth MJ. Immune surveillance of tumors. *J Clin Invest* (2007) 117:1137–46. doi: 10.1172/JCI31405

28. Schättler H, Ledzewicz U. *Optimal control for mathematical models of cancer therapies*. New York: Springer (2015).

29. Castiglione F, Piccoli B. Cancer immunotherapy, mathematical modeling and optimal control. *J Theo Biol* (2007) 247:723–32. doi: 10.1016/j.jtbi.2007.04.003

30. Ledzewicz U, Faraji Mosalman MS, Schättler H. Optimal controls for a mathematical model of tumor-immune interactions under targeted chemotherapy with immune boost. *Discrete Continuous Dynamical Systems Ser B* (2013) 18:1031–51. doi: 10.3934/dcdsb.2013.18.1031

31. Jarrett AM, Faghihi D, Hormuth II D, Lima E, Virostko J, Biros G, et al. Optimal control theory for personalized therapeutic regimens in oncology: Background, history, challenges, and opportunities. *J Clin Med* (2020) 9(5):1314. doi: 10.3390/jcm9051314

32. Ledzewicz U, Schättler H. Optimal and suboptimal protocols for a class of mathematical models of tumor anti-angiogenesis. *J Theo Biol* (2008) 252:295–312. doi: 10.1016/j.jtbi.2008.02.014

33. Sharp JA, Browning A, Mapder T, Baker C, Burrage K, Simpson M. Designing combination therapies using multiple optimal controls. *J Theor Biol* (2020) 497:110277. doi: 10.1016/j.jtbi.2020.110277

34. Ledzewicz U, Schättler H. On the role of pharmacometrics in mathematical models for cancer treatments. *Disc Cont Dyn Syst B* (2021) 26:483–99. doi: 10.3934/dcdsb.2020213

35. Skipper HE. On mathematical modeling of critical variables in cancer treatment (goals: better understanding of the past and better planning in the future). *Bul Math Biol* (1986) 48:253–78. doi: 10.1016/S0092-8240(86)90027-3

36. Serre R, Benzekry S, Padovani L, Meille C, Andr´e N, Ciccolini J, et al. Mathematical modeling of cancer immunotherapy and its synergy with radiotherapy. *Cancer Res* (2016) 76:4931–40. doi: 10.1158/0008-5472.CAN-15-3567

37. Bekker RA, Zahid MU, Binning JM, Spring B, Hwu P, Pilon-Thomas S, et al. Rethinking the immunotherapy numbers game. *J ImmunoTher Cancer* (2022) 10 (7):2022. doi: 10.1136/jitc-2022-005107

38. Bonnard B, Chyba M. Singular trajectories and their role in control theory. In: *Mathématiques & Applications*, vol. 40. Paris: Springer-Verlag (2003).

39. Bressan A, Piccoli B. *Introduction to the mathematical theory of control*. Springfield, Mo, USA: AIMS (2007).

40. Pontryagin LS, Boltyanskii VG, Gamkrelidze RV, Mishchenko EF. *The mathematical theory of optimal processes*. New York: Macmillan (1964).

41. Schättler H, Ledzewicz U. *Geometric optimal control*. New York: Springer (2012).

42. Ledzewicz U, Maurer H, Schättler H. Bang-bang optimal controls for a mathematical model of chemo- and immunotherapy in cancer. *Discr Cont Dyn Syst B* (2023). doi: 10.3934/dcdsb.2023141

43. Ledzewicz U, Schättler H. On the optimal control problem for a model of the synergy of chemo- and immunotherapy. *Opt Cont Meth Appl* (2023). doi: 10.1002/oca.3016

frontiers | Frontiers in Immunology

TYPE Original Research
PUBLISHED 15 February 2024
DOI 10.3389/fimmu.2024.1323319

OPEN ACCESS

EDITED BY
Vladimir A. Kuznetsov,
Upstate Medical University, United States

REVIEWED BY
Jianqiang Xu,
Dalian University of Technology, China
Ramray Bhat,
Indian Institute of Science (IISc), India
Hermann Frieboes,
University of Louisville, United States

*CORRESPONDENCE
Jeffrey West
jeffrey.west@moffitt.org
Alexander R. A. Anderson
Alexander.Anderson@moffitt.org

RECEIVED 17 October 2023
ACCEPTED 18 January 2024
PUBLISHED 15 February 2024

CITATION
West J, Rentzeperis F, Adam C, Bravo R, Luddy KA, Robertson-Tessi M and Anderson ARA (2024) Tumor-immune metaphenotypes orchestrate an evolutionary bottleneck that promotes metabolic transformation.
Front. Immunol. 15:1323319.
doi: 10.3389/fimmu.2024.1323319

Tumor-immune metaphenotypes orchestrate an evolutionary bottleneck that promotes metabolic transformation

Jeffrey West[1*], Frederika Rentzeperis[2], Casey Adam[3], Rafael Bravo[1], Kimberly A. Luddy[4], Mark Robertson-Tessi[1] and Alexander R. A. Anderson[1*]

[1]Integrated Mathematical Oncology Department, H. Lee Moffitt Cancer Center & Research Institute, Tampa, FL, United States, [2]Department of Mathematics, Dartmouth College, Hanover, NH, United States, [3]Department of Engineering Science, University of Oxford, Oxford, United Kingdom, [4]Cancer Biology and Evolution Program, H. Lee Moffitt Cancer Center & Research Institute, Tampa, FL, United States

Introduction: Metabolism plays a complex role in the evolution of cancerous tumors, including inducing a multifaceted effect on the immune system to aid immune escape. Immune escape is, by definition, a collective phenomenon by requiring the presence of two cell types interacting in close proximity: tumor and immune. The microenvironmental context of these interactions is influenced by the dynamic process of blood vessel growth and remodelling, creating heterogeneous patches of well-vascularized tumor or acidic niches.

Methods: Here, we present a multiscale mathematical model that captures the phenotypic, vascular, microenvironmental, and spatial heterogeneity which shapes acid-mediated invasion and immune escape over a biologically-realistic time scale. The model explores several immune escape mechanisms such as i) acid inactivation of immune cells, ii) competition for glucose, and iii) inhibitory immune checkpoint receptor expression (PD-L1). We also explore the efficacy of anti-PD-L1 and sodium bicarbonate buffer agents for treatment. To aid in understanding immune escape as a collective cellular phenomenon, we define immune escape in the context of six collective phenotypes (termed "meta-phenotypes"): Self-Acidify, Mooch Acid, PD-L1 Attack, Mooch PD-L1, Proliferate Fast, and Starve Glucose.

Results: Fomenting a stronger immune response leads to initial benefits (additional cytotoxicity), but this advantage is offset by increased cell turnover that leads to accelerated evolution and the emergence of aggressive phenotypes. This creates a bimodal therapy landscape: either the immune system should be maximized for complete cure, or kept in check to avoid rapid evolution of invasive cells. These constraints are dependent on heterogeneity in vascular context, microenvironmental acidification, and the strength of immune response.

Discussion: This model helps to untangle the key constraints on evolutionary costs and benefits of three key phenotypic axes on tumor invasion and treatment: acid-resistance, glycolysis, and PD-L1 expression. The benefits of concomitant anti-PD-L1 and buffer treatments is a promising treatment strategy to limit the adverse effects of immune escape.

KEYWORDS

tumor-immune cell interaction, agent-based modeling (ABM), metaphenotype, metabolism, evolution

1 Introduction

Metabolism plays a complex but key role in the evolution of cancerous tumors. Localized hypoxia due to vascular instability and dysfunction leads to acidification of the tumor microenvironment. Decreased pH selects for acid-resistant tumor-cell phenotypes, followed by the emergence of aerobic glycolysis [i.e., the Warburg effect (1)]. Further microenvironmental acidification by these metabolically aggressive cells foments acid-mediated invasion (2–4). This nonlinear evolutionary trajectory through a range of metabolic phenotypes has been studied clinically, experimentally, and theoretically (5–8).

The effect of metabolic processes on the immune system is a multifaceted interaction between intracellular metabolism of many varied cell types with the surrounding microenvironment. Immunometabolism is a growing area of study (9) where systems biology and mathematical approaches are highly suited to studying tumorimmune dynamics (10–16), whether using non-spatial continuum approaches (17) or spatial agent-based models (18). However, very few tumor-immune models to date have incorporated the effects of cancer metabolism on immune function (19).

1.1 Metabolism and the tumor-immune response

Cytotoxic T lymphocytes (CTL, also known as α/β CD8+ effector T-cells) are key players in adaptive immune response which are activated via antigen presentation during the body's initial inflammatory response and subsequently rapidly proliferate. Programmed cell death-1 (PD-1) is an inhibitory immune checkpoint receptor expressed on activated CTLs, and programmed cell death ligand-1 (PD-L1) is a cell surface marker that activates PD-1 signaling (20). Some cancers constitutively express PD-L1, leading to the development of anti-PD-1/PD-L1 therapy to counter this immune escape mechanism. Immune escape or evasion mechanisms may select for subclonal populations capable of withstanding immune predation (21), often well before tumor invasion into normal tissue (22).

We investigate two key connections between tumor metabolism and immune function: acid-inactivation and glucose competition. Acidic microenvironments have been shown to inactivate otherwise viable CTLs (23), as cells rescued from low pH environments had the ability to regain effector function (24). Tumor acidity also promotes regulatory T-cell (Treg) activity as well as an increase of PD-1 expression on Tregs, indicating that PD-1 blockade may increase suppressive capacity (25). Tumor-infiltrating CD8+ T-cells require glucose to support their killing function, hence competing for glucose with cancer cells dampens their anti-cancer response (26). In contrast, Tregs avoid competition for glucose through rewired metabolism away from aerobic glycolysis, which enhances their immune-suppression function within the tumor (27).

Acid-inactivation and glucose competition may diminish immunotherapy efficacy, suggesting a potential synergy between targeting intratumoral pH and immune checkpoint blockade. For example, combining oral bicarbonate buffering with immunotherapy (adoptive T-cell transfer, anti-CTLA4, or anti PD-1) increased responses in murine cancer models, presumably due to increased immune activity in a less acidic microenvironment (24). Another study showed that targeting bicarbonate transporters (e.g. SLC4A4) known to contribute to extracellular pH during progression of pancreatic adenocarcinomas (PDAC) (28) reduces tumor acidity, increases activation, cytotoxic activity, and perfusion of CD8+ T-cells, and sensitizes PDAC-bearing mice to immune checkpoint inhibition (28). Mechanistic modeling has been used to investigate the treatment effects of systemic pH buffers (sodium bicarbonate) to limit microenvironmental selection for acid-adapted phenotypes, resulting in significantly delayed carcinogenesis in TRAMP mice (7, 29). Buffers reduce intratumoral and peritumoral acidosis, inhibiting tumor growth (5) and reducing spontaneous and experimental metastases (30, 31).

1.2 The tumor-immune gambit

The back and forth of cancer treatment and a tumor's evolutionary response has been compared to a chess match (32).

Similarly, we show that immune predation of tumors can be likened to an "immune gambit", where a temporary sacrifice of (normal glycolytic) cells on the periphery leads to long-term acceleration of the invasion of aggressive (highly glycolytic) phenotypes into surrounding tissue. Vascular dynamics are often abnormal in tumors whereby areas of poor vascularization are prone to develop acidic niches. We show that poor vascularization selects for aggressive phenotypes while high vascularization undergoes low levels of evolution. This phenomena has a Goldilocks effect, which occurs only under moderate levels of immune response. The immune gambit is described as a collective phenotype, which critically depends on the interplay between local vascularization, immune infiltration, and immune evasive phenotypes (PD-L1).

1.3 Collective cellular phenotypes: the "Metaphenotype"

In order to describe the collective nature of phenotypes operating within the context of surrounding cells and environmental conditions, we propose the concept of a "metaphenotype". Each of these metaphenotypes account for phenotypic traits (e.g. PD-L1 expression or glycolytic rate) as well as surrounding environmental context (e.g. local glucose or pH concentration), and competition with neighboring cell types (immune, cancer, normal). A mathematical model is the ideal testing ground for defining collective phenotypes because it enables precise characterization of local context. A simple, contrived example in Figure 1 illustrates the need to quantify context-dependent selection in this model. This figure shows the time-evolution of identical phenotypic compositions that have varied initial spatial configurations (mixed or shell). The mixed configuration of low glycolysis (blue) and high glycolysis (purple) phenotypes leads to no evolution. The volumetric concentration of acid produced by aggressive cells is not enough to cause invasion when highly glycolytic cells are seeded far apart but artificially placing the aggressive high glycolysis phenotypes on the rim leads to invasion from increased volumetric acid via a group-effect. Clearly, both tumor phenotypic composition and neighboring context are important.

1.4 Mathematical modeling of immune metaphenotypes

Below, we propose and define six metaphenotypes in the context of immune escape and immunotherapy (see Figure 2). Then, we present a hybrid multiscale agent-based mathematical model that incorporates phenotypic, vascular, microenvironmental, and spatial heterogeneity to investigate the evolution of aerobic glycolysis in response to immune predation, over a biologically-realistic temporal scale (Figure 3). Next, we model immune predation by T-cells in the metabolically altered tumor microenvironment, including immune escape mechanisms such as acid-mediated inactivation of T-cells, T-cell inhibition by checkpoint ligand expression on tumor cells, and T-cell glucose deprivation (Figure 4). Finally, we quantify the evolution of metaphenotypes over time, illustrating the explanatory power of collective phenotypes in describing the response to buffer therapy and anti-PD-L1 in mono- and combination therapy (Figure 5).

2 Methods

2.1 Defining collective cellular phenotypes: immune metaphenotypes

First, we define six collective phenotypes (metaphenotypes) through the lens of immune escape (see Venn diagram in Figure 2A). Each metaphenotype is contingent on a recent tumor-immune interaction and defined in the context of local microenvironment, with the exception of a "null" metaphenotype: Immune Desert. The "null" metaphenotype is the lack of collective behavior: Immune Desert are cells that do not interact with T-cells. Next, we quantify two PD-L1 metaphenotypes: a counter-attack

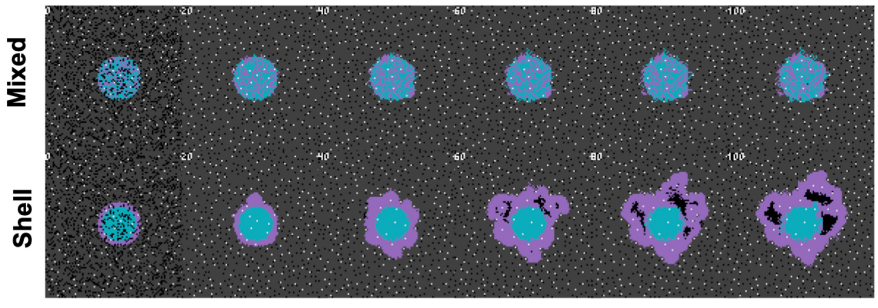

FIGURE 1
Collective phenotypes drive acid-mediated invasion. Spatial and temporal evolution of two distinct initial spatial configurations of identical numbers of cellular phenotypes leads to differential outcomes due to context-dependent selection. A low glycolysis phenotype (blue) and a high glycolysis phenotype (purple) compete for resources according to the rules outlined in section S1. Top row: a mixed configuration leads to no evolution. Acid-mediated invasion does not occur because the volumetric concentration of acid produced by aggressive cells is not enough to cause invasion when highly glycolytic cells are seeded far apart. Bottom row: In contrast, artificially placing the aggressive high glycolysis phenotypes on the rim leads to invasion from increased volumetric acid via a group-effect. Note: this figure has shorter timescales than subsequent figures, as it is seeded with pre-existing heterogeneity.

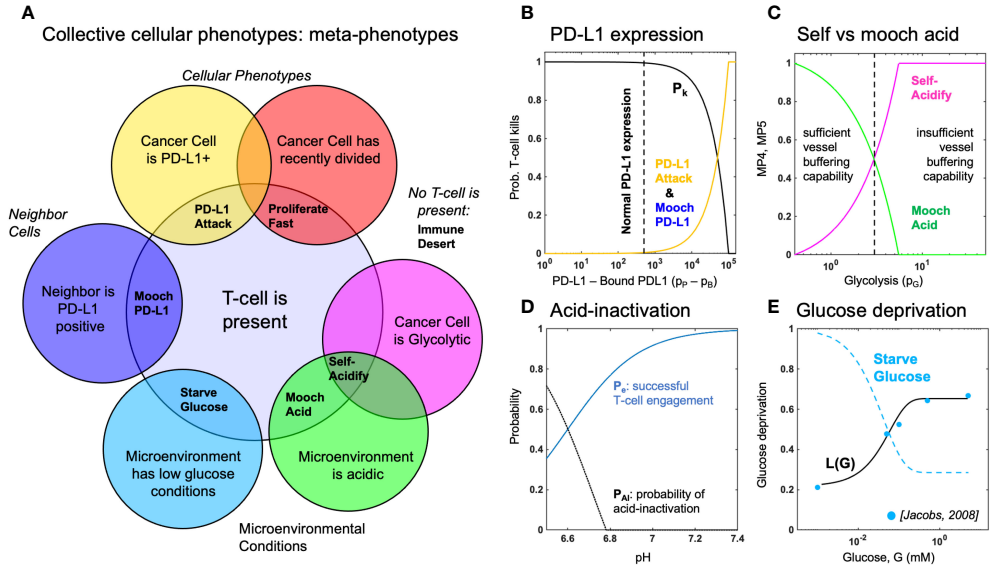

FIGURE 2
Defining metaphenotypes in the context of immune escape. **(A)** Six collective cellular metaphenotypes are defined as cancer cells with a given phenotype (e.g. PD-L1), microenvironmental condition (e.g. high acid or low glucose), or neighboring cell. Immune desert is the absence of recent immune interaction. **(B)** PD-L1 metaphenotypes depend on the likelihood of T-cell kill as a function of PD-L1 expression of self (PD-L1 Attack) or neighbor (Mooch PD-L1). **(C)** Acidification metaphenotypes depend on the rate of acidification contributed by self (Self-Acidify) or neighbors (Mooch acid). **(D)** The rate of acid-inactivation of T-cells. **(E)** Data from ref. 33 (blue dots) was used to parameterize T-cell death rate in low glucose, shown in Equation 20. The Starve Glucose metaphenotype expression corresponds to low glucose concentrations.

(tumor cell with high PD-L1 expression that has recently interacted with a T-cell; PD-L1 Attack, yellow), and a mooching PD-L1 (Mooch PD-L1, blue). As seen in Figure 2B, PD-L1 Attack is high in cells with high PD-L1 expression while Mooch PD-L1 is high in cells with low PD-L1 expression, but with neighbors that are high in PD-L1 Attack. See Box 1, Equations 3, 4. Two metaphenotypes rely on acid-inactivation: self-acidifying (highly glycolytic cells which secrete acid; Self-Acidify, pink) and non-producers (reside in acidic niche but do not produce acid; Mooch Acid, green). As seen in Figure 2C, Self-Acidify is high in cells with a high glycolytic phenotype, hence high acid production (see 5). In contrast, Mooch Acid cells have low glycolytic phenotype (not producing acid) but reside in highly a acidic niche that inactivates T-cells (Figure 2D). See Box 1, Equations 5–7. We also consider a proliferative phenotype that has recently divided into empty space (Proliferate Fast; red). See Box 1, Equation 8. Tumor cells also compete with immune cells for glucose (Starve Glucose; light blue). Figure 2E illustrates that Starve Glucose reside in areas with a high probability that T-cells die due to low glucose concentration. See Box 1, Equation 9. Importantly, each of these metaphenotypes (excluding Immune Dessert; see Equation 2) is contingent on a recent tumor-immune interaction, allowing us to track *effective* collective phenotypes: only metaphenotypes which survive an immune interaction.

2.2 Hybrid discrete-continuum multiscale model

We utilize this metaphenotype framework to better understand and predict tumor-immune interactions using a hybrid discrete-continuum multiscale model built using the Hybrid Automata Library framework (36). The mathematical model here is an extension of an experimentally validated multiscale model of cancer metabolism that incorporates the production of acid and acquired resistance to extracellular pH (6–8, 37) Figure 3A visualizes the model, which simulates a two-dimensional slice (panel A) through a tumor via a coupled cellular automata and partial differential equation model. A snapshot of multi-scale hybrid cellular automata model is shown (left-to-right) of the tumor spatial map, phenotypes, T-cells, diffusible molecules (oxygen, glucose, acid), PD-L1 and immune susceptibility. Values for parameterization are shown in Table 1. Values for parameters are typically identical to previous publications using the non-immune metabolism model (6, 7), except where parameter values are shown in brackets. In these cases, a parameter sweep is performed across the full range in order to determine the effect of the parameter on outcomes and test hypotheses. For convenience, we re-write the full model description, rules, and cell behaviors in Section S1.

3 Results

3.1 The effect of vasculature renewal and stability on tumor size and phenotype

In Figure 3, simulations are shown with the absence of immune predation to establish the model's baseline dynamics, before quantifying immune predation in the next figure. The model tracks two tumor phenotypes: acid resistance and glycolysis (Figure 3B), which vary according to vascularization settings. The model contains two vascularization parameters: the rate of new

10.3389/fimmu.2024.1323319

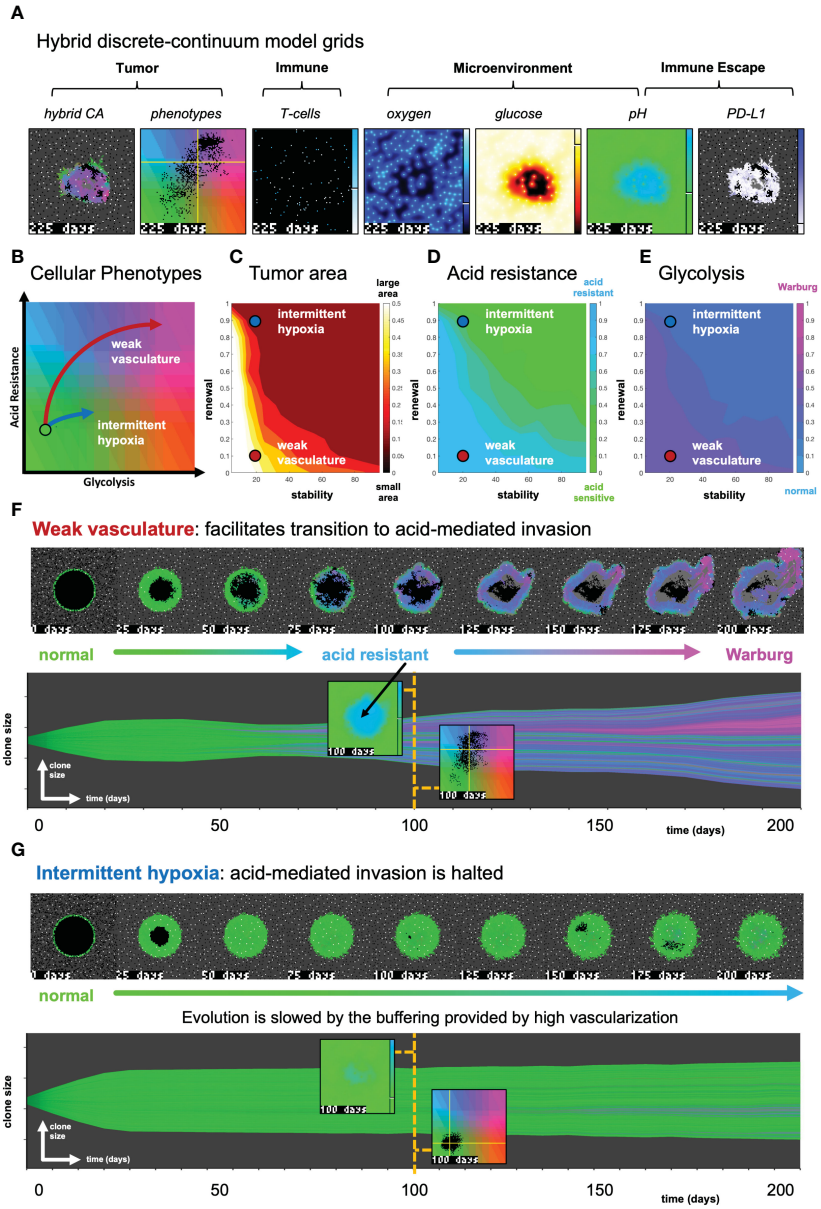

FIGURE 3
The effect of vasculature renewal and stability on tumor size and phenotype. **(A)** Hybrid discrete-continuum model grids. **(B)** Schematic of phenotypic trajectory of weak versus intermittent hypoxia vascular conditions. **(C–E)** N = 10 stochastic realizations are simulated, and the average tumor area **(C)**, acid resistance phenotype **(D)**, and glycolytic phenotype **(E)** across 10 values of stability ($v_{mean} \in$ [0,100] days), and 10 values of renewal ($p_{ang} \in$ [0,1]). **(F)** An example of "weak vasculature" (v_{mean}= 20; p_{ang}= 0.1). Acidic conditions in tumor core select for acid resistant and glycolytic Warburg phenotype. **(G)** An example realization of "intermittent hypoxia" (v_{mean}= 20; p_{ang}= 0.9), where selection is limited because of adequate vascularization within the tumor core. See associated Supplementary Video S2.

vessel formation (vascular renewal) in hypoxic conditions and the average number of days before vessel collapse (vascular stability).

We compare two classifications of vasculature: weak vasculature (associated with low vessel stability and low rates of vessel renewal) and intermittent hypoxia (associated with low stability, but high renewal). Intermittent hypoxia has been shown to be an evolutionary driver of selection in tumors via environmental changes in glucose, oxygen, and acidity (see ref. 4 for a recent review).

Figures 3C–E show the average tumor area (C), and tumor phenotypes (D,E) for simulations across a range of vascular settings (no immune). Weak vasculature (low stability and renewal) typically results in larger tumors, more acid resistant phenotypes, and highly glycolytic phenotypes. Weak vasculature induces an acidic niche in the tumor core, selecting for acid-resistant phenotypes (blue). Increased turnover enables increased evolution and selection for aggressive Warburg phenotypes (pink), leading to acid-mediated invasion into surrounding normal tissue. Intermittent hypoxia (low vascular stability with high rates of renewal) generally leads to lower rates of selection and subsequently less invasion (Figure 3B).

Spatial maps of phenotypes are shown over time in Figures 3F, G along with a visualization called "phenotypic barcoding", which visualizes the clone size, phenotype and lineage information over time (8) using the

10.3389/fimmu.2024.1323319

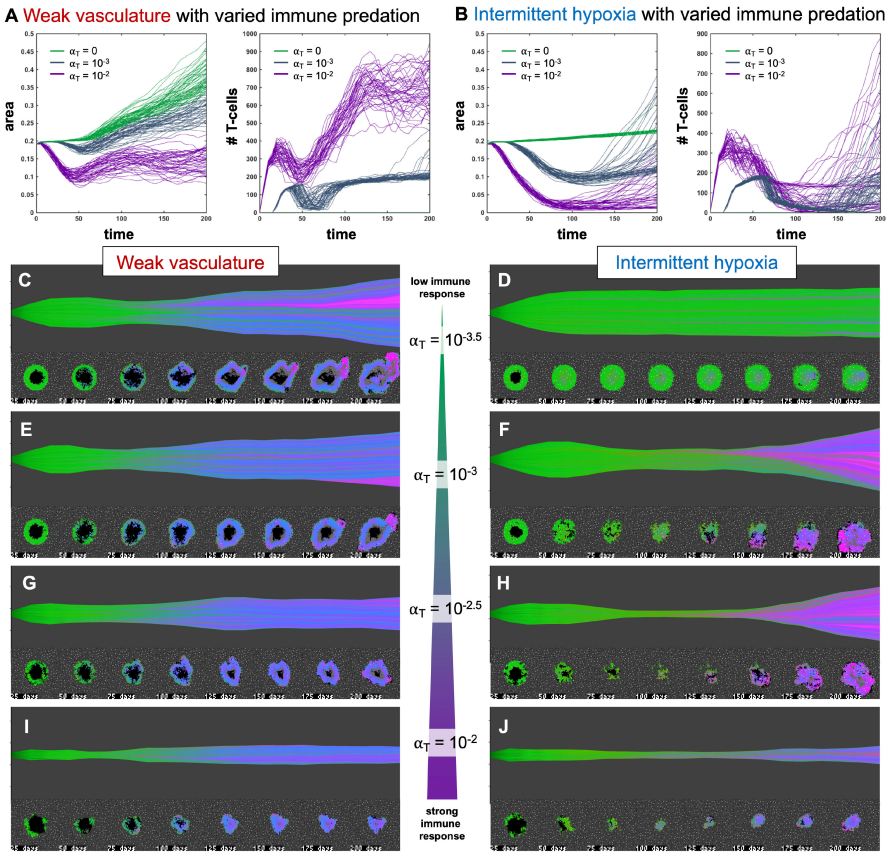

FIGURE 4
Immune predation induces an evolutionary bottleneck. **(A, B)** Tumor area over time (left) and the number of T-cells for weak vasculature **(A)** and intermittent hypoxia vasculature **(B)** conditions), shown for no T-cells (green; $\alpha_T = 0$), medium (blue-gray; $\alpha_T = 10^{-3}$) and high (purple; $\alpha_T = 10^{-2}$) immune response rates. **(C–J)** Example simulation stochastic realizations are shown across a range of immune response from low (top) to high (bottom). Immune predation tends to suppress tumor growth in weak vasculature conditions. In contrast, immune predation induces an evolutionary bottleneck for medium immune response rates (e.g. see **F, H**), causing aggressive tumor growth compared to the baseline of no immune response.

EvoFreq R package (38) (for more information on interpreting phenotypic barcoding plots, see Supplementary Figure S6). Figure 3F depicts the process by which weak vasculature selects for aggressive tumor growth. Acidic conditions in the tumor core (low glucose, low oxygen, and high pH) cause rapid death of glycolytically normal tumor cells with low levels of acid resistance. Selection for acid resistance occurs first (blue phenotypes), followed by selection for highly glycolytic tumor cells (pink phenotypes) which eventually invade into surrounding tissue. Conversely, in Figure 3G, intermittent hypoxia conditions result in little selection. The well-vascularized tumor core limits selection for aggressive phenotypes. This result underscores the importance of understanding the baseline vascular conditions before modeling the complex dynamics with the additional immune predation. A snapshot of the intratumoral oxygen, immune susceptibility (see Equation 21), phenotypes, and pH is shown at the end of each simulation.

3.2 Immune predation induces an evolutionary bottleneck

Figure 4 shows the response of two vascular conditions (weak and intermittent hypoxia) under no immune response (green; $\alpha_T = 0$), medium (blue-gray; $\alpha_T = 10^{-3}$) and high (purple; $\alpha_T = 10^{-2}$) immune response rates. Immune cells are recruited in proportion to tumor size and response rate, α_T.

Immune response tends to suppress tumor growth in weak vasculature conditions (Figure 4A, left). Compared to baseline tumor growth, all levels of immune response result in greater tumor suppression. In contrast, immune predation in intermittent hypoxia conditions often leads to an initial response but fast regrowth (Figure 4B, left). This is confirmed by visual inspection of the phenotypic barcoding visualizations in Figures 4C–J. Weak vascular conditions select for aggressive phenotypes with little-to-no immune presence (Figure 4C). The addition of immune cells only serves to slow an already aggressive tumor (Figures 4E, G, I). In stark contrast, intermittent hypoxia conditions rarely select for strong growth in the absence of immune predation (Figure 4D). Immune predation serves as a selection pressure, in conditions where there would otherwise be very little selection.

Immune predation under intermittent hypoxia conditions induces an evolutionary bottleneck for medium immune response rates (e.g. see F, H), causing fast selection for aggressive growth compared to the baseline of no immune response. Interestingly, this effect occurs on a “Goldilocks” scale. The long neck of the bottleneck

10.3389/fimmu.2024.1323319

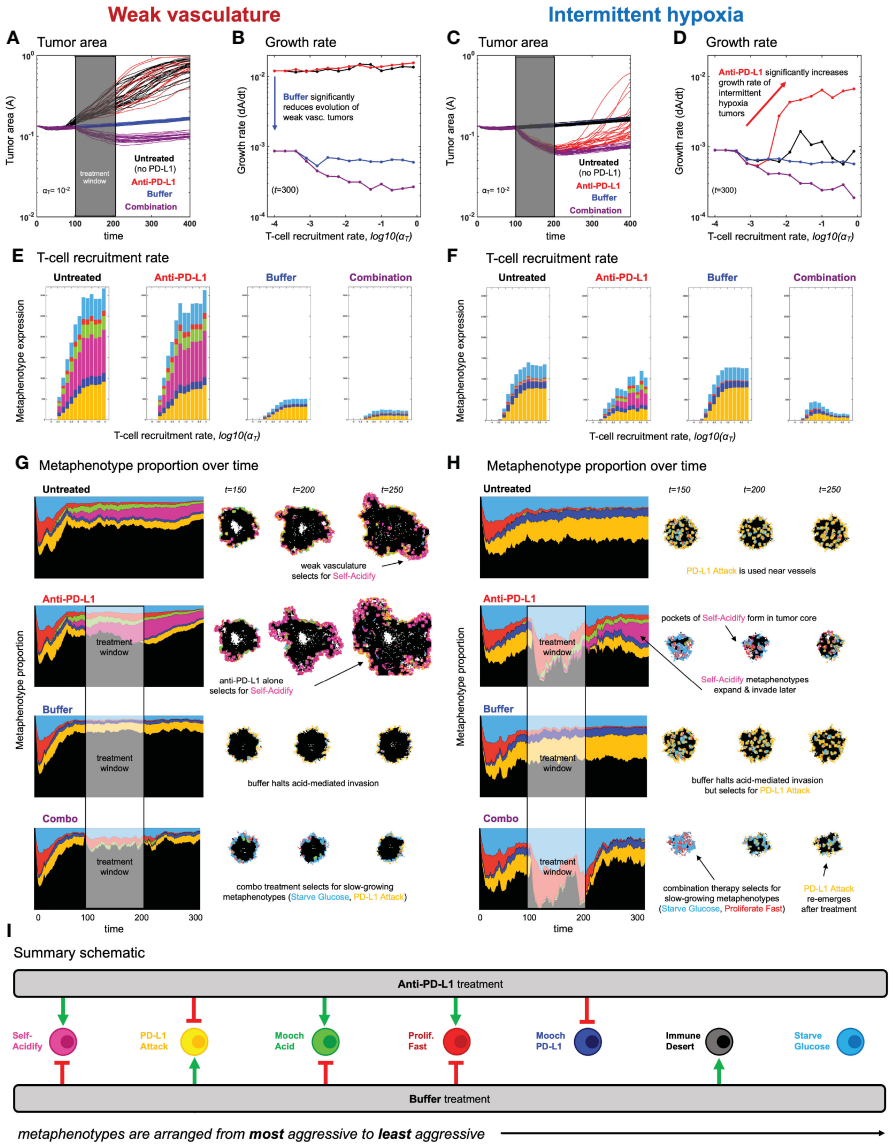

FIGURE 5
Evolution of metaphenotypes under treatment. Outcomes of tumor response and immune escape can be explained by observing the evolution of metaphenotypes under treatment with anti-PD-L1 (red) and buffer (blue), given in isolation or combination (purple). **(A)** Tumor area over time (weak vasculature) **(B)** growth rate over time (weak vasculature). **(C)** Tumor area over time (intermittent hypoxia vasculature) **(D)** growth rate over time (intermittent hypoxia vasculature). **(E, F)** Final distribution of metaphenotypes (exlcuding Immune Desert, see Supplementary Figure S7) at t = 300, repeated for weak vasculature **(E)** and intermittent hypoxia **(F)**. **(G, H)** Muller plots showing the frequency of metaphenotypes over time in untreated and mono- or combination therapy, with snapshots of spatial configurations during and after treatment, with moderate immune predation ($\alpha_T = 10^{-2}$). See associated Supplementary Videos S3, S4 and Supplementary Figure S7. **(I)** Summary schematic. Each metaphenotype is ordered from most aggressive to least aggressive in facilitating acid-mediated invasion and tumor growth under immune predation. This interaction diagram describes the role of two treatments (anti-PD-L1, buffer) in promoting (green) or inhibiting (red) each metaphenotype. Metaphenotypes names are shown on the left, and defined mathematically in Box 2. Broadly, the two treatments offset one another by inhibiting the metaphenotypes that the opposite treatment promotes.

is associated with higher rates of tumor turnover (due to immune attack), selecting for phenotypes which are 1) inside an immune-evasive niche or 2) rapidly divide to outgrow immune kill.

Note: Figure 4 does not include immune escape mechanisms, which will be included in subsequent figures. The temporary bottleneck may be relevant to treatment with immune checkpoint inhibitors, enabling immune infiltration and predation of established tumors but leading to only a partial response (24, 39, 40).

3.3 Metaphenotypes explain immune escape under treatment

After establishing the baseline dynamics without (Figure 3) and with (Figure 4) immune predation, we next consider two treatments to mitigate immune escape and to reduce tumor growth: anti-PD-L1 and a pH buffer given in isolation or combination. A short window of treatment is simulated and results are compared to the untreated

BOX 1 Defining metaphenotypes.

Let $T(x, y)$ be a two-dimensional grid representing the time since the last T-cell interaction has occurred within the local neighborhood of grid location (x, y). We define the tumor-immune interaction grid, $I(x, y)$, where $I = 1$ if an immune cell has traversed within a cancer cell's neighborhood within the previous T_w days and $I = 0$ otherwise at the current timestep, t.

$$I(x,y) = \begin{cases} 1, & \text{if } T(x,y) \geq t - T_w \\ 0, & \text{otherwise} \end{cases} \tag{1}$$

Metaphenotypes (MP) are defined in such a way that MP expression is scaled from zero to one and each cell can take on multiple MP: $\vec{M} = \{m_1, m_2, \ldots, m_7\}$ where $m_i \in [0, 1]$

2.1.1 MP1: Immune desert

We first consider the abscence of immune interaction: the immune desert metaphenotype, MP1, given by one minus I(x,y) given by Equation 1.

$$\text{MP1}(x,y) = 1 - I(x,y) \tag{2}$$

2.1.2 MP2: PD-L1 attack

Next, we classify cells which employ the PD-L1 counter-attack, defined as high PD-L1 expression (low probability of T-cell kill; see Equation 17) with a recent T-cell interaction:

$$\text{MP2}(x,y) = \underbrace{(1 - P_k)}_{\text{Prob. avoiding T-cell kill}} \times \underbrace{I(x,y)}_{\text{recent T-cell interaction}} \tag{3}$$

2.1.3 MP3: Mooch PD-L1

In contrast to MP2, cells which interact with T-cells but have low PD-L1 expression can rely on ("mooch") neighboring cell protection. Here, the metaphenotype is proportional to neighborhood PD-L1 expression.

$$\text{MP3}(x,y) = \underbrace{P_k}_{\text{Prob. T-cell kill}} \times \underbrace{1 - I(x,y)}_{\text{no T-cell interactions}} \times \max_{j \in N_m} \text{PD-L1}_j \tag{4}$$

where N_m is a Moore neighborhood of $N_m = 8$ neighbors.

2.1.4 MP4: Self-acidify

As cell increase glycolytic capacity (phenotype value p_G), more protons are added. The per cell proton production rate is given by:

$$p_R = f_H(1 - B(t)) \tag{5}$$

where proton production (see Box 2, Equation 14) rate is scaled by buffer treatment concentration, $B(t)$ (34, 35).

$$\text{MP4}(x,y) = \underbrace{P_{AI}(x,y)}_{\text{Probability of Acid-Inactivation}} \times \underbrace{\bar{p}_R}_{\text{scaled proton production rate}} \times \underbrace{I(x,y)}_{\text{recent T-cell interaction}} \tag{6}$$

where the production rate, $\bar{p}_R$, is normalized such that any value for phenotype above the buffering capability of a vessel is assumed to be mostly self-acidify metaphenotype (MP4), while below is assumed to be mostly mooch acid (MP5).

2.1.5 MP5: Mooch acid

Similarly, the mooch acidify metaphenotype occurs when the probability of T-cell acid-inactivation is high, but where the highly acidic microenvironment is not due to self-acidification.

$$\text{MP5}(x,y) = \underbrace{P_{AI}(x,y)}_{\text{Probability of Acid-Inactivation}} \times \underbrace{(1 - \bar{p}_R)}_{\text{scaled proton production rate}} \times \underbrace{I(x,y)}_{\text{recent T-cell interaction}} \tag{7}$$

This metaphenotype typically occurs early in simulations in empty regions without tumor or vasculature.

2.1.6 MP6: Proliferate fast

$$\text{MP6}(x,y) = \left(1 - \underbrace{\frac{D_{x,y}}{T_m}}_{\text{fraction of cell cycle completed}}\right) \times \underbrace{I(x,y)}_{\text{recent T-cell interaction}} \tag{8}$$

where D_i is the time until next division for the cell at location (x, y) and T_m is the inter-mitotic cell division time for a metabolically normal cell.

2.1.7 MP7: Starve glucose

Tumor cells may also compete with T-cells to starve immune cells of glucose, giving rise to the following metaphenotype:

$$\text{MP7}(x,y) = \underbrace{P_g}_{\text{Prob. T-cell dies in low glucose}} \times \underbrace{I(x,y)}_{\text{recent T-cell interaction}} \tag{9}$$

baseline. As seen in Figures 5A–D, combination therapy outperforms monotherapy in both vascular settings, but vascular dynamics drive differences in monotherapy outcomes. For example, anti-PD-L1 (red) therapy does not appreciably slow tumor evolution or growth in weak vasculature (Figures 5A, B). In contrast, anti-PD-L1 does induce large tumor remission in intermittent hypoxia (Figures 5C, D), albeit only temporarily before a strong relapse. These results are seen across a range of immune recruitment rates (Figures 5B, D).

The metaphenotypes leading to immune escape are shown in Figures 5E, F for each treatment scenario. As T-cell recruitment rate increases left-to-right, tumors evolve metaphenotypes in response to immune infiltration. Vascularization drives differential selection

10.3389/fimmu.2024.1323319

TABLE 1 Model parameterization.

Parameters	Value	Units	Description
δ_x	20	μm	Diameter of CA grid point
p_D	0.005	1/d	Normal tissue death rate
$p_\triangle$	0.7	1/d	Death probability in poor conditions
p_n	5e-4	1/d	Necrotic turnover rate
D_O	1820	$\mu m^2/s$	Diffusion rate of oxygen
D_g	500	$\mu m^2/s$	Diffusion rate of glucose
D_H	1080	$\mu m^2/s$	Diffusion of protons
O_O	0.0556	mmol/L	Oxygen concentration in blood
G_O	5	mmol/L	Glucose concentration in blood
pH_O	7.4	pH	pH of blood
V_O	0.012	mmol/L/s	Maximal oxygen consumption
k_O	0.005	mmol/L	Half-max oxygen concentration
k_G	0.04	mmol/L	Half-max glucose concentration
k_H	2.5e-4	–	Proton buffering coefficient
A_d	0.35	–	ATP threshold for death
A_q	0.8	–	ATP threshold for quiescence
$p_{H,min}$	6.1	pH	Maximal acid resistance phenotype
$p_{H,norm}$	6.65	pH	Normal acid resistance phenotype
ΔH	0.003	pH	Phenotype variation rate (acid res.)
$p_{G,max}$	50	–	Maximal glycolytic phenotype
ΔG	0.15	–	Phenotype variation rate (glycolysis)
τ_{min}	0.95	Days	Minimum cell cycle time
σ_{min}	80	μm	Minimum vessel spacing
σ_{mean}	150	μm	Mean vessel spacing
v_{mean}	[5, 100]	Days	Vessel stability
p_{ang}	[0, 1]	–	Angiogenesis rate
T_M	1	–	Probability T-cell moves
τ_T	4	–	T-cell response delay
α_T	[1e-4,1e-1]	–	T-cell recruitment rate
β_T	10	Days	Non-activated T-cell decay
$p_{P,min}$	5	–	Maximal PD-L1 phenotype
$p_{P,norm}$	2.7	–	Normal PD-L1 phenotype
ΔP	[0,1]	–	Phenotype variation rate (PD-L1)
d_e	0.042	Days	T-cell engagement duration
H_e	6.6	–	half-max pH T-cell engagement time
σ_e	4	–	steepness of T-cell engagement time
H_p	6.6	–	half-max pH T-cell engagement probability
σ_p	6	–	steepness of T-cell engagement probability
L_i	65.35	percent	T-cell survival rate in high glucose
L_0	21.78	percent	T-cell survival rate in low glucose
L_g	-16.67	percent	T-cell glucose deprivation parameter
D_A	100	$\mu m^2/s$	Anti-PD-L1 diffusion parameter
γ_A	0.5	$1/s$	Anti-PD-L1 natural decay rate
γ_P	0.001	$1/s$	Cellular bound PD-L1 decay rate

of metaphenotypes in baseline untreated dynamics. Weak vasculature (panel E; untreated) is associated with acidification metaphenotypes (Self-Acidify, pink; Mooch Acid, green). These are aggressive, highly glycolytic metaphenotypes that facilitate acid-mediated invasion. In contrast, intermittent hypoxia (panel F; untreated) selects for PD-L1-based immune-escape mechanisms (PD-L1 Attack, yellow; Mooch PD-L1, dark blue).

Treatment alters the type and magnitude of metaphenotype expression. Anti-PD-L1 selects for acidification metaphenotypes (Self-Acidify or Mooch Acid) in both vascularization cases. Buffer treatment eliminates the emergence of both Self-Acidify and Mooch Acid phenotypes by slowing evolution (e.g. refer to Figure 3B). But in response, PD-L1 Attack is selected (yellow). Only combination therapy targets both acidification metaphenotypes and PD-L1 phenotypes. Tracking the response of metaphenotypes to treatment explains why combination therapy is ideal for minimizing tumor growth, compared to monotherapy options. Importantly, only combination decreases the sum total of metaphenotypes expressed, and specifically targets aggressive phenotypes (Self-Acidify and Mooch Acid) across both vascularization scenarios.

3.4 Spatial configuration of metaphenotypes under treatment

The explanatory power of these defined metaphenotypes is seen most clearly by observing their spatial arrangement under high immune predation (see Figures 5G, H and associated Supplementary Videos S2, S3). For example, weak vasculature (Figure 5G) is associated with the Self-Acidify and PD-L1 Attack metaphenotypes on the

invasive front of the tumor. Much of the tumor interior is unaffected by immune cells (Immune Desert), regardless of tumor phenotype. Treatment with Anti-PD-L1 selects for the aggressive Self-Acidify metaphenotype, while Buffer selects for PD-L1 Attack on the tumor rim. Combination therapy is required to achieve maximum tumor response, resulting in small tumors consisting mostly of non-aggressive metaphenotypes (Starve Glucose or Proliferate Fast).

In contrast, under intermittent hypoxia vasculature the Immune Desert comprises a much lower fraction of tumor metaphenotypes, as this improved vascularization delivers T-cells into the tumor core. PD-L1 Attack is used near blood vessels and on the tumor rim, and Self-Acidify does not occur due to low turnover in untreated conditions. Treatment with Anti-PD-L1 negates immune escape from PD-L1 Attack, inducing cellular turnover and subsequently selecting for Self-Acidify and Mooch Acid metaphenotypes. Combination therapy results in small, slow-growing tumors with less aggressive metaphenotypes (Mooch PD-L1 and Starve Glucose).

In both vasculature settings, cells slightly inset from the rim use metaphenotypes that Mooch Acid and Mooch PD-L1 from cells on the rim (see Supplementary Videos S2, S3) while cells in regions of high turnover employ the Proliferate Fast metaphenotype. Starve Glucose remains at low levels throughout all treatment modalities and vasculature settings. As seen in the (Supplementary Videos S2, S3), it is difficult to determine the major driver of immune escape from the maps of phenotypes alone, as areas of high glycolysis and high PD-L1 are each spatially heterogeneous and overlapping. There likely exists heterogeneity in vascular stability and renewal rates within a single patient's tumor, which may drive heterogeneous metaphenotype expression (see Supplementary Video S5).

4 Discussion

Several factors contribute to a lack of responsiveness to immune checkpoint blockade, including abnormal tumor microenvironment where poor tumor perfusion hinders drug delivery and increases immunosuppression (41). Poor vascularization also leads to a hypoxic and therefore acidic microenvironment, increasing acid-mediated immunosuppression. The modeling we present here recapitulates this trend, as immune predation is less effective in weak vascularized tumors than in intermittently vascularized tumors. The importance of acidity in modulating immune response in cancer is only just beginning to be understood. Our results highlight the potential utility in buffering agents combined with immunotherapy. Whilst such buffering agents are not yet used in cancer treatment due to GI irritability and subsequent patient non-compliance, efforts continue to develop a buffer therapy that patients can tolerate and that is convenient to administer (42). Tumor acidosis can also be addressed by more indirect means. Some preclinical work has shown the potential influence of diet on acid buffering, but this remains poorly studied and may have limited effect on tumor pH (43).

Drugs that alter the vasculature are another possible indirect method for altering tumor pH. Development of agents that promote stable tumor vasculature would reduce acidosis and also increase both immune cell access and systemic-delivered drug penetration. However, there are potential risks to increasing tumor vascularity, regarding increased nutrient delivery and a higher potential for metastatic spread. Vascular renormalization can be enhanced through administration of anti-angiogenic agents (e.g., anti-vascular endothelial growth factor agents) to fortify immature blood vessels and improve tumor perfusion (44). However, our results indicate that administration of immune checkpoint blockade in tumors with increased vascularization may lead to a short-term good response but poor long-term outcomes as selection for increased glycolysis occurs. Mathematical modeling allows for direct comparison of initially identical simulations in the absence (Figure 3) and presence (Figure 4) of immune predation. We observe an immune gambit under high vascular renewal (intermittent hypoxia), due to an evolutionary bottleneck. The impact of this evolutionary bottleneck is reduced when anti-PD-L1 is combined with buffer therapy.

Characterization of collective phenotypes into metaphenotypes enables a straightforward explanation of the effect of treatment in a complex, multi-scale model. This characterization is necessary, in part, due to the fact that acid-mediated invasion is a collective phenotype phenomenon (Figure 1). Immune escape is also, by definition, a collective phenomenon by requiring the presence of two cell types in close proximity: tumor and immune. A summary schematic of the results is shown in Figure 5I. The interaction diagram describes the role of anti-PD-L1 and buffer in either promoting (green) or inhibiting (red) each metaphenotype. Broadly, the two treatments offset one another by inhibiting the metaphenotypes that the opposite treatment promotes. The two exceptions, starve glucose and immune desert, are both non-aggressive phenotypes. This summary schematic illustrates the utility of defining metaphenotypes in the context of treatment to provide insight into immune-escape dynamics. The most dominant mechanism of immune escape seen in the model is the lack of immune interactions (immune desert), especially when the tumor bed is poorly vascularized. Tumor-expressed PD-L1 is a viable immune-escape mechanism in the absence of treatment, across a range of vascularization, but treatment with anti-PD-L1 selects for the two acid-inactivation metaphenotypes (Self-Acidify and Mooch Acid). Environmental conditions must also consider neighboring (and self) cellular phenotypes. A cell in acidic conditions may rely on acid-inactivation either by self-production of acid or mooching from neighboring producer cells, a form of "public good" (45). Buffer therapy limits selection for self-acidification, driving selection toward less aggressive metaphenotypes (Glucose Starvation or Immune Desert). It's also important to note that mooching metaphenotypes only occur in the presence of non-mooching phenotypes. Because of this, and the fact that phenotypes of individual cells change only slowly (upon division), mooching phenotypes are not expected to be a viable long-term immune escape strategy, but limited to transient, local patches co-localized with non-moochers. However, in a model where the ratio of two phenotypes is determined stochastically, for example, a population of both phenotypes could coexist for a longer period of time.

It would be of interest to test the predictions of this model, and as described above, previous experimental exploration of acid-mediated invasion and immune suppression aligns with the findings of our paper (3, 7, 19, 24). New technology has enabled spatially resolved transcriptomics which can quantify cellular heterogeneity in context of spatial information (46). However, the

metaphenotype as a dynamic spatiotemporal metric is a challenge to measure (47), since most spatially resolved methods of interrogating a tumor *in vivo* are either destructive or of low resolution, and therefore lack the needed temporal component. Novel *in vivo* live-imaging technologies are one possible route to investigate how the different cellular phenotypes in the tumor environment change over time in response to emergent physiological changes and to therapeutic interventions (48). Another option would be the use of organoid cultures(e.g. 49), especially in conjunction with a 3D printer that could initialize different spatial configurations of the cells and environment for testing of hypotheses (50, 51).

The modeling framework presented here is not without its limitations. For example, 1) it is a two-dimensional representation of a three-dimensional tumors, 2) tumors may be heterogeneous in vasculature conditions, 3) we ignore directed motion of immune cells, and 4) parameters are an estimation based on literature values but may in reality be patient-specific. We also note limitations regarding the fundamental biological assumptions made in the model. For one, we are modeling the dominant form of cellular metabolism, namely the glycolytic and aerobic respiration pathway, but this is not the only source of cellular energy. Other forms involving glutamate, lactate, and more have been observed in tumor cells and would potentially alter how cells evolve in different environments. Another simplification involves the dynamics of immune response. T-cell activation, recruitment, engagement, and tolerance are all highly complex processes involving numerous cell types and cytokines, dynamic expression of different surface markers, and processes that work on many different timescales. Here we have limited ourselves to the influx of active T cells and not modeled upstream processes, nor immunosuppression generated by factors other than checkpoints and pH (e.g., regulatory T cells and other suppressive cells, TGF-beta and other suppressive secreted factors, and variable tumor antigenicity). These additional elements of immune response and tumor escape would certainly be worthy of further investigation in future work but will of course add significant complexity.

The intimate feedback between a growing tumor and the homeostatic tissue it is invading drives both ecological and evolutionary dynamics that should not be ignored in modern cancer therapy. The results we presented here indicate that treatments that modulate context may turn out to be just as important as those that target the tumor.

Data availability statement

The original contributions presented in the study are included in the article/Supplementary Material. Further inquiries can be directed to the corresponding authors.

Author contributions

JW: Conceptualization, Formal analysis, Investigation, Methodology, Visualization, Writing – original draft, Writing – review & editing. FR: Formal analysis, Investigation, Methodology, Visualization, Writing – review & editing. CA: Formal analysis, Investigation, Methodology, Visualization, Writing – review & editing. RB: Formal analysis, Investigation, Methodology, Visualization, Writing – review & editing. KL: Conceptualization, Formal analysis, Methodology, Validation, Visualization, Writing – original draft, Writing – review & editing. MR-T: Conceptualization, Formal analysis, Investigation, Methodology, Visualization, Writing – original draft, Writing – review & editing. AA: Conceptualization, Formal analysis, Funding acquisition, Methodology, Project administration, Resources, Supervision, Validation, Visualization, Writing – original draft, Writing – review & editing.

Funding

The author(s) declare financial support was received for the research, authorship, and/or publication of this article. The authors gratefully acknowledge funding by the National Cancer Institute via the Cancer Systems Biology Consortium (CSBC) U54CA274507 and U01CA232382, the Physical Sciences Oncology Network (PSON) U54CA193489, and support from the Moffitt Center of Excellence for Evolutionary Therapy.

Conflict of interest

The authors declare that the research was conducted in the absence of any commercial or financial relationships that could be construed as a potential conflict of interest.

Publisher's note

Supplementary material

The Supplementary Material for this article can be found online at: https://www.frontiersin.org/articles/10.3389/fimmu.2024.1323319/full#supplementary-material

References

1. Warburg O. Uber den stoffwechsel der karzinomezellen. *Biochem Z* (1924) 152:309–44.

2. Gatenby R, Gawlinski E, Gmitro A, Kaylor B, Gillies R. Acid-mediated tumor invasion: a multidisciplinary study. *Cancer Res* (2006) 66:5216.

3. Estrella V, Chen T, Lloyd M, Wojtkowiak J, Cornnell HH, Ibrahim-Hashim A, et al. Acidity generated by the tumor microenvironment drives local invasion. *Cancer Res* (2013) 73:1524–35.

4. Gillies RJ, Brown JS, Anderson AR, Gatenby RA. Eco-evolutionary causes and consequences of temporal changes in intratumoural blood flow. *Nat Rev Cancer* (2018) 18:576–85.

5. Silva AS, Yunes JA, Gillies RJ, Gatenby RA. The potential role of systemic buffers in reducing intratumoral extracellular ph and acid-mediated invasion. *Cancer Res* (2009) 69:2677–84.

6. Robertson-Tessi M, Gillies RJ, Gatenby RA, Anderson AR. Impact of metabolic heterogeneity on tumor growth, invasion, and treatment outcomes. *Cancer Res* (2015) 75:1567–79. doi: 10.1158/0008-5472.CAN-14-1428

7. Ibrahim-Hashim A, Robertson-Tessi M, Enriquez-Navas PM, Damaghi M, Balagurunathan Y, Wojtkowiak JW, et al. Defining cancer subpopulations by adaptive strategies rather than molecular properties provides novel insights into intratumoral evolution. *Cancer Res* (2017) 77:2242–54. doi: 10.1158/0008-5472.CAN-16-2844

8. Damaghi M, West J, Robertson-Tessi M, Xu L, Ferrall-Fairbanks MC, Stewart PA, et al. The harsh microenvironment in early breast cancer selects for a warburg phenotype. *Proc Natl Acad Sci* (2021) 118(3):e2011342118. doi: 10.1073/pnas.2011342118

9. Makowski L, Chaib M, Rathmell JC. Immunometabolism: From basic mechanisms to translation. *Immunol Rev* (2020) 295:5–14. doi: 10.1111/imr.12858

10. Purohit V, Wagner A, Yosef N, Kuchroo VK. Systems-based approaches to study immunometabolism. *Cell Mol Immunol* (2022) 19(3):409–20. doi: 10.1038/s41423-021-00783-9

11. Kirschner D, Panetta J. Modeling immunotherapy of the tumor-immune interaction. *J Math Biol* (1998) 37:235–52. doi: 10.1007/s002850050127

12. de Pillis L, Radunskaya A, Wiseman C. A validated mathematical model of cell-mediated immune response to tumor growth. *Cancer Res* (2005) 65:7950. doi: 10.1158/0008-5472.CAN-05-0564

13. Mallet DG, De Pillis LG. A cellular automata model of tumor–immune system interactions. *J Theor Biol* (2006) 239:334–50. doi: 10.1016/j.jtbi.2005.08.002

14. Robertson-Tessi M, El-Kareh A, Goriely A. A mathematical model of tumor–immune interactions. *J Theor Biol* (2012) 294:56–73. doi: 10.1016/j.jtbi.2011.10.027

15. Robertson-Tessi M, El-Kareh A, Goriely A. A model for effects of adaptive immunity on tumor response to chemotherapy and chemoimmunotherapy. *J Theor Biol* (2015) 380:569–84. doi: 10.1016/j.jtbi.2015.06.009

16. Bottino D, Liu R, Bazzazi H, Venkatakrishnan K. Quantitative translation in immuno-oncology research and development. *Clin Pharmacol Ther* 108(3):430.

17. Mahlbacher GE, Reihmer KC, Frieboes HB. Mathematical modeling of tumor-immune cell interactions. *J Theor Biol* (2019) 469:47–60. doi: 10.1016/j.jtbi.2019.03.002

18. Norton K-A, Gong C, Jamalian S, Popel AS. Multiscale agent-based and hybrid modeling of the tumor immune microenvironment. *Processes* (2019) 7:37. doi: 10.3390/pr7010037

19. El-Kenawi A, Gatenbee C, Robertson-Tessi M, Bravo R, Dhillon J, Balagurunathan Y, et al. Acidity promotes tumour progression by altering macrophage phenotype in prostate cancer. *Br J Cancer* (2019) 121:556–66. doi: 10.1038/s41416-019-0542-2

20. Brown JA, Dorfman DM, Ma FR, Sullivan EL, Munoz O, Wood CR, et al. Blockade of programmed death-1 ligands on dendritic cells enhances t cell activation and cytokine production. *J Immunol* (2003) 170:1257–66. doi: 10.4049/jimmunol.170.3.1257

21. Rosenthal R, Swanton C, McGranahan N. Understanding the impact of immune-mediated selection on lung cancer evolution. *Br J Cancer* (2021) 124 (10):1615–7. doi: 10.1038/s41416-020-01232-6

22. Mascaux C, Angelova M, Vasaturo A, Beane J, Hijazi K, Anthoine G, et al. Immune evasion before tumour invasion in early lung squamous carcinogenesis. *Nature* (2019) 571:570–5. doi: 10.1038/s41586-019-1330-0

23. Wu H, Estrella V, Beatty M, Abrahams D, El-Kenawi A, Russell S, et al. T-cells produce acidic niches in lymph nodes to suppress their own effector functions. *Nat Commun* (2020) 11:1–13. doi: 10.1038/s41467-020-17756-7

24. Pilon-Thomas S, Kodumudi KN, El-Kenawi AE, Russell S, Weber AM, Luddy K, et al. Neutralization of tumor acidity improves antitumor responses to immunotherapy. *Cancer Res* (2016) 76:1381–90. doi: 10.1158/0008-5472.CAN-15-1743

25. Kumagai S, Koyama S, Itahashi K, Tanegashima T, Lin YT, Togashi Y, et al. Lactic acid promotes pd-1 expression in regulatory t cells in highly glycolytic tumor microenvironments. *Cancer Cell* (2022) 40(2):201–18.

26. Chang C-H, Qiu J, O'Sullivan D, Buck MD, Noguchi T, Curtis JD, et al. Metabolic competition in the tumor microenvironment is a driver of cancer progression. *Cell* (2015) 162:1229–41.

27. Watson MJ, Vignali PD, Mullett SJ, Overacre-Delgoffe AE, Peralta RM, Grebinoski S, et al. Metabolic support of tumour-infiltrating regulatory t cells by lactic acid. *Nature* (2021) 591:645–51.

28. Cappellesso F, Orban MP, Shirgaonkar N, Berardi E, Serneels J, Neveu MA, et al. Targeting the bicarbonate transporter slc4a4 overcomes immunosuppression and immunotherapy resistance in pancreatic cancer. *Nat Cancer 1–20* (2022) 3(12):1464–83.

29. Ibrahim-Hashim A, Cornnell HH, Abrahams D, Lloyd M, Bui M, Gillies RJ, et al. Systemic buffers inhibit carcinogenesis in tramp mice. *J Urol* (2012) 188(2):624–31.

30. Robey IF, Baggett BK, Kirkpatrick ND, Roe DJ, Dosescu J, Sloane BF, et al. Bicarbonate increases tumor ph and inhibits spontaneous metastases. *Cancer Res* (2009) 69:2260–8.

31. Hashim AI, Cornnell HH, Coelho Ribeiro MDL, Abrahams D, Cunningham J, Lloyd M, et al. Reduction of metastasis using a non-volatile buffer. *Clin Exp Metastasis* (2011) 28:841–9. doi: 10.1007/s10585-011-9415-7

32. Beckman RA, Yeang C-H. Nonstandard personalized medicine strategies for cancer may lead to improved patient outcomes. *Personalized Med* (2014) 11:705–19. doi: 10.2217/pme.14.57

33. Jacobs SR, Herman CE, MacIver NJ, Wofford JA, Wieman HL, Hammen JJ, et al. Glucose uptake is limiting in t cell activation and requires cd28-mediated aktdependent and independent pathways. *J Immunol* (2008) 180:4476–86.

34. Mendler AN, Hu B, Prinz PU, Kreutz M, Gottfried E, Noessner E. Tumor lactic acidosis suppresses ctl function by inhibition of p38 and jnk/c-jun activation. *Int J Cancer* (2012) 131:633–40.

35. Rothstein TL, Mage M, Jones G, McHugh LL. Cytotoxic t lymphocyte sequential killing of immobilized allogeneic tumor target cells measured by time-lapse microcinematography. *J Immunol* (1978) 121:1652–6.

36. Bravo RR, Baratchart E, West J, Schenck RO, Miller AK, Gallaher J, et al. Hybrid automata library: A flexible platform for hybrid modeling with real-time visualization. *PloS Comput Biol* (2020) 16:1–28. doi: 10.1371/journal.pcbi.1007635

37. Anderson AR. A hybrid mathematical model of solid tumour invasion: the importance of cell adhesion. *Math Med Biology: A J IMA* (2005) 22:163–86. doi: 10.1093/imammb/dqi005

38. Gatenbee CD, Schenck RO, Bravo RR, Anderson AR. Evofreq: visualization of the evolutionary frequencies of sequence and model data. *BMC Bioinf* (2019) 20:1–4. doi: 10.1186/s12859-019-3173-y

39. Nishino M, Ramaiya NH, Hatabu H, Hodi FS. Monitoring immune-checkpoint blockade: response evaluation and biomarker development. *Nat Rev Clin Oncol* (2017) 14:655–68. doi: 10.1038/nrclinonc.2017.88

40. Miao Y, Yang H, Levorse J, Yuan S, Polak L, Sribour M, et al. Adaptive immune resistance emerges from tumor-initiating stem cells. *Cell* (2019) 177:1172–1186. doi: 10.1016/j.cell.2019.03.025

41. Munn LL, Jain RK. Vascular regulation of antitumor immunity. *Science* (2019) 365:544–5. doi: 10.1126/science.aaw7875

42. Gillies RJ, Ibrahim-Hashim A, Ordway B, Gatenby RA. Back to basic: Trials and tribulations of alkalizing agents in cancer. *Front Oncol* (2022) 12:981718.

43. Pilot C, Mahipal A, Gillies R. Buffer therapy—buffer diet. *J Nutr Food Sci* (2018) 8(02):684. doi: 10.4172/2155-9600.1000685

44. Mpekris F, Voutouri C, Baish J.W, Duda D.G, Munn L.L, Stylianopoulos T, et al. Combining microenvironment normalization strategies to improve cancer immunotherapy. *Proc Natl Acad Sci* (2020) 117:3728–37. doi: 10.1073/pnas.1919764117

45. Archetti M, Pienta KJ. Cooperation among cancer cells: applying game theory to cancer. *Nat Rev Cancer* (2019) 19:110–7. doi: 10.1038/s41568-018-0083-7

46. Marx V. Method of the year: spatially resolved transcriptomics. *Nat Methods* (2021) 18:9–14. doi: 10.1038/s41592-020-01033-y

47. West J, Robertson-Tessi M, Anderson AR. Agent-based methods facilitate integrative science in cancer. *Trends Cell Biol* (2023) 33:300–11. doi: 10.1016/j.tcb.2022.10.006

48. Alieva M, Wezenaar AK, Wehrens EJ, Rios AC. Bridging live-cell imaging and next-generation cancer treatment. *Nat Rev Cancer* (2023) 23:731–45. doi: 10.1038/s41568-023-00610-5

49. Strelez C, Jiang HY, Mumenthaler SM. Organs-on-chips: A decade of innovation. *Trends Biotechnol* (2023) 41:278–80. doi: 10.1016/j.tibtech.2023.01.004

50. Moghimi N, Hosseini SA, Dalan AB, Mohammadrezaei D, Goldman A, Kohandel M. Controlled tumor heterogeneity in a co-culture system by 3d bio-printed tumor-onchip model. *Sci Rep* (2023) 13:13648.

51. Nguyen DT, Famiglietti JE, Smolchek RA, Dupee Z, Diodati N, Pedro DI, et al. 3d *in vitro* platform for cell and explant culture in liquid-like solids. *Cells* (2022) 11:967.

frontiers | Frontiers in Immunology

TYPE Original Research
PUBLISHED 07 March 2024
DOI 10.3389/fimmu.2024.1358019

OPEN ACCESS

EDITED BY
Heiko Enderling,
University of Texas MD Anderson Cancer Center, United States

REVIEWED BY
Teddy Lazebnik,
University College London, United Kingdom
Federica Eduati,
Eindhoven University of Technology, Netherlands

*CORRESPONDENCE
Trachette L. Jackson
tjacks@umich.edu

RECEIVED 19 December 2023
ACCEPTED 21 February 2024
PUBLISHED 07 March 2024

CITATION
Bergman DR, Wang Y, Trujillo E, Fernald AA, Li L, Pearson AT, Sweis RF and Jackson TL (2024) Dysregulated FGFR3 signaling alters the immune landscape in bladder cancer and presents therapeutic possibilities in an agent-based model.
Front. Immunol. 15:1358019.
doi: 10.3389/fimmu.2024.1358019

Dysregulated FGFR3 signaling alters the immune landscape in bladder cancer and presents therapeutic possibilities in an agent-based model

Daniel R. Bergman[1], Yixuan Wang[1], Erica Trujillo[2], Anthony A. Fernald[2], Lie Li[2], Alexander T. Pearson[2], Randy F. Sweis[2] and Trachette L. Jackson[1]*

[1]Department of Mathematics, University of Michigan, Ann Arbor, MI, United States, [2]Department of Medicine, Section of Hematology/Oncology, The University of Chicago, Chicago, IL, United States

Bladder cancer is an increasingly prevalent global disease that continues to cause morbidity and mortality despite recent advances in treatment. Immune checkpoint inhibitors (ICI) and fibroblast growth factor receptor (FGFR)-targeted therapeutics have had modest success in bladder cancer when used as monotherapy. Emerging data suggests that the combination of these two therapies could lead to improved clinical outcomes, but the optimal strategy for combining these agents remains uncertain. Mathematical models, specifically agent-based models (ABMs), have shown recent successes in uncovering the multiscale dynamics that shape the trajectory of cancer. They have enabled the optimization of treatment methods and the identification of novel therapeutic strategies. To assess the combined effects of anti-PD-1 and anti-FGFR3 small molecule inhibitors (SMI) on tumor growth and the immune response, we built an ABM that captures key facets of tumor heterogeneity and $CD8^+$ T cell phenotypes, their spatial interactions, and their response to therapeutic pressures. Our model quantifies how tumor antigenicity and FGFR3 activating mutations impact disease trajectory and response to anti-PD-1 antibodies and anti-FGFR3 SMI. We find that even a small population of weakly antigenic tumor cells bearing an FGFR3 mutation can render the tumor resistant to combination therapy. However, highly antigenic tumors can overcome therapeutic resistance mediated by FGFR3 mutation. The optimal therapy depends on the strength of the FGFR3 signaling pathway. Under certain conditions, ICI alone is optimal; in others, ICI followed by anti-FGFR3 therapy is best. These results indicate the need to quantify FGFR3 signaling and the fitness advantage conferred on bladder cancer cells harboring this mutation. This ABM approach may enable rationally designed treatment plans to improve clinical outcomes.

KEYWORDS

agent-based model, bladder cancer, FGFR3, immune checkpoint inhibition, CD8+ T cells, Fas/Fas ligand, perforin/granzyme, antigenicity

1 Introduction

Bladder cancer, any tumor that originates in the urinary bladder, is the tenth most commonly diagnosed cancer worldwide, and its prevalence is increasing globally (1). While treatment options for bladder cancer have expanded in recent years, the 5-year survival rate remains low, highlighting the clinical need for new therapeutic approaches (2, 3).

In recent decades, there have been significant advancements in developing innovative therapeutic options that target tumors with specific molecular perturbations (2). These novel treatment options, referred to as targeted therapies, have revolutionized the approach to managing several cancer types (2). Within the complex landscape of bladder cancer, genomic analysis has revealed that about 80% of early-stage bladder cancers exhibit frequent alterations in fibroblast growth factor receptor 3 (FGFR3) that lead to both over-expression and constitutive activation, even in the absence of its natural ligand (4, 5). These mutations in FGFR3 lead to both increased proliferation and survival of bladder cells, making this protein not only a potent oncogenic driver in bladder cancer but also a predictive biomarker of response to FGFR3 small molecule inhibitors (5, 6). Evidence has also linked the presence of FGFR3 mutations to a lack of immune infiltrate, specifically $CD8^+$ T cells (7), highlighting the need to understand the role of this mutation in perturbing the immune response.

In addition to small molecular inhibitors targeting FGFR3 mutations, immune checkpoint inhibition (ICI) is another avenue of therapeutic efficacy. Monoclonal antibodies targeting immune checkpoint pathways have yielded favorable outcomes for some patients with bladder cancer (8). Nevertheless, the objective response rate to these treatments alone remains disappointingly low, and FGFR3 mutations potentially hinder the impact of ICI immunotherapy (9).

Given the modest efficacy of targeted small molecule inhibitors and monoclonal antibodies when administered as monotherapies, synergistically combining potent immune checkpoint and specific FGFR3 inhibitors may improve therapeutic response rates. Emerging clinical data indicate combinations are feasible and suggest improved efficacy (10, 11). However, determining the optimal and most effective dosing strategies while minimizing toxicities remains elusive, underscoring the need for further exploration and innovation.

Mathematical modeling is a tool that has been successfully deployed to enhance our understanding of biological systems, including how to combine multiple therapeutics to improve efficacy. Ordinary differential equation (ODE) modeling has been used to predict patient responses to intermittent androgen deprivation in prostate cancer (12) and has demonstrated promising results in informing a pilot clinical study treating patients with metastatic castration-resistant prostate cancer (13). Similar work has been undertaken with PARP inhibitors for the treatment of ovarian cancer (14). In bladder cancer, ODE models have been used to understand immunotherapy response (15–17). We previously analyzed a model of FGFR3 mutation in bladder cancer, considering the therapeutic efficacy of combination ICI and a small molecule inhibitor (SMI) of FGFR3 (18).

Such ODE models have been most commonly used due to their high level of abstraction resulting in computationally tractable, often reductionist systems that can be calibrated to time course data and be used to predict with high accuracy scalar metrics such as tumor volume. The limitation of these models is their lack of spatial context and intra-compartment cellular heterogeneity. Partial differential equation (PDE) modeling, accounting for the spatial context and thereby cell-cell interactions, has been used to study cancer immunotherapies (19). Agent-based models (ABMs), moreover, provide a modular, mechanistic framework to incorporate these features and further interrogate the dynamic processes that determine tumor evolution and response to therapy (20–24). In particular, they include cell-cell interactions, hybrid modeling of diffusive molecules, and therapeutic interventions (25, 26). Additionally, some models include other aspects important to cancer biology such as evolution and the extracellular matrix (27, 28). Even while techniques are being developed to calibrate these computationally expensive, stochastic models to real-world data (29–31), ABMs are situated to integrate domain expertise and bioinformatics analyses in a unified framework that can both generate and test hypotheses to advance basic and translational science (32).

In this paper, we develop a 3D multiscale, ABM of the tumor immune landscape to predict, understand, and suggest ways to improve ICI and small molecule inhibitor therapies that target the frequently mutated FGFR3 receptor in bladder cancer. The ICI we consider here is anti-PD-1 monoclonal antibodies that block signaling in the PD-1/PD-L1 axis. We also use the model to gain a robust understanding of how FGFR3 mutations affect the immune system and ultimately impact the efficacy of combining these two therapies. We simultaneously explore the impact of heterogeneity in antigen expression by tumor cells, resulting in differential activation of T cell-mediated killing pathways. As higher antigen levels have been correlated with more perforin/granzyme activity in $CD8^+$ T cells (33), we assume that cytotoxic T lymphocytes (CTLs) employ perforin/granzyme to eliminate high antigen tumor cells but resort to Fas ligand (FasL) for the elimination of low antigen tumor cells. We first show how the response to ICI monotherapy depends on the tumor composition–both antigenicity and FGFR3 mutation status–and the resulting immune infiltrate. We then look at how FGFR3-targeted therapy can improve upon ICI therapy and work synergistically to improve outcomes in certain contexts. Finally, we identify how the strength of the constitutively active FGFR3 pathway can alter these results in a clinically relevant manner.

2 Methods

We employ a 3D, on-lattice ABM that includes heterogeneous tumor cells and CTLs as agents. Throughout, we use “immune cells”, “CTLs”, and “$CD8^+$ T cells” interchangeably. Tumor cells have three dimensions along which they can differ from one another: antigenicity, FGFR3 mutation, and FGFR3 dimer concentration. Parent tumor cells pass all three characteristics onto their daughter cells. Tumor antigenicity and FGFR3 mutation are binaries divided into low vs. high and wild type vs.

mutant, respectively. FGFR3 dimer concentration is a continuous state variable governed by kinetic equations (Section S1.6. Tumor cells secrete immune stimulatory factor (ISF) into the local neighborhood of the tumor microenvironment (TME) depending on their antigenicity with high antigen (HA) tumor cells contributing more than low antigen (LA) tumor cells. Tumor cells possessing the FGFR3 mutation will be able to undergo ligand-independent dimerization of their FGFR3 monomers, leading to changes in their proliferation and apoptosis rates. In addition, this FGFR3 signaling limits the CTL infiltration rate into the TME (Section 2.3) Moreover, our hybrid, continuous-discrete ABM includes two diffusible therapeutic agents: an anti-FGFR3 small molecule inhibitor and an anti-PD-1 monoclonal antibody. Each agent has its own pharmacokinetic (PK) model. Further details of these PK models and the effects of these agents can be found in Section S1.6) and Section S1.8), respectively.

Figure 1 is a schematic diagram of the algorithm for simulating the ABM. The TME is initialized with 100 tumor cells near the center of the TME. No immune cells are present initially. The simulation is discretized into uniform time steps. For each iteration of the modeling loop, FGFR3 state variables are updated first, followed by tumor events. Each tumor cell can either attempt to proliferate or undergo apoptosis. Next, PD-1/PD-L1 state variables are updated, followed by immune events. Each immune cell can perform one of six actions: proliferation, death, migration, conjugation with a tumor cell, deactivation, and activation-induced cell death (AICD). After immune events are completed, apoptotic tumor cells are removed from the ABM. If it is time to administer the next round of therapy, it is added into the central compartment of the corresponding PK model. Otherwise, the model goes into the next iteration. Below is a selection of details about the how tumor and immune cell events are decided for each cell, and how FGFR3 and PD-1/PD-L1 related concentrations are calculated at each update. Full models details can be found in the Supplement. Model parameters are chosen from literature when available. Otherwise, they are estimated to be biologically reasonable values. See the Supplement for model parameters. Because of the stochasticity of the model, we run ten simulations per parameter set to understand the behavior and outcomes of the ABM more comprehensively.

2.1 Tumor cell events

During each tumor time step Δt = 15min, for each tumor cell, a random tumor event is chosen based on the probabilities of proliferation and apoptosis. The probability of each event occurring during this time step follows an exponential

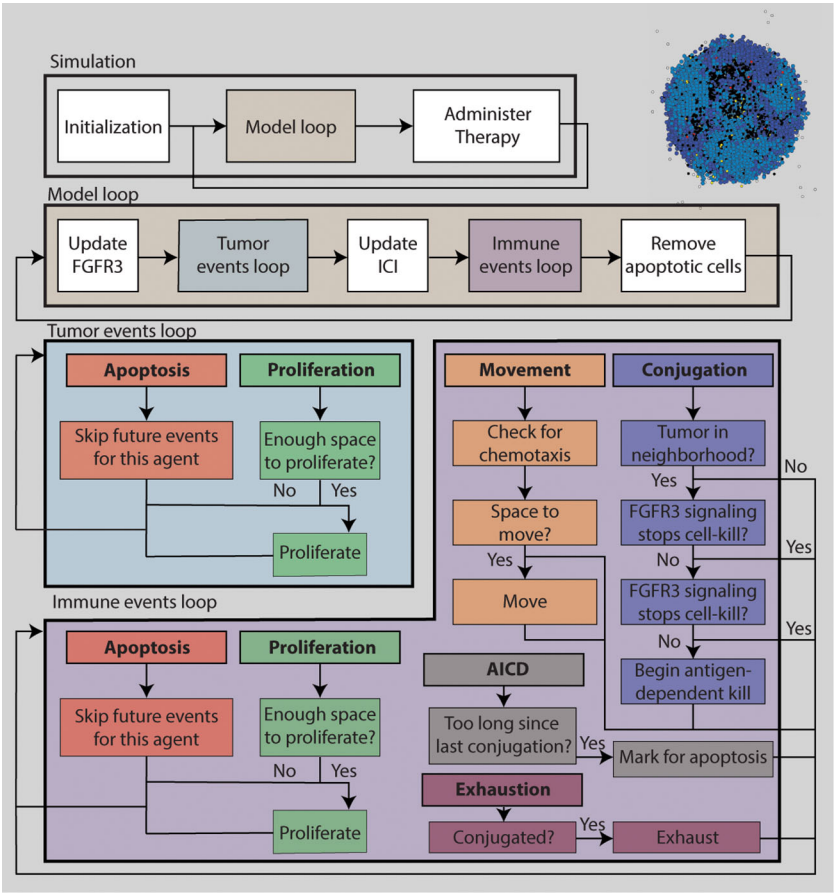

FIGURE 1
A flowchart describing the simulation algorithm.

distribution with a given rate of event. Tumor cells proliferate at a cell-dependent rate, which is the sum of a base rate α_T and an FGFR3-induced rate increase. This increase is directly proportional to the active FGFR3 dimer fractional occupancy ϕ_D, defined as the ratio of the concentration of active dimers on this tumor cell to the average concentration of total FGFR3 on tumor cells harboring the FGFR3 mutation. Proliferation of tumor cells is density-dependent, i.e. when the number of neighbors exceed a certain threshold, the tumor cell cannot proliferate. Moreover, tumor cells undergo apoptosis at a base rate δ_T. FGFR3 signaling decreases the rate of apoptosis and this decrease is dependent on ϕ_D of each tumor cell.

Tumor cells with low antigenicity have a fitness advantage compared to HA tumor cells in that LA tumor cells produce less ISF and are eliminated by CTLs at a slower rate. See Section 2.2 and Section S1 for further details.

2.2 Immune cell events

A static vasculature model is included to model the influx of therapeutic agents and immune cells (Section S1.3). Blood vessels are located on the border of the ABM lattice and lattice sites here are referred to as "perivascular". Immune cells are recruited into the TME after each tumor update based on the size of the tumor at the start of the iteration. We assume that the rate of immune cells arriving in the TME is directly proportional to the tumor size. These new immune cells are placed randomly at empty perivascular lattice sites, from which they enter the TME.

To account for the faster timescale of immune cell migration, immune time steps are set to Δt_{imm} = 7.5min. At each time step, an immune event is randomly chosen from proliferation, apoptosis, movement, conjugation with a tumor cell, exhaustion and AICD, based on the probability of each event. The probability is calculated from the rate of each event in a similar way as tumor events.

Immune cells proliferate at a base rate of α_I unless the immune cell is either currently conjugated with a tumor cell or has already become exhausted. The proliferation rate is increased based on the local ISF concentration. As with tumor cells, immune cells must have sufficient space to proliferate. Immune cells undergo apoptosis at a base rate of δ_I at all times. If the CTL is engaged with a tumor cell when it is undergoing apoptosis, the CTL stops attacking the tumor cell. Non-exhausted immune cell move in the TME at a constant rate of movement, m. To allow for persistent movement in a single direction, and to improve simulation efficiency, immune cells move n_{move} steps at a time, with each step moving to a neighboring lattice site. The direction of movement is chosen randomly, but movement tends towards the direction with higher concentrations of ISF, accounting for the distance between lattice sites in the Moore neighborhood. Detailed calculations of movement gradient is found in Section S1.5.3. Unengaged, active immune cells attempt to conjugate with a non-apoptotic, neighboring tumor cell at a constant rate, β. If the immune cell successfully engages the tumor cell, then the immune cell is labeled as engaged and starts to eliminate the tumor cell. We assume that immune cells employ the perforin/granzyme pathway to clear the HA cells, eliminating them in 30min (33). By contrast, immune cells use the Fas/FasL pathway to clear LA tumor cells, taking 2h to successfully induce apoptosis in the target cell. This difference in targeting mechanism follows from observations that in the absence of antigen, T cells preferentially employ FasL to target tumor cells (33).

Conjugation ends when either the tumor cell becomes apoptotic or the immune cell becomes exhausted. All immune cells in the model are assumed active upon reaching the TME and thus express PD-1 and are thus subject to PD-1 signaling, which can trigger exhaustion (34). The rate at which immune cells become exhausted is affected by the concentration of the PD-1-PD-L1 complex, following a Hill function. Exhausted immune cells wait to die and otherwise affect the system only by taking up space. Furthermore, immune cells can undergo AICD at a constant rate of d_a when they go long periods without conjugating with a tumor cell (35, 36).

2.3 FGFR3 effects

To compute the amount of FGFR3 signaling and the effects of an FGFR3 inhibitor on tumor cells, we employ a global method developed in (37). Rather than using local concentrations of receptors, inhibitor, and complexes as state variables in an ordinary differential equation (ODE) for every tumor cell, we divide the TME into regions and update state variables averaged within these regions. To account for intra-region heterogeneity, we further divide each region into three subregions: non-mutantoccupied, mutant-occupied, and tumor-free. Section S1.6 contains full details of the system of ODEs describing FGFR3 dimerization, reactions between monomers, dimers and the FGFR3 inhibitor, diffusion of the inhibitor, as well as pharmacokinetics.

As discussed in Section 2.1, FGFR3 signaling alters tumor cell fate decisions by increasing the proliferation rate and decreasing the apoptosis rate. We also assume that FGFR3 signaling has downstream effects on the immune system. In accordance with observations that harboring an FGFR3 mutation correlates with lower $CD8^+$ T cell infiltration (7), we assume that FGFR3 signaling decreases the immune recruitment rate by a factor dependent on the average ϕ_D value across all FGFR3 mutant tumor cells.

2.4 PD-1/PD-L1/aPD-1 effects

To determine the amount of PD-1 signaling on each immune cell, we make use of another implementation of a global method (37) similar to that used for FGFR3 inhibitor and a quasi-equilibrium assumption. We first solve reaction-diffusion equations for PD-1 inhibitor reacting with PD-1 on immune cells to obtain the average free PD-1 across all regions in the TME. This quantity is used as an initial condition for solving the PD-1-PD-L1 reaction to obtain the concentration of PD-1-PD-L1 complex, which determines the rate of exhaustion of immune cells as described in Section 2.2. Details of the equations are found in Section S1.8.

3 Results

3.1 ICI response depends on tumor composition

We first analyze the effect of ICI on tumor growth and its efficacy's dependence on the initial composition of the tumor. The initial FGFR3 mutant cell proportions are varied between 0% (wild type, WT), 50%, and 100% (mutant, Mut). The initial tumor antigenicity proportions are similarly varied between 100% low antigen (LA) cells, 100% high antigen (HA) cells, and a 50-50 split. At initialization, these features are assigned independently so that all included pairings are equally represented at the start of a simulation. We first observe that the 100% HA WT tumors (Figure 2A, bottom-left) regress spontaneously even without treatment, indicating that at least one of these fitness advantages (loss of antigenicity or gain of FGFR3 mutation) must be acquired for progression. If only one is acquired, tumors grew, but ICI alone is successful (Figure 2A, bottom row and left column). Importantly, this indicates that HA tumors retain sensitivity to ICI despite an FGFR3 mutation. We also note that in the LA WT case, ICI does eventually result in elimination, but only after the tumor nearly reaches carrying capacity. Finally, the remaining four panels represent tumors with a subpopulation of LA Mut cells, and none of these respond to ICI.

To understand the role of the immune response in effecting these outcomes, we looked at the CTL infiltrate throughout the TME at a time point prior to any of the observed peaks in tumor burden. We measure CTL infiltrate here as the percentage of all cells in the TME that are CTLs. In other words, before the tumor began to shrink. Thus, we selected Day 20 for the control arm and Day 12 for the ICI arm. In the control arm, only HA WT tumors regressed and contained more than 12% CTLs on Day 20 (Figure 2B, top row). The dashed line indicates the 12% mark. In the ICI arm, however, the total CTL infiltrate was not an effective predictor of tumor response as no threshold could be drawn to divide responders and non-responders agnostic to initial tumor composition (Figure 2B, bottom row). Response under ICI was more driven by antigen burden and absence of FGFR3 activation.

We next quantified the change in tumor composition under control and ICI. In both of these arms, the more fit cells (LA and Mut) gradually take over the tumor (Figures 2C, D). Under ICI, this shift accelerates so that the fitter, more immune-evasive cells compose more of the tumor at endpoint (Figure 2D). That is, the failure of ICI produces a tumor population with faster growth dynamics and more resistant to immune clearance.

3.2 Infiltration of immune cells depends on tumor composition

To further understand the role of tumor composition on the efficacy of the immune response, we measured the spatial colocalization of CTLs within the tumor. Analogous to tissue sections, we first considered the density of CTLs within the middle z-slice of the tumor (Supplementary Figure 1). We found that significant shifts in the CTL density occurred between the WT and the mixed mutant tumors (Figure 3A). Specifically, within a given antigenic status (columns of A), the comparison between blue (WT) and red (mixed mutant) always produces a significant difference in CTL density in both the control and ICI arms. Note we only show comparisons of single-step changes in the composition and within therapy arms. More specifically, we only show significant differences between neighboring colors of the same column or neighboring columns of the same color. We observe that

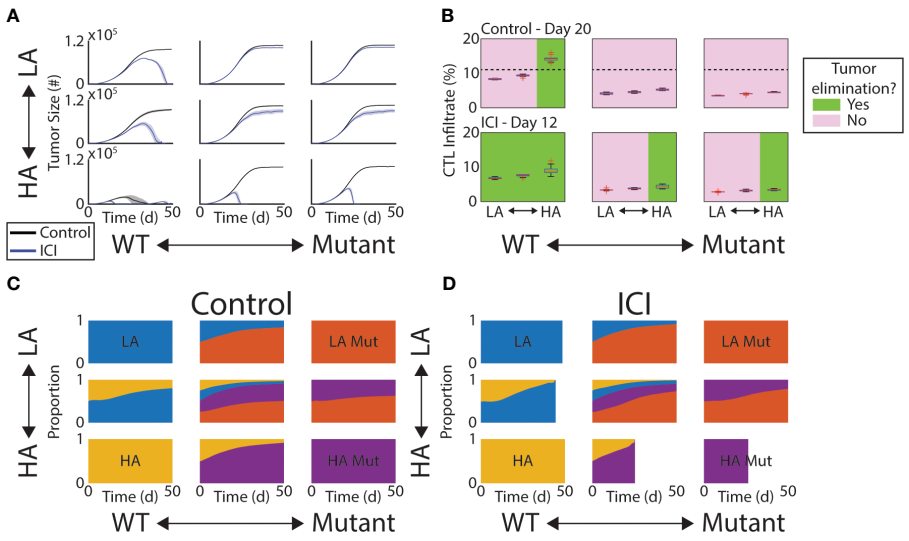

FIGURE 2
Response to ICI depends on tumor composition. **(A)** Mean tumor size (solid lines) and ±1 standard deviation across each simulated initial tumor composition and under control (black) and ICI (blue). **(B)** Box plots of CTL infiltrate as percentage of all cells at Day 20 (control, top row) or Day 12 (ICI, bottom row). Green (pink) panels indicate the condition does (not) result in tumor elimination. Dashed line in top row indicates a threshold separating these two outcomes. **(C, D)** Time series of tumor composition under control **(C)** and ICI **(D)**. In **(D)**, some are cutoff due to the tumor being completely eliminated across all replicates.

10.3389/fimmu.2024.1358019

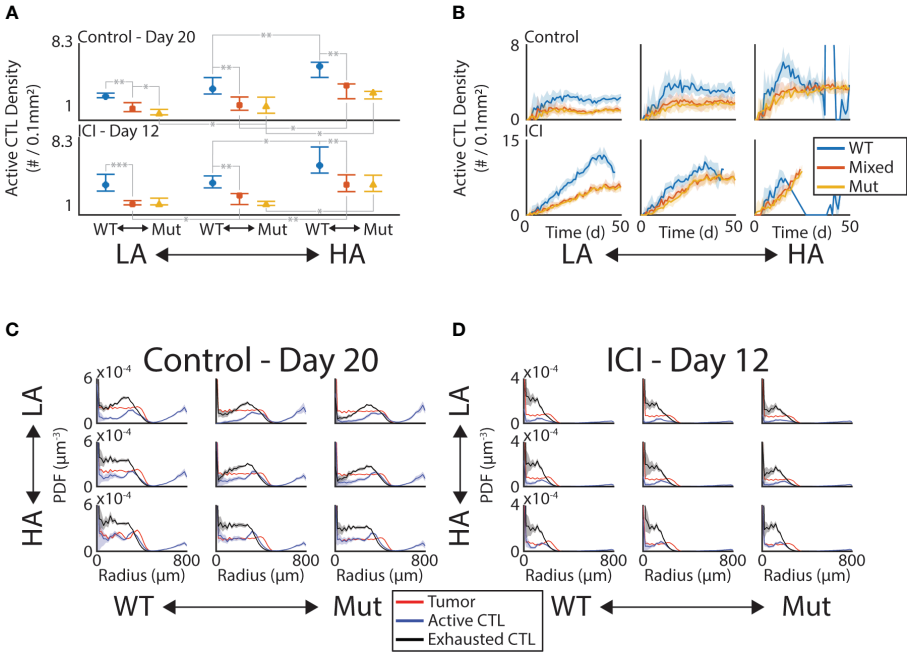

FIGURE 3
CTL infiltration is sensitive to tumor composition and ICI. **(A)** Density of active CTLs within convex hull of tumor in the middle *z*-slice on Day 20 (control, top row) and Day 12 (ICI, bottom row). Significant differences at the 0.05 (*), 0.01 (**), and 0.001 (***) levels are shown for "neighboring" initial conditions. "Neighboring" meaning one change in either the initial antigenicity or the initial mutant proportion. **(B)** Time series of active CTL density in convex hull in control (top row) and ICI (bottom row). Mean (solid line) ±1 standard deviation (shaded area) shown. C-D. PDF density of tumor (red), active CTL (blue), and exhausted CTL (black) compartments at Day 20 (**C**, control) and Day 12 (**D**, ICI). These are computed with respect to the lattice-based volume of the spherical shell at each radius.

this mutation-dependent pattern persists over time (Figure 3B) by computing the active CTL density in this convex hull throughout the simulation and grouping by therapy (rows) and antigen status (columns). The active CTL density in the absence of mutant tumor cells is consistently higher than that in the presence of mutant tumor cells, with the exception of the time period of tumor elimination observed in the rightmost column of Figure 3B.

To see if the immune activity was uniform throughout the tumor mass, we looked at the density of active and exhausted CTLs as a distance from the tumor center. By computing the probability density function (PDF) normalized by the volume of the spherical shell of each bin, we can identify the radii at which these immune cell phenotypes are enriched (Figures 3C, D). Note that as these are PDFs, their integral is 1, meaning these curves do not contain information about the total number of cells in each compartment. This allows a comparison between the relative enrichment on the same set of axes. The red curves in each panel show the tumor density, giving a baseline to compare against that is nearly uniform up to the leading edge of the tumor where this curve rapidly drops to 0. In the control case, both the active (blue) and exhausted (black) CTLs peak just inside the leading edge of the tumor and decrease towards the tumor center in most conditions. Under ICI, these peaks occur deeper in the tumor and the decrease in density towards the tumor center is less pronounced. This increased depth of penetration on ICI occurs despite the measurement occurring 8 days earlier than the control case, indicating that the CTLs are benefiting from ICI even far from the vasculature.

3.3 Anti-FGFR3 targeted therapy synergizes with ICI

We next introduced a small molecule inhibitor of FGFR3 into the simulations to characterize potential synergies with ICI. To focus on the outcome of these simulations and make comparisons to mouse model experiments, we report the model metrics on Day 25, a typical endpoint for the mouse model experiments. Indeed, the *in silico* growth curves in Figure 2A show similar trends as our previously published mouse model experiments (18) (Supplementary Figure 2). Using a Gaussian kernel to smooth the outcomes at Day 25, we see that anti-FGFR3 monotherapy does decrease Day 25 tumor burden for tumors with mutants present, as illustrated by the red peaks of the PDFs lying to the left of the black peaks in the middle and right column of Figure 4A. Nonetheless, the relative efficacy of anti-FGFR3 monotherapy compared with ICI depends on the antigenicity of the tumor, as seen by the different relative positions of blue and red peaks in the middle and right column of Figure 4A. Specifically, targeted therapy is most effective with LA tumors (top row) and least with HA tumors (bottom row). Measuring the efficacy of these therapies by their reduction in tumor cell count compared to control (Figure 4B), they exhibit synergistic effects, i.e., more than the sum of the individual effects, in tumors with LA mutants, i.e., the tumors that did not respond to ICI alone.

We then looked at the composition of the TME at the Day 25 endpoint. We first looked at the relative abundances of tumor subtypes and observed only modest shifts in composition across

10.3389/fimmu.2024.1358019

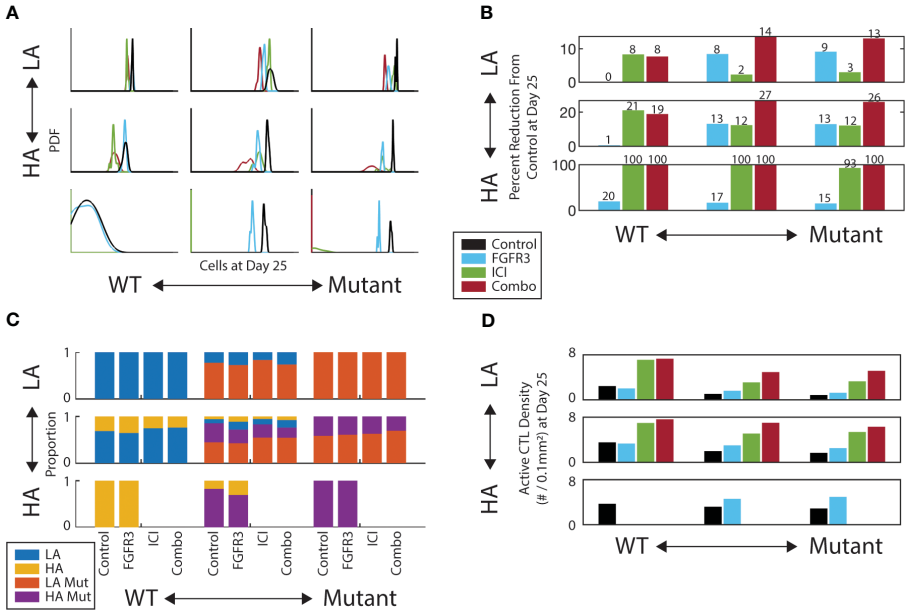

FIGURE 4
FGFR3-targeted therapy has a modest effect on both tumor burden and composition. **(A)** Gaussian kernel-smoothed histograms of tumor burden at Day 25. **(B)** Percent reduction of tumor burden on Day 25 for each therapy relative to control. **(C)** Tumor composition on Day 25 for each therapy and initial composition. Missing bars indicate all replicates experienced tumor elimination by Day 25. **(D)** Active CTL density in the convex hull of the middle z-slice of tumor on Day 25. Same color scheme as **A**.

therapies conditioned on the initial composition (Figure 4C). Notably, there is a slight increase in the proportion of non-mutants (LA/blue and HA/yellow) under targeted therapy in the mixed mutant tumors (middle column). Regarding CTL infiltration into the tumor, the targeted therapy does increase the CTL colocalization with tumor cells, but only by a modest amount (Figure 4D). This helps explain the synergy between these two therapies: the anti-FGFR3 therapy neutralizes the proliferation and apoptosis advantages with little change in immune activity, while ICI increases the immune activity.

3.4 FGFR3 signal strength modulates optimal therapy

Having identified the synergy between these two drugs, we next test the sensitivity of this synergy to the FGFR3-mediated fitness advantages. We focus on the two cases in which we could achieve upwards of 30% reduction in tumor burden by Day 25: HA mixed mutants and HA mutants. We test the following four therapy schedules to compare against the control: FGFR3 monotherapy, ICI monotherapy, FGFR3 followed by ICI (FGFR3 1st), and ICI followed by FGFR3 (ICI 1st) (Supplementary Figure 3). In the two combination therapies, the first therapeutic option is given in weeks 2-3 and the second is given in 3-4 (Supplementary Figure 3). For each of these schedules, we test 50 parameter combinations of the FGFR3-related proliferation and apoptosis parameters. In Figure 5, we display these on the x- and y-axes, respectively, by computing the proliferation rate and expected time to apoptosis assuming the FGFR3 dimerization reaction is at equilibrium without targeted therapy. For each of these 50 parameter combinations, we identify the minimal therapy that leads to the maximal response, which we define using a decision diagram (Supplementary Figure 6). Briefly, we focus on a 30% reduction, i.e., some response, and a 90% reduction, i.e., a near complete response.

With a heterogeneous population with regards to the FGFR3 mutation, low proliferation rates of FGFR3 mutants results in a situation in which ICI monotherapy results in at least 90% reduction in tumor burden on Day 25 relative to control (Figure 5A). At higher proliferation rates, ICI monotherapy cannot produce even a 30% reduction (Supplementary Figure 7A). Instead, at a proliferation rate of 1.75d^{-1}, combination therapy sequenced so that ICI is given first can result in 30% or 90% tumor reduction when apoptosis occurs on the time scale of years or weeks, respectively. At proliferation rates above 1.75d^{-1}, these therapies are ineffective with one exception.

With HA mutants, the pattern is similar but with one notable difference. At lower proliferation rates, ICI monotherapy does produce a 30% reduction in tumor burden (Supplementary Figure 7B), but combination therapy is necessary to elicit a 90% reduction by Day 25 (Figure 5B). This is due to the longer timescale for ICI to reduce the tumor burden (Supplementary Figure 2.1). Indeed, anti-FGFR3 monotherapy produces a stronger response initially due to its direct effect on tumor fitness and its faster pharmacokinetics (Supplementary Figures 4, 5). One consequence of this slower response to ICI is that the maximal tumor burden peaks at a high value. Even in the parameter regions in which ICI monotherapy results in 90% tumor reduction, this peak can be more than double the peak with ICI followed by targeted therapy (Supplementary Figure 2.1).

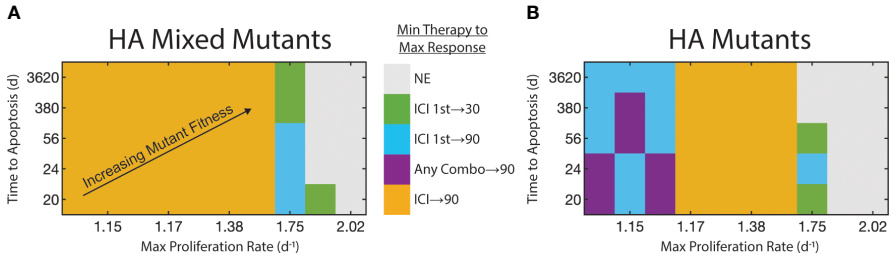

FIGURE 5
Strength of FGFR3 signaling pathway affects therapy selection. FGFR3-mediated maximum proliferation rate for mutants shown on *x*-axis. FGFR3-mediated expected time to apoptosis for mutants shown on *y*-axis. FGFR3 mutant fitness increases towards top-right. Color of tile at each parameter pair indicates the minimal therapy required to get the maximum observed response. We binned responses to not effective (reduction< 30%), effective (30% ≤ reduction < 90%), and highly effective (reduction ≥ 90%). If both monotherapies (or both staggered combination therapies) are equally effective, both are indicated here. **(A)** For HA tumors with a mix of WT and mutants. **(B)** For HA tumors with only mutants.

4 Discussion

We present here the first ABM of bladder cancer growth with FGFR3 mutation and an adaptive immune response under combination ICI and targeted therapy. The model predicts that highly antigenic tumors that elicit a perforin-based response from CTLs respond to ICI (Figure 2A) unless constitutively active FGFR3 signaling greatly accelerates tumor cells cycling (Figure 5). This response is driven by deeper penetration of CTLs towards the tumor center, resulting in an accumulation of these cells in both active and exhausted states (Figures 3C, D). When a highly antigenic tumor is entirely composed of cells harboring an activating FGFR3 mutation, anti-FGFR3 therapy may be necessary to minimize tumor burden as ICI shifts the balance in the tumor-CTL interactions towards tumor cell lysis and away from CTL exhaustion (Supplementary Figure 2.1).

When a tumor contains even a small population of lowly antigenic tumor cells, for which CTLs rely on Fas/FasL to induce tumor cell apoptosis, the tumor becomes resistant to both therapies whether alone or in combination. Though these two drugs can exhibit synergy in these conditions, the reduction in tumor burden does not exceed 27% in our model. Across all therapies, the LA mutant compartment dominates the tumor (Figure 4C, red bars). This occurs even as these therapies successfully bring CTLs within the tumor boundary (Figure 4D). This raises a concern that these two therapies may reduce tumor burden in the short term but at the cost of creating a more resistant tumor phenotype. These findings are consistent with emerging clinical data which indicate that combination therapy has relatively high response rates but low duration of response (11). With additional therapies that can successfully control this resistant population, adaptive therapeutic strategies may prove most efficacious, providing at least a control on tumor growth, while foreclosing on the possibility of complete tumor regression (38).

Recent data from the EV-302 study has shifted front line therapy to combination of the anti-PD-1 antibody pembrolizumab given with enfortumab vedotin, an antibody-drug conjugate (39). With this shift, understanding the optimal strategy for anti-FGFR therapy becomes even more salient as there is no current standard of care in the second line. Our analysis suggests that FGFR3 status coupled with antigenicity will likely provide key indicators to guide clinicians in the event that this front line therapy fails. While work remains to validate our model and translate the results to human patients, our algorithmic decision tree (Supplementary Figure 6) and the resulting outcome landscapes (Figure 5) portend the potential for clinicians to make use of these model-derived results to achieve desired patient outcomes. This highlights a strength of mechanistic and dynamic modeling, namely the ability to identify key correlates and explain their contribution to biological outcomes.

This study operated under the assumption that aberrant FGFR3 signaling directly decreased CTL infiltration into the TME. A mechanistic link has not been firmly established, but emerging evidence supports this assumption (7, 40). Further research into the mechanisms by which FGFR3 signaling alters the immune landscape will be critical to fully elucidate why FGFR3 mutant bearing tumors suppress immune infiltration and how this can be overcome therapeutically.

This is also the first ABM to consider multiple mechanisms of lytic activity carried out by $CD8^+$ T cells. The assumption that the fast perforin/granzyme pathway is used to eliminate HA tumor cells but the slow FasL pathway is used for LA tumor cells contributes to the different outcomes predicted by the model. While there is evidence that antigenicity plays a role in how a T cell attacks a target tumor cell, it remains unclear how specific this action is and how it may vary by antigen affinity or phenotypic changes in the lifespan of a T cell. Information-theoretic approaches have recently been used to predict the maximal number of distinct antigen concentrations a CAR T cell can theoretically recognize given the constraints of the downstream signaling pathways (41). Studies building on this approach will quantify what T cells are capable of distinguishing in terms of antigen and what other factors may modulate this capability. This will in turn allow for more accurate modeling of tumor-immune interactions as mediated by antigen.

This study is not without limitations. Model parameters are largely selected from the literature and not constrained by the particular disease model we are considering. Furthermore, while these results do qualitatively agree with past research, a more rigorous and quantitative approach with direct experimental evidence would strengthen the claims and make them more readily applicable. Finally, with a model of this size and modularity, it is difficult to assess the sensitivity of our results to modeling assumptions and parameters as we would expect this space to be highly nonlinear.

By resolving the above questions and concerns using an interdisciplinary approach involving *in vitro* and *in vivo* model systems as well as other computational approaches such as bioinformatics, we can iterate on this process to create a more robust *in silico* model of bladder cancer. Such a model will feed forward into these very pipelines with new mathematically-based hypotheses that can accelerate our discovery of rationally designed treatment plans to improve clinical outcomes.

Data availability statement

The original contributions presented in the study are included in the article/Supplementary Material. Further inquiries can be directed to the corresponding author.

Author contributions

DB: Formal analysis, Investigation, Methodology, Software, Visualization, Writing – original draft, Writing – review & editing. YW: Investigation, Writing – original draft, Writing – review & editing. ET: Writing – review & editing. AF: Writing – review & editing. LL: Investigation, Writing – review & editing. AP: Conceptualization, Funding acquisition, Methodology, Supervision, Writing – original draft, Writing – review & editing. RS: Conceptualization, Funding acquisition, Methodology, Supervision, Writing – original draft, Writing – review & editing. TJ: Conceptualization, Funding acquisition, Investigation, Methodology, Resources, Supervision, Writing – original draft, Writing – review & editing.

Funding

The author(s) declare financial support was received for the research, authorship, and/or publication of this article. This work was supported by NIH/NCI U01CA243075 (AP, RS, TJ) and NIH K08 CA234392 (RS).

Conflict of interest

The authors declare that the research was conducted in the absence of any commercial or financial relationships that could be construed as a potential conflict of interest.

Publisher's note

Supplementary material

The Supplementary Material for this article can be found online at: https://www.frontiersin.org/articles/10.3389/fimmu.2024.1358019/full#supplementary-material

References

1. Halaseh SA, Halaseh S, Alali Y, Ashour ME, Alharayzah MJ, Alharayzeh MJ. A review of the etiology and epidemiology of bladder cancer: All you need to know. *Cureus*. (2022) 14. doi: 10.7759/cureus.27330

2. Bogen JP, Grzeschik J, Jakobsen J, Bähre A, Hock B, Kolmar H. Treating bladder cancer: engineering of current and next generation antibody-, fusion protein-, mrna-, cell-and viral-based therapeutics. *Front Oncol*. (2021) 11:672262. doi: 10.3389/fonc.2021.672262

3. Bilim V, Kuroki H, Shirono Y, Murata M, Hiruma K, Tomita Y. Advanced bladder cancer: Changing the treatment landscape. *J Personalized Med*. (2022) 12:1745. doi: 10.3390/jpm12101745

4. Scheepbouwer C, Meyer S, Burggraaf MJ, Jose J, Molthoff CF. A multimodal imaging approach for longitudinal evaluation of bladder tumor development in an orthotopic murine model. *PloS One*. (2016) 11:e0161284. doi: 10.1371/journal.pone.0161284

5. Casadei C, Dizman N, Schepisi G, Cursano MC, Basso U, Santini D, et al. Targeted therapies for advanced bladder cancer: new strategies with fgfr inhibitors. *Ther Adv Med Oncol*. (2019) 11:1758835919890285. doi: 10.1177/1758835919890285

6. Ascione CM, Napolitano F, Esposito D, Servetto A, Belli S, Santaniello A, et al. Role of fgfr3 in bladder cancer: Treatment landscape and future challenges. *Cancer Treat Rev*. (2023) 115:102530. doi: 10.1016/j.ctrv.2023.102530

7. Sweis RF, Spranger S, Bao R, Paner GP, Stadler WM, Steinberg G, et al. Molecular drivers of the non–t-cell-inflamed tumor microenvironment in urothelial bladder cancer. *Cancer Immunol Res*. (2016) 4:563–8. doi: 10.1158/2326-6066.CIR-15-0274

8. Hsu F-S, Su C-H, Huang K-H. A comprehensive review of us fda-approved immune checkpoint inhibitors in urothelial carcinoma. *J Immunol Res*. (2017) 2017. doi: 10.1155/2017/6940546

9. Kacew A, Sweis RF. Fgfr3 alterations in the era of immunotherapy for urothelial bladder cancer. *Front Immunol*. (2020) 11:575258. doi: 10.3389/fimmu.2020.575258

10. Rosenberg JE, Gajate P, Morales-Barrera R, Lee J-L, Necchi A, Penel N, et al. (2021).

11. Siefker-Radtke AO, Powles T, Moreno V, Kang TW, Cicin I, Girvin A, et al. *Erdafitinib (erda) vs erda plus cetrelimab (erda+ cet) for patients (pts) with metastatic urothelial carcinoma (muc) and fibroblast growth factor receptor alterations (fgfra): Final results from the phase 2 norse study*. Alexandria, Virginia, USA: American Society of Clinical Oncology (2023). doi: 10.1200/JCO.2023.41.16_suppl.4504

12. Brady-Nicholls R, Nagy JD, Gerke TA, Zhang T, Wang AZ, Zhang J, et al. Prostatespecific antigen dynamics predict individual responses to intermittent androgen deprivation. *Nat Commun*. (2020) 11:1750. doi: 10.1038/s41467-020-15424-4

13. Brady-Nicholls R, Zhang J, Zhang T, Wang AZ, Butler R, Gatenby RA, et al. Predicting patient-specific response to adaptive therapy in metastatic castration-resistant prostate cancer using prostate-specific antigen dynamics. *Neoplasia*. (2021) 23:851–8. doi: 10.1016/j.neo.2021.06.013

14. Strobl M, Martin AL, West J, Gallaher J, Robertson-Tessi M, Gatenby R, et al. Adaptive therapy for ovarian cancer: An integrated approach to parp inhibitor scheduling. *bioRxiv*. (2023). doi: 10.1101/2023.03.22.533721

15. Bunimovich-Mendrazitsky S, Byrne H, Stone L. Mathematical model of pulsed immunotherapy for superficial bladder cancer. *Bull Math Biol*. (2008) 70:2055–76. doi: 10.1007/s11538-008-9344-z

16. Breban R, Bisiaux A, Biot C, Rentsch C, Bousso P, Albert M. Mathematical model of tumor immunotherapy for bladder carcinoma identifies the limitations of the innate immune response. *OncoImmunology*. (2012) 1:9–17. doi: 10.4161/onci.1.1.17884

17. Savchenko E, Rosenfeld A, Bunimovich-Mendrazitsky S. Mathematical modeling of bcg-based bladder cancer treatment using socio-demographics. *Sci Rep*. (2023) 13:18754. doi: 10.1038/s41598-023-45581-7

18. Okuneye K, Bergman D, Bloodworth JC, Pearson AT, Sweis RF, Jackson TL. A validated mathematical model of fgfr3-mediated tumor growth reveals pathways to

harness the benefits of combination targeted therapy and immunotherapy in bladder cancer. *Comput Syst Oncol*. (2021) 1:e1019. doi: 10.1002/cso2.1019

19. Lai X, Friedman A. Combination therapy of cancer with cancer vaccine and immune checkpoint inhibitors: A mathematical model. *PloS One*. (2017) 12:e0178479. doi: 10.1371/journal.pone.0178479

20. Ghaffarizadeh A, Heiland R, Friedman SH, Mumenthaler SM, Macklin P. Physicell: An open source physics-based cell simulator for 3-d multicellular systems. *PloS Comput Biol*. (2018) 14:e1005991. doi: 10.1371/journal.pcbi.1005991

21. Bravo RR, Baratchart E, West J, Schenck RO, Miller AK, Gallaher J, et al. Hybrid automata library: A flexible platform for hybrid modeling with real-time visualization. *PloS Comput Biol*. (2020) 16:e1007635. doi: 10.1371/journal.pcbi.1007635

22. Miller AK, Bishop RT, Li T, Shain KH, Nerlakanti N, Lynch CC, et al. The bone ecosystem facilitates multiple myeloma relapse and the evolution of heterogeneous proteasome inhibitor resistant disease. *bioRxiv*. (2022), 2022–11. doi: 10.1101/2022.11.13.516335

23. Bergman D, Marazzi L, Chowkwale M, Bidanta S, Mapder T, Li J, et al. Physipkpd: A pharmacokinetics and pharmacodynamics module for physicell. *Gigabyte*. (2022) 2022. doi: 10.1101/2022.09.12.507681

24. Ponce-de Leon M, Montagud A, Noël V, Meert A, Pradas G, Barillot E, et al. Physiboss 2.0: a sustainable integration of stochastic boolean and agent-based modelling frameworks. *NPJ Syst Biol Appl*. (2023) 9:54. doi: 10.1038/s41540-023-00314-4

25. Kather JN, Poleszczuk J, Suarez-Carmona M, Krisam J, Charoentong P, Valous NA, et al. In silico modeling of immunotherapy and stroma-targeting therapies in human colorectal cancer. *Cancer Res*. (2017) 77:6442–52. doi: 10.1158/0008-5472.CAN-17-2006

26. Aguilar B, Gibbs DL, Reiss DJ, McConnell M, Danziger SA, Dervan A, et al. A generalizable data-driven multicellular model of pancreatic ductal adenocarcinoma. *Gigascience*. (2020) 9:giaa075. doi: 10.1093/gigascience/giaa075

27. West J, Schenck RO, Gatenbee C, Robertson-Tessi M, Anderson AR. Normal tissue architecture determines the evolutionary course of cancer. *Nat Commun*. (2021) 12:2060. doi: 10.1038/s41467-021-22123-1

28. Poonja S, Forero Pinto A, Lloyd MC, Damaghi M, Rejniak KA. Dynamics of fibril collagen remodeling by tumor cells: A model of tumor-associated collagen signatures. *Cells*. (2023) 12:2688. doi: 10.3390/cells12232688

29. Jain HV, Norton K-A, Prado BB, Jackson TL. Smore pars: A novel methodology for bridging modeling modalities and experimental data applied to 3d vascular tumor growth. *Front Mol Biosci*. (2022) 9:1056461. doi: 10.3389/fmolb.2022.1056461

30. Cess CG, Finley SD. Calibrating agent-based models to tumor images using representation learning. *PloS Comput Biol*. (2023) 19:e1011070. doi: 10.1371/journal.pcbi.1011070

31. Gonçalves IG, Hormuth DA, Prabhakaran S, Phillips CM, García-Aznar JM. Physicool: A generalized framework for model calibration and optimization of modeling projects. *GigaByte*. (2023) 2023. doi: 10.46471/gigabyte.77

32. Johnson JA, Stein-O'Brien GL, Booth M, Heiland R, Kurtoglu F, Bergman D, et al. Digitize your biology! modeling multicellular systems through interpretable cell behavior. *bioRxiv*. (2023), 2023–09. doi: 10.1101%2F2023.09.17.557982

33. Hassin D, Garber OG, Meiraz A, Schiffenbauer YS, Berke G. Cytotoxic t lymphocyte perforin and fas ligand working in concert even when fas ligand lytic action is still not detectable. *Immunology*. (2011) 133:190–6. doi: 10.1111/imm.2011.133.issue-2

34. Budimir N, Thomas GD, Dolina JS, Salek-Ardakani S. Reversing t-cell exhaustion in cancer: lessons learned from pd-1/pd-l1 immune checkpoint blockade. *Cancer Immunol Res*. (2022) 10:146–53. doi: 10.1158/2326-6066.CIR-21-0515

35. Green DR, Droin N, Pinkoski M. Activation-induced cell death in t cells. *Immunol Rev*. (2003) 193:70–81. doi: 10.1034/j.1600-065X.2003.00051.x

36. Krammer PH, Arnold R, Lavrik IN. Life and death in peripheral t cells. *Nat Rev Immunol*. (2007) 7:532–42. doi: 10.1038/nri2115

37. Bergman D, Sweis RF, Pearson AT, Nazari F, Jackson TL. A global method for fast simulations of molecular dynamics in multiscale agent-based models of biological tissues. *Iscience*. (2022) 25. doi: 10.1016/j.isci.2022.104387

38. Hansen E, Read AF. Cancer therapy: Attempt cure or manage drug resistance? *Evol Appl*. (2020) 13:1660–72. doi: 10.1111/eva.12994

39. Powles T, Valderrama BP, Gupta S, Bedke J, Kikuchi E, Hoffman-Censits J, et al. Lba6 ev-302/keynote-a39: Open-label, randomized phase iii study of enfortumab vedotin in combination with pembrolizumab (ev+ p) vs chemotherapy (chemo) in previously untreated locally advanced metastatic urothelial carcinoma (la/muc). *Ann Oncol*. (2023) 34:S1340. doi: 10.1016/j.annonc.2023.10.106

40. Ruan R, Li L, Li X, Huang C, Zhang Z , Zhong H, et al. Unleashing the potential of combining fgfr inhibitor and immune checkpoint blockade for fgf/fgfr signaling in tumor microenvironment. *Mol Cancer*. (2023) 22:60. doi: 10.1186/s12943-023-01761-7

41. Tserunyan V, Finley S. Information-theoretic analysis of a model of car-4-1bb-mediated nfκb activation. *Bull Math Biol*. (2024) 86:5. doi: 10.1007/s11538-023-01232-6

frontiers | Frontiers in Immunology

TYPE Review
PUBLISHED 12 March 2024
DOI 10.3389/fimmu.2024.1363144

OPEN ACCESS

EDITED BY
Heiko Enderling,
University of Texas MD Anderson Cancer Center, United States

REVIEWED BY
Jaya Lakshmi Thangaraj,
University of California, San Diego, United States
Nahum Puebla-Osorio,
University of Texas MD Anderson Cancer Center, United States
Ibrahim Chamseddine,
Harvard Medical School, United States

*CORRESPONDENCE
Sarah C. Brüningk
sarah.brueningk@hest.ethz.ch

RECEIVED 29 December 2023
ACCEPTED 20 February 2024
PUBLISHED 12 March 2024

CITATION
Metzcar J, Jutzeler CR, Macklin P, Köhn-Luque A and Brüningk SC (2024) A review of mechanistic learning in mathematical oncology.
Front. Immunol. 15:1363144.
doi: 10.3389/fimmu.2024.1363144

A review of mechanistic learning in mathematical oncology

John Metzcar [1,2], Catherine R. Jutzeler [3,4], Paul Macklin [1], Alvaro Köhn-Luque [5,6] and Sarah C. Brüningk [3,4]*

[1]Intelligent Systems Engineering, Luddy School of Informatics, Computing, and Engineering, Bloomington, IN, United States, [2]Informatics, Luddy School of Informatics, Computing, and Engineering, Bloomington, IN, United States, [3]Department of Health Sciences and Technology (D-HEST), Eidgenössische Technische Hochschule Zürich (ETH), Zürich, Switzerland, [4]Swiss Institute of Bioinformatics (SIB), Lausanne, Switzerland, [5]Oslo Centre for Biostatistics and Epidemiology, Faculty of Medicine, University of Oslo, Oslo, Norway, [6]Oslo Centre for Biostatistics and Epidemiology, Research Support Services, Oslo University Hospital, Oslo, Norway

Mechanistic learning refers to the synergistic combination of mechanistic mathematical modeling and data-driven machine or deep learning. This emerging field finds increasing applications in (mathematical) oncology. This review aims to capture the current state of the field and provides a perspective on how mechanistic learning may progress in the oncology domain. We highlight the synergistic potential of mechanistic learning and point out similarities and differences between purely data-driven and mechanistic approaches concerning model complexity, data requirements, outputs generated, and interpretability of the algorithms and their results. Four categories of mechanistic learning (sequential, parallel, extrinsic, intrinsic) of mechanistic learning are presented with specific examples. We discuss a range of techniques including physics-informed neural networks, surrogate model learning, and digital twins. Example applications address complex problems predominantly from the domain of oncology research such as longitudinal tumor response predictions or time-to-event modeling. As the field of mechanistic learning advances, we aim for this review and proposed categorization framework to foster additional collaboration between the data- and knowledge-driven modeling fields. Further collaboration will help address difficult issues in oncology such as limited data availability, requirements of model transparency, and complex input data which are embraced in a mechanistic learning framework

KEYWORDS

mathematical modeling, machine learning, deep learning, ODE (ordinary differential equation), mechanistic learning

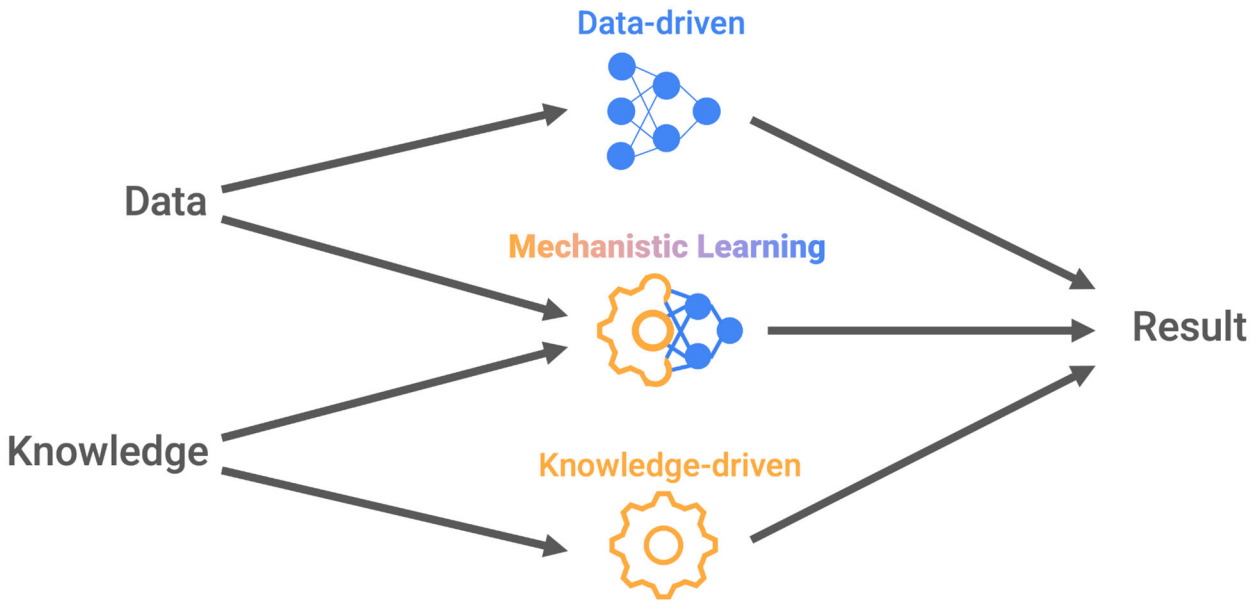

GRAPHICAL ABSTRACT
Data and knowledge both drive the progress of research and are the cornerstones of modeling. Depending on the emphasis, both data-driven (exemplified by machine and deep learning) and knowledge-driven (exemplified by mechanistic mathematical modeling) models generate novel results and insights. Mechanistic learning describes approaches that employ both data and knowledge in a complimentary and balanced way.

1 Introduction

An increasing understanding of cancer evolution and progression along with growing multi-scale biomedical datasets, ranging from molecular to population level, is driving the research field of mathematical oncology (1). Mathematical oncology aims to bridge the gaps between medicine, biology, mathematics, and computer science to advance cancer research and clinical care. Both data and understanding of cancer biology contribute to this aim. Furthermore, modeling in the context of clinical application poses a range of challenges that need to be met in order to ensure practical translation: data sparsity, heterogeneity, and source bias need to be accounted for, while the complexity of the model has to remain balanced regarding flexibility, interpretability, and explainability. Finally, one must consider the risk of model overfitting, together with robustness and generalization strength.

Data science may be defined as "*a set of fundamental principles that support and guide the principled extraction of information and knowledge from data*" (2). Here, problem-solving is approached from the perspective of a learning process accomplished through observing diverse examples (3). Relationships between various types of input data (e.g., omics and imaging) and outcomes (e.g., overall survival) are abstracted where a mechanistic understanding of a relationship is missing or otherwise not accounted for. In this context, we refer to it as "data-driven" modeling. For oncology, data-driven approaches address a variety of applications to further scientific progress and task automation. Prime examples include predictions of drug response, tumor subtyping, and outcome as well as auto-segmentation of tumors on imaging.

An alternative is to formulate a specific guess on how relevant variables interact between input and output through the formulation of a mathematical model. Bender defines a mathematical model as an "*abstract, simplified, mathematical construct related to part of reality and created for a particular purpose*" (4). Here the formulation of deliberate approximations of reality through equations or rules is key (5). In turn, the quality and limits of this approximation, which we refer to as "knowledge-driven" modeling, are validated with data. Independent of the use of a data science or a mathematical modeling formulation, "data" and "knowledge" are indispensable. The emphasis on data and knowledge may vary leading to the terminology of "data-driven" and "knowledge-driven" modeling (6). The fluid boundaries between these concepts motivate their combination.

The evolving field of mechanistic learning (7, 8) aims to describe synergistic combinations of classical mathematical modeling and data science (9, 10). In this review, we provide an overview of the key aspects of these approaches, explain possible ways of combining them, present a selection of examples, and discuss how mechanistic learning can thrive in mathematical oncology. In doing so, we aim to draw awareness to similarities and synergies between knowledge- and data-driven modeling, noting that this combination could help push mathematical oncology into the clinic as reliable, data-supported, and explainable models in the context of oncology (11).

2 Contrasting "knowledge-driven" and "data-driven" modeling"

As per definition, data- and knowledge-driven modelling are complementary perspectives for approaching research questions. Here, we address similarities and differences to understand synergies at the interface of these fluid concepts.

2.1 Knowledge-driven modeling approximates biomedical understanding

According to Rockne et al. (1), the goal of knowledge-driven modeling is to describe the behavior of complex systems based on an understanding of the underlying mechanisms rooted in fundamental principles of biology, chemistry, and physics. While the formulation of the "model", i.e. the approximation of reality, is flexible, the overarching aim is to gain a deeper understanding of processes driving the system's behavior often through simulation and analysis of unobserved scenarios. Here, mathematical formulas or systematic processes are purposefully crafted to reflect key aspects of reality with inevitable simplifying assumptions. For example, dimensionality is reduced, dynamic processes are approximated as time-invariant, or biological pathways are reduced to key components (12). Conceptualizing these assumptions requires a deep understanding of the biomedical processes and modeling goals. These demands are met through interdisciplinary collaboration and validation. In the absence of experimental data, it is still possible to analyze and simulate to expose dynamics emerging from model building blocks (13–15). These extrapolations beyond the range of validation data are rooted in the confidence in the quality of the approximation of the biomedical reality, i.e. the quality of the knowledge and its implementation.

It is tempting to suggest that knowledge-driven models are inherently interpretable. Yet, the implementation of chains of relationships can formulate complex inverse problems. Subsequently, *post hoc* processing through parameter identifiability and sensitivity analyses is key (16, 17). This can identify previously unknown interactions between system components to generate hypotheses for experimental and clinical validation.

Knowledge-driven modeling has successfully been applied to investigate different aspects of cancer including somatic cancer evolution and treatment. We refer the interested reader to recent review articles (18, 19) covering for instance different fractionation schemes for radiotherapy (20, 21), the onset and influence of treatment-induced tumor resistance (22), or cancer evolution (23). A popular application of knowledge-driven models is the simulation of *in silico* trials for hypothesis generation in simulated cohorts (24–26).

2.2 Data-driven models extract information from data

A common understanding of data-driven modeling (e.g. - machine learning, deep learning and classical statistics) is the creation of insight from empirical examples (27). A performance metric (28, 29) is optimized to uncover patterns and relationships between input data and output task. The validity of data-driven models should be studied carefully, in particular the dependency of the results on the chosen performance metric (29). It is also key to consider the optimization convergence. If this process fails, the model will be uninformative.

Purely data-driven models do not readily leverage the community's understanding of the system under study but instead often employ highly parameterized models. The many degrees of freedom allow flexibility to approximate complex and mechanistically unknown relationships, e.g. deep neural networks act as "universal function approximators" (30). New information can be extracted from the data through this structuring but the extensive parameterization may obscure how the decision process is formed. *Post hoc* processing is required to uncover the nature of the approximated relationship through interpretability and explainability analysis (31). The models' flexibility also makes them vulnerable to overfitting. Appropriately large amounts of training data and stringent data splits for fitting (training) and validation (32) are necessary to mitigate this risk. Data quantity and quality, i.e. its task specificity and ability to cover a variety of relevant scenarios, are equally important.

Generally, the application focus differs from that of knowledge-driven models. Generalization beyond the observed data space is often challenging (33). It is essential to rely on robust training regimes (34) and consider model limitations as performance is compromised in scenarios not (sufficiently) covered by data (33).

In summary, data-driven approaches are powerful tools for knowledge generation. In oncology, data-driven approaches have previously contributed substantially to scientific progress and process automation (35). To name just a few examples, (un-) supervised machine learning has greatly supported areas of drug response prediction (36, 37) and molecular tumor subtype identification (38, 39), whereas generative models and deep learning have revolutionized computer vision tasks such as volumetric tumor segmentation (40, 41), image-based outcome predictions (42, 43) and automated intervention planning.

2.3 Identifying similarities and boundaries between knowledge-driven and data-driven modeling

Table 1 summarizes and contrasts key characteristics of the extremes of purely data- and knowledge-driven modeling, yet boundaries between these models remain fluid for many applications. The fundamental steps of data- and knowledge-driven modeling have parallels despite varying terminology: a subset of data is used to construct and calibrate the model, then further data is necessary for validation and refinement. In data-driven modeling, we first formulate the learning task (i.e. identifying features, labels, and loss function), and architecture selection. In knowledge-driven modeling, we start by deriving equations/mathematical rules. Both algorithms are subsequently compared to real-world data to optimize hyperparameters (i.e., structural model implementations) and to learn model parameters for fitting. The same optimization principles apply but the extent to which mechanistic priors are accounted for in the design of the objective function varies. Finally,

TABLE 1 General conceptual differences between knowledge-driven vs. data-driven modeling.

Knowledge-driven modeling	Data-driven modeling
The current "knowledge" drives the implementation of an educated guess regarding the studied relationship. *Example: Modeling of tumor growth based on the assumption of an exponential time dependency.*	The empirical reality is approximated through a (complex) relationship. *Example: A time series of tumor growth data is approximated by a long-short-term-memory network comprising thousands of parameters.*
Data serves the purpose of validation of the implemented estimate of reality. *Example: The assumption of exponential tumor growth does not allow fitting of an observed tumor volume trajectory.*	Empirical observations dictate the extraction of information. *Example: Tumor recurrence can be predicted from imaging. Interpretability analysis revealed that tumor shape was driving this* prediction.
Generate novel hypotheses for causal mechanisms. *Example: The addition of a reasonable but previously unknown mechanism to the model enables reproduction of experimental results.*	Isolate relevant inputs from empirical datasets for a given output. *Example: Principal component analysis is used to show main factors to explain the variance in the data*
Deductive capability: extrapolation to predictions about behaviors not present in original data *Example: A model described tumor response to a single radiotherapy fraction well. Predictions of tumor response to multiple fractions are possible.*	Inductive capability: interpolation of data with limited extrapolation horizon *Example: Prediction if a tumor responds to radiotherapy (represented in the training data) - this model cannot predict if the tumor will still respond if we change the delivery (i.e. fractionation) of the treatment.*
Predict or describe dynamics of the overall system. *Example: By modeling thousands of individual cells the overall dynamic growth response of a tumor is observed.*	Infer dynamics from the overall system while governing equations and parameters are not exactly known *Example: The prediction of cell states based on environmental and transcriptomic data*
Small but specific data set is needed for validation *Example: 2-3 diffusion-weighted MRI scans suffice to fit a mechanistic tumor growth model to data of an individual patient.*	Large number of parameters (thousands, millions or more), requiring data-intensive training/fitting *Example: For the prediction of tumor response to radiotherapy, 100s of patient images were used to train a deep convolutional neural network.*
Limiting factor(s): Quality of assumptions; parameter sensitivity *Example: If the underlying assumptions do not hold up upon model fitting, the model needs to be reworked.*	Limiting factor(s): Quality and quantity of data; model structure such as choice of features (inputs) *Example: A large number of diverse training examples are needed to fit a complex architecture.*

Some aspects here are taken from Baker et al. (9).

validation, ideally on independently sourced data, is performed to assess the model's performance.

Given these similarities and differences, it is important to account for possible challenges upon combining approaches. Model bias or conflicting information generated by addressing the same task with differently motivated approaches needs to be carefully considered. At the same time, there exists ample room to harness synergies between knowledge and data-driven modeling under the umbrella of mechanistic learning. Specifically, differences regarding data requirements, model complexity, extrapolation, and application regimes imply that a combination of both approaches may mitigate individual limitations. For example, parameters of a mechanistic mathematical model can be estimated by a deep learning algorithm from complex multi-omics data or knowledge-driven descriptions can be used to constrain the large range of possible solutions of a complex data-driven approach to a meaningful subset. In the following sections, we provide a detailed overview of how these combinations can be achieved and provide real-world application examples to motivate these.

3 Facets of mechanistic learning

"Mechanistic learning" (7, 8) can take on many facets by shifting the emphasis of the "data" and "knowledge" paradigms upon model design and fitting. While a partition of mechanistic learning into simulation-assisted machine learning, machine-learning-assisted simulation, and a hybrid class for approaches falling between these definitions is intuitive at first (44), it fails to describe the variety of hybrid approaches. We suggest a more abstract classification (Figure 1):

- Sequential - Knowledge-based and data-driven modeling are applied sequentially building on the preceding results
- Parallel - Modeling and learning are considered parallel alternatives to complement each other for the same objective
- Extrinsic - High-level *post hoc* combinations
- Intrinsic - Biomedical knowledge is built into the learning approach, either in the architecture or the training phase

Whereas sequential and parallel combinations make a deliberate choice of aspects of data- and knowledge-driven models to coalesce, extrinsic and intrinsic combinations actively interlace these. Thus, the complexity with respect to implementation and interpretation grows from sequential to intrinsic combinations. While most implementations readily fit into one of these four classes, we emphasize that we do not consider the combinations as discrete encapsulated instances. Instead, we view all synergistic combinations on a continuous landscape between the two extremes of purely knowledge- and data-driven models (Figure 2).

3.1 Sequential combinations

Sequential approaches harness knowledge and data-driven aspects as sequential and computationally independent tasks by disentangling the parameter/feature estimation and forecasting steps. They strive to attain mechanistic learning objectives by interlinking inputs from one approach with another. This could involve utilizing data-driven methods for estimating mechanistic model parameters or

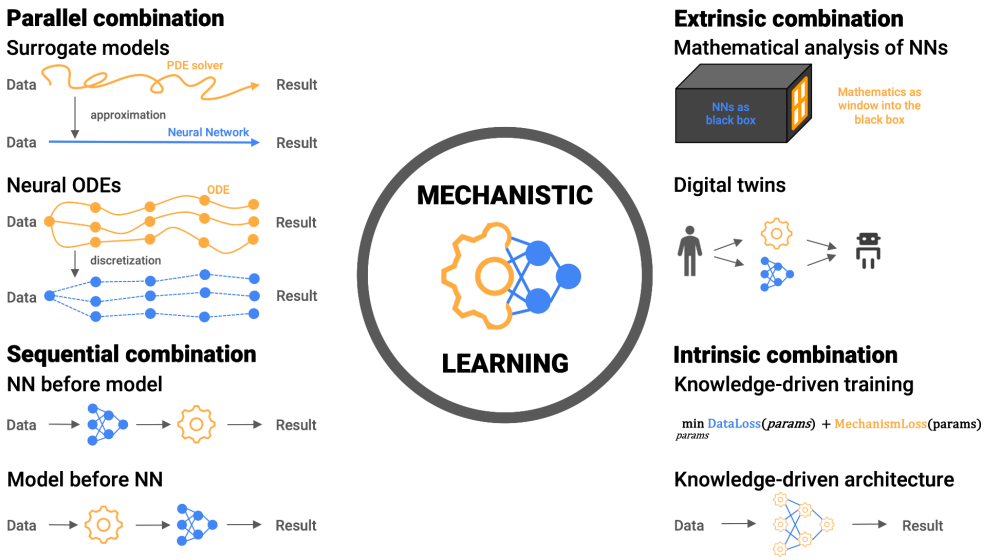

FIGURE 1
Examples of mechanistic learning structured in four combinations: Parallel combinations (top left) with examples of surrogate models and neural ordinary differential equations (ODEs). Data- and knowledge-driven models act as alternatives to complement each other for the same objective. Sequential combinations (bottom left) apply data- and knowledge-driven models in sequence to ease the calibration and validation steps. Extrinsic combinations (top right) combine knowledge-driven and data-driven modeling at a higher level. For example, mathematical analysis of data-driven models and their results or as complementary tasks for digital twins. Intrinsic combinations (bottom right), like physics- and biology-informed neural networks include the knowledge-driven models into the data-driven approaches. Knowledge is included in the architecture of a data-driven model or as a regularizer to influence the learned weights.

implementing feature selection in a data-driven model guided by mechanistic priors. Although sequential frameworks are straightforward to implement and interpret, often their computational demands increase significantly, taking into account both computational requirements and the limitations inherent in the individual approaches (e.g., data requirements, accuracy of prior knowledge).

3.1.1 Domain knowledge to steer data-driven model inputs and architecture choices

In medical science, data availability remains a key challenge (45). However, there often exists a strong hypothesis regarding the driving features of a specific prediction task. A simple but effective means of improving the performance of data-driven algorithms is a deliberate choice of model architecture, data preprocessing, and model inputs.

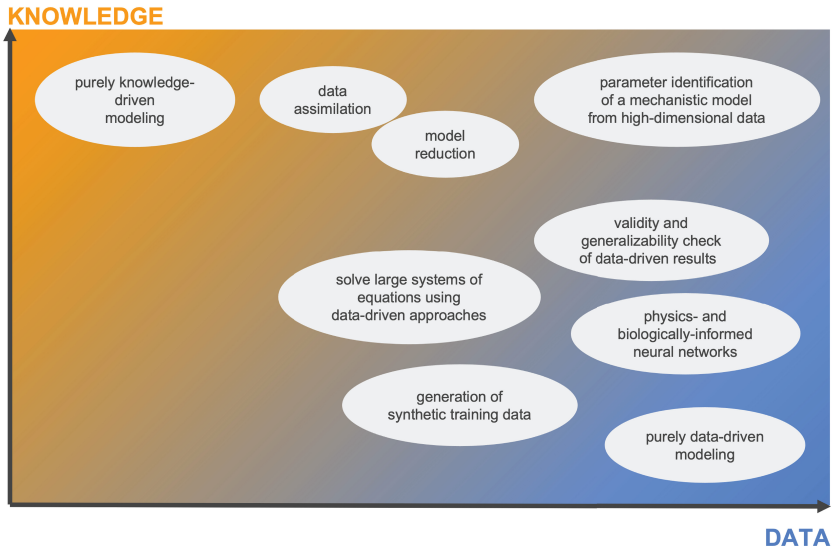

FIGURE 2
The mechanistic learning landscape shows room for the combination of data-driven and knowledge-driven modeling. We suggest that purely data-driven or purely knowledge-driven models represent the extremes of a data-knowledge surface with ample room for combinations in different degrees of synergism. Further, in the left-bottom corner with almost no data nor knowledge, any modeling or learning technique is limited.

For example, focusing the input of a deep neural network to disease-relevant subregions of an image boosted classification performance in a data-limited setting (46), and expert-selected features were used to reduce data requirements of image processing tasks dimensionality and data requirements of image processing tasks (47). Similarly important is a deliberate choice of model architecture (48–50). For instance, while convolutional blocks are the staple for computer vision tasks, similar approaches exist for sequential data (e.g. sequence-to-sequence transformers, recurrent neural networks, or graph-based models (51, 52)). While no mechanistic modeling is conducted *per se* deliberate feature and architecture selection includes additional information. Ultimately, features can also be identified by knowledge-driven modeling (53, 54).

3.1.2 Mechanistic feature engineering

Feature engineering is the process of designing input features from raw data (55). This process can be guided by a deeper understanding of the underlying mechanisms, including physical and biochemical laws or causal relationships.

Aspects of a mechanistic model can serve as input features to or outputs from machine learning models. This strategy of "mechanistic feature engineering", was used by Benzekry et al. to predict overall survival in metastatic neuroblastoma patients (56). First, a mechanistic model of metastatic dissemination and growth was fitted to patient-specific data. Then, a multivariate Cox regression model predicted overall survival from available clinical data with or without patient-specific mechanistic model parameters. They found that including the fitted mechanistic model parameters greatly enhanced the predictive power of the regression. One problem in this truly sequential setting is that it is difficult to address uncertainty propagation. Therefore, a challenging limitation persists, as the propagation of uncertainties and prediction errors may amplify within the context of the complete framework.

3.1.3 Data-driven estimation of mechanistic model parameters

A common problem in knowledge-driven modeling for longitudinal predictions is parameter identifiability and fitting given limited data and complex systems of equations. The bottleneck lies in the lack of a detailed understanding of the mechanistic relation between input data and desired output, rather than a purely computational limitation.

Similar to using mechanistic feature engineering for data-driven model inputs, data-driven approaches can also be employed to discover correlations within unstructured, high-dimensional data to provide inputs to knowledge-driven models. Depending on the specific application a range of methods are possible: imaging data are preprocessed by convolutional architectures, whereas omics data could be processed with network analysis, graph-based, or standard machine learning models. These correlations are then harnessed to predict the parameters of a mechanistic approach. Importantly, each model is implemented and trained/fitted independently, implying a high-level, yet easily interpretable combination. This sequential combination harnesses the ability of data-driven models to extract information in the form of summarizing parameters from high dimensional and heterogeneous data types. Importantly, the type of data required for such analysis needs to meet the criteria of knowledge-driven (e.g., longitudinal information) and data-driven (e.g., sufficient sample size) approaches alike - this may restrict applicability in light of limited data quality or excessive noise. Similarly, limitations such as robustness and prediction performance for the estimated parameters should be considered.

In practice, Perez-Aliacar et al. (57) predicted parameters of their mechanistic model of glioblastoma evolution from fluorescent microscopy images. This combination of models has also been suggested in the context of data-driven estimation of pharmacokinetic parameters for drugs (58). Moreover, data-driven models enable parameter inference by studying parameter dependencies of simulation results through approximate Bayesian computation (59, 60) or genetic algorithms (61).

3.1.4 Data-driven estimation of mechanistic model residuals

Another sequential construct consists in using machine learning models to predict the residuals of a mechanistic model prediction. Kielland et al. utilized this technique to forecast breast cancer treatment outcomes under combination therapy from gene expression data (62). Initially, a mechanistic model of the molecular mechanisms was calibrated with cell line data to enable patient-specific predictions. Subsequently, various machine learning models were employed to predict the residuals of the mechanistic model from the available expression of more than 700 genes. While the performance of the combined strategy was comparable to using machine learning alone, it offered three advantages. First, the mechanistic model provided a molecular interpretation of treatment response. Additionally, this approach facilitated the discovery of important genes not included in the mechanistic model. Hence, this approach can potentially incorporate emerging biological knowledge and new therapeutics without additional data required for machine learning alone. Note that this sequential strategy facilitates the inclusion of both mechanistically understood features and others that may not be as clear, a common scenario in treatment forecasting.

In summary, sequential combinations are attractive due to their clear path toward implementation and interpretation with limitations due to prerequisites on data, mechanistic understanding or uncertainty propagation. While future directions may dive deeper into harnessing more complex input data (e.g. multi-omics, multimodal) for mechanistic model inputs, the technical advancement for sequential combinations remains dictated by the progress in the individual fields.

3.2 Parallel combinations

Parallel combinations blend advantages of purely data- or knowledge-driven models without changing the anticipated evaluation endpoint. These are alternatives for the same task as a purely data- or knowledge-driven approach and hence aspects concerning data requirements, implementation, model robustness, and performance can be compared. This makes them attractive for

high-stakes decision scenarios, such as clinical application (e.g. tumor growth prediction).

3.2.1 Neural networks as surrogate models

Many phenomena in oncology can be readily formulated using large systems of equations. However, solving large models comes at a high computational cost. Utilizing methods such as model order reduction aids in optimizing the computational efficiency of the solving process. This approach typically demands substantial mathematical expertise and is not suitable for time- or resource-constrained scenarios such as real-world clinical deployment. Neural networks, as universal function approximators, offer an efficient alternative. In practice, data-driven models are trained on numerical simulation results and approximate a solution to the system of equations. The inference step of the successfully trained model takes a fraction of the computational resources compared to the full mechanistic model (63, 64).

A related concept is the generation of vast amounts of "synthetic" training data (65) based on a small set of "original" data points. While synthetic training data can improve the accuracy of many learning-based systems, care needs to be taken to prevent encoding faulty concepts or misleading biases into the training data that are not present in reality (66, 67). Any uncertainty or bias introduced during the training of the synthetic data generator is inherent in the resulting samples. This limitation could easily be overlooked within downstream tasks, underscoring the importance of meticulously designing a surrogate model.

For example, Ezhov et al. (68) introduced a deep learning model performing inverse model inference to obtain the patient-specific spatial distribution of brain tumors from magnetic resonance images, addressing the computational limitations of previous partial differential equation (PDE)-based spatial tumor growth and response models. A similar brain tumor growth model based on an encoder-decoder architecture trained on 6,000 synthetic tumors generated from a PDE model (69).

3.2.2 Neural ordinary differential equations — neural networks as discretized ordinary differential equations

The term "neural ordinary differential equation", or "neural ODE" originated from the notion of viewing neural networks as discretized ODEs or considering ODEs to be neural networks with an infinite amount of layers (70–72). In that sense, the knowledge-driven approaches using ODEs and the data-driven approach using neural networks are parallel perspectives of the same concept. While not every data-driven model can be interpreted as discretized ODEs and not every question for ODEs can be answered by a discretization to a neural network, neural ODEs can often be a helpful concept to translate between knowledge- and data-driven modeling. More generally, a neural ODE can also be seen as a differential equation that uses a neural network to parameterize the vector field. As such, this approach offers advantages over neural networks, including high-capacity function approximation and easy trainability, together with the extensive available theory and tools for the numerical treatment of differential equations. In addition, the continuous-time regime of differential equations allows treating irregular time series data in a natural way (73).

Neural ODEs have already been used for a variety of tasks in oncology ranging from genome-wide regulatory dynamics (74) and breast tumor segmentation in medical images (75) to time-to-event modeling (76). Importantly, neural ODEs can generate realistic synthetic data, such as longitudinal patient trajectories. As these synthetic patient data are anonymous, regularly sampled, and complete (i.e. no missing data) they address key challenges of medical data analytics: data privacy, limited data, missing data, variable data quality, and sampling time points. Synthetic patients can be shared across institutes as high-quality samples to train large-scale models, ensuring compliance with international data privacy regulations (77).

3.2.3 Learning a mechanistic model equation

While oncology research generates vast amounts of data, extracting and consolidating mechanistic understanding from data is a laborious process reliant on human experts. Symbolic regression allows for automated and data-driven discovery of governing laws expressed as algebraic or differential equations. This method finds a symbolic mathematical expression that accurately matches a dataset of label-feature pairs. Two prominent symbolic regression techniques are genetic programming-based optimization (78) and sparse regression (79). In genetic programming, closed-form expressions are represented as trees and evolved such that trees with high goodness-of-fit are selected for further exploration. In sparse regression strategies, the target expression is assumed to be a linear combination of certain "basis functions", and L1 regularization is used to select and weight a small combination of them.

Despite remarkable success in physics (78), symbolic regression applications in oncology are still scarce. In one example, by Brummer et al. (80), sparse regression was employed to estimate a system of ODEs from *in vitro* CAR T-cell glioma therapy data. Compared to knowledge-based models, this data-driven approach offers new insights into the biological dynamics as the model form is not constrained.

However, estimating derivatives from high noise and sparse longitudinal measurements, like many from clinical oncology, remains challenging. Several groups have used variational formulations of ODEs and PDEs in the optimization step without relying on estimating derivatives from noisy and sparse data (81–83). Bayesian approaches applied to genetic programming have also proven successful in situations where existing non-Bayesian approaches failed (84). Other promising directions in oncological research are Koopman theory (85) and the universal differential equation framework (86), where neural networks are used to model all or part of a differential equation, facilitating the discovery of governing equations, or parts of them, in cases where data are limited.

3.3 Extrinsic combinations

Extrinsic combinations make use of both mechanistic and data-driven approaches to address different aspects of the same problem or to post-process the output of a data-driven implementation.

3.3.1 Digital twins

Originating from analogies in manufacturing and engineering, the concept of digital twins (87–89) has recently gained interest in the oncology community. A digital twin is an *in silico* patient "twin" that recapitulates important patient characteristics and is used to simulate alternative treatment strategies and forecast disease progression (90). In the context of precision medicine, this implies that alternative treatment scenarios are simulated with the digital twin to select an optimal strategy. Hence, predictive modeling of longitudinal information regarding the expected patient trajectory is provided. The computational framework behind the digital twin can be based on mechanistic, data-driven, or a combined set of algorithms. We highlight the potential of combining mechanistic and data-driven modeling as side-by-side tasks, covering different aspects of one unifying digital twin.

Typically, for mechanistic digital twins, a mathematical framework describes the dynamics of tumor size, morphology, composition, and other biomarkers (91). The data-driven analogy is represented by machine learning algorithms, e.g., k-nearest neighbors but also more advanced architectures, to provide a prediction of the endpoint of interest based on established databases (92, 93). Both knowledge- and data-driven models enable the real-time adaptation of treatment protocols by simulating a range of scenarios. Importantly, harnessing the strengths of each method should be considered for optimal results. For instance, a data-driven prediction task could inform on patient subgrouping and identify likely outcomes, whereas mechanistic modeling would explore personalized treatment alternatives. Generally, digital twins can also serve as "virtual controls" to benchmark the efficacy of the patient's current treatment regimen (94, 95). Wu et al. provide an in-depth review regarding the specific application example of digital twins for oncology applications including a mention of the roles of data-driven image analysis and knowledge-driven modeling. The trade-off between application focus and computational complexity of a digital twin has to be considered in light of the data available which may restrict the feasible complexity and performance. Limitations, such as the requirement for longitudinal data, the complexity of mid-treatment adjustment in clinical settings, and the overall complexity regarding a high-stakes decision process need to be accounted for (89).

3.3.2 Complementary postprocessing: mathematical analysis of data-driven models and data-driven analysis of mathematical simulations

Data-driven approaches are trained to optimize a performance metric, but performance alone is not driving a model's application in (clinical) practice. Here, quantification of the uncertainty of model results, model robustness, as well as interpretability to explain why a model arrived at a certain conclusion are equally important (96). These questions are usually studied under the term explainable AI; for a survey we refer to Roscher et al. (97). Progress in advanced explainable AI dictates a mechanistic interpretation of a model's decision-making process (98).

Addressing many of the questions related to deep learning is only possible using mathematical methods, i.e., challenges in the field of data-driven models are transformed to mathematical conjectures that are subsequently (dis)proven. This approach ensures that the results generated by models are mathematically reliable and transparent and thus better suited for clinical implementations.

Numerous examples underscore this point and provide motivation for employing intricate architecture designs based on mathematical formulations. A specific instance involves learning a specialized representation that elucidates cancer subtyping from multi-omics inputs, including transcriptomic, proteomic, or metabolomic data (77).

Data assimilation techniques bridge numerical models and observational data through optimization of starting conditions. Typical examples are Kalman or particle filter methods (99, 100), which can improve the accuracy of numerical predictions. For the interpretation and validation of simulation results, tools from data-driven modeling can be used to detect patterns in simulations (101). This approach is already performed in research fields outside the oncology domain (102). A prime example is the post-processing of complex numerical weather forecasting predictions using deep learning to boost overall performance (103, 104). Within oncology applications, machine learning and Bayesian statistics have also been used for uncertainty quantification which is important for clinical translation (105–107).

3.4 Intrinsic combinations

This combination incorporates a mechanistic formulation within a machine learning model either upon training as a contribution to the formulated objective function or *a priori* as a way of choosing the architecture of the data-driven model. As such, these are densely interconnected combinations.

3.4.1 Regularizing the loss function using prior knowledge

Mechanism-informed neural networks such as physics-informed neural networks (PINNs) (108, 109) use mechanistic regularization upon training, i.e., equation-regularization, by guiding the possible solutions to physically relevant ones. The loss function combines performance loss with a regularization term assessing the deviation from a predefined set of equations. This approach reduces overfitting and ensures physically meaningful predictions. The final neural network will not satisfy the equations exactly but approximate them for the areas where training data is available. PINNs can be valuable for deciding whether an equation can be used to describe data by considering several related equations as regularizers.

Equation-regularization has previously been shown to enhance both the performance and interpretability of data-driven architectures. In the context of oncology, one example includes the modeling of tumor growth dynamics (110). Ayensa-Jiménez et al (111) used physically-guided NNs with internal variables to

model the evolution of glioblastoma as a "go-or-grow" process given constrained resources such as metabolites and oxygen. The model-free nature of their approach allows for the incorporation of data from various boundary conditions and external stimuli, resulting in accurate tumor progression predictions even under different oxygenation conditions.

3.4.2 Incorporating knowledge into the machine learning model architecture

Rather than optimizing a network architecture through regularization, biology-informed neural networks constrain the model architecture to biological priors from the start. Typically in the context of network analysis, biological priors such as known interactions between genes and/or transcription factors are translated to nodes and edges in a graph (112, 113). The network is constrained to an established connectivity profile which greatly reduces the model complexity compared to a fully connected network. Similar to transfer learning where a different data-rich scenario is used to pretrain a model prior to refining specific weights on the limited target data, this approach uses expert insight to preset connections and weights. Lagergren et al. (114) proposed biology-informed neural networks that learn the nonlinear terms of a governing system, eliminating the need for explicitly specifying the mechanistic form of a PDE as is the case for PINNs. They tested their approach on real-world biological data to uncover previously overlooked mechanisms. Another example is given by Przedborski et al. (115) who used biology-informed neural networks to predict patient response to anti-PD-1 immunotherapy and present biomarkers and possible mechanisms of drug resistance. Their model offers insights for optimizing treatment protocols and discovering novel therapeutic targets. Indeed, this approach has found several applications, e.g., for the prediction of prostate cancer (112) and drug discovery (116). Despite similar naming conventions, biology- and physics-informed neural networks refer to distinct approaches. The latter distinguishes itself by integrating biological realism and enhancing interpretability for applications that predominately rely on multi-scale, multi-source data (such as omics). However, profound insight regarding the formulated biological process is indispensable. PINN applications regularize, i.e. do not strictly constrain implying more flexibility yet less interpretability.

Finally, in the context of generative approaches, differential equations have previously been incorporated into (deep) neural networks through variational autoencoders. While current examples were obtained from medical applications other than oncology (117, 118), they represent elegant solutions to allow for dynamic deep learning despite limited data, given careful hyperparameter tuning.

3.4.3 Hierarchical modeling

Hierarchical nonlinear models, also referred to as nonlinear mixed effects models, are a widely used framework to analyze longitudinal measurements on a number of individuals, when interest focuses on individual-specific characteristics (119). For instance, early in drug development, pharmacokinetics studies are carried out to gain insights into within-subject pharmacokinetics processes of absorption, distribution, and elimination (120). Typically, a parametric nonlinear model describing drug concentration change over time (individual-level model) is coupled with a linear model describing the relation between pharmacokinetic parameters and individual features (population-level model). One of the simplest population-level models is the random intercept model, which models individual parameter values as normally distributed around a typical value. This enables information sharing through each individual's contribution to determine the typical value, while simultaneously allowing individual parameters that match the observed measurements. Moreover, in contrast to the sequential approach (section 3.1.3), hierarchical models allow for the propagation of uncertainty between the individual-level and population-level models. Applications in oncology range from tumor growth (121) to mutational dynamics in circulating tumor DNA (122) or metastatic dissemination (123).

Interestingly, hierarchical models have the potential to benefit from more sophisticated data-driven approaches to integrate high-throughput data, such as omics or imaging (8). This can be done by changing the linear covariate model with more complex machine learning algorithms able to capture complex relations between the parameters of the individual-level model and the high dimensional covariates (124, 125), and/or by using Bayesian inference (38).

4 Conclusion and perspective

Recently, machine and deep learning have become ubiquitous given their indisputable potential to learn from data (126). However, it is evident that medical applications, especially in oncology, are currently constrained by the extent and diversity of available data. Moreover, clinical translation involves high-stakes decisions that need to be backed up by evidence. The oncology field must address the critical challenges of limited data availability, model transparency, and complex input data. To overcome these bottlenecks, we need data-efficient, comprehensible, and robust solutions. Despite the growing interest in mechanistic mathematical modeling for medical applications, the success and opportunity of data-driven models must be taken into account. Strategically integrating knowledge- and data-driven modeling in mechanistic learning represents a logical progression to tackle the challenges in mathematical oncology. It aims to facilitate accurate, personalized predictions, leading to a more comprehensive understanding of cancer evolution, progression, and response.

Here, we identified opportunities for synergistic combinations and provided a snapshot of the current state-of-the-art for how such combinations are facilitated for oncology applications. We highlighted similarities in the mathematical foundation and implementation structure of optimization processes and pointed out differences with respect to data requirements and the role of knowledge and data in these approaches. It is important to structure the growing landscape of models at the interface of data- and knowledge-driven implementations. We hence propose systemizing combinations in four general categories: sequential, parallel,

intrinsic, and extrinsic combinations. While sequential and parallel combinations are intuitive and easily implemented, intrinsic and extrinsic combinations incorporate a stronger degree of interlacing that requires a deeper understanding of both data science and mathematical theory. The choice of analysis tool should always keep in mind the quality, size, and type of data and knowledge in light of the underlying research question. An intentional combination of machine learning and mechanistic mathematical modeling can then leverage the strengths of both approaches to tackle complex problems, gain deeper insights, and develop more accurate and robust solutions. Mechanistic learning can take on many facets and is foreseen to grow in importance in the context of mathematical oncology with a particular focus on explainable AI, handling of limited data (e.g. efficient architecture design, data augmentation), and generation of precision oncology solutions. In this review, we discussed only the core concepts. Given the fluid boundaries between data- and knowledge-driven models and in light of the variety of approaches within each of these domains, an exhaustive listing of all combinations is infeasible. However, several future directions stand out. For instance, hybrid modeling with Bayesian statistics, deep generative approaches, or specific training regimes, including semi-supervised (contrastive) or reinforcement learning, are worth mentioning. Finally, despite the positive notion regarding mechanistic learning, certain limitations persist within both separate and combined approaches. Specifically ethical considerations should be addressed. These may arise from data privacy, algorithmic bias, or the clinical implementation of hybrid models.

Finally, with this work we strive to motivate a more active exchange between machine learning and mechanistic mathematical modeling researchers given the many parallels in terms of methodologies and evaluation endpoints, and the powerful results produced by mechanistic learning.

Author contributions

JM: Conceptualization, Formal analysis, Visualization, Writing – original draft, Writing – review & editing. CJ: Conceptualization, Supervision, Writing – review & editing. PM: Conceptualization, Supervision, Writing – review & editing. AK: Conceptualization, Writing – original draft, Writing – review & editing. SB: Conceptualization, Formal analysis, Project administration, Writing – original draft, Writing – review & editing.

Funding

The author(s) declare that financial support was received for the research, authorship, and/or publication of this article. JM was supported by NSF 1735095 - NRT: Interdisciplinary Training in Complex Networks and Systems. CJ was supported by the Swiss National Science Foundation (Ambizione Grant [PZ00P3_186101]). PM was supported in part by Cancer Moonshot funds from the National Cancer Institute, Leidos Biomedical Research Subcontract 21X126F, and by an Indiana University Luddy Faculty Fellowship. AK-L's work was funded by the research centers BigInsight (Norges Forskningsråd project number 237718) and Integreat (Norges Forskningsråd project number 332645). SB was supported by the Botnar Research Center for Child Health Postdoctoral Excellence Programme (#PEP-2021-1008). Open access funding by ETH Zurich.

Acknowledgments

We thank Alexander Zeilmann and Saskia Haupt for many fruitful discussions and helpful contributions without which this manuscript would not have been possible. The collaboration that led to the design of this manuscript was fostered during the 2023 Banff International Research Station (BIRS) Workshop on Computational Modelling of Cancer Biology and Treatments (23w5007) initiated by Prof. M. Craig and Dr. A. Jenner.

Conflict of interest

The authors declare that the research was conducted in the absence of any commercial or financial relationships that could be construed as a potential conflict of interest.

Publisher's note

References

1. Rockne RC, Scott JG. Introduction to mathematical oncology. *JCO Clin Cancer Inform*. (2019) 1–4. doi: 10.1200/CCI.19.00010

2. Provost F, Fawcett T. Data science and its relationship to big data and data-driven decision making. *Big Data*. (2013) 1:51–9. doi: 10.1089/big.2013.1508

3. Géron A. *Hands-on Machine Learning with Scikit-Learn, Keras, and TensorFlow: Concepts, Tools, and Techniques to Build Intelligent Systems*. Sebastopol, California, USA:O'Reilly (2019).

4. Bender EA. *An Introduction to Mathematical Modeling*. New York: Wiley (1978).

5. Murray JD. *Mathematical Biology: I. An Introduction* Vol. 17. New York, NY: Springer New York (2002).

6. Obot OU, Attai KF, Onwodi GO. Integrating knowledge-driven and data-driven methodologies for an efficient clinical decision support system. In: Connolly TM, Papadopoulos P, Soflano M, editors. *Advances in Medical Technologies and Clinical Practice*. (Hershey, Pennsylvania, USA: IGI Global) (2022). p. 1–28.

7. Ciccolini J, Barbolosi D, André N, Barlesi F, Benzekry S. Mechanistic learning for combinatorial strategies with immuno-oncology drugs: can model-informed designs help investigators? *JCO Precis Oncol*. (2020) 4(4):486–91. doi: 10.1200/PO.19.00381

8. Benzekry S. Artificial intelligence and mechanistic modeling for clinical decision making in oncology. *Clin Pharmacol Ther*. (2020) 108:471–86. doi: 10.1002/cpt.1951

9. Baker RE, Peña J-M, Jayamohan J, Jérusalem A. Mechanistic models versus machine learning, a fight worth fighting for the biological community? *Biol Lett*. (2018) 14:20170660. doi: 10.1098/rsbl.2017.0660

10. Lorenzo G, Ahmed SR, Hormuth DA, Vaughn B, Kalpathy-Cramer J, Solorio L, et al. Patient-specific, mechanistic models of tumor growth incorporating artificial intelligence and big data. (2023). doi: 10.48550/ARXIV.2308.14925

11. Hatzikirou H. Combining dynamic modeling with machine learning can be the key for the integration of mathematical and clinical oncology: Comment on "Improving cancer treatments via dynamical biophysical models" by M. Kuznetsov, J. Clairambault, V. Volpert. *Phys Life Rev*. (2022) 40:1–2. doi: 10.1016/j.plrev.2022.01.002

12. Blair RH, Trichler DL, Gaille DP. Mathematical and statistical modeling in cancer systems biology. *Front Physiol*. (2012) 3. doi: 10.3389/fphys.2012.00227

13. Altrock PM, Liu LL, Michor F. The mathematics of cancer: integrating quantitative models. *Nat Rev Cancer*. (2015) 15:730–45. doi: 10.1038/nrc4029

14. Khajanchi S, Nieto JJ. Mathematical modeling of tumor-immune competitive system, considering the role of time delay. *Appl Math Comput*. (2019) 340:180–205. doi: 10.1016/j.amc.2018.08.018

15. Yasemi M, Jolicoeur M. Modelling cell metabolism: A review on constraint-based steady-state and kinetic approaches. *Processes*. (2021) 9:322. doi: 10.3390/pr9020322

16. Renardy M, Hult C, Evans S, Linderman JJ, Kirschner DE. Global sensitivity analysis of biological multiscale models. *Curr Opin Biomed Eng*. (2019) 11:109–16. doi: 10.1016/j.cobme.2019.09.012

17. Wieland F-G, Hauber AL, Rosenblatt M, Tönsing C, Timmer J. On structural and practical identifiability. *Curr Opin Syst Biol*. (2021) 25:60–9. doi: 10.1016/j.coisb.2021.03.005

18. Rockne RC, Scott JG. The 2019 mathematical oncology roadmap. *Phys Biol*. (2019) 16:041005. doi: 10.1088/1478-3975/ab1a09

19. McDonald TO, Cheng Y-C, Graser C, Nicol PB, Temko D, Michor F. Computational approaches to modelling and optimizing cancer treatment. *Nat Rev Bioeng*. (2023) 1:695–711. doi: 10.1038/s44222-023-00089-7

20. Ghaderi N, Jung J, Brüningk SC, Subramanian A, Nassour L, Peacock J. A century of fractionated radiotherapy: how mathematical oncology can break the rules. *Int J Mol Sci*. (2022) 23:1316. doi: 10.3390/ijms23031316

21. McMahon SJ, Prise KM. Mechanistic modelling of radiation responses. *Cancers*. (2019) 11:205. doi: 10.3390/cancers11020205

22. Yin A, Moes DJAR, Hasselt JGC, Swen JJ. & Guchelaar, H. A review of mathematical models for tumor dynamics and treatment resistance evolution of solid tumors. *CPT Pharmacomet Syst Pharmacol*. (2019) 8:720–37. doi: 10.1002/psp4.12450

23. Beerenwinkel N, Schwarz RF, Gerstung M, Markowetz F. Cancer evolution: mathematical models and computational inference. *Syst Biol*. (2015) 64:e1–e25. doi: 10.1093/sysbio/syu081

24. Brüningk SC, Peacock J, Whelan CJ, Brady-Nicholls R, Yu H-HM, Sahebjam S, et al. Intermittent radiotherapy as alternative treatment for recurrent high grade glioma: a modeling study based on longitudinal tumor measurements. *Sci Rep*. (2021) 11:20219. doi: 10.1038/s41598-021-99507-2

25. Sung W, Hong TS, Poznansky MC, Paganetti H, Grassberger C. Mathematical modeling to simulate the effect of adding radiation therapy to immunotherapy and application to hepatocellular carcinoma. *Int J Radiat Oncol*. (2022) 112:1055–62. doi: 10.1016/j.ijrobp.2021.11.008

26. Wang H, et al. In silico simulation of a clinical trial with anti-CTLA-4 and anti-PD-L1 immunotherapies in metastatic breast cancer using a systems pharmacology model. *R Soc Open Sci*. (2019) 6:190366. doi: 10.1098/rsos.190366

27. Igual L, Seguí S. Introduction to data science. In: *Introduction to Data Science*. Springer International Publishing, Cham (2017). p. 1–4.

28. Sharma M. State-of-the-art in performance metrics and future directions for data science algorithms. *J Sci Res*. (2020) 64:221–38. doi: 10.37398/JSR

29. Wang Q, Ma Y, Zhao K, Tian Y. A comprehensive survey of loss functions in machine learning. *Ann Data Sci*. (2022) 9:187–212. doi: 10.1007/s40745-020-00253-5

30. Lu Y, Lu J. A universal approximation theorem of deep neural networks for expressing probability distributions. In: Larochelle H, Ranzato M, Hadsell R, Balcan MF, Lin H, editors. *Advances in Neural Information Processing Systems*, vol. 33. Curran Associates, Inc., Cambridge, Massachusetts, USA (2020). p. 3094–105.

31. Linardatos P, Papastefanopoulos V, Kotsiantis S. Explainable AI: A review of machine learning interpretability methods. *Entropy*. (2020) 23:18. doi: 10.3390/e23010018

32. Yeom S, Giacomelli I, Fredrikson M, Jha S. (2018). Privacy risk in machine learning: analyzing the connection to overfitting, in: *2018 IEEE 31st Computer Security Foundations Symposium (CSF)*, IEEE, Oxford. (IEEE, New York, New York, USA), pp. 268–82. doi: 10.1109/CSF.2018.00027

33. Cao X, Yousefzadeh R. Extrapolation and AI transparency: Why machine learning models should reveal when they make decisions beyond their training. *Big Data Soc*. (2023) 10. doi: 10.1177/20539517231169731

34. Augustin M, Meinke A, Hein M. Adversarial robustness on in- and out-distribution improves explainability. In: Vedaldi A, Bischof H, Brox T, Frahm J-M, editors. *Computer Vision – ECCV 2020*, vol. 12371. Springer International Publishing, Cham (2020). p. 228–45.

35. Kann BH, Hosny A, Aerts HJWL. Artificial intelligence for clinical oncology. *Cancer Cell*. (2021) 39:916–27. doi: 10.1016/j.ccell.2021.04.002

36. Baptista D, Ferreira PG, Rocha M. A systematic evaluation of deep learning methods for the prediction of drug synergy in cancer. *PloS Comput Biol*. (2023) 19: e1010200. doi: 10.1371/journal.pcbi.1010200

37. Baptista D, Ferreira PG, Rocha M. Deep learning for drug response prediction in cancer. *Brief Bioinform*. (2021) 22:360–79. doi: 10.1093/bib/bbz171

38. Lee SY. Bayesian nonlinear models for repeated measurement data: an overview, implementation, and applications. *Mathematics*. (2022) 10:898. doi: 10.3390/math10060898

39. Liu X, Yoo C, Xing F, Oh H, Fakhri GE, Kang J-W, et al. Deep unsupervised domain adaptation: A review of recent advances and perspectives. (2022). doi: 10.48550/arXiv.2208.07422

40. Jiang H, Diao Z, Yao Y-D. Deep learning techniques for tumor segmentation: a review. *J Supercomput*. (2022) 78:1807–51. doi: 10.1007/s11227-021-03901-6

41. Jyothi P, Singh AR. Deep learning models and traditional automated techniques for brain tumor segmentation in MRI: a review. *Artif Intell Rev*. (2022) 56:2923–69. doi: 10.1007/s10462-022-10245-x

42. Kaur I, Doja MN, Ahmad T. Data mining and machine learning in cancer survival research: An overview and future recommendations. *J Biomed Inform*. (2022) 128:104026. doi: 10.1016/j.jbi.2022.104026

43. Lu S-C, Xu C, Nguyen CH, Geng Y, Pfob A, Sidey-Gibbons C. Machine learning–based short-term mortality prediction models for patients with cancer using electronic health record data: systematic review and critical appraisal. *JMIR Med Inform*. (2022) 10:e33182. doi: 10.2196/33182

44. von Rueden L, Mayer S, Sifa R, Bauckhage C, Garcke J. Combining machine learning and simulation to a hybrid modelling approach: current and future directions. In: Berthold MR, Feelders A, Krempl G, editors. *Advances in Intelligent Data Analysis XVIII*. Springer International Publishing, Cham (2020). p. 548–60.

45. Rajpurkar P, Chen E, Banerjee O, Topol EJ. AI in health and medicine. *Nat Med*. (2022) 28:31–8. doi: 10.1038/s41591-021-01614-0

46. Brüningk SC, Hensel F, Lukas LP, Kuijs M, Jutzeler CR, Rieck B. (2021). Back to the basics with inclusion of clinical domain knowledge - A simple, scalable and effective model of Alzheimer's Disease classification, in: *Proceedings of the 6th Machine Learning for Healthcare Conference*, PMLR., pp. 730–54.

47. Rawat RR, Ruderman D, Macklin P, Rimm DL, Agus DB. Correlating nuclear morphometric patterns with estrogen receptor status in breast cancer pathologic specimens. *NPJ Breast Cancer*. (2018) 4:32. doi: 10.1038/s41523-018-0084-4

48. Culos A, Tsai AS, Stanley N, Becker M, Ghaemi MS, McIlwain DR, et al. Integration of mechanistic immunological knowledge into a machine learning pipeline improves predictions. *Nat Mach Intell*. (2020) 2:619–28. doi: 10.1038/s42256-020-00232-8

49. Fabris F, Freitas AA. New KEGG pathway-based interpretable features for classifying ageing-related mouse proteins. *Bioinformatics*. (2016) 32:2988–95. doi: 10.1093/bioinformatics/btw363

50. Zhang W, Chien J, Yong J, Kuang R. Network-based machine learning and graph theory algorithms for precision oncology. *NPJ Precis Oncol*. (2017) 1:1–15. doi: 10.1038/s41698-017-0029-7

51. Gaudelet T, Day B, Jamasb AR, Soman J, Regep C, Liu G, et al. Utilizing graph machine learning within drug discovery and development. *Brief Bioinform*. (2021) 22: bbab159. doi: 10.1093/bib/bbab159

52. Li MM, Huang K, Zitnik M. Graph representation learning in biomedicine and healthcare. *Nat Biomed Eng*. (2022) 6:1353–69. doi: 10.1038/s41551-022-00942-x

53. Kather JN, Charoentong P, Suarez-Carmona M, Herpel E, Klupp F, Ulrich A, et al. High-throughput screening of combinatorial immunotherapies with patient-specific *in silico* models of metastatic colorectal cancer. *Cancer Res*. (2018) 78:5155–63. doi: 10.1158/0008-5472.CAN-18-1126

54. Bull JA, Byrne HM. Quantification of spatial and phenotypic heterogeneity in an agent-based model of tumour-macrophage interactions. *PloS Comput Biol*. (2023) 19: e1010994. doi: 10.1371/journal.pcbi.1010994

55. Zheng A, Casari A. *Feature engineering for machine learning: principles and techniques for data scientists*. Beijing: Boston: O'Reilly (2018).

56. Benzekry S, Sentis C, Coze C, Tessonnier L, André N. Development and validation of a prediction model of overall survival in high-risk neuroblastoma using mechanistic modeling of metastasis. *JCO Clin Cancer Inform*. (2021) 5(5):81–90. doi: 10.1200/CCI.20.00092

57. Pérez-Aliacar M, Doweidar MH, Doblaré M, Ayensa-Jiménez J. Predicting cell behaviour parameters from glioblastoma on a chip images. A deep learning approach. *Comput Biol Med*. (2021) 135:104547. doi: 10.1016/j.compbiomed.2021.104547

58. Mavroudis PD, Teutonico D, Abos A, Pillai N. Application of machine learning in combination with mechanistic modeling to predict plasma exposure of small molecules. *Front Syst Biol*. (2023) 3:1180948. doi: 10.3389/fsysb.2023.1180948

59. Pesonen H, Simola U, Köhn-Luque A, Vuollekoski H, Lai X, Frigessi A, et al. ABC of the future. *Int Stat Rev*. (2022) 91(2):243–68. doi: 10.1111/insr.12522

60. Rocha HL, Godet I, Kurtoglu F, Metzcar J, Konstantinopoulos K, Bhoyar S, et al. A persistent invasive phenotype in post-hypoxic tumor cells is revealed by fate mapping and computational modeling. *iScience*. (2021) 24. doi: 10.1101/2020.12.30.424757

61. Akasiadis C, Ponce-de-Leon M, Montagud A, Michelioudakis E, Atsidakou A, Alevizos E, et al. Parallel model exploration for tumor treatment simulations. *Comput Intell*. (2022) 38:1379–401. doi: 10.1111/coin.12515

62. Kielland A. *Integrating Biological Domain Knowledge in Machine Learning Models for Cancer Precision Medicine*. Oslo: University of Oslo (2023).

63. Gu Y, Ng MK. Deep neural networks for solving large linear systems arising from high-dimensional problems. (2022). doi: 10.48550/ARXIV.2204.00313

64. Jiang Z, Jiang J, Yao Q, Yang G. A neural network-based PDE solving algorithm with high precision. *Sci Rep*. (2023) 13:4479. doi: 10.1038/s41598-023-31236-0

65. Nikolenko SI. *Synthetic Data for Deep Learning* Vol. 174. . Cham: Springer International Publishing (2021). doi: 10.1007/978-3-030-75178-4

66. Gherman IM, Abdallah ZS, Pang W, Gorochowski TE, Grierson CS, Marucci L. Bridging the gap between mechanistic biological models and machine learning surrogates. *PloS Comput Biol*. (2023) 19:e1010988. doi: 10.1371/journal.pcbi.1010988

67. Rocha HL, de O. Silva JV, Silva RS, Lima EABF, Almeida RC. Bayesian inference using Gaussian process surrogates in cancer modeling. *Comput Methods Appl Mech Eng*. (2022) 399:115412. doi: 10.1016/j.cma.2022.115412

68. Ezhov I, Scibilia K, Franitza K, Steinbauer F, Shit S, Zimmer L, et al. Learn-Morph-Infer: A new way of solving the inverse problem for brain tumor modeling. *Med Image Anal*. (2023) 83:102672. doi: 10.1016/j.media.2022.102672

69. Jain RK, Gupta A, Ali WH, Lermusiaux PFJ. GlioMod: spatiotemporal-aware glioblastoma multiforme tumor growth modeling with deep encoder-decoder networks. (2022). doi: 10.1101/2022.11.06.22282010

70. Chen RTQ, Rubanova Y, Bettencourt J, Duvenaud D. Neural ordinary differential equations. (2019). doi: 10.48550/arXiv.1806.07366

71. Weinan E. A proposal on machine learning via dynamical systems. *Commun Math Stat*. (2017) 5:1–11. doi: 10.1007/s40304-017-0103-z

72. Haber E, Ruthotto L. Stable architectures for deep neural networks. *Inverse Probl*. (2018) 34:014004. doi: 10.1088/1361-6420/aa9a90

73. Kidger P. On neural differential equations. Doctoral thesis, Mathematical Institute, University of Oxford. (2022), 231 pp. doi: 10.48550/arXiv.2202.02435

74. Hossain I, Fanfani V, Quackenbush J, Burkholz R. Biologically informed NeuralODEs for genome-wide regulatory dynamics. (2023). doi: 10.21203/rs.3.rs-2675584/v1

75. Ru J, Lu B, Chen B, Shi J, Chen G, Wang, et al. Attention guided neural ODE network for breast tumor segmentation in medical images. *Comput Biol Med*. (2023) 159:106884. doi: 10.1016/j.compbiomed.2023.106884

76. Moon I, Groha S, Gusev A. SurvLatent ODE: A Neural ODE based time-to-event model with competing risks for longitudinal data improves cancer-associated Venous Thromboembolism (VTE) prediction. (2022). doi: 10.48550/arXiv.2204.09633

77. Wendland P, Birkenbihl C, Gomez-Freixa M, Sood M, Kschischo M, Fröhlich H. Generation of realistic synthetic data using Multimodal Neural Ordinary Differential Equations. *NPJ Digit Med*. (2022) 5:1–10. doi: 10.1038/s41746-022-00666-x

78. Schmidt M, Lipson H. Distilling free-form natural laws from experimental data. *Science*. (2009) 324:81–5. doi: 10.1126/science.1165893

79. Brunton SL, Proctor JL, Kutz JN. Discovering governing equations from data by sparse identification of nonlinear dynamical systems. *Proc Natl Acad Sci*. (2016) 113:3932–7. doi: 10.1073/pnas.1517384113

80. Brummer AB, Xella A, Woodall R, Adhikarla V, Cho H, Gutova M, et al. Data driven model discovery and interpretation for CAR T-cell killing using sparse identification and latent variables. *Front Immunol*. (2023) 14. doi: 10.3389/fimmu.2023.1115536

81. Kacprzyk K, Qian Z, van der Schaar M. D-CIPHER: discovery of closed-form partial differential equations. *International Conference on Learning Representations*. ICLR, Appleton WI (2022). doi: 10.48550/arXiv.2206.10586

82. Messenger DA, Bortz DM. Weak SINDy for partial differential equations. *J Comput Phys*. (2021) 443:110525. doi: 10.1016/j.jcp.2021.110525

83. Qian Z, Kacprzyk K, van der Schaar M. D-CODE: discovering closed-form ODEs from observed trajectories. *International Conference on Learning Representations*. ICLR, Appleton WI (2022). Available at: https://openreview.net/forum?id=wENMvIsxNN.

84. Guimerà R, Reichardt I, Aguilar-Mogas A, Massucci FA, Miranda M, Pallarès J, et al. A Bayesian machine scientist to aid in the solution of challenging scientific problems. *Sci Adv*. (2020) 6:eaav6971. doi: 10.1126/sciadv.aav6971

85. Brunton SL, Budišić M, Kaiser E, Kutz JN. Modern koopman theory for dynamical systems. *SIAM Rev*. (2022) 64:229–340. doi: 10.1137/21M1401243

86. Rackauckas C, Ma Y, Martensen J, Warner C, Zubov K, Supekar R, et al. Universal differential equations for scientific machine learning. (2021). doi: 10.48550/arXiv.2001.04385

87. Hernandez-Boussard T, Macklin P, Greenspan EJ, Gryshuk AL, Stahlberg E, Syeda-Mahmood T, et al. Digital twins for predictive oncology will be a paradigm shift for precision cancer care. *Nat Med*. (2021) 27:2065–6. doi: 10.1038/s41591-021-01558-5

88. Kaul R, Ossai C, Forkan ARM, Jayaraman PP, Zelcer J, Vaughan S, et al. The role of AI for developing digital twins in healthcare: The case of cancer care. *WIREs Data Min Knowl Discovery*. (2023) 13:e1480. doi: 10.1002/widm.1480

89. Wu C, Lorenzo G, Hormuth DA, Lima EABF, Slavkova KP, DiCarlo JC. Integrating mechanism-based modeling with biomedical imaging to build practical digital twins for clinical oncology. *Biophys Rev*. (2022) 3:021304. doi: 10.1063/5.0086789

90. Fertig EJ, Jaffee EM, Macklin P, Stearns V, Wang C. Forecasting cancer: from precision to predictive medicine. *Med*. (2021) 2:1004–10. doi: 10.1016/j.medj.2021.08.007

91. Sager S. Digital twins in oncology. *J Cancer Res Clin Oncol*. (2023) 149:5475–5477. doi: 10.1007/s00432-023-04633-1

92. Mourtzis D, Angelopoulos J, Panopoulos N, Kardamakis D. A smart ioT platform for oncology patient diagnosis based on AI: towards the human digital twin. *Proc CIRP*. (2021) 104:1686–91. doi: 10.1016/j.procir.2021.11.284

93. Wan Z, Dong Y, Yu Z, Lv H, Lv Z. Semi-supervised support vector machine for digital twins based brain image fusion. *Front Neurosci*. (2021) 15. doi: 10.3389/fnins.2021.705323

94. Swanson KR, Rostomily RC, Alvord EC. A mathematical modelling tool for predicting survival of individual patients following resection of glioblastoma: a proof of principle. *Br J Cancer*. (2008) 98:113–9. doi: 10.1038/sj.bjc.6604125

95. Jackson PR, Juliano J, Hawkins-Daarud A, Rockne RC, Swanson KR. Patient-specific mathematical neuro-oncology: using a simple proliferation and invasion tumor model to inform clinical practice. *Bull Math Biol*. (2015) 77:846–56. doi: 10.1007/s11538-015-0067-7

96. Molnar C. *Interpretable Machine Learning: A Guide for Making Black Box Models Explainable*. Munich, Germany: Christoph Molnar (2022).

97. Roscher R, Bohn B, Duarte MF, Garcke J. Explainable machine learning for scientific insights and discoveries. *IEEE Access*. (2020) 8:42200–16. doi: 10.1109/Access.6287639

98. Ladbury C, Zarinshenas R, Semwal H, Tam A, Vaidehi N, Rodin AS, et al. Utilization of model-agnostic explainable artificial intelligence frameworks in oncology: a narrative review. *Transl Cancer Res*. (2022) 11(10):3853–3868. doi: 10.21037/tcr

99. Kim Y, Bang H, Kim Y, Bang H. Introduction to kalman filter and its applications. In: *Introduction and Implementations of the Kalman Filter*. IntechOpen, London, United Kingdom (2018).

100. Elfring J, Torta E, van de Molengraft R. Particle filters: A hands-on tutorial. *Sensors*. (2021) 21:438. doi: 10.3390/s21020438

101. Macklin P. When seeing isn't believing: how math can guide our interpretation of measurements and experiments. *Cell Syst*. (2017) 5:92–4. doi: 10.1016/j.cels.2017.08.005

102. Ozik J, Collier N, Heiland R, An G, Macklin P. Learning-accelerated discovery of immune-tumour interactions. *Mol Syst Des Eng*. (2019) 4:747–60. doi: 10.1039/C9ME00036D

103. Grönquist P, Yao C, Ben-Nun T, Dryden N, Dueben P, Li S, et al. Deep learning for post-processing ensemble weather forecasts. *Philos Trans R Soc Math Phys Eng Sci*. (2021) 379:20200092. doi: 10.1098/rsta.2020.0092

104. Li W, Pan B, Xia J, Duan Q. Convolutional neural network-based statistical post-processing of ensemble precipitation forecasts. *J Hydrol*. (2022) 605:127301. doi: 10.1016/j.jhydrol.2021.127301

105. Liang B, Tan J, Lozenski L, Hormuth DA, Yankeelov TE, Villa U, et al. Bayesian inference of tissue heterogeneity for individualized prediction of glioma growth. *IEEE Trans Med Imaging*. (2023) 42(10). doi: 10.1109/TMI.2023.3267349

106. Lipkova J, Angelikopoulos P, Wu S, Alberts E, Wiestler B, Diehl C, et al. Personalized radiotherapy design for glioblastoma: integrating mathematical tumor models, multimodal scans, and bayesian inference. *IEEE Trans Med Imaging*. (2019) 38:1875–84. doi: 10.1109/TMI.42

107. Lima EABF, Faghihi D, Philley R, Yang J, Virostko J, Phillips CM, et al. Bayesian calibration of a stochastic, multiscale agent-based model for predicting in *vitro* tumor growth. *PloS Comput Biol*. (2021) 17:e1008845. doi: 10.1371/journal.pcbi.1008845

108. Cuomo S, Di Cola VS, Giampaolo F, Rozza G, Raissi M, Piccialli F. Scientific machine learning through physics–informed neural networks: where we are and what's next. *J Sci Comput*. (2022) 92:88. doi: 10.1007/s10915-022-01939-z

109. Raissi M, Perdikaris P, Karniadakis GE. Physics-informed neural networks: A deep learning framework for solving forward and inverse problems involving nonlinear partial differential equations. *J Comput Phys*. (2019) 378:686–707. doi: 10.1016/j.jcp.2018.10.045

110. Zhu A. Accelerating parameter inference in diffusion-reaction models of glioblastoma using physics-informed neural networks. *SIAM Undergrad Res Online*. (2022) 15. doi: 10.1137/22S1472814

111. Ayensa-Jiménez J, Doweidar MH, Sanz-Herrera JA, Doblare M. Understanding glioblastoma invasion using physically-guided neural networks with internal variables. *PloS Comput Biol*. (2022) 18:e1010019. doi: 10.1371/journal.pcbi.1010019

112. Elmarakeby HA, Hwang J, Arafeh R, Crowdis J, Gang S, Liu D, et al. Biologically informed deep neural network for prostate cancer discovery. *Nature*. (2021) 598:348–52. doi: 10.1038/s41586-021-03922-4

113. Yazdani A, Lu L, Raissi M, Karniadakis GE. Systems biology informed deep learning for inferring parameters and hidden dynamics. *PloS Comput Biol*. (2020) 16:e1007575. doi: 10.1371/journal.pcbi.1007575

114. Lagergren JH, Nardini JT, Baker RE, Simpson MJ, Flores KB. Biologically-informed neural networks guide mechanistic modeling from sparse experimental data. *PloS Comput Biol*. (2020) 16:e1008462. doi: 10.1371/journal.pcbi.1008462

115. Przedborski M, Smalley M, Thiyagarajan S, Goldman A, Kohandel M. Systems biology informed neural networks (SBINN) predict response and novel combinations for PD-1 checkpoint blockade. *Commun Biol*. (2021) 4:877. doi: 10.1038/s42003-021-02393-7

116. Greene CS, Costello JC. Biologically informed neural networks predict drug responses. *Cancer Cell*. (2020) 38:613–5. doi: 10.1016/j.ccell.2020.10.014

117. Hackenberg M, Harms P, Pfaffenlehner M, Pechmann A, Kirschner J, Schmidt T, et al. Deep dynamic modeling with just two time points: Can we still allow for individual trajectories? *Biom J*. (2022) 64:1426–45. doi: 10.1002/bimj.202000366

118. Qian Z, Zame W, Fleuren L, Elbers P, van der Schaar M. Integrating expert ODEs into neural ODEs: pharmacology and disease progression. In: *Advances in Neural Information Processing Systems*, vol. 34. Curran Associates, Inc., Red Hook, New York, USA (2021). p. 11364–83.

119. Davidian M, Giltinan DM. Nonlinear models for repeated measurement data: An overview and update. *J Agric Biol Environ Stat*. (2003) 8:387–419. doi: 10.1198/1085711032697

120. Bonate PL, Vicini P. Preclinical pharmacokinetic–pharmacodynamic modeling and simulation in drug. In: *Preclinical Drug Development*. CRC Press, Boca Raton, Florida, USA (2010).

121. Ribba B, Holford N, Magni P, Trocóniz I, Gueorguieva I, Girard P, et al. A review of mixed-effects models of tumor growth and effects of anticancer drug treatment used in population analysis. *CPT Pharmacomet Syst Pharmacol*. (2014) 3:113. doi: 10.1038/psp.2014.12

122. Janssen JM, Verheijen RB, Van Duijl TT, Lin L, Van Den Heuvel MM, Beijnen JH, et al. Longitudinal nonlinear mixed effects modeling of EGFR mutations in ctDNA as predictor of disease progression in treatment of EGFR -mutant non-small cell lung cancer. *Clin Transl Sci*. (2022) 15:1916–25. doi: 10.1111/cts.13300

123. Bigarré C, Bertucci F, Finetti P, Macgrogan G, Muracciole X, Benzekry S. Mechanistic modeling of metastatic relapse in early breast cancer to investigate the biological impact of prognostic biomarkers. *Comput Methods Programs Biomed*. (2023) 231:107401. doi: 10.1016/j.cmpb.2023.107401

124. Lai TL, Shih M-C, Wong SP. A new approach to modeling covariate effects and individualization in population pharmacokinetics-pharmacodynamics. *J Pharmacokinet Pharmacodyn*. (2006) 33:49–74. doi: 10.1007/s10928-005-9000-2

125. Knights J, Chanda P, Sato Y, Kaniwa N, Saito Y, Ueno H, et al. Vertical integration of pharmacogenetics in population PK/PD modeling: A novel information theoretic method. *CPT Pharmacomet Syst Pharmacol*. (2013) 2:25. doi: 10.1038/psp.2012.25

126. Fox G, Glazier JA, Kadupitiya JCS, Jadhao V, Kim M, Qui, et al. (2019). Learning everywhere: pervasive machine learning for effective high-performance computation, in: *2019 IEEE International Parallel and Distributed Processing Symposium Workshops (IPDPSW)*, IEEE, New York, New York, USA. pp. 422–9. doi: 10.1109/IPDPSW.2019.00081

frontiers | Frontiers in Immunology

TYPE Original Research
PUBLISHED 18 April 2024
DOI 10.3389/fimmu.2024.1358478

OPEN ACCESS

EDITED BY
Heiko Enderling,
University of Texas MD Anderson Cancer Center, United States

REVIEWED BY
Jaya Lakshmi Thangaraj,
University of California, San Diego, United States
Thomas Pabst,
Bern University Hospital, Switzerland
Yang Zhang,
University of California, Irvine, United States

*CORRESPONDENCE
Vikram Adhikarla
vadhikarla@coh.org
Russell C. Rockne
rrockne@coh.org

RECEIVED 19 December 2023
ACCEPTED 21 March 2024
PUBLISHED 18 April 2024

CITATION
Adhikarla V, Awuah D, Caserta E, Minnix M, Kuznetsov M, Krishnan A, Wong JYC, Shively JE, Wang X, Pichiorri F and Rockne RC (2024) Designing combination therapies for cancer treatment: application of a mathematical framework combining CAR T-cell immunotherapy and targeted radionuclide therapy.
Front. Immunol. 15:1358478.
doi: 10.3389/fimmu.2024.1358478

Designing combination therapies for cancer treatment: application of a mathematical framework combining CAR T-cell immunotherapy and targeted radionuclide therapy

Vikram Adhikarla[1*], Dennis Awuah[2], Enrico Caserta[3], Megan Minnix[4], Maxim Kuznetsov[1], Amrita Krishnan[2], Jefferey Y. C. Wong[5], John E. Shively[4], Xiuli Wang[2], Flavia Pichiorri[3] and Russell C. Rockne[1*]

[1]Department of Computational and Quantitative Medicine, Beckman Research Institute, City of Hope National Medical Center, Duarte, CA, United States, [2]Department of Hematology and Hematopoietic Cell Transplantation, Beckman Research Institute, City of Hope National Medical Center, Duarte, CA, United States, [3]Department of Hematologic Malignancies Translational Science, Beckman Research Institute, City of Hope National Medical Center, Duarte, CA, United States, [4]Department of Molecular Imaging and Therapy, Beckman Research Institute, City of Hope National Medical Center, Duarte, CA, United States, [5]Department of Radiation Oncology, City of Hope National Medical Center, Duarte, CA, United States

Introduction: Cancer combination treatments involving immunotherapies with targeted radiation therapy are at the forefront of treating cancers. However, dosing and scheduling of these therapies pose a challenge. Mathematical models provide a unique way of optimizing these therapies.

Methods: Using a preclinical model of multiple myeloma as an example, we demonstrate the capability of a mathematical model to combine these therapies to achieve maximum response, defined as delay in tumor growth. Data from mice studies with targeted radionuclide therapy (TRT) and chimeric antigen receptor (CAR)-T cell monotherapies and combinations with different intervals between them was used to calibrate mathematical model parameters. The dependence of progression-free survival (PFS), overall survival (OS), and the time to minimum tumor burden on dosing and scheduling was evaluated. Different dosing and scheduling schemes were evaluated to maximize the PFS and optimize timings of TRT and CAR-T cell therapies.

Results: Therapy intervals that were too close or too far apart are shown to be detrimental to the therapeutic efficacy, as TRT too close to CAR-T cell therapy results in radiation related CAR-T cell killing while the therapies being too far apart result in tumor regrowth, negatively impacting tumor control and survival. We show that splitting a dose of TRT or CAR-T cells when administered in combination is advantageous only if the first therapy delivered can produce a significant benefit as a monotherapy.

Discussion: Mathematical models are crucial tools for optimizing the delivery of cancer combination therapy regimens with application along the lines of achieving cure, maximizing survival or minimizing toxicity.

KEYWORDS

radionuclide, combination therapy, myeloma, CAR T cells, daratumumab, mathematical model, targeted alpha therapy

1 Introduction

Chemotherapy and external beam radiation therapy have been traditional approaches for treating hematological malignancies. External beam radiation therapy has typically been employed for treatment of solitary plasmacytomas and as a palliative measure for more widespread disease (1, 2). The primary disadvantage of external beam radiotherapy is the toxicity to normal cells present near malignant cells in the bone marrow. Thus, its role has been limited in the treatment of hematological malignancies. In contrast, immunotherapy-based approaches have been employed in standard regimens and have led to significant improvements in patient disease remission (3). The dysregulation of the immune system in multiple myeloma (MM) and its targeting by immunotherapies has been a key reason for immunotherapy success (4). In particular, Chimeric Antigen Receptor T cells (CAR-T cells) have recently come to the fore due to their efficacy against several hematological malignancies including MM, leukemia and B-cell malignancies (5). CAR-T cells are T cells that have been engineered to target a receptor on the tumor cells thus binding them to tumor cells for direct effect. B-Cell Maturation Antigen (BCMA) targeting CAR-T cells have recently been approved by the FDA for treatment of MM (6). While these novel immunotherapies have created a significant impact, most patients still experience relapse, leading to unsuccessful treatment (7), supporting the need to develop novel combinatorial approaches for complete disease eradication.

Targeted radionuclide therapy (TRT) is a form of radiation therapy in which a radionuclide delivering radiation is attached to an agent that targets tumor cells (8). The advantage of TRT is that it is both highly targeted and delivered systemically. In addition, the radionuclide can be chosen with a half-life that is appropriate for balancing efficacy and toxicity of the treatment. For example, we have shown that the targeted alpha particle therapy (TAT) with ^{225}Ac conjugated to the CD38 receptor targeting antibody daratumumab demonstrated superior efficacy without added toxicity in treatment of disseminated multiple myeloma in a mouse model as compared to a beta particle emitter ^{177}Lu (9). The shorter range (< 100 μm) but higher potency (given by their high linear energy transfer) of alpha particles emitted from ^{225}Ac and its daughters was crucial in targeting the cancer cells but sparing the normal tissue cells in the bone marrow. While TAT was associated with increased survival, it alone did not result in curative responses. To address this limitation of radionuclide therapies, we and others (10–12) have investigated the addition of immune-based therapies to TRT as a potentially curative combination therapy approach.

Selecting the dosing, timing, and sequencing of any combination therapy approach experimentally is challenging due to the number of possible combinations to be tested; therefore a more efficient method of experimental design to achieve optimal therapy regimens is useful and increasingly becoming essential (13). Fortunately, mathematical models aided by experimental data exemplify a way for achieving optimal combination of therapies. Combining multiple therapies can result in synergistic, additive or antagonistic effects. Methods have been proposed to quantify (14, 15) and optimize (16–18) these effects. Combination therapy optimization using mathematical models can be performed at several levels depending on our knowledge of the system parameters (19). Many types of therapy combinations have been investigated using mathematical models (20). In particular, mathematical models of tumor-immune system dynamics have been proposed to optimize and personalize immunotherapies (21–23) either on their own or in combination with chemotherapy (24). Additionally, mathematical modeling of radiation therapy using the linear-quadratic model (25) to optimize patient-specific treatment regimens has been investigated for decades (26, 27). The proposed radiobiological models have been used to study both tumor and normal tissue radiation dose-response effects (28–30). The modeling efforts using radiobiological models and their variations span both external beam, brachytherapy as well as targeted radionuclide radiotherapies (30–35). Recognizing the synergy between immunotherapies and radiation therapy, mathematical models utilizing the external beam radiation therapy and immunotherapies have been proposed (36, 37) in order to tailor the dose of external beam radiation therapy to elicit systemic immune response as well as to study the effect of radiation therapy on different immune populations (38, 39).

We recently proposed a mathematical model for optimization of targeted radionuclide therapy with CAR-T cell therapy (40). The model considered the tumor response to targeted radionuclide and CAR-T cell therapies as monotherapies and preclinical data from each set of monotherapy experiments was used to characterize the model. Different timing schedules of TAT and CAR-T cell therapies were tested *in silico*, and it was shown that the timing between the two therapies for maximizing the survival metrics was highly dependent on the tumor proliferation rate. Elucidating the

mathematical parameters relevant for multiple therapies gives a novel way of investigating the dosing, timing, and the sequence of combination therapies and generate *in silico* therapeutic regimens that can then be tested *in vivo*.

Here we validate the mathematical model against experimental data where the timing of the CAR-T cell therapy is varied keeping the TAT dosage and timing constant. Model parameters are elucidated from the experimental data to optimize the timing of CAR-T cell therapy post-TAT by maximizing the progression-free survival. The effect of fractionated dosing of both TRT and CAR-T cell therapies on the survival metrics is also studied. In addition, multiple dosing strategies for TRT and CAR-T cell therapies are tested to analyze whether the splitting and scheduling of the doses result in improved tumor control or survival.

2 Methods

2.1 Mathematical model

The framework of the combined mathematical model for TRT and CAR T-cell therapy dynamics is given by the set of differential equations as described below (Figure 1) (40). This simplified model considers only the tumor cells, CAR-T cells, and action of the TRT.

$$\frac{dN_T}{dt} = \rho N_T - H(t-\tau_{TRT})k_{Rx_T}N_T - H(t-\tau_{CAR\ T})k_1 N_T N_C \quad (1)$$

$$\frac{dN_R}{dt} = H(t-\tau_{TRT})k_{Rx_T}N_T - H(t-\tau_{CAR\ T})k_1 N_R N_C - k_{cl}N_R \quad (2)$$

$$\frac{dN_C}{dt} = k_2(N_T+N_R)N_C - H(t-\tau_{TRT})k_{Rx_C}N_C - \theta N_C \quad (3)$$

$$k_{Rx_i} = \alpha_i R_0 e^{-\lambda(t-t_{TRT})} + \frac{2\beta_i R_0^2}{\gamma-\lambda}(e^{-2\lambda(t-t_{TRT})} - e^{-(\lambda+\gamma)(t-t_{TRT})})\gamma\lambda \quad (4)$$

Here, N_T and N_R represent the number of tumor cells that are unirradiated and irradiated respectively. N_C represents the number of CAR-T cells in the system, and k_1 and k_2 represent the killing rate of tumor cells by CAR-T cells and the proliferation/exhaustion rate of CAR-T cells respectively. θ and k_{cl} are the clearance rates of CAR-T cells and irradiated tumor cells from the system. t_{TRT} and t_{CART} are the time points at which TRT and CAR-T therapy are given via a Heaviside function H(t). The parameters α and β are radiobiological constants from the linear-quadratic model with $\beta = 0$ for high linear energy transfer alpha particle-based therapy. The parameter R_0 is the initial dose rate given as $R_0 = \eta A_{inj}$, where A_{inj} is the injected radioactivity. Parameters, values, and units are given in Table 1. The immune system as well as other populations of normal cells are not considered in this simplified model. The subscript *i* in equation (4) indicates the type of cell population which can either be T for tumor or C for CAR-T cells.

2.2 Experimental data

To benchmark the model and to optimize the timing of CAR-T and TRT therapies, data on monotherapies of TRT using ^{225}Ac-daratumumab targeting CD38 receptor and CAR-T cells targeting CS1 receptor as well as combination of these therapies was analyzed (11). Briefly, NOD.Cg-Prkdcscid Il2rgtm1Wjl/SzJ mice (NSG; 6–10 weeks old; Jackson Laboratory) (IACUC 21034) were engrafted with 5×10^6 MM.1S eGFP-ffluc lines intravenously (I.V.) and randomized into groups 6 days post tumor injection (day 6), based on bioluminescence imaging (BLI). All mice were followed weekly over the course of therapy using BLI to measure tumor burden. Day 0 was taken as the day MM.1S cells were inoculated in the mice. Six groups of mice (n = 8 each except CAR-T only group) with multiple myeloma are considered: *(a)* Untreated mice serving as controls (Group-0) *(b)* TRT (day 7) only post tumor inoculation (Group-T7) *(c)* TRT (day 7) and CAR-T cells (day 18) (Group-T7C18) *(d)* TRT(d7) and CAR-T cells (d25) (Group-T7C25) *(e)* TRT (d7) + CAR-T (d32) (Group-T7C32) and *(f)* CAR-T cell monotherapy administered on day 7 (n = 7) (Group-C7). For groups c, d, and e, the CAR-T cell doses were planned to be administered on day 14, 21, and 28 respectively. However, due to

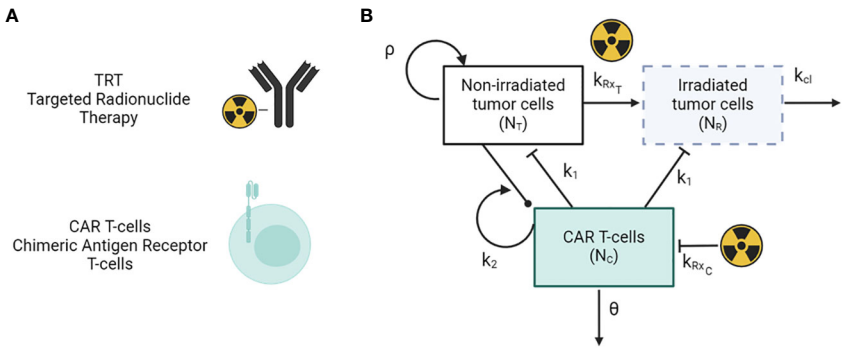

FIGURE 1
(A) Antibody-based TRT and CAR T-cells therapy modalities. **(B)** Schematic of the mathematical model of TRT and CAR-T cell therapy.

10.3389/fimmu.2024.1358478

TABLE 1 Constants and global parameters for the mathematical model estimated from experimental data.

Parameter	Symbol	Value	Comments
Effective decay constant (1/day)	λ	0.07	Accounts for biological clearance and physical decay
Tumor proliferation rate (1/day)	ρ	0.208	Global parameter set optimized value
Clearance rate of irradiated tumor cells (1/day)	k_{cl}	0.45	Global parameter set optimized value
CAR-T cell killing rate (1/day/cell)	k_1	$3.01x10^{-7}$	Optimized from data
CAR-T cell proliferation/ exhaustion rate (1/day/cell)	k_2	2.34×10^{-14}	Global optimized and kept as constant for individual mice
CAR-T cell death rate (1/day)	θ	0.035	Global parameter set optimized value
Tumor cell radiosensitivity (1/Gy) *	α_T	1.43	Global parameter set optimized value
CAR-T cell radiosensitivity (1/Gy) *	α_C	1.01	Global optimized and kept as constant for individual mice
Activity to dose conversion factor (Gy/day/μCi)	η	1.44	Global optimized and kept as constant for individual mice

*Note that the radiosensitivity coefficients incorporate the effect of the radiobiological effectiveness of high linear-energy transfer radiation as is the case in ^{225}Ac alpha particle therapy.

experimental logistical considerations, the actual dates of administration were 18, 25, and 32 respectively. BLI images and raw data can be found in the experimental publication (11).

2.3 Benchmarking model parameters

The tumor proliferation rate ρ was calculated from untreated control tumor data by fitting an exponential function to the individual mice tumor burden trajectories over time as measured with BLI (Supplementary Figure 1). The average BLI measurement on day 7 post inoculation and the average proliferation rate ρ across all untreated mice was then used to back calculate what the BLI would have been on day 0 based on the exponential tumor growth formalism. A single BLI to tumor cell conversion factor was then calculated by taking the ratio of BLI flux on day 0 and the number of injected MM.1S cells. For the treated groups, the following parameters and quantities were held constant based on the experimental conditions: CAR-T cell dose (N_{C0}), injected radioactivity (A_0), effective TRT decay rate (λ), and initial tumor burden ($N_T(t = 0)$). Other parameters (ρ, η, α_T, α_C, k_1, k_2, θ and k_{cl}) were allowed to vary and were optimized simultaneously for all cohorts yielding a single parameter set for all mice. This approach identifies parameters for CAR-T cell and tumor cell radiosensitivity, tumor proliferation, CAR-T cell and TRT killing rate and TRT clearance that are specific to the MM.1S myeloma cell line, the CS1 CAR T-cells and the ^{225}Ac-daratumamab therapies across treatment groups. The parameter set that is common and shared across treatment groups for all mice is referred to henceforth as the global parameter set.

Once the global parameter set for TRT and CAR-T cells therapy was calculated as above, these parameter values were set as initial conditions for individual mice to allow for individual mice variations across the parameter set. Thus, mice-specific parameters were calculated by allowing the individual parameters to vary by +/- 50% from the global parameter values. Mice-specific parameters included: ρ, α_T, k_1, θ and k_{cl}. For individual mice data optimization, η, α_C, and k_2 were held constant to the global parameter set.

2.4 Optimizing single administration of CAR-T therapy with respect to TRT and influence of therapy interval on model parameters

The benchmarked global parameter set was used to test the optimal timing of CAR-T cell therapy post TRT. With TRT injection on day 7 after MM.1S cell inoculation, the time of CAR-T cell delivery was varied from day 8 (following day administration) until day 50 (43 days following TRT). Progression free survival (PFS) was calculated for each scenario. Progression-free survival was defined as the amount of time from the start of TRT for the tumor burden to attain the same size as at the start of treatment. If no reduction in tumor burden was observed, the PFS was set to zero days. CAR-T cell therapy timing that maximized the PFS was taken as the optimal therapy timing.

The influence of variation in individual model parameters on the optimal timing of CAR-T cell therapy after TRT was tested. For this purpose, the parameter set obtained from fitting the model to individual mice tumor trajectories (with 50% uncertainty from global parameter set) was used. The minimum and maximum values of the individual parameters were calculated from this parameter set and a new synthetic parameter set was created with parameters randomly and uniformly generated between these limits. Using this synthetic parameter set, the range of CAR-T injection days that resulted in the maximum PFS was calculated. In this manner, 1000 synthetic parameter sets were generated by sampling the parameters 1000 times. The resulting histogram of CAR-T injection days for maximum PFS was generated by summarizing the data from all 1000 simulations. For visualization purposes, the dependence of PFS on TRT to CAR-T therapy interval for five synthetic parameter set runs is shown and a histogram of CAR-T infusion days that maximized the PFS for each of these 5 parameter sets is shown. Similar analysis was done

for parametric variation with 10% and 30% uncertainty (Supplementary Figure 3).

2.5 Impact of TRT and CAR-T cell therapy dosing and scheduling on survival metrics

Both TRT and CAR-T cell doses were varied between 20% of the experimental dose to 200% of the experimental dose. For TRT this range was 1.48 to 14.8 kBq and for CAR-T cells it was from 0.2 to 2 million cells. Both therapies were simulated with the model as monotherapies *in silico* to evaluate the impact of therapy dose on the time to minimum tumor burden (t_{min}), the progression free survival and the overall survival (OS). Overall survival was defined to be the time interval between the tumor cell injection and the time at which the number of tumor cells reaches 10^{11}. The minimum dose demonstrating an advantage in PFS was noted. Time to minimum tumor burden (t_{min}) is defined as time difference between the start of the first treatment and the day of the minimum tumor burden. If no reduction in tumor was observed t_{min} was set to zero. The impact of two doses of TRT or two doses of CAR-T therapy were tested. Mathematically, this is done by adding the second TRT or CAR-T therapy term to Equations (1) through Equation (4). For TRT, two doses of 3.7 kBq each were simulated with variable timing between them. For the CAR-T cell therapy, two doses of 0.5 million cells with variable timing between them were simulated. Minimum therapy interval demonstrating an advantage in PFS was noted.

2.6 Optimizing multiple administrations of CAR-T and TRT treatments

Based on the evaluation of tumor burden at different CAR-T and TRT dose levels, a multiple administration dosing scheme was created. A single dose of 7.4 kBq of TRT was administered for maximum efficacy while two separate doses of 1 million CAR-T cells each were administered. The therapies were administered *in silico* in an alternating fashion with the TRT dose given in between two CAR-T doses. While other regimens can also be explored, we tested this dosing scheme here.

Based on the above dosing schemes, a strategy for maximizing PFS was tested. First, CAR-T cell therapy (1 million cells – dose 1) was given on day 7. The timing of sequential TRT (7.4 kBq) and the subsequent CAR-T cell therapy (1 million cells – dose 2) was varied. Tumor burden, PFS and OS were calculated for each of the simulated therapeutic scenarios. To test the effect of model parameter variability on the optimal timing of the doses, the parameter limits from individual mice fits with 30% variation from baseline parameters are used to randomly generate 100 synthetic parameter sets, which was observed to sufficiently characterize the distribution. For visualization, two synthetic parameter sets are simulated and creation of histograms demonstrating the range of TRT and CAR-T therapy timings that yielded the highest PFS are shown.

3 Results

3.1 Benchmarking model parameter set for individual mice

Due to the variability in response among mice within a treatment group, we fit the model to each mouse tumor growth curve, allowing 50% variation in the parameters from the global parameter set (Figures 2A–E). PFS for each group (Figure 2F) show that treatment group with TRT dose on day 7 and CAR-T cell dose on day 25 resulted in the greatest PFS. Large uncertainty in PFS was found for treatment with TRT on day 7 and CAR-T cell therapy on day 32, suggesting that the overall efficacy of the combination therapy decreases and becomes highly uncertain if the interval between therapies is too long. Analogous to Figure 2, the model-data fit using global parameters is provided in the supplement (Supplementary Figure 2).

3.2 Optimizing single administration of CAR-T therapy with respect to TRT and influence of therapy interval on model parameters

The global parameter set was used to simulate variable CAR-T therapy intervals post-TRT. Temporal dynamics of tumor and CAR-T cell numbers are shown in Figure 3A. PFS curves from 5 synthetic parameter sets (including the benchmarked one in black) are shown in Figure 3B. There is a range of therapy intervals for which the PFS is maximum (black arrow). The CAR-T cell administration day that yielded the maximum PFS for each of these curves is plotted (Figure 3C). The procedure for generation of histogram of optimal CAR-T cell therapy administration day for maximizing PFS using these 5 synthetic datasets is also shown. The histogram created from 1000 synthetic parameter sets shows a well-defined peak at day 27-28 post-tumor inoculation (Figure 3D) indicating this to be the CAR-T cell therapy administration day for maximizing PFS. The synthetic parameter sets used for the results shown incorporate 50% variability from the global parameter set. Similar results are obtained with 10% or 30% uncertainty in parameters (Supplementary Figure 3).

Figure 3E shows the parameter variation between groups. α_T is seen to be increasing with increased interval between therapies – indicating that more of the tumor reduction is due to TRT rather than CAR-T. Thus, the group-specific parameters show that the effectiveness of CAR-T therapy is lower with increased intervals between the therapy. Similarly, the value of k_1 (CAR-T cell killing rate) is lower and θ (CAR-T cell persistence) is higher indicating again the reduced effectiveness of CAR-T cell therapy. These results can potentially point to a changing landscape of tumor cell mutations with increased tumor burden. This reduced effectiveness of CAR-T cell therapy with increased therapy interval is not captured with the overall survival metric obtained from the model.

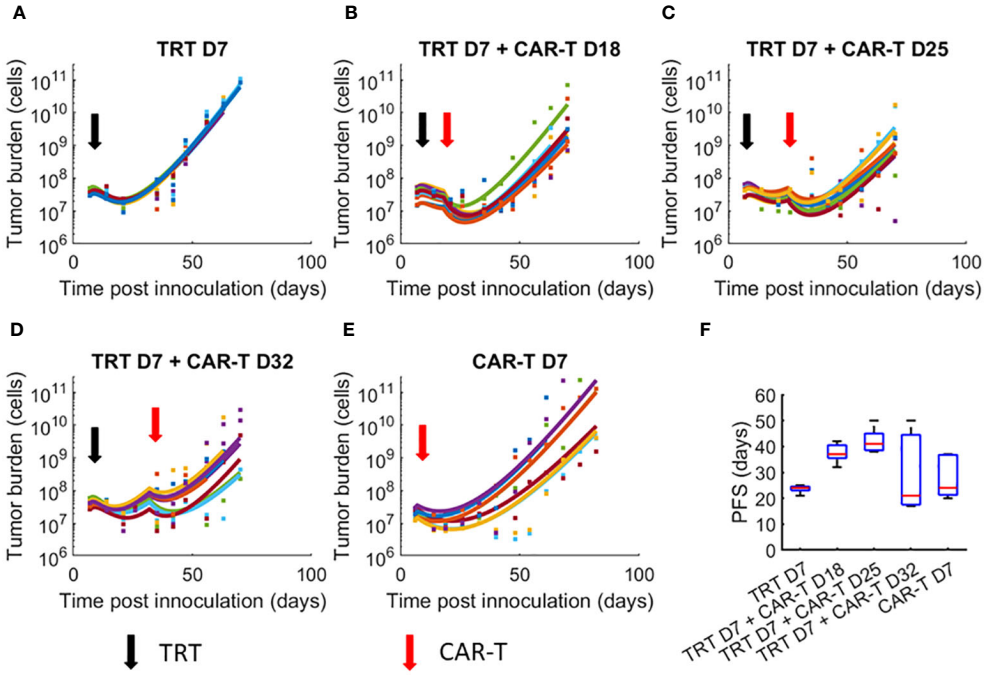

FIGURE 2
Dynamics of tumor growth in response to TRT and CAR-T combination therapies. Datapoints show the tumor cell numbers calculated from the experimental BLI data while the curves show the model fits to data. Individual mice parameters were limited to ±50% of the parameters obtained from the global parameter set. **(A)** TRT D7 only **(B)** TRT D7 + CAR-T cell D18 therapy. **(C)** TRT D7 + CAR-T cell D25 therapy. **(D)** TRT D7 + CAR-T cell D32 therapy. **(E)** CAR-T cell D7 therapy. **(F)** PFS obtained for each treatment group. The TRT D7 + CAR-T cells D25 therapy group demonstrated the highest PFS.

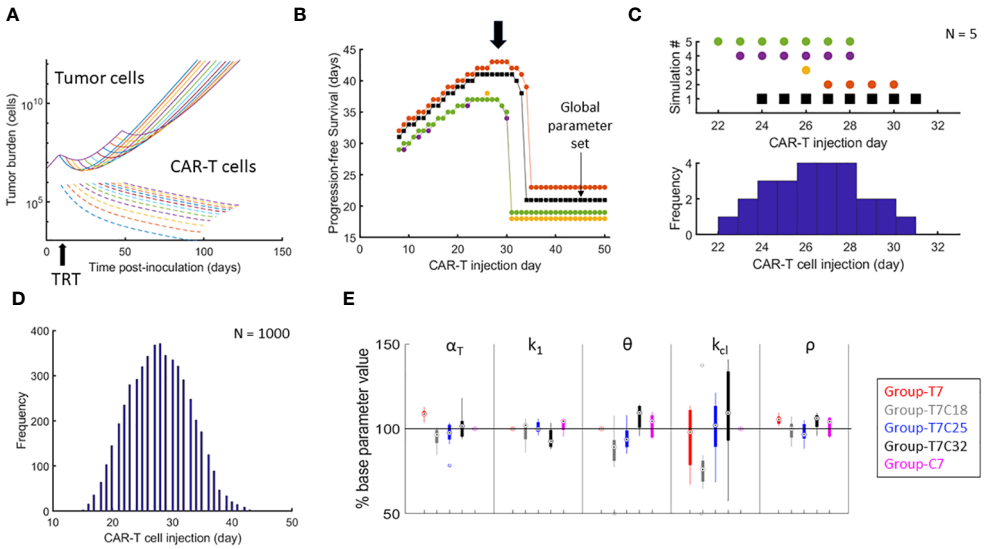

FIGURE 3
Optimizing the timing of CAR-T cell therapy after TRT and parametric variations attributed to treatment intervals. **(A)** Temporal development of tumor and CAR-T cells based on the global parameter set with TRT administered on day 7 and CAR-T cell therapy administered on one of the days from day 8 to day 50. **(B)** PFS calculated from day of TRT. Results of 5 synthetic parameter set runs are shown with global parameter set in black. For the global parameter set, maximum PFS is observed when CAR-T cells are delivered between day 25 and 34. Note that there is a range of CAR-T cell administration dates that yield highest PFS (black arrow). **(C)** The day when the PFS was maximum for each simulation run from B is shown along with the corresponding histogram demonstrating how the variability in parameters between different simulation runs impacts the variability in day of optimal CAR-T cell infusion. **(D)** Histogram showing the range of CAR-T injection days for which the maximum PFS was found with 1000 synthetic parameter set simulations. CAR-T cells infused on day 27 on average had the highest probability of maximizing PFS. **(E)** Distributions of model parameters for individual mice tumor growth curves are shown with parameters limited to ±50% of the parameters obtained from the benchmarked parameter set for (1) d7 TRT only (2) d7 TRT + d18 CAR-T cell therapy. (3) d7 TRT + d25 CAR-T cell therapy. (4) d7 TRT + d32 CAR-T cell therapy. (5) CAR-T cell monotherapy.

3.3 Impact of TRT and CAR-T cell therapy dosing and scheduling on survival metrics

Figures 4A, B show the impact of reduction in injected radioactivity on tumor burden and survival metrics. Figures 4C, D show the analogous impact of dose reduction in CAR-T cell numbers. In both cases, no reduction in PFS is observed below a certain dose level (about 6.3 kBq for TRT and 0.7 million cells for CAR-T cells). Doses below this level only result in slowing down of the disease burden. Overall survival is seen to linearly increase with increasing dose indicating the dose proportional gain in survival time.

Reducing the TRT dose (Figure 4F) of the first cycle to 3.7 kBq does not give an advantage in the PFS indicating that a critical dose is required initially for a multiple dose cycle. The highest PFS is found when the entire 7.4 kBq dose is delivered on day 7. Thus the 7.4 kBq dose that has been used in the experimental group is used for further simulations and the TRT dose is not split into two. Similar effects were observed when a 1 million CAR-T cell dose is split into two.

The impact of splitting TRT and CAR-T doses and varying the interval between these doses is shown (Figures 4E–H). At 3.7 kBq per TRT dose and 0.5 million cells per CAR-T dose, the second dose does not show improved PFS if it is administered after 5 days (after day 12) after the first dose (on day 7). The dependence of overall survival on therapy interval is seen to be low, with OS comparable across different therapy timing. However, this metric does not capture the parametric changes that happen when therapy interval is decreased (Figure 4D).

3.4 Optimizing multiple administrations of CAR-T and TRT treatments

After the first dose of CAR-T cell therapy, the timing of the following dose of TRT and CAR-T cell therapy needs to be optimized to yield maximum PFS (Figure 5A). If any of the therapies are given too close to each other, the resulting death of CAR-T cells due to radiation results in lower PFS. Similarly, having the therapies spaced too far apart can also result in lower PFS due to loss of benefit of the combination. The maximum PFS is observed when timing the second therapy close to the point when the tumor volume returns to the baseline. The creation of histograms for TRT and CAR-T therapies administration days that yielded the maximum PFS is shown (Figure 5B) using two synthetic parameter sets as examples. The procedure is analogous to the histogram creation in Figure 3C except that here there are two therapy sequence timings to be optimized (TRT and CAR-T dose 2) instead of one. Based on 100 synthetic parameter set simulations (Figure 5C) the maximum PFS is seen when TRT is delivered on day 33 and dose 2 of CAR-T cell therapy is given on day 56.

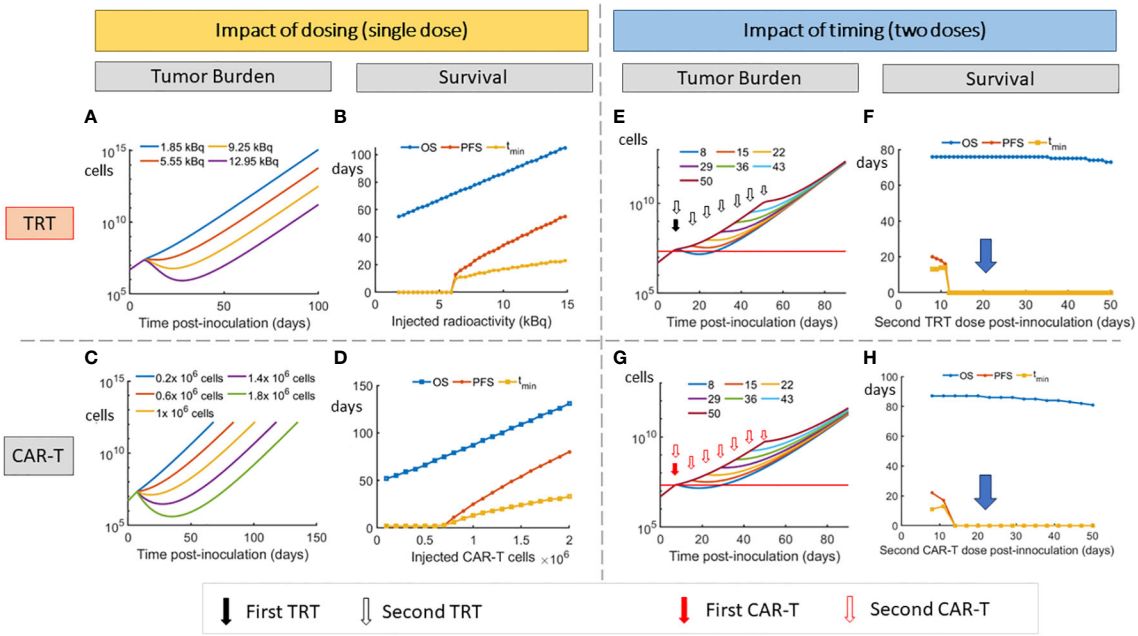

FIGURE 4
Impact of dosing and scheduling of TRT and CAR-T cell therapies on tumor burden and survival. Impact of TRT dose on **(A)** tumor volume and **(B)** Survival metrics. Impact of CAR-T cell therapy dose on **(C)** tumor volume and **(D)** Survival metrics. A threshold of approximately 6.3 kBq for TRT and 0.7 million CAR-T cells is required to observe an increase in PFS. Impact of timing of second dose of TRT on tumor burden **(E)** and survival **(F)**. Impact of timing of second dose of CAR-T cell therapy on tumor burden **(G)** and Survival **(H)**. When splitting the doses, the TRT dose was 3.7 kBq while CAR-T cell dose was 0.5 million cells for each administration. At these doses, the second dose needs to be given before day 12 for either TRT or CAR-T therapy to note any advantage in PFS. The model predicts that 7.4 kBq single dose or 1 million CAR-T cell dose that are split into two doses have a minimal effect on survival (D,E blue arrow).

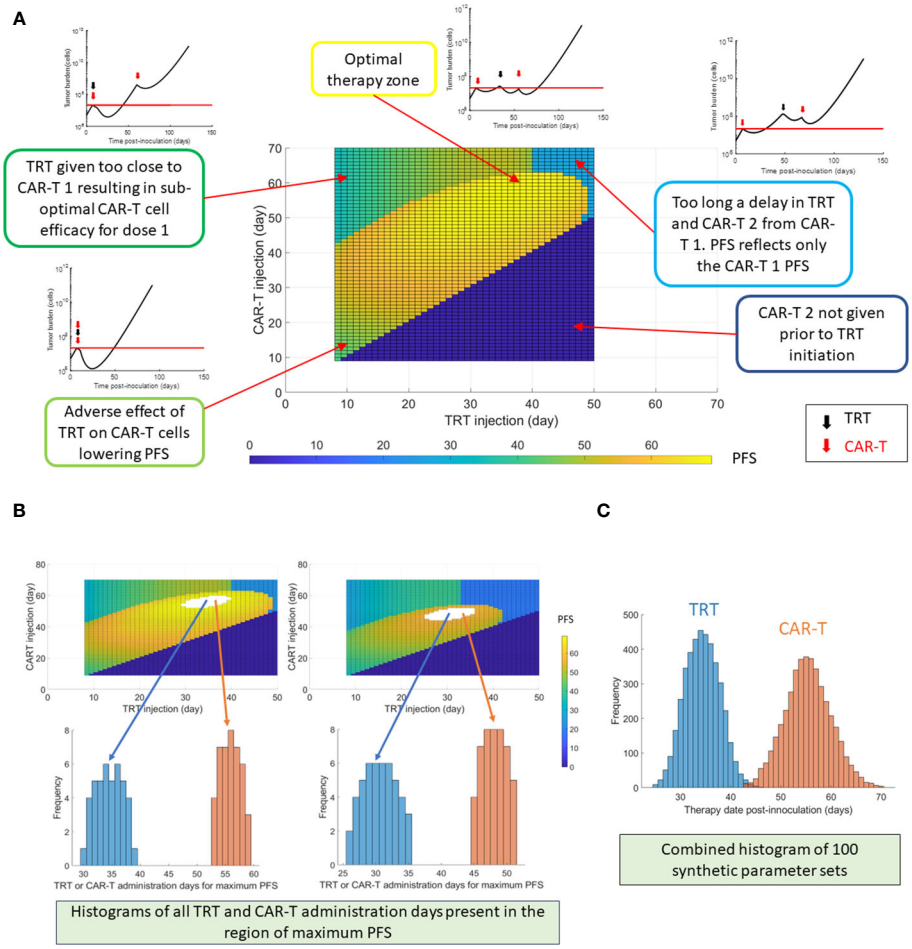

FIGURE 5
Optimization of multiple dosing schedules. The timing of the following sequential therapies was optimized: CAR-T cell therapy (dose 1 always on day 7) + TRT + CAR-T cell therapy repeated dose (dose 2), by maximizing the PFS. **(A)** Progression-free survival (PFS) shown as a function of TRT and CAR-T dose timings following the first CAR-T dose given on day 7. The tumor burden curves corresponding to different zones of the PFS map are also shown. **(B)** Example histogram creation of TRT and CAR-T cell dose timings that yielded the highest PFS based on two synthetic parameter sets. It should be noted that combination of both TRT and CAR-T therapy timings contribute to maximizing the PFS. The TRT and CAR-T histograms cannot be viewed in isolation. **(C)** TRT and CAR-T histograms created using 100 synthetic parameter sets generated within 30% uncertainty from global parameter set. Of these 100 synthetic parameter set simulations, maximum PFS was found roughly 400 times when the TRT injection was delivered on day 33 and CAR-T cells were infused on day 56. For each parameter set simulation, a PFS map as in **(A)** is observed – thus there are multiple CAR-T and TRT administration days that yield highest PFS.

4 Discussion

In this work we show a modeling framework of combined TRT and CAR-T cell therapy applied to experimental data. We have elucidated the parameters that are relevant for this combination in a murine model of multiple myeloma. We show that splitting of therapy doses is advantageous only if the first therapy can produce a significant benefit on its own. The model provides a quantitative framework to optimize the dosing of immunotherapies and targeted radionuclide therapies.

We optimized the TAT and CAR-T model parameters such that a single parameter set with 50% uncertainty can explain the differences in the tumor burden curves between individual mice. Such an approach can facilitate *in silico* optimization of the two therapies, where a single parameter set is associated with each of the therapies. While the introduction of uncertainties in the parameters results in better individual tumor curve fits, more information about CAR-T cell dynamics within the system can be highly informative regarding the model parameters. In particular, the value of CAR-T cell proliferation (k_2) was predicted to be small relative to other rate constants.

The optimized value of tumor proliferation rate ($\rho = 0.21$ day^{-1}) is smaller than the one calculated from untreated controls ($\rho = 0.27$ day^{-1}) which is used for BLI to tumor cell number conversion. There can be two reasons for this. First, the long-term growth of the tumor burden could be sigmoidal in nature instead of exponential as assumed in the model resulting in slowing down of the tumor growth at later stages as compared to the initial stages. Secondly, it could be that the post-treatment phenotype of the tumor cells could be more resistant and could grow slower in comparison to the pre-treatment phenotype. Such a scenario would also support the reduced effectiveness of CAR-T cell therapy when the interval between the therapies is increased

(Figure 3E). The resistance of tumor cell population to therapy can be mitigated by combination therapy approaches targeting two different types of treatment sensitivities. Gatenby et al. (41) introduced the ecological evolutionary dynamics concept of 'first strike-second strike' approach (42) to strategically sequence therapies for tumor cure. The first strike reduces the size and heterogeneity of the tumor cell population while the second strike(s) pushes the population below a critical threshold that eventually results in tumor cell eradication. Relevant to the combinations used in this work, radiation therapy could be considered the tumor debulking treatment prior to CAR-T cell therapy (43).

Based on the mathematical model, it might be feasible to delay the delivery of the CAR-T cell dose post-TRT (CAR-T cells on day 25 *vs* 32), since the overall survival might increase. However, it comes at the cost of higher uncertainty in the PFS indicating that other factors that are not captured in the model might influence tumor growth that might let it escape treatment. Notably, the parameter evaluation for TRT + d32 CAR-T cell treatment indicates lower efficacy of CAR-T cells compared to other treatment combinations. This increased therapy interval can also potentially increase the mutational burden of the tumor and might lead to reduced therapy effectiveness.

In the current work, the optimization of multiple therapy combinations is done with the goal of maximizing PFS. Another strategy could be minimizing the tumor burden with the goal of curative response. For different therapy regimens, it could be tested whether tumor burden predicted by the model would be low enough for cure in contrast to a strategy for maximizing PFS, thus giving the model the flexibility to test different scenarios.

The mice experiments used in this work have been performed on immunocompromised mice. Thus, the effect of radiation on stimulating immune system is not present in this mouse model. This data presents a cleaner model system for elucidating the effect of CAR-T cells on the tumor volume by eradicating the influence of other immune system components that can affect tumor volume. The impact of radiation on the immune system will need to be incorporated for optimizing therapeutic regimens in humans.

Biological variability in both preclinical and clinical realms is a determinant of heterogeneous response to therapies both in terms of efficacy and toxicity. To this end, the model assumes that a set of model parameters is shared between the mice in the same group, albeit with some uncertainty. Here we have chosen the model parameters within a group to vary by 50% from the group mean. This uncertainty level was chosen to capture expected variation in mice groups based on our previous experience (40); and is enough to demonstrate the differences in mean response to therapy between the groups while at the same time accommodating qualitatively reasonable fits to individual mice. In patients, the model can be personalized better by delivering multiple cycles of therapy and evaluating the patient response to individual doses to tailor the next dose or therapy sequence. To this end clinical trials evaluating targeted radionuclide therapy using ^{225}Ac-DOTA-Dara (Clinical trial identifier: NCT05363111) and CS1-CAR-T cell therapy (Clinical trial identifier: NCT03710421) as monotherapies in multiple myeloma patients are being evaluated to study patient response (toxicity and efficacy) to these agents. The combination of these therapies can bring synergistic effects and unique challenges. Radiation from TRT can give rise to non-specific immune response of CAR-T cells and might result in T-cell activation and priming. Abscopal effects of radiation that might be based on systemic responses can also result in increased efficacy compared to model predictions. A possible side effect especially relevant to targeted alpha particle therapies like ^{225}Ac is the impact of these agents on the tumor vasculature. Depending on the specific tumor, its vasculature and the radiation dose delivered, a complex non-linear relationship might exist for vasculature killing that might impact the delivery of subsequent therapies. Studying the spatio-temporal nature of tumor response to different doses while at the same time imaging the accumulation of these agents in tumors (as being done in the ^{225}Ac-Dara trial NCT05363111) can be key to develop more sophisticated mathematical models that can further optimize therapeutic regimen with targeted radionuclide therapies.

An obvious result is that higher dose of a therapy, the higher chance of cure; suggesting that the shorter the interval between two cycles of a therapy, the better the tumor reduction to the limit that CAR-T cells are not significantly damaged by the radiation. However, the interval between therapies cannot be shortened indefinitely. Reduced interval between TRT and CAR-T cell therapy results in death of CAR-T cells. On the other hand, reduced interval between two CAR-T cell doses or two TRT doses can be equivalent to a single high dose of that therapy. The radiation dose to organs at risk needs to be considered in a way that the rejuvenation of the organ at risk yields a therapeutic advantage when delivering a second cycle of the therapy. In the case of TAT, it could be the bone marrow while CAR-T cell toxicity can be in the form of cytokine release syndrome. Thus, a combination therapy where the two toxicity risks are unrelated to each other is seen to provide the best tumor control and delay tumor growth. Thus, the rationale for use of immunotherapies with TRT as part of a therapy regimen is strong and justifies its use for further investigation.

Data availability statement

The data generated in this work are available in the article and the Supplemental File. The BLI data associated with the work is provided as another supplementary file. The associated code for analysis can be found at https://github.com/cohmathonc/TRT-and-CAR-T-cell-combination-therapy.git.

Ethics statement

The animal study was approved by City of Hope Institutional Animal Care and Use Committee. The study was conducted in accordance with the local legislation and institutional requirements.

Author contributions

VA: Conceptualization, Formal analysis, Investigation, Methodology, Validation, Writing – original draft, Writing –

review & editing. DA: Data curation, Formal analysis, Investigation, Validation, Writing – review & editing. EC: Data curation, Formal analysis, Investigation, Validation, Writing – review & editing. MM: Data curation, Formal analysis, Investigation, Validation, Writing – review & editing. MK: Formal analysis, Validation, Writing – review & editing. AK: Formal analysis, Validation, Writing – review & editing. JW: Formal analysis, Validation, Writing – review & editing. JS: Formal analysis, Funding acquisition, Investigation, Project administration, Supervision, Validation, Writing – review & editing. XW: Formal analysis, Funding acquisition, Investigation, Project administration, Resources, Supervision, Validation, Writing – review & editing. FP: Formal analysis, Funding acquisition, Investigation, Project administration, Supervision, Validation, Writing – review & editing. RR: Conceptualization, Formal analysis, Funding acquisition, Investigation, Methodology, Project administration, Supervision, Validation, Writing – original draft, Writing – review & editing.

Funding

The author(s) declare financial support was received for the research, authorship, and/or publication of this article. This research was supported by the National Institutes of Health, National Cancer Institute R01-CA238429-01 (FP, JS, RR and XW). Research reported in this publication included work performed in the Analytical Cytometry, Small Animal Imaging and Biostatics and Mathematical Oncology Shared Resources supported by the National Cancer Institute of the National Institutes of Health under grant number P30CA033572. The content is solely the responsibility of the authors and does not necessarily represent the official views of the National Institutes of Health.

Conflict of interest

The authors declare that the research was conducted in the absence of any commercial or financial relationships that could be construed as a potential conflict of interest.

The author(s) declared that they were an editorial board member of Frontiers, at the time of submission. This had no impact on the peer review process and the final decision.

Publisher's note

Supplementary material

The Supplementary Material for this article can be found online at: https://www.frontiersin.org/articles/10.3389/fimmu.2024.1358478/full#supplementary-material

References

1. Talamo G, Dimaio C, Abbi KK, Pandey MK, Malysz J, Creer MH, et al. Current role of radiation therapy for multiple myeloma. *Front Oncol.* (2015) 5:40. doi: 10.3389/fonc.2015.00040

2. Tsang RW, Campbell BA, Goda JS, Kelsey CR, Kirova YM, Parikh RR, et al. Radiation therapy for solitary plasmacytoma and multiple myeloma: guidelines from the international lymphoma radiation oncology group. *Int J Radiat Oncol Biol Phys.* (2018) 101:794–808. doi: 10.1016/j.ijrobp.2018.05.009

3. Lanier OL, Perez-Herrero E, Andrea APD, Bahrami K, Lee E, Ward DM, et al. Immunotherapy approaches for hematological cancers. *iScience.* (2022) 25:105326. doi: 10.1016/j.isci.2022.105326

4. Russell BM, Avigan DE. Immune dysregulation in multiple myeloma: the current and future role of cell-based immunotherapy. *Int J Hematol.* (2023) 117:652–9. doi: 10.1007/s12185-023-03579-x

5. Teoh PJ, Chng WJ. CAR T-cell therapy in multiple myeloma: more room for improvement. *Blood Cancer J.* (2021) 11:84. doi: 10.1038/s41408-021-00469-5

6. Rendo MJ, Joseph JJ, Phan LM, DeStefano CB. CAR T-cell therapy for patients with multiple myeloma: current evidence and challenges. *Blood Lymphat Cancer.* (2022) 12:119–36. doi: 10.2147/BLCTT.S327016

7. "SEER*Explorer: An interactive website for SEER cancer statistics. Available online at: https://seer.cancer.gov/statistics-network/explorer/.

8. Sgouros G, Bodei L, McDevitt MR, Nedrow JR. Radiopharmaceutical therapy in cancer: clinical advances and challenges. *Nat Rev Drug Discovery.* (2020) 19:589–608. doi: 10.1038/s41573-020-0073-9

9. Minnix M, Adhikarla V, Caserta E, Poku E, Rockne R, Shively JE, et al. Comparison of CD38-Targeted alpha- Versus beta-Radionuclide Therapy of Disseminated Multiple Myeloma in an Animal Model. *J Nucl Med.* (2021) 62:795–801. doi: 10.2967/jnumed.120.251983

10. Zhang Z, Liu X, Chen D, Yu J. Radiotherapy combined with immunotherapy: the dawn of cancer treatment. *Signal Transduct Target Ther.* (2022) 7:258. doi: 10.1038/s41392-022-01102-y

11. Awuah D, Minnix M, Caserta E, Tandoh T, Adhikarla V, Poku E, et al. Sequential CAR T cell and targeted alpha immunotherapy in disseminated multiple myeloma. *Cancer Immunol Immunother.* (2023) 72:2841–9. doi: 10.1007/s00262-023-03461-z

12. Wang Y, Deng W, Li N, Neri S, Sharma A, Jiang W, et al. Combining immunotherapy and radiotherapy for cancer treatment: current challenges and future directions. *Front Pharmacol.* (2018) 9:185. doi: 10.3389/fphar.2018.00185

13. Ruiz-Cerda L, Asin-Prieto E, Parra-Guillen ZP, Troconiz IF. The long neglected player: modeling tumor uptake to guide optimal dosing. *Clin Cancer Res.* (2018) 24:3236–8. doi: 10.1158/1078-0432.CCR-18-0580

14. Chou TC. Drug combination studies and their synergy quantification using the Chou-Talalay method. *Cancer Res.* (2010) 70:440–6. doi: 10.1158/0008-5472.CAN-09-1947

15. Duarte D, Vale N. Evaluation of synergism in drug combinations and reference models for future orientations in oncology. *Curr Res Pharmacol Drug Discovery.* (2022) 3:100110. doi: 10.1016/j.crphar.2022.100110

16. Jonsson VD, Blakely CM, Lin L, Asthana S, Matni N, Olivas V, et al. Novel computational method for predicting polytherapy switching strategies to overcome tumor heterogeneity and evolution. *Sci Rep.* (2017) 7:44206. doi: 10.1038/srep44206

17. Bozic I, Reiter JG, Allen B, Antal T, Chatterjee K, Shah P, et al. Evolutionary dynamics of cancer in response to targeted combination therapy. *Elife.* (2013) 2:e00747. doi: 10.7554/eLife.00747

18. Poels KE, Schoenfeld AJ, Makhnin A, Tobi Y, Wang Y, Frisco-Cabanos H, et al. Identification of optimal dosing schedules of dacomitinib and osimertinib for a phase I/

II trial in advanced EGFR-mutant non-small cell lung cancer. *Nat Commun*. (2021) 12:3697. doi: 10.1038/s41467-021-23912-4

19. Day RS. Treatment sequencing, asymmetry, and uncertainty: protocol strategies for combination chemotherapy. *Cancer Res*. (1986) 46:3876–85.

20. Malinzi J, Basita KB, Padidar S, Adeola HA. Prospect for application of mathematical models in combination cancer treatments. *Inf Med Unlocked*. (2021) 23. doi: 10.1016/j.imu.2021.100534

21. Ribba B, Boetsch C, Nayak T, Grimm HP, Charo J, Evers S, et al. Prediction of the optimal dosing regimen using a mathematical model of tumor uptake for immunocytokine-based cancer immunotherapy. *Clin Cancer Res*. (2018) 24:3325–33. doi: 10.1158/1078-0432.CCR-17-2953

22. Butner JD, Dogra P, Chung C, Pasqualini R, Arap W, Lowengrub J, et al. Mathematical modeling of cancer immunotherapy for personalized clinical translation. *Nat Comput Sci*. (2022) 2:785–96. doi: 10.1038/s43588-022-00377-z

23. Sahoo P, Yang X, Abler D, Maestrini D, Adhikarla V, Frankhouser D, et al. Mathematical deconvolution of CAR T-cell proliferation and exhaustion from real-time killing assay data. *J R Soc Interface*. (2020) 17:20190734. doi: 10.1098/rsif.2019.0734

24. Piretto E, Delitala M, Ferraro M. How combination therapies shape drug resistance in heterogeneous tumoral populations. *Lett Biomathematics*. (2018) 5: S160–77. doi: 10.1080/23737867.2018.1465862

25. Douglas BG, Fowler JF. The effect of multiple small doses of x rays on skin reactions in the mouse and a basic interpretation. *Radiat Res*. (1976) 66:401–26. doi: 10.2307/3574407

26. Jones B, Dale RG. The evolution of practical radiobiological modelling. *Br J Radiol*. (2019) 92:20180097. doi: 10.1259/bjr.20180097

27. Niraula D, Cui S, Pakela J, Wei L, Luo Y, Ten Haken RK, et al. Current status and future developments in predicting outcomes in radiation oncology. *Br J Radiol*. (2022) 95:20220239. doi: 10.1259/bjr.20220239

28. Baumann M, Petersen C. TCP and NTCP: a basic introduction. *Rays*. (2005) 30:99–104.

29. Mesbahi A, Oladghaffari M. An overview on the clinical application of radiobiological modeling in radiation therapy of cancer. *Int J Radiol Radiat Ther*. (2017) 2(1):9–14. doi: 10.15406/IJRRT

30. Gong J, Dos Santos MM, Finlay C, Hillen T. Are more complicated tumour control probability models better? *Math Med Biol*. (2013) 30:1–19. doi: 10.1093/imammb/dqr023

31. Neira S, Gago-Arias A, Guiu-Souto J, Pardo-Montero J. A kinetic model of continuous radiation damage to populations of cells: comparison to the LQ model and application to molecular radiotherapy. *Phys Med Biol*. (2020) 65:245015. doi: 10.1088/1361-6560/aba21d

32. Sgouros G, Dewaraja YK, Escorcia F, Graves SA, Hope TA, Iravani A, et al. Tumor response to radiopharmaceutical therapies: the knowns and the unknowns. *J Nucl Med*. (2021) 62:12S–22S.

33. Macklis RM, Lin JY, Beresford B, Atcher RW, Hines JJ, Humm JL. Cellular kinetics, dosimetry, and radiobiology of alpha-particle radioimmunotherapy: induction of apoptosis. *Radiat Res*. (1992) 130:220–6. doi: 10.2307/3578279

34. Kuznetsov M, Kolobov A. Optimization of antitumor radiotherapy fractionation via mathematical modeling with account of 4 R's of radiobiology. *J Theor Biol*. (2023) 558:111371. doi: 10.1016/j.jtbi.2022.111371

35. Yonekura Y, Toki H, Watabe T, Kaneda-Nakashima K, Shirakami Y, Ooe K, et al. Mathematical model for evaluation of tumor response in targeted radionuclide therapy with (211)At using implanted mouse tumor. *Int J Mol Sci*. (2022) 23. doi: 10.3390/ijms232415966

36. Bekker RA, Kim S, Pilon-Thomas S, Enderling H. Mathematical modeling of radiotherapy and its impact on tumor interactions with the immune system. *Neoplasia*. (2022) 28:100796. doi: 10.1016/j.neo.2022.100796

37. Poleszczuk J, Enderling H. The optimal radiation dose to induce robust systemic anti-tumor immunity. *Int J Mol Sci*. (2018) 19(11):3377. doi: 10.20944/preprints201809.0230.v1

38. Sung W, Cho B. Modeling of radiation effects to immune system: a review. *J Korean Phys Soc*. (2022) 81:1013–9. doi: 10.1007/s40042-022-00574-z

39. Cho YB, Yoon N, Suh JH, Scott JG. Radio-immune response modelling for spatially fractionated radiotherapy. *Phys Med Biol*. (2023) 68. doi: 10.1101/2023.04.28.538767

40. Adhikarla V, Awuah D, Brummer AB, Caserta E, Krishnan A, Pichiorri F, et al. A mathematical modeling approach for targeted radionuclide and chimeric antigen receptor T cell combination therapy. *Cancers (Basel)*. (2021) 13. doi: 10.20944/preprints202109.0300.v1

41. Gatenby RA, Zhang J, Brown JS. First strike-second strike strategies in metastatic cancer: lessons from the evolutionary dynamics of extinction. *Cancer Res*. (2019) 79:3174–7. doi: 10.1158/0008-5472.CAN-19-0807

42. Raup D. Extinction: bad genes or bad luck? *New Sci*. (1991) 131:46–9.

43. Fang PQ, Gunther JR, Wu SY, Dabaja BS, Nastoupil LJ, Ahmed S, et al. Radiation and CAR T-cell therapy in lymphoma: future frontiers and potential opportunities for synergy. *Front Oncol*. (2021) 11:648655. doi: 10.3389/fonc.2021.648655

frontiers | Frontiers in Immunology

TYPE Original Research
PUBLISHED 07 May 2024
DOI 10.3389/fimmu.2024.1384509

OPEN ACCESS

EDITED BY
Heiko Enderling,
University of Texas MD Anderson Cancer Center, United States

REVIEWED BY
Noemi Picco,
Swansea University, United Kingdom
Jesse Kreger,
University of Southern California, United States

*CORRESPONDENCE
Tobias Idor Boklund
boklund@ruc.dk

†These authors have contributed equally to this work and share last authorship

RECEIVED 09 February 2024
ACCEPTED 27 March 2024
PUBLISHED 07 May 2024

CITATION
Boklund TI, Snyder J, Gudmand-Hoeyer J, Larsen MK, Knudsen TA, Eickhardt-Dalbøge CS, Skov V, Kjær L, Hasselbalch HC, Andersen M, Ottesen JT and Stiehl T (2024) Mathematical modelling of stem and progenitor cell dynamics during ruxolitinib treatment of patients with myeloproliferative neoplasms. *Front. Immunol.* 15:1384509. doi: 10.3389/fimmu.2024.1384509

Mathematical modelling of stem and progenitor cell dynamics during ruxolitinib treatment of patients with myeloproliferative neoplasms

Tobias Idor Boklund [1*], Jordan Snyder [1], Johanne Gudmand-Hoeyer [1], Morten Kranker Larsen [2], Trine Alma Knudsen [2], Christina Schjellerup Eickhardt-Dalbøge [2], Vibe Skov [2], Lasse Kjær [2], Hans C. Hasselbalch [2], Morten Andersen [1†], Johnny T. Ottesen [1†] and Thomas Stiehl [1,3†]

[1]Centre for Mathematical Modeling - Human Health and Disease, IMFUFA, Department of Science and Environment, Roskilde University, Roskilde, Denmark, [2]Department of Hematology, Zealand University Hospital, Roskilde, Denmark, [3]Institute for Computational Biomedicine and Disease Modeling, RWTH Aachen University, Aachen, Germany

Introduction: The Philadelphia chromosome-negative myeloproliferative neoplasms are a group of slowly progressing haematological malignancies primarily characterised by an overproduction of myeloid blood cells. Patients are treated with various drugs, including the JAK1/2 inhibitor ruxolitinib. Mathematical modelling can help propose and test hypotheses of how the treatment works.

Materials and methods: We present an extension of the Cancitis model, which describes the development of myeloproliferative neoplasms and their interactions with inflammation, that explicitly models progenitor cells and can account for treatment with ruxolitinib through effects on the malignant stem cell response to cytokine signalling and the death rate of malignant progenitor cells. The model has been fitted to individual patients' data for the *JAK2* V617F variant allele frequency from the COMFORT-II and RESPONSE studies for patients who had substantial reductions (20 percentage points or 90% of the baseline value) in their *JAK2* V617F variant allele frequency (n = 24 in total).

Results: The model fits very well to the patient data with an average root mean square error of 0.0249 (2.49%) when allowing ruxolitinib treatment to affect both malignant stem and progenitor cells. This average root mean square error is much lower than if allowing ruxolitinib treatment to affect only malignant stem or only malignant progenitor cells (average root mean square errors of 0.138 (13.8%) and 0.0874 (8.74%), respectively).

Discussion: Systematic simulation studies and fitting of the model to the patient data suggest that an initial reduction of the malignant cell burden followed by a monotonic increase can be recapitulated by the model assuming that ruxolitinib

10.3389/fimmu.2024.1384509

affects only the death rate of malignant progenitor cells. For patients exhibiting a long-term reduction of the malignant cells, the model predicts that ruxolitinib also affects stem cell parameters, such as the malignant stem cells' response to cytokine signalling.

KEYWORDS

mathematical modelling, ordinary differential equations, myeloproliferative neoplasms (MPN), parameter estimation, JAK2 V617F, ruxolitinib, blood cancer, stem cells

1 Introduction

The Philadelphia chromosome-negative myeloproliferative neoplasms (MPNs) are a group of slowly progressing haematological malignancies primarily characterised by an overproduction of myeloid blood cells (1). Without treatment, they result in severe complications such as thrombosis, bleeding, infections (1), bone marrow failure, and progression to acute myelogenous leukaemia (2). The three most common MPN subtypes, essential thrombocythaemia (ET), polycythaemia vera (PV), and primary myelofibrosis (PMF), are diagnosed according to World Health Organisation (WHO) and International Consensus Classification (ICC) criteria (3), including mutational status, elevation of different cell counts (red, white, and platelets), and bone marrow morphology. A frequent common factor for the 3 subtypes of MPNs is the driver mutation *JAK2* V617F (hereinafter referred to as just *JAK2*) which is present in approximately 55% of ET patients, 98% of PV patients and 60% of PMF patients (3). Other known driver mutations in MPNs are found in the genes *CALR* and *MPL*. A subset of patients with MPN carries none of these mutations, and these patients are referred to as being triple-negative (3). In the cases where a driver mutation is present, it results in overactivation of the JAK-signal transducer and STAT-signalling (4).

The hematopoietic system is responsible for the formation of blood cells. It consists of cells of different maturity levels, starting with the least mature haematopoietic stem cells (HSCs) in the bone marrow (5), continuing with the more mature so-called progenitor and precursor cells, and ending with the fully mature cells in the peripheral blood. All haematopoietic cells are derived from the HSCs. HSC proliferation needs to fulfil two roles: maintaining the HSC pool and producing more mature committed cells that will eventually become fully mature. The hematopoietic system is subjected to a complex regulatory network which adapts the production of mature cells to the current state of the organism. It is believed that MPNs develop from a single mutated stem cell that proliferates and slowly produces both mutated stem cells, mutated progenitors, and consequently also mutated mature cells (3). If this mutated stem cell and its offspring have a proliferative advantage over the wild type cells, the mutated clone will expand and potentially cause an MPN disease. It is estimated that the time from the acquisition of the mutation to MPN diagnosis is multiple decades (3, 4). Over even longer time scales, the mutated clone may outcompete and completely eradicate the wild type cells if not treated.

The most common treatments of patients with MPN are hydroxyurea, a cytoreductive treatment that helps control the number of blood cells (2), and interferon-α-2a, a cytokine which is mainly depleting the bone marrow of mutated stem cells by driving them to differentiate (6). In this work, we focus on modelling the treatment with another drug: ruxolitinib (RUX), a JAK1/2 inhibitor that works by targeting the JAK1 and JAK2 kinases (4, 7) (see section 2.1.3 for more details about modelling the effects of treatment with RUX). RUX is indicated for the treatment of disease related symptoms in myelofibrosis patients and in PV patients who are resistant or intolerant to hydroxyurea, but to our knowledge its effects on the abundance of mutated cells is not yet fully understood. Studies show that RUX reduces symptom burden, spleen size, and elevated blood cell counts, thereby increasing the quality of life of the treated patients (2, 8–11), and the drug also has anti-inflammatory effects (8, 9). Mouse studies suggest that RUX primarily targets progenitors and precursor cells (12). An *in vitro* study of another JAK inhibitor, AZD1480, shows that stem cells may escape the effects of JAK inhibition (9, 13). If stem cells also escape the effects of RUX, its effects alone are insufficient to cure the disease. To cure the patients, the mutated stem cells must be eradicated (9), or, given the slow growth of the clone, reduced significantly in number. Making measurements of stem cells is neither economically nor technically practical in a routine clinical setting, and therefore it is challenging to quantify the abundance of mutated cells in the stem cell population. Clinically, the *JAK2* variant allele frequency (VAF, also called the allele burden) in the peripheral blood is used to monitor treatment response and disease progression. In patients with MPN, both heterozygous and homozygous clones are observed with ET being characterised by heterozygosity and PV by homozygosity (14).

Thus, a VAF measurement of 50% could in principle mean that either 100% of cells carry a heterozygous mutation or that 50% of cells carry a homozygous mutation. In practice, a mixture of wild-type, homozygous, and heterozygous cells might be the most probable scenario. In the COMFORT-II study, the median reduction in *JAK2* VAF for 69 myelofibrosis patients during treatment with RUX was 7.0% (absolute), and 15 out of 69 had a reduction equal to or above 20% (absolute) after 48 weeks (11). In the RESPONSE study, among 104 *JAK2*-positive PV patients treated with RUX, a gradual response was seen in the mean *JAK2* VAF, and after 208 weeks the mean reduction was 40% (relative) (15).

Mechanistic mathematical modelling is a versatile tool to gain insight into complex biological processes based on limited data. Although stem cells are difficult to quantify, we can make inference about processes on the stem cell level using a mathematical model and measurements from peripheral blood. Mathematical modelling has for a long time been an important part of the study of cancers, haematopoiesis, and haematopoietic malignancies and has been employed to investigate questions such as stem cell and mature cell dynamics (16–20) and their role during disease and therapy (21), mutation acquisition and development (22, 23), clonal selection and architecture (24, 25), the role of inflammation in haematological malignancies (26–28), model-based prognostication (29, 30), therapy modelling (31, 32), and optimisation of therapy (33, 34). In this work, we extend a previous model of MPN disease dynamics and the role of inflammation in MPN, the Cancitis model (26, 28). Specifically, we extend the model by including the effects of RUX therapy in the model and by adding a progenitor compartment in the hopes of more accurately accounting for the effects of RUX on different cell types. The original Cancitis model has been successfully applied to data from patients with MPN and can capture key features of MPN progression and treatment with interferon-α-2a (31). Here we extend this work to model data from patients responding well to treatment with RUX.

The main objective of this work is to understand which effects of RUX treatment can explain sustained reductions in the *JAK2* VAF. In particular, we are interested in investigating whether such sustained patient responses are possible if RUX does not affect the stem cells at all, or if an effect on the stem cell level is the most straightforward explanation for the reduction observed in some patients. Determining whether or not RUX can affect and potentially eradicate the mutated stem cells is necessary to determine whether or not RUX monotherapy can potentially be a cure for MPN diseases and for predicting the patient response in case of treatment discontinuation. If the treatment does not affect the mutated stem cells, the effects of RUX are most probably palliative, and we expect that a patient discontinuing the treatment would show a disease progression. Mathematical modelling can help identify the impact of RUX on different cell types and predict patient responses to changes in the treatment schedule. A clear picture of the RUX mode of action is also important for understanding RUX's role in combination therapy. Currently, studies of combination therapy with interferon-α-2a and RUX show promising results (35). To fully understand the effects of such a combination treatment with possible synergies between the drugs, a natural starting point is understanding each drug's effects separately.

2 Materials and methods

The model is implemented in MATLAB version R2023b. A script simulating the model with and without treatment can be accessed on GitHub[1].

2.1 Mechanistic mathematical model of MPN disease progression and RUX treatment

2.1.1 Mechanistic mathematical model of MPN disease progression

We first describe the model of MPN cell dynamics in absence of treatment. The new model is a compartmental differential equation model with compartments for stem, progenitor, and mature blood cells for both healthy wild type cells and malignant cells carrying the *JAK2* mutation. In addition, there is a compartment of cellular debris from dead cells and a compartment of the cytokine signalling affecting the stem cells in the bone marrow. The compartments and their relations are depicted in Figure 1, an overview of the variables used is given in Table 1, and the equations used in the model are given in Equations (1) and (2).

In the model, stem cells are capable of self-renewing as well as differentiating into progenitor cells, and progenitor cells are again capable of self-renewing [although to a lesser degree than stem cells (38)] and differentiating into mature cells. The fraction of cell divisions resulting in daughter cells adopting the same fate as the parent cell is referred to as the self-renewal fraction (38, 39). Since in reality there are many stages of cell differentiation that we lump together into "progenitors", we include amplification factors from each maturity stage to the next. This is a well-established approach which has already been used in (16). Mature and progenitor cells can die. We assume that the death rate of stem cells is small enough as to be negligible, and therefore we exclude stem cell death from the model. We assume that the *JAK2* mutation can affect the rates of these processes, but not their kind. In other words, the wild type and malignant cell lineages are governed by the same key mechanisms, i.e. self-renewal, differentiation and death, and thus they obey equations of the same form but possibly with different parameter values.

Regulation of the haematopoietic system in our model occurs via a crowding effect on the stem cells (described in the model by the functions ϕ_x and ϕ_y) and feedback through cytokine signalling (described in the model by the variable s). The crowding effect, inspired by other modelling works (19, 20, 30, 40), models the competition for space in the stem cell niche in the bone marrow. If stem cells cannot reside in the stem cell niche, they lose stemness due to death or differentiation. In this model, this effect is described by the monotonically decreasing functions ϕ_x and ϕ_y in Equation (2) which are identical to the ones in (28). The cytokine feedback is modelled by saturating functions, in this case Michaelis-Menten

1 https://github.com/TobiasBoklund/Math_Modelling_of_RUX_Treatment_in_MPN.git.

10.3389/fimmu.2024.1384509

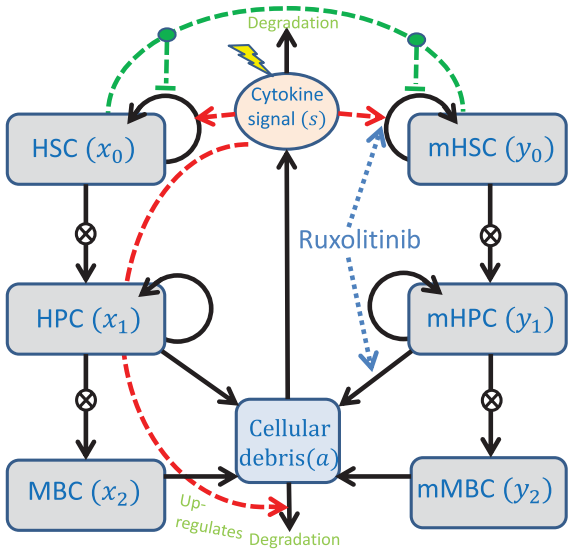

FIGURE 1
Conceptual compartment diagram of the model. See the text for further description of the model. The lightning symbol represents external factors affecting the cytokines. HSC, Haematopoietic stem cells; HPC, Haematopoietic progenitor cells; MBC, Mature blood cells; mHSC, Malignant haematopoietic stem cells; mHPC, Malignant haematopoietic progenitor cells; mMBC, Malignant mature blood cells.

TABLE 1 Overview of the variables used in the model.

Variable	Description	Expected maximal order of magnitude	Source
x_0	Number of haematopoietic stem cells (HSCs)	1.0×10^5	(36, 37)
x_1	Number of haematopoietic progenitor cells (HPCs)	2.5×10^6	(36)
x_2	Number of mature blood cells (MBCs)	6.4×10^{11}	(36)
y_0	Number of malignant haematopoietic stem cells (mHSCs)	1.7×10^5	Chosen
y_1	Number of malignant haematopoietic progenitor cells (mHPCs)	7.6×10^6	Chosen
y_2	Number of malignant mature blood cells (mMBCs)	2.7×10^{12}	Chosen
a	Cellular debris	1.7×10^3	Chosen and (28)
s	Cytokine signal	2.0	Chosen

See Equations (1) and (2) for the corresponding differential equation for each variable. All variables are considered to have unit 1, i.e. we provide total cell counts.

expressions, that up-regulate the self-renewal fraction of stem cells through the bone marrow microenvironment. The cytokine level is up-regulated by the amount of cellular debris, as well as by an external inflammatory load (representing, e.g., smoking or other illnesses). Debris from dead cells accumulate and is cleared at a rate proportional to the cytokine level. It is important to note that the cytokine level, s, is a lumped parameter that represents different feedbacks in the body, including the immune system's response to cell death (both at equilibrium and as a response to externally imposed cell death) and inflammation.

Using these assumptions, the differential equations describing the system are given by

$$\underbrace{\dot{x}_0}_{\text{rate of change of HSCs}} = \underbrace{\alpha_{x_0}}_{\text{proliferation rate}} \left(\underbrace{\overbrace{p_{x_0}}^{\text{max. self-renewal fraction}} \overbrace{\phi_x(x_0, y_0)}^{\text{crowding}} \overbrace{\frac{s}{s_{x_0} + s}}^{\text{cytokine signal}}}_{\text{self-renewal}} - \underbrace{\left(1 - p_{x_0} \phi_x(x_0, y_0) \frac{s}{s_{x_0} + s}\right)}_{\text{differentiation}} \right) x_0, \tag{1a}$$

$$\underbrace{\dot{x}_1}_{\text{rate of change of HPCs}} = \underbrace{\alpha_{x_1}}_{\text{proliferation rate}} \left(\underbrace{p_{x_1}}_{\text{self-renewal}} - \underbrace{(1 - p_{x_1})}_{\text{differentiation}} \right) x_1 + \underbrace{A_{x_0}}_{\text{amplification}} \underbrace{2\,\alpha_{x_0} \left(1 - p_{x_0} \phi_x(x_0, y_0) \frac{s}{s_{x_0} + s}\right) x_0}_{\text{influx from HSCs}} - \underbrace{d_{x_1}\, x_1}_{\text{death}}, \tag{1b}$$

$$\underbrace{\dot{x}_2}_{\text{rate of change of MBCs}} = \underbrace{A_{x_1}}_{\text{amplification}} \underbrace{2\,\alpha_{x_1}(1 - p_{x_1}) x_1}_{\text{influx from HPCs}} - \underbrace{d_{x_2}\, x_2}_{\text{death}}, \tag{1c}$$

$$\underbrace{\dot{y}_0}_{\text{rate of change of mHSCs}} = \underbrace{\alpha_{y_0}}_{\text{proliferation rate}} \left(\underbrace{\overbrace{p_{y0}}^{\text{max. self-renewal fraction}} \overbrace{\phi_y(x_0, y_0)}^{\text{crowding}} \overbrace{\frac{s}{s_{y_0} + s}}^{\text{cytokine signal}}}_{\text{self-renewal}} - \underbrace{\left(1 - p_{y_0} \phi_y(x_0, y_0) \frac{s}{s_{y_0} + s}\right)}_{\text{differentiation}} \right) y_0, \tag{1d}$$

$$\underbrace{\dot{y}_1}_{\text{rate of change of mHPCs}} = \underbrace{\alpha_{y_1}}_{\text{proliferation rate}} \left(\underbrace{p_{y_1}}_{\text{self-renewal}} - \underbrace{(1-p_{y_1})}_{\text{differentiation}} \right) y_1 + \underbrace{A_{y_0}}_{\text{amplification}} \underbrace{2\,\alpha_{y_0} \left(1 - p_{y_0}\,\phi_y(x_0,\, y_0)\,\frac{s}{s_{y_0}+s} \right) y_0}_{\text{influx from mHSCs}} - \underbrace{d_{y_1}\,y_1}_{\text{death}}, \tag{1e}$$

$$\underbrace{\dot{y}_2}_{\text{rate of change of mMBCs}} = \underbrace{A_{y_1}}_{\text{amplification}}\ \underbrace{2\,\alpha_{y_1}(1-p_{y_1})y_1}_{\text{influx from mHPCs}} - \underbrace{d_{y_2}\,y_2}_{\text{death}}, \tag{1f}$$

$$\underbrace{\dot{a}}_{\text{rate of change of debris}} = \underbrace{d_{x_1}\,x_1 + d_{y_1}y_1 + d_{x_2}x_2 + d_{y_2}y_2}_{\text{dead cells}} - \underbrace{e_a\,as}_{\text{degradation}}, \tag{1g}$$

$$\underbrace{\dot{s}}_{\text{rate of change of cytokine signal}} = \underbrace{r_s\,a}_{\text{production}} - \underbrace{e_s\,s}_{\text{degradation}} + \underbrace{I}_{\text{external factors}}, \tag{1h}$$

where ϕ_x and ϕ_y are given by

$$\underbrace{\phi_x\,(x_0,\, y_0)}_{\text{crowding function for HSCs}} = \frac{1}{1 + \underbrace{c_{xx}\,x_0}_{\text{inhibition by HSCs}} + \underbrace{c_{xy}\,y_0}_{\text{inhibition by mHSCs}}}, \tag{2a}$$

$$\underbrace{\phi_y\,(x_0,\, y_0)}_{\text{crowding function for mHSCs}} = \frac{1}{1 + \underbrace{c_{yx}\,x_0}_{\text{inhibition by HSCs}} + \underbrace{c_{yy}\,y_0}_{\text{inhibition by mHSCs}}}, \tag{2b}$$

An explanation of the sources, estimations, and choices of the default parameter values used in the model is given in section S1 of the supplementary. There, we also show a simple sensitivity analysis of the system. This shows that the model is most sensitive to changes in p_{x_0} and p_{y_0} followed by c_{xx}, c_{yx}, α_{y_0}, and s_{x_0}. These parameters are the most sensitive because they, except α_{y_0}, determine the self-renewal fraction of the healthy and the malignant stem cells, the products $p_{x_0}\,\phi_x(x_0,\, y_0)\frac{s}{s_{x_0}+s}$ and, $p_{y0}\phi_y(x_0,\, y_0)\frac{s}{s_{y_0}+s}$, respectively, and that the self-renewal fraction is the main contributor to the overall fitness of each of the cell lines (25). Analogous results have been reported for other models (20, 24, 29, 30). An overview of the parameter values used in this work can be found in Table 2. The model is designed to be generally applicable to patients with MPN, but due to biological variation the parameter values might vary from patient to patient. In this work, the parameter values used give a typical course of the disease. For future reference, we refer to s_{x_0} and s_{y_0} as the half-saturation constants of the healthy and malignant, respectively, stem cell response to cytokine signalling.

2.1.2 Steady states of the model

Next, we present the steady states of the model to illustrate the range of behaviours that can be captured by it. The steady states of the system in Equations (1) and (2) arise as solutions of complicated rational equations which we solve numerically. We define a biologically feasible steady state as a solution to the steady state problem in which all variables are real and non-negative. For the standard parameter values given in Table 2, there exist 12 possible steady states of which 5 are biologically feasible. The local stabilities of these steady states are calculated numerically using the eigenvalues of the corresponding Jacobian matrices, see Table 3. We denote a steady state without any cells as "trivial", a steady state with only healthy cells as "healthy", and a steady state with only malignant cells as "malignant".

From Table 3, we see that for the standard parameter values in Table 2, there exists a locally stable trivial steady state, two locally unstable healthy steady states, and both a locally stable and a locally unstable malignant steady state. Thus, two locally stable steady states exist: a trivial one and a malignant one. However, if one considers the case with 0 malignant cells, i.e. $y_0 = y_1 = y_2 = 0$ and then disregards the equations for these variables, only the trivial and the healthy steady states remain, and in this case the healthy steady state with 9.9×10^4 stem cells, for which the model was calibrated (see section S1 of the supplementary for more details), becomes locally stable. It may seem a bit counter-intuitive that the trivial steady state is locally stable both in the case with and without malignant cells present. However, numerical experiments show that for the case of only healthy cells being present, x_0, x_1, and x_2 should all be below 3.24% of their locally stable healthy steady state values for the system to approach the trivial steady state, and for the case of only malignant cells being present, y_0, y_1, and y_2 should all be below 0.10% of their locally stable malignant steady state values for the system to approach the trivial steady state. If this is not the case, the system approaches the locally stable healthy steady state and the locally stable malignant steady state, respectively. Thus, in conclusion, with the standard choice of parameters in Table 2, the system approaches the locally stable malignant steady state unless extremely few cells are present. In the case of only healthy cells being present, the system instead approaches the (in that case) locally stable healthy steady state.

TABLE 2 Parameter values for the model in Equations (1) and (2).

Parameter	Description	Value	Unit	Source
α_{x_0}	Proliferation rate of HSCs	3.6×10^{-3}	day^{-1}	(37, 41)
α_{y_0}	Proliferation rate of mHSCs	5.4×10^{-3}	day^{-1}	Estimated
p_{x_0}	Self-renewal fraction for HSCs	0.89	1	Estimated
p_{y_0}	Self-renewal fraction for mHSCs	0.97	1	Chosen
c_{xx}	Constant for HSCs inhibiting HSC self-renewal	5.6×10^{-6}	1	Estimated
c_{yx}	Constant for HSCs inhibiting mHSC self-renewal	5.2×10^{-6}	1	Estimated
c_{xy}	Constant for mHSCs inhibiting HSC self-renewal	5.4×10^{-6}	1	Estimated
c_{yy}	Constant for mHSCs inhibiting mHSC self-renewal	5.0×10^{-6}	1	Estimated
s_{x_0}	Half-saturation constant for cytokine signal for HSCs	1.4×10^{-1}	1	Chosen
s_{y_0}	Half-saturation constant for cytokine signal for mHSCs	7.1×10^{-2}	1	Chosen
A_{x_0}	Amplification factor from HSCs to HPCs	3.4×10^{1}	1	Estimated
A_{y_0}	Amplification factor from mHSCs to mHPCs	3.4×10^{1}	1	Estimated
α_{x_1}	Proliferation rate of HPCs	1.1×10^{-2}	day^{-1}	Chosen
α_{y_1}	Proliferation rate of mHPCs	1.7×10^{-2}	day^{-1}	Chosen
p_{x_1}	Self-renewal fraction for HPCs	0.445	1	Chosen
p_{y_1}	Self-renewal fraction for mHPCs	0.485	1	Chosen
d_{x_1}	Death rate of HPCs	3.7×10^{-3}	day^{-1}	Chosen
d_{y_1}	Death rate of mHPCs	3.7×10^{-3}	day^{-1}	Chosen
A_{x_1}	Amplification factor from HPCs to MBCs	3.2×10^{6}	1	Estimated
A_{y_1}	Amplification factor from mHPCs to mMBCs	3.2×10^{6}	1	Estimated
d_{x_2}	Death rate of MBCs	1.5×10^{-1}	day^{-1}	(36)
d_{y_2}	Death rate of mMBCs	1.5×10^{-1}	day^{-1}	(36)
e_a	Degradation rate for a	1.2×10^{8}	day^{-1}	Estimated
r_s	Production rate for s	8.6×10^{-2}	day^{-1}	(28)
e_s	Degradation rate for s	7.2×10^{1}	day^{-1}	Estimated
I	External up-regulation of s	2	day^{-1}	(28)

A unit of 1 means that the given parameter is dimensionless.

2.1.3 Modelling patient responses to treatment with ruxolitinib

Now, we discuss how the effects of RUX can be accounted for in the model. RUX is a non-specific JAK1/2 inhibitor that targets the JAK1 and JAK2 kinases (7), and it has multiple effects on patients with MPN. In the following, we investigate potential effects of RUX on mutated cells. As a readout for therapy effects, we use the *JAK2* VAF. Studies have shown that RUX treatment reduces blood cell counts both in mice (12) and in humans (2, 8, 11). In mice, RUX is unable to target the mutated disease-initiating stem cells, but it

TABLE 3 Biologically feasible steady states for the model in Equations (1) and (2) with the standard choice of parameters in Table 2.

x_0	x_1	x_2	y_0	y_1	y_2	a	s	Type	Stability
0	0	0	0	0	0	0	2.8×10^{-2}	Trivial	Locally stable
3.2×10^{3}	8.0×10^{4}	2.1×10^{10}	0	0	0	1.4×10^{2}	1.9×10^{-1}	Healthy	Locally unstable
9.9×10^{4}	2.5×10^{6}	6.3×10^{11}	0	0	0	8.1×10^{2}	9.9×10^{-1}	Healthy	Locally unstable
0	0	0	1.6×10^{2}	6.8×10^{3}	2.4×10^{9}	4.0×10^{1}	7.6×10^{-2}	Malignant	Locally unstable
0	0	0	1.7×10^{5}	7.6×10^{6}	2.7×10^{12}	1.7×10^{3}	2.0	Malignant	Locally stable

depletes erythroid progenitors and precursors (12). As mentioned in the introduction, an *in vitro* study of another JAK inhibitor, AZD1480, shows that stem cells may escape the effects of JAK inhibition (13). Additionally, RUX gives mild reductions in the *JAK2* VAF in mice and minimal to moderate reductions in humans with high variability between patients (2, 9), and the reductions are sustained on therapy (2, 9, 11, 15).

Systematic numerical analysis of the model specified in Equations (1) and (2) reveals that a sustained reduction in *JAK2* VAF can only be achieved if treatment with RUX affects the mHSC dynamics described by Equation (1d) (see section S3 of the supplementary for more details). Biologically, this can be interpreted as a direct effect on the mHSCs or an effect on the mHSC response to the cytokine signal for these cells. Here, we choose to interpret one effect of RUX as a reduction of the cytokine-induced up-regulation of mHSC self-renewal. This is achieved by letting RUX increase s_{y_0}. To model the reduction of cell counts and the targeting of progenitor cells, we also let RUX affect the death rate of malignant progenitor cells, i.e. we let it increase d_{y_1}. The numerical experiments with the model also reveal that this effect alone can give rapid reductions in the blood cell counts, and it can also reduce the *JAK2* VAF in the short term. In the long term, however, the *JAK2* VAF typically increases again when only this parameter is increased.

Let $\widetilde{s_{y_0}}$ and $\widetilde{d_{y_1}}$ denote the values of s_{y_0} and d_{y_1}, respectively, for a given patient during treatment with RUX, let $\rho_{s_{y_0}}$ and $\rho_{d_{y_1}}$ denote patient specific parameters describing the strength of a given patient's response to RUX treatment in terms of s_{y_0} and d_{y_1}, and let $c_R(t)$ denote the dose of RUX that the given patient is receiving measured in mg/day. Then, we assume that the effects of RUX treatment are dose-dependent in the following way:

$$\widetilde{s_{y_0}}(t) = (1 + c_R(t)\rho_{s_{y_0}})s_{y_0}, \tag{3a}$$

$$\widetilde{d_{y_1}}(t) = (1 + c_R(t)\rho_{d_{y_1}})d_{y_1}. \tag{3b}$$

In this work, we consider only the case of $\rho_{s_{y_0}} \geq 0$ and $\rho_{d_{y_1}} \geq 0$, i.e. that RUX can increase the values of s_{y_0} and d_{y_1}. It is worth pointing out that only relative changes in $c_R(t)$ matter, as a scaling of $c_R(t)$ can be compensated for by using the inverse scaling for $\rho_{s_{y_0}}$ and $\rho_{d_{y_1}}$. Using these updated parameter values due to RUX treatment and collecting some terms from Equation (1) for brevity, the model takes the following form during treatment:

$$\dot{x}_0 = \alpha_{x_0}\left(2p_{x_0}\phi_x(x_0, y_0)\frac{s}{s_{x_0} + s} - 1\right)x_0, \tag{4a}$$

$$\dot{x}_1 = \alpha_{x_1}(2p_{x_1} - 1)x_1 + 2A_{x_0}\alpha_{x_0}\left(1 - p_{x_0}\phi_x(x_0, y_0)\frac{s}{s_{x_0} + s}\right)x_0 - d_{x_1}x_1, \tag{4b}$$

$$\dot{x}_2 = 2A_{x_1}\alpha_{x_1}(1 - p_{x_1})x_1 - d_{x_2}x_2, \tag{4c}$$

$$\dot{y}_0 = \alpha_{y_0}\left(2p_{y_0}\phi_y(y_0, y_0)\frac{s}{(1+c_R(t)\rho_{s_{y_0}})s_{y_0}+s} - 1\right)y_0, \tag{4d}$$

$$\dot{y}_1 = \alpha_{y_1}(2p_{y_1} - 1)y_1 + 2A_{y_0}\alpha_{y_0}\left(1 - p_{y_0}\phi_y(x_0, y_0)\frac{s}{(1 + c_R(t)\rho_{s_{y_0}})s_{y_0}+s}\right)y_0 - (1 + c_R(t)\rho_{d_{y_1}})d_{y_1}y_1, \tag{4e}$$

$$\dot{y}_2 = 2A_{y_1}\alpha_{y_1}(1 - p_{y_1})y_1 - d_{y_2}y_2, \tag{4f}$$

$$\dot{a} = d_{x_1}x_1 + d_{y_1}y_1 + d_{x_2}x_2 + d_{y_2}y_2 - e_a as, \tag{4g}$$

$$\dot{s} = r_s a - e_s s + I, \tag{4h}$$

where the ϕ-functions are once again given in Equation (2), and the assumed effects of RUX are highlighted in blue and cyan.

2.2 Data

The largest part of the data used in this work is taken from the COMFORT-II study (11). The COMFORT-II study was an open-label phase 3 randomised controlled study that investigated the safety and efficacy of ruxolitinib vs. best available therapy (BAT) in 219 patients with myelofibrosis (MF). The primary end point of the study was the percentage of patients with at least a 35% reduction in spleen volume after 48 weeks, but an exploratory response assessment included monitoring the *JAK2* VAF (42). More information about the study can be found in (11, 42)[2]. In the supplementary of (11), trajectories of the evolution of the *JAK2* VAF are presented for 18 individual patients who achieved a reduction in *JAK2* VAF of at least 20% (absolute) after 48 or 72

weeks of RUX treatment. This is approximately 16.5% of the patients from the study who were treated with RUX and were carrying the *JAK2* V617F mutation. We include these 18 patients in our study.

Additional data were obtained from the RESPONSE study (15). The RESPONSE study was an open-label phase 3 randomised controlled study that investigated the safety and efficacy of ruxolitinib vs. BAT in 222 patients with polycythaemia vera (PV). The primary end point of the study was haematocrit control through week 32 and at least a 35% reduction in spleen volume after 32 weeks (43). The study also monitored the *JAK2* VAF (15, 43)[3]. In (15), trajectories of the evolution of the *JAK2* VAF are presented for a number of patients who crossed over from interferon-α-2a to RUX and for patients who achieved a 90% (relative) reduction in *JAK2* VAF. From the latter category, 6 patients received only RUX, and we include data from these 6 patients in the data used in this work. We assign the numbers 19 through 24 to the patients from the RESPONSE study. These 6 patients correspond to approximately 6% of the patients from the study who were treated with RUX and were carrying the *JAK2* V617F mutation.

It is important to note that we do not have access to the full data sets from the COMFORT-II and RESPONSE studies but only to the data shown in the respective publications, which is precisely the data for patients achieving substantial (defined as above for the respective studies) reductions in their *JAK2* VAF. This is a limited subset of the patients in the respective studies, and the rest of the patients in the studies have not responded as well to the treatment. However, if the model developed here can fit to the patients experiencing the largest reductions in *JAK2* VAF, it seems reasonable to assume that the model may also fit to patients achieving a more modest response in their *JAK2* VAF as this requires less drastic changes to the parameters of the model as a result of the treatment. While it would be optimal to have data for all levels of response to the treatment, we can still learn about the most important mechanisms of RUX by considering patients responding well to the treatment.

We do not have access to changes to the dosing of RUX for the individual patients. In the COMFORT-II study, the median daily dose was 40 mg/day for patients with platelet counts above 200×10^9 L^{-1} and 30 mg/day for patients with platelet counts between 100×10^9 L^{-1} and 200×10^9 L^{-1} (11). Both median daily doses were slightly decreasing over time during the study. Here, we compromise and assume that the dose for the available COMFORT-II patients was constant at 35 mg/day, i.e. $c_R(t) = 35$ for these patients. In the RESPONSE study, the initial dose was 20 mg/day (15), and therefore we assume that $c_R(t) = 20$ for these patients. We once again emphasise that the absolute value of $c_R(t)$ is irrelevant for each patient, and only relative changes matter. The absolute value is only used to compare the resulting values of $\widetilde{s_{y_0}}(t)$ and $\widetilde{d_{y_1}}(t)$ between patients. Since we assume a constant daily dose of RUX for all patients, the time-dependence of $\widetilde{s_{y_0}}(t)$ and $\widetilde{d_{y_1}}(t)$ vanishes, and hereinafter we do not write it explicitly.

All patient data used in this work were extracted from plots in the publications mentioned above using WebPlotDigitizer[4].

2.3 Fitting the model to clinical data

We fit the model to the *JAK2* VAF of the patients using the patient-specific parameters $\rho_{s_{y_0}}$ and $\rho_{d_{y_1}}$. For each patient, we compute the values of $\rho_{s_{y_0}}$ and $\rho_{d_{y_1}}$ that give model predictions the closest to their *JAK2* VAF data in a nonlinear least squares framework as described in section S4 of the supplementary. In all calculations, the *JAK2* VAF is used as a decimal number, but it is plotted as a percentage as this is what is most commonly done in the clinic. The quality of the fits is quantified using the root mean squared error (RMSE). For data points $\{y_i\}_{i=1}^m$ and model predictions $\left\{\hat{y}_i(t_i;\, \rho_{s_{y_0}},\, \rho_{d_{y_1}})\right\}_{i=1}^m$, the RMSE is given by

$$\mathrm{RMSE} = \sqrt{\frac{1}{m}\sum_{i=1}^{m}\left(y_i - \hat{y}(t_i;\, \rho_{s_{y_0}},\, \rho_{d_{y_1}})\right)^2}.$$

The RMSE is easier to interpret than the sum of squared errors since, due to the square root, it has the same unit as the data themselves, and it gives a measure of the typical (but not the mean) error between the model and the data. For example, an RMSE-value of 0.05 (5%) means that the typical difference between the *JAK2* VAF data and the model predictions is 0.05 (5%).

We use the *JAK2* VAF as a proxy for the fraction of mutated (malignant) cells, and we make the simplifying assumption that all mutated cells are homozygous. This assumption is motivated by the observation that the average *JAK2* VAF of the 24 patients used in this work was approximately 76% at the initiation of the respective studies (see section 2.2 for further description of the data used). If we assume that all cells in a given patient are mutated and let a denote the fraction of mutated cells that are homozygous, the *JAK2* VAF is given by $V = \frac{1}{2}(1-a) + a = \frac{1}{2}(1+a)$. From this expression, we can calculate that in the "worst" case where all cells are mutated, if the *JAK2* VAF is 0.76 (76%), at least the fraction 0.52 (52%) of the cells must be homozygous. If not all cells are mutated, an even higher percentage of the cells must be homozygous. Therefore, we will use the fraction

$$g(x_2,\, y_2) = \frac{y_2}{x_2 + y_2},$$

with the output from the model in Equations (1) or (4) as our best estimate of the *JAK2* VAF and thus compare this quantity to the available measurements.

2 https://clinicaltrials.gov/study/NCT00934544.

3 https://clinicaltrials.gov/study/NCT01243944.

4 https://automeris.io/WebPlotDigitizer/.

3 Results

3.1 Model simulations suggest that RUX must affect both stem cells and progenitor cells to achieve sustained reductions in the *JAK2* VAF

As described in section 2, our model consists of 8 ordinary differential equations [see Equations (1) and (2)] describing the time evolution of the number of healthy and malignant stem cells, healthy and malignant progenitor cells, healthy and malignant mature cells, the cellular debris, and a cytokine signal. In this model, we have interpreted the effects of RUX as affecting the half-saturation constant of the malignant stem cell response to the cytokine signal, s_{y_0}, and the death rate of malignant progenitor cells, d_{y_1} [see Equations (1) and (3)]. As motivated in section 2.1.3, the effect on s_{y_0} is needed for the model to achieve sustained reductions in the *JAK2* VAF on therapy (2, 9, 11, 15), and the effect on d_{y_1} models the reduction in blood cell counts (2, 8, 11) through targeting of the mutated progenitor cells (12). To show how these effects synergise, we simulate the population dynamics of healthy and malignant cells for a typical *in silico* patient with different adjustments to the default values of s_{y_0} and d_{y_1}. Specifically, we are investigating how to achieve the (relatively) quick and monotonic reduction in *JAK2* VAF that some patients experience.

We initialise the simulations with the initial conditions $x_0(0)=1.0\times10^5$, $x_1(0)=2.5\times10^6$, $x_2(0)=6.4\times10^{11}$, $y_0(0)=1$, $y_1(0)=0$, $y_2(0)=0$, $a(0)=8.1\times10^2$, and $s(0)=1$. These initial conditions approximately correspond to the second healthy steady state in Table 3, for which the model was calibrated (see section S1 of the supplementary) with one malignant stem cell added. After 30 years, the *JAK2* VAF has reached approximately 50%, and we initiate treatment with RUX. Since the effects of RUX on cell kinetics are not well understood, we consider four scenarios of how the treatment may affect the parameters of the model: a) RUX has no effect on the patient. b) RUX affects only the half-saturation constant for the malignant stem cells, s_{y_0}. c) RUX affects only the death rate of malignant progenitor cells, d_{y_1} d) RUX affects both s_{y_0} and d_{y_1}. These scenarios are based on the hypothesised mechanisms of RUX interpreted in terms of the model (see section 2.1.3). Scenario a) illustrates the scenario of a patient not responding to the treatment. This could for example be a patient who is resistant to RUX. It also illustrates the behaviour of the model in absence of treatment. Scenarios b) and c) illustrate the model behaviour when RUX causes only one of the two hypothesised treatment effects from section 2.1.3. This illustrates the individual effect of each of the two hypothesised treatment effects in the model and could illustrate the scenarios of patients in whom the treatment affects only one of the two parameters. Finally, scenario d) illustrates the model behaviour when RUX causes both of the hypothesised treatment effects. The results of the simulations of all four scenarios are shown in Figure 2.

In all subfigures of Figure 2, we see that the number of malignant cells and the *JAK2* VAF rise from close to 0 and until treatment initiation at time 30 years. From Figure 2A, we see that if a) RUX has no effect on the patient, the number of malignant cells continues to increase before saturating while all the healthy cells are outcompeted, and the *JAK2* VAF increases to 100%. From Figure 2B, we see that if b) the treatment with RUX affects only the half-saturation constant of the mHSCs, s_{y_0}, the mHSCs are outcompeted, and the patient is cured, but only after a considerable period of several decades. However, more mHPC and mMBC are produced initially due to increased differentiation of the mHSCs, and both the number of mHPC, the number of mMBC, and the *JAK2* VAF grow during approximately the first year of treatment before declining. In this simulation, it takes approximately 2 years before the number of mMBCs returns to its level just before treatment initiation and approximately 4 years before the *JAK2* VAF returns to its level just before treatment initiation. Thus, this type of effect might actually be harmful to the patient in the first couple of years. Furthermore, this temporary increase of the *JAK2* VAF is not observed, and thus, this effect alone cannot explain the available data. However, without affecting the stem cells directly, i.e. their proliferation rate, their maximal self-renewal fraction, their interactions with each other (the crowding effects), or introducing a death rate for them (see section S3 of supplementary for plots showing some of these effects), adjusting the half-saturation constant of the mHSC, s_{y_0}, is the only possibility for observing a sustained reduction in the cell counts and the *JAK2* VAF. From Figure 2C, we see that if c) the treatment with RUX changes only the death rate of the mHPCs, d_{y_1}, the number of mHPCs, the number of mMBCs, and the *JAK2* VAF will decrease for approximately half a year and adjust to a new quasi-steady state, but since the mHSCs are completely unaffected, the number of these continues to grow. After the initial decline due to the increased death rate of mHPCs, the number of mHPCs and the number of mMBCs grow slowly with the mHSCs, and eventually all the healthy cells are outcompeted. Thus, affecting d_{y_1} alone is not curative and cannot explain the monotonically decreasing *JAK2* VAF observed in some patients. Summing up, letting RUX affect only s_{y_0} or d_{y_1} alone is not sufficient to explain the quick and monotonic reduction in *JAK2* VAF that some patients experience during treatment. However, in Figure 2D we see that if d) the treatment with RUX affects both s_{y_0} and d_{y_1}, and the respective parameters are sufficiently increased compared to the scenario without treatment, both the number of mHSCs, mHPCs, mMBCs, and the *JAK2* VAF may all monotonically decrease during treatment, and thus the patient will experience remission in both the long and the short run. Thus, changing both s_{y_0} and d_{y_1} simultaneously is one mechanism in the model that can explain the effect of RUX treatment.

3.2 The proposed model can recapitulate the response dynamics during RUX therapy

To further investigate and quantify the effects of RUX treatment on the half-saturation constant for the mHSCs' response to the cytokine signal, s_{y_0}, and the death rate of the mHPCs, d_{y_1}, we fit the model in Equation (4) to individual patients' data. More precisely, we adapt the parameters $\rho_{s_{y_0}}$ and $\rho_{d_{y_1}}$ describing the size of each patient's change in s_{y_0} and d_{y_1}, respectively, due to the treatment with RUX to obtain the optimal fits. The results for the individual patients can be seen in detail in section S6 of the supplementary,

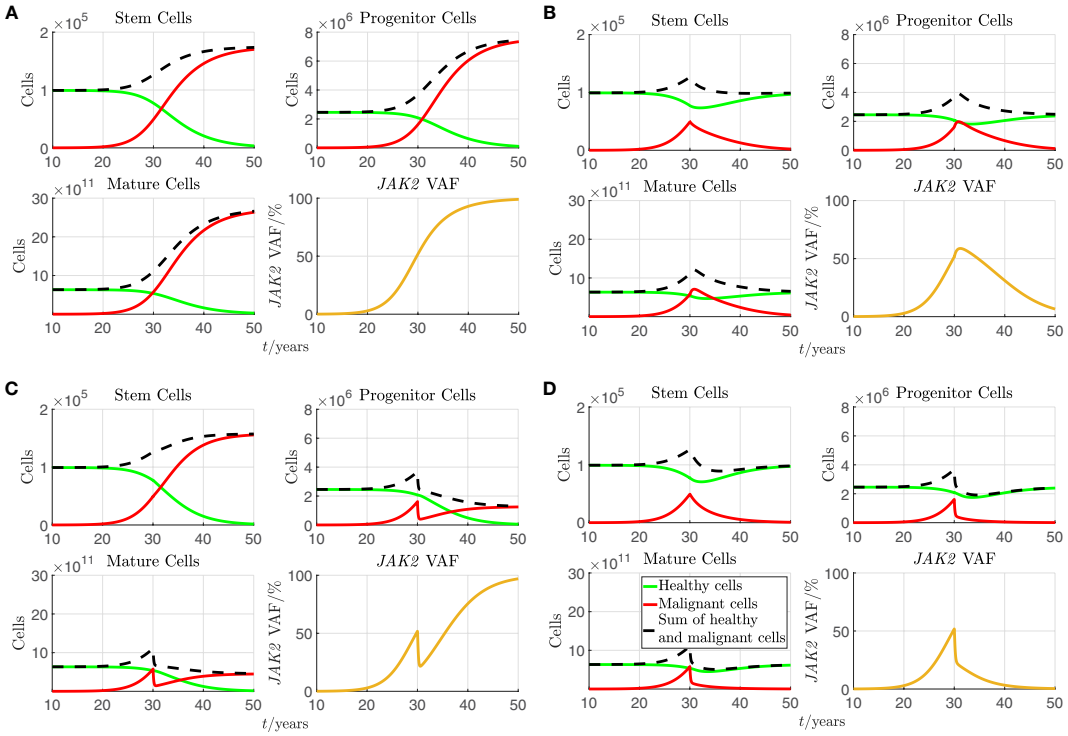

FIGURE 2
A simulation of the stem, progenitor and mature cell counts and the *JAK2* VAF based on Equations (1) and (2) with the standard parameters from Table 2. As initial conditions, we choose $x_0(0) = 1.0 \times 10^5$, $x_1(0) = 2.5\times10^6$, $x_2(0) = 6.4\times10^{11}$, $y_0(0) = 1$, $y_1(0) = 0$, $y_2(0) = 0$, $a(0) = 8.1\times10^2$, and $s(0) = 1$. For the plots of cell counts, the green curves represent the number of healthy cells, the solid red curves represent the number of malignant cells, and the dashed black curves represent the sum of healthy and malignant cells. Treatment is initiated after 30 years in the simulation. **(A)** No effect of treatment. **(B)**. s_{y_0} increased to 6 times its standard value during treatment. **(C)** d_{y_1} to 6 times its standard value during treatment. **(D)** s_{y_0} and d_{y_1} to 6 times their standard values during treatment.

some representative examples of fits are shown in Figure 3, and all fits are presented in Figures 4, 5. In these figures, time $t = 0$ is defined as the time of the first available *JAK2* VAF measurement. Using the fits, we are able to quantify how much the affected parameters change for each patient (see Table 4) and to make predictions of the time dynamics of the *JAK2* VAF for each patient if the treatment is continued (see section S6 of the supplementary). We also compare the model fits with RUX affecting both s_{y_0} and d_{y_1} (Figures 3–5) to the cases of RUX affecting only s_{y_0} or d_{y_1} (effectively setting $\rho_{d_{y_1}} = 0$ and $\rho_{s_{y_0}} = 0$, respectively, see the figures in section S7 of the supplementary). It should be noted that the reported approximate 95% confidence intervals (CIs) are calculated by sampling 1000 pairs of the parameters from their estimated approximate joint distribution, simulating the model with the sampled parameters, and finally taking the middle 95% predicted *JAK2* VAF values of these simulations. The sampling procedure can produce negative values of the parameters, in which case we choose to resample the corresponding samples. More details are given in section S4 of the supplementary.

Figure 3A shows that for patient 1, the model fits very well to the *JAK2* VAF with an RMSE-value of 0.0170 (1.70%) for the *JAK2* VAF data and approximate 95% CIs of mean width 0.0978 (9.78%) for the time shown in the plot. Figure 3B shows another example of a good fit for patient 2 with an RMSE-value of 0.0253 (2.53%) for the *JAK2* VAF data and approximate 95% CIs of mean width 0.141 (14.1%) for the time shown in the plot. Compared to patient 1, the model predicts that for this patient, RUX treatment affects only d_{y_1} (since $\rho_{s_{y_0}} = 0$), and therefore the reduction in *JAK2* VAF is temporary, and the patient is not cured in the long run. In fact, this turns out to be the case for 5 out of the 24 patients, namely patients 2, 3, 13, 15, and 17. This shows that our model is able to classify patients in terms of their response to RUX, which has the potential to be of key clinical significance. For these 5 patients, their *JAK2* VAF is initially decreasing and then increasing at later time points. The fits for these patients are shown in Figures 4, 5 and in more detail in section S6 of the supplementary. Figure 3C shows the worst fit of the model to the available data. This happens for patient 3 with an RMSE-value of 0.0739 (7.39%) for the *JAK2* VAF data and approximate 95% CIs of mean width 0.483 (48.3%) for the time shown in the plot. For this patient, we are therefore very uncertain about the future development of the *JAK2* VAF. Figure 3D shows another example of a good fit to the data for a patient from the RESPONSE study with an RMSE-value of 0.0147 (1.47%) for the *JAK2* VAF data and approximate 95% CIs of mean width 0.0853 (8.53%) for the time shown in the plot. This shows that the model and the data fitting are robust with respect to the medical studies and the diagnoses of the patients (myelofibrosis in COMFORT-II, PV in RESPONSE).

Plots showing the convergence of the fitting procedure to the final fits using all data are shown in section S6 of the supplementary.

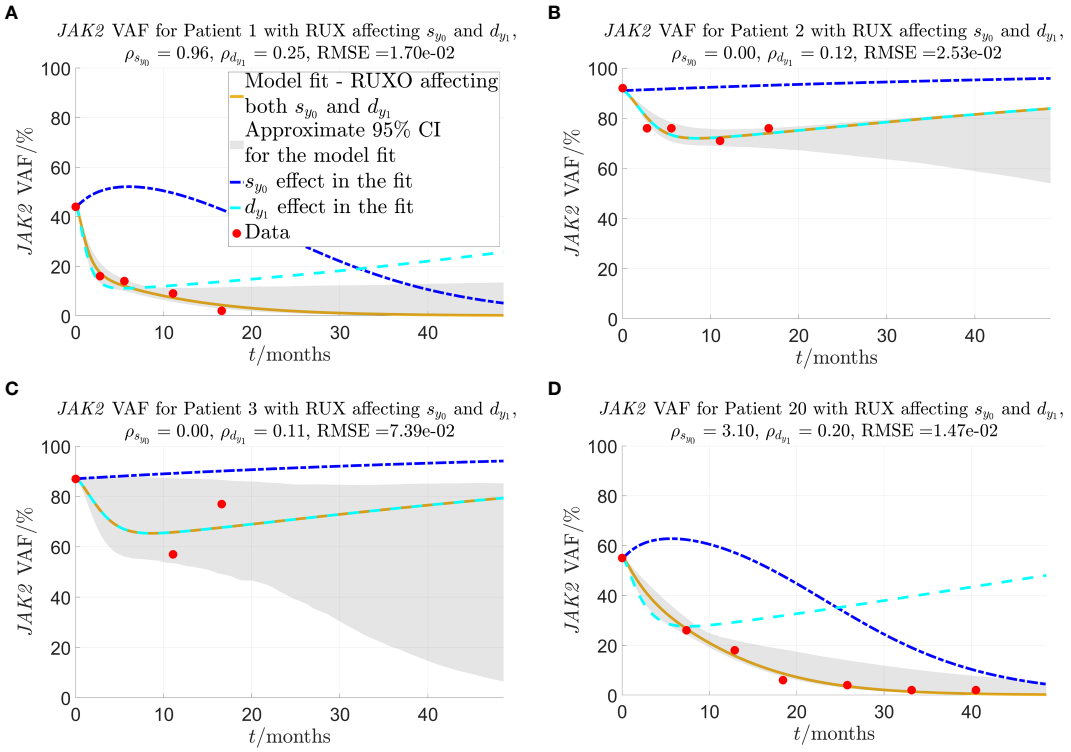

FIGURE 3
Model fit to selected individual patients as described in sections 2.2-2.3. $\rho_{s_{y_0}}$ and $\rho_{d_{y_1}}$ are the fitted parameters that quantify the strength of the given patient's response to RUX treatment in terms of the effect on s_{y_0} and d_{y_1}, respectively. The solid yellow curves show the optimal fit of the model to the *JAK2* VAF data. In the fit, it is assumed that both parameters $\rho_{s_{y_0}}$ (response of mHSCs to cytokine signal) and $\rho_{d_{y_1}}$ (malignant progenitor cell death) are affected by RUX at the same time. To visualise the impact of each of the two effects (changed response to cytokines and increased progenitor death) on the *JAK2* VAF dynamics, the dashed lines show the time evolution of *JAK2* VAF if either $\rho_{d_{y_1}}$ (blue) or $\rho_{s_{y_0}}$ (cyan) is set to 0 and the respective other parameter remains unchanged. The red dots are the data. **(A)** Patient 1, one of the patients for whom the model fits very well, and for whom the model predicts that RUX affects both s_{y_0} and d_{y_1}. **(B)** Patient 2, a patient for whom the model fits quite well, and the model predicts that RUX affects only d_{y_1} ($\rho_{s_{y_0}} = 0$). **(C)** Patient 3, the patient for whom the model fits worst. **(D)** Patient 20, a patient from the RESPONSE study for whom the model fits very well, and for whom the model predicts that RUX affects both s_{y_0} and d_{y_1}.

Boxplots of the RMSE-values for all data points as function of the number of data points used in the fit is shown in Supplementary Figure S15. Overall, the quality of the fits improves significantly when more data points are added. The mean RMSE of the fits is 0.25 (25%) when only 2 data points are used in the calculation of the optimal fit, and 0.09 (9%), 0.05 (5%), and 0.03 (3%) when 3, 4, and 5 data points are used, respectively.

Figure 6 shows histograms of the RMSE-values from fitting the model to all 24 patients and allowing RUX treatment to affect the half-saturation constant for the mHSCs' response to the cytokine signal, s_{y_0}, and the death rate of the mHPCs, d_{y_1}, at the same time and either effect separately. Here, we see that the RMSE-values are much smaller when allowing RUX treatment to affect both s_{y_0} and d_{y_1} than when allowing it to affect only one of them. We obtain a mean RMSE-value of 0.0249 (2.49%) when both s_{y_0} and d_{y_1} can be affected at the same timed compared to 0.138 (13.8%) and 0.0874 (8.74%) when only s_{y_0} or d_{y_1} can be affected, respectively. Additionally, when RUX is allowed to affect both s_{y_0} and d_{y_1}, the model fits achieve an RMSE-value equal to or below 0.02 (2%) for 14 out of 24 patients (approximately 58.3% of patients) and equal to or below 0.04 (4%) for 19 out of 24 patients (approximately 79.2% of patients). The corresponding numbers are 0 (0%) and 0 (0%) when allowing RUX treatment to affect only s_{y_0}, and 1 (approximately 4.17% of patients) and 6 (25.0% of patients) when allowing RUX treatment to affect only d_{y_1}. Thus, the model fits much better to the available data in the scenario where RUX treatment affects both s_{y_0} and d_{y_1} compared to the scenarios where it affects only one of the parameters, supporting the hypothesis that RUX treatment affects parameters in both the equations for the number of malignant stem cells and the number of malignant progenitor cells. Plots of the optimal model fits to the data for the individual patients when allowing RUX treatment to affect only s_{y_0} or d_{y_1} are shown in section S7 of the supplementary.

Finally, in Table 4 we compare the fitted half-saturation constant for the mHSCs' response to the cytokine signal, s_{y_0}, and the fitted death rate of the mHPCs, d_{y_1}, before and during RUX treatment. A graphical illustration with histograms of $\widetilde{s_{y_0}}$ and $\widetilde{d_{y_1}}$ is shown in Supplementary Figure S17. We consider the scenario where both parameters can change in the presence of RUX. On average during treatment, s_{y_0} is increased to 21.7 times its pre-treatment value (an increase from 7.1×10^{-2} to 1.6) with a standard deviation of 20.9 times, and d_{y_1} is increased to 5.35 times its pre-

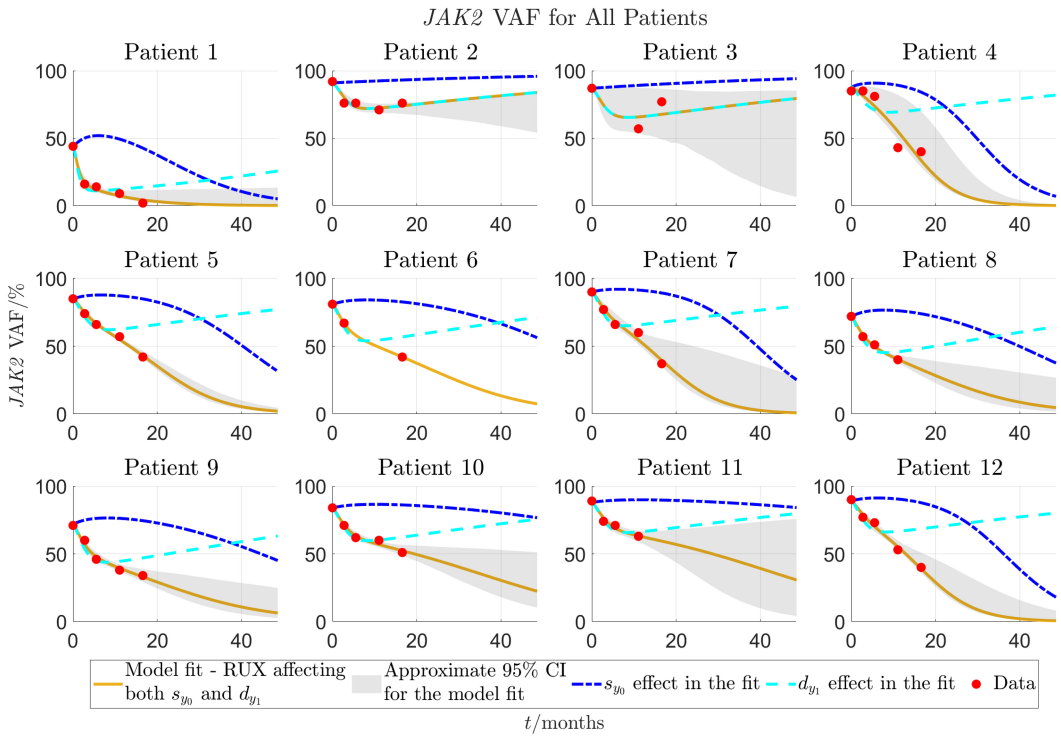

FIGURE 4
Model fit to individual patients' data for patients 1-12 as described in sections 2.2-2.3. The solid yellow curves show the optimal fits of the model to the *JAK2* VAF data. In the fit it is assumed that both parameters $\rho_{s_{y_0}}$ (response of mHSCs to cytokine signal) and $\rho_{d_{y_1}}$ (malignant progenitor cell death) are affected by RUX at the same time. To visualise the impact of each of the two effects (changed response to cytokines and increased progenitor death) on the VAF dynamics, the dashed lines show the time evolution of JAK2 VAF if either $\rho_{d_{y_1}}$ (blue) or $\rho_{s_{y_0}}$ (cyan) is set to 0 and the respective other parameter remains unchanged. The red dots are the data. Patients 1-12 are from the COMFORT-II study.

treatment value (an increase from 3.7×10^{-3} day^{-1} to 2.0×10^{-2} day^{-1}) with a standard deviation of 2.21 times. Thus, the treatment seems to have a substantial effect on the cell parameters of the responding patients. In the summary statistics for the changes in s_{y_0} just mentioned, we have disregarded patients 4, 22, 23, and 24 who are considered outliers due to them having s_{y_0} increased to 3.19×10^6, 8.55×10^6, 1.48×10^8, and 229 times their pre-treatment values, respectively. Similarly, in the summary statistics for d_{y_1} just mentioned, we have disregarded patients 15 and 17 who are considered to be outliers due to them having d_{y_1} increased to 29.5 and 37.9 times their pre-treatment values, respectively. See Table 4 for the full details. For the cases where the lower limit of the approximate 95% CIs of the fitted parameters $\rho_{s_{y_0}}$ and $\rho_{d_{y_1}}$ is less than 0, this should be interpreted as a lower limit of 0 as the optimal fit is calculated under the conditions $\rho_{s_{y_0}} \geq 0$ and $\rho_{d_{y_1}} \geq 0$.

4 Discussion

In this work, we have proposed a mechanistic model of RUX treatment in MPN patients. The model is able to capture quantitative *JAK2* VAF dynamics in patients showing significant VAF reductions in response to RUX. In the model, RUX affects the malignant HSCs' response to the cytokine signal and the malignant progenitor cell death rate. The former is quantified by the half-saturation constant, s_{y_0}, and the latter is denoted by d_{y_1}. The mean RMSE-value of the fits is 0.0249 (2.49%) when allowing RUX treatment to affect both s_{y_0} and d_{y_1}. The model suggests that a RUX-dependent increase of malignant progenitor cell death and a RUX-dependent down-regulation of the response of malignant HSCs to the feedback signal are sufficient to reproduce clinical data. The results should be interpreted as model-generated hypotheses which require further experimental validation.

To achieve lasting reductions in *JAK2* VAF in the model simulations, as is seen for at least some patients, any kind of treatment must affect parameters which are linked to the stem cell population dynamics, i.e. the stem cell proliferation rates and/or their self-renewal fraction. If a treatment does not affect these quantities, the model predicts that the treatment will only cause temporary reductions in *JAK2* VAF before it starts increasing again. This is in contrast to some sources stating that RUX is not able to target the disease-initiating malignant stem cells in mice (12) and in humans (9). As 18 of the 24 patients considered in this work have not had an increase in *JAK2* VAF from one measurement to another, our model predicts that RUX could affect the mHSCs by inhibiting their response to the cytokine signalling in the bone marrow, i.e. by increasing the half-saturation constant for the mHSCs' response to the cytokine signal, s_{y_0}. However, as seen from the fitting to individual patients' *JAK2* VAF data, the best fits for the 5 patients numbered 2, 3, 13, 15, and 17 are obtained by the

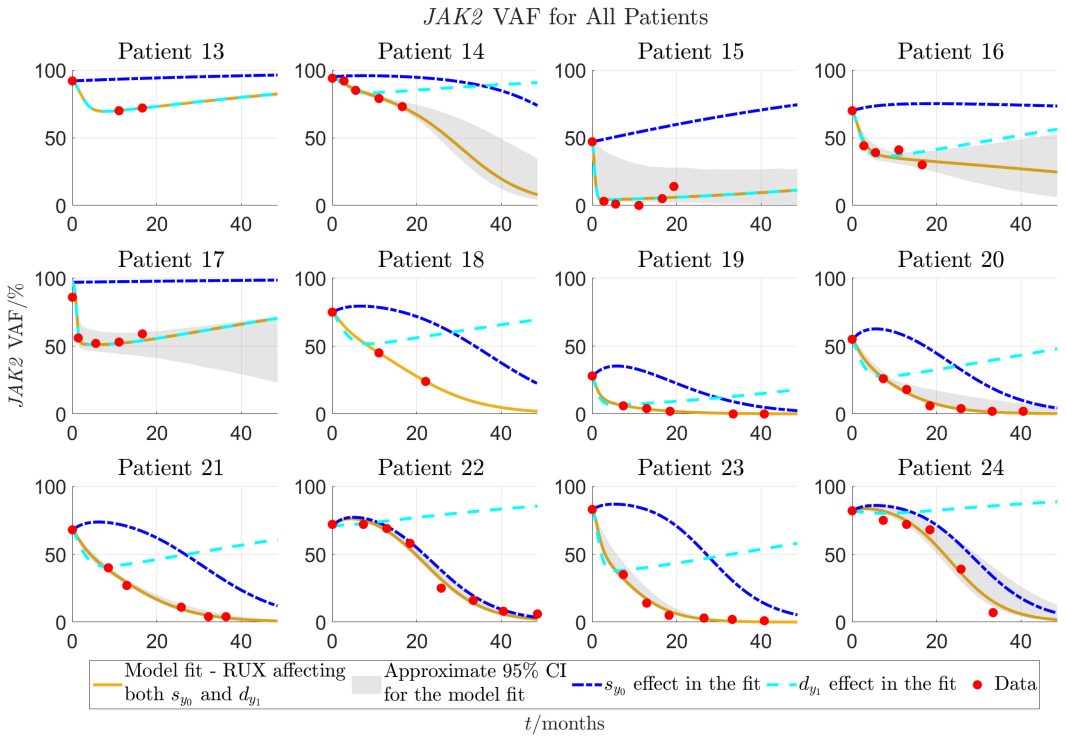

FIGURE 5
Continuation of Figure 4 for patients 13-24. Patients 13-18 are from the COMFORT-II study, and patients 19-24 are from the RESPONSE study.

RUX treatment not affecting s_{y_0} but instead affecting only the death rate of the malignant progenitor cells, d_{y_1}. Thus, it is possible that RUX treatment does not affect the stem cell parameters in some patients, but that it does so in others. The 5 patients in this data set for whom the best fits are obtained by having RUX not affecting stem cell parameters are precisely the ones experiencing an initial reduction in *JAK2* VAF followed by a monotonic increase at the later time points. The final patient experiencing an increase in *JAK2* VAF from one measurement to another is patient 16. For this patient, the *JAK2* VAF increases from measurement 3 to measurement 4, but then decreases again from measurement 4 to measurement 5. Therefore, the model predicts that RUX treatment also affects s_{y_0} for this patient. Thus, our hypothesis from this data fitting is that if a patient experiences an initial reduction in *JAK2* VAF followed by monotonic growth, RUX affects only progenitor cell parameters for this patient. If this is not the case, most typically due to monotonic reductions in the *JAK2* VAF in this data set, the model predicts that RUX affects some stem cell parameter for the given patient, for example s_{y_0}. This hypothesis can theoretically be tested by making measurements of cell lines and in animal models. The model predicts that the sustained reductions in *JAK2* VAF are due to a reduction in the number of malignant stem cells. Thus, the model predicts that for the patients experiencing sustained reductions in *JAK2* VAF, continued treatment with RUX may ultimately result in a complete eradication of malignant cells.

It is important to point out that the model here is fitted to data from patients who achieved a reduction in *JAK2* VAF of at least 20% (absolute) after 48 or 72 weeks of treatment in the COMFORT-II study and at least 90% (relative) in the RESPONSE study, and these constitute only a subset of the cohorts (approximately 16.5% and 6% of *JAK2* positive patients treated with RUX, respectively). Since we do not have access to the data of the rest of the patients in these studies, it is impossible to fit the model to their data. However, since these patients have experienced only modest reductions in their *JAK2* VAF (or maybe even increases), it seems reasonable to assume that the model could possibly fit to these patients without changing s_{y_0} in response to RUX treatment. Thus, it is possible that for the majority of patients, RUX treatment does not affect the stem cell parameters, but for a minority of patients it does so in addition to affecting the progenitor parameters. In the latter case we observe monotonically decreasing *JAK2* VAF dynamics.

For patients 4, 22, 23, and 24, the model predicts that s_{y_0} should be increased to 3.19×10^6, 8.55×10^6, 1.48×10^8, and 229 times its pre-treatment value, respectively, to obtain the optimal fits. This seems excessive, but due to the Michaelis-Menten functional form in which s_{y_0} appears, $\frac{s}{s_{y_0}+s}$, these increases all effectively reduce the self-renewal fraction of the mHSCs, $p_{y_0}\phi_y(y_0, y_0)\frac{s}{s_{y_0}+s}$, to 0. If s_{y_0} is sufficiently high, the self-renewal fraction becomes insensitive to changes of this parameter.

Processes not considered in the model can lead to disagreements between data and simulations. Some major potential sources of model error are the following:

- *Biological variation between patients:* To avoid overfitting and to keep the model as simple and interpretable as possible, we have fitted the model to the data by letting

10.3389/fimmu.2024.1384509

TABLE 4 Overview of the fitted parameters, $\rho_{s_{y_0}}$ and $\rho_{d_{y_1}}$, and the parameter values $\widetilde{s_{y_0}}$ and $\widetilde{d_{y_1}}$ from Equation (3) during RUX treatment for all patients.

Patient	Dose/ mg/day	$\rho_{s_{y_0}}$ / (mg/day)$^{-1}$ (approx. 95% CI)	$\widetilde{s_{y_0}}/1$	$\frac{\widetilde{s_{y_0}}}{s_{y_0}}$	$\rho_{d_{y_1}}$ / (mg/day)$^{-1}$ (approx. 95% CI)	$\widetilde{d_{y_1}}$ / day^{-1}	$\frac{\widetilde{d_{y_1}}}{d_{y_1}}$
1	35	0.959 (-1.55, 3.46)	2.47	34.6	0.248 (0.166, 0.329)	0.0358	9.66
2	35	0 (-0.226, 0.226)	0.0714	1	0.122 (0.0805, 0.164)	0.0195	5.27
3	35	0 (-6.47, 6.47)	0.0714	1	0.11 (-1.37, 1.59)	0.018	4.86
4	35	9.13e+04 (-1.45e+10, 1.45e+10)	2.28e+05	3.19e+06	0.0994 (-0.0156, 0.214)	0.0166	4.48
5	35	0.861 (0.342, 1.38)	2.22	31.1	0.108 (0.0914, 0.125)	0.0177	4.79
6	35	0.397 (0.394, 0.399)	1.06	14.9	0.118 (0.118, 0.118)	0.019	5.12
7	35	1.43 (-1.04, 3.91)	3.66	51.2	0.155 (0.0971, 0.213)	0.0238	6.43
8	35	0.443 (-0.196, 1.08)	1.18	16.5	0.102 (0.0845, 0.119)	0.0169	4.57
9	35	0.367 (0.0253, 0.708)	0.988	13.8	0.109 (0.0859, 0.133)	0.0178	4.82
10	35	0.245 (-0.000628, 0.492)	0.685	9.59	0.112 (0.0897, 0.134)	0.0182	4.92
11	35	0.221 (-0.632, 1.07)	0.623	8.72	0.12 (0.0812, 0.159)	0.0193	5.2
12	35	1.93 (-0.735, 4.59)	4.89	68.4	0.131 (0.0956, 0.166)	0.0206	5.58
13	35	0 (-0.0839, 0.0839)	0.0714	1	0.161 (0.131, 0.192)	0.0246	6.64
14	35	0.635 (0.0722, 1.2)	1.66	23.2	0.116 (0.087, 0.144)	0.0187	5.05
15	35	0 (-0.527, 0.527)	0.0714	1	0.813 (-0.632, 2.26)	0.109	29.5
16	35	0.125 (-0.199, 0.449)	0.383	5.37	0.143 (0.0923, 0.194)	0.0223	6.01
17	35	0 (-0.173, 0.173)	0.0714	1	1.05 (0.57, 1.54)	0.14	37.9
18	35	0.765 (0.763, 0.767)	1.16	16.3	0.0882 (0.0881, 0.0883)	0.0102	2.76
19	20	1.74 (0.361, 3.12)	2.55	35.8	0.379 (0.305, 0.452)	0.0317	8.58
20	20	3.1 (-0.874, 7.07)	4.5	63	0.198 (0.148, 0.249)	0.0184	4.96
21	20	1.78 (0.784, 2.78)	2.62	36.7	0.176 (0.142, 0.21)	0.0167	4.52
22	20	4.28e+05 (-1.29e+11, 1.29e+11)	6.11e+05	8.55e+06	0.00826 (-0.0264, 0.043)	0.00431	1.17
23	20	7.38e+06 (-2.6e+13, 2.6e+13)	1.05e+07	1.48e+08	0.483 (0.274, 0.693)	0.0395	10.7
24	20	11.4 (-96.5, 119)	16.3	229	0.0268 (-0.0374, 0.0911)	0.00568	1.54

Note that patients from the COMFORT-II trial (numbered 1-18) received a different daily dose of RUX than patients from the RESPONSE study (numbered 19-24).

The fractions $\frac{\widetilde{s_{y_0}}}{s_{y_0}}$ and $\frac{\widetilde{d_{y_1}}}{d_{y_1}}$ are the ratios between the respective parameters during and before treatment. For the cases where the lower limit of the approximate 95% CIs of the fitting parameters $\rho_{s_{y_0}}$ and $\rho_{d_{y_1}}$ is less than 0, this should be interpreted as a lower limit of 0 as the optimal fit is calculated under the conditions $\rho_{s_{y_0}} \geq 0$ and $\rho_{d_{y_1}} \geq 0$.

RUX affect only two parameters and letting all other parameters be equal for all patients. In reality, RUX may affect more than the two parameters investigated. Furthermore, the remaining parameters most probably differ between patients and may even vary over time for each specific individual, e.g. due to differences in age, sex, BMI, etc. However, changing some parameters, for example e_a, r_s, e_s, and I, results in only minor effects on the cell counts and the *JAK2* VAF (see sections S2 (sensitivity analysis) and S3 (numerical experiments) of the supplementary for more details). Therefore, we believe that we have captured the most important effects of RUX in this model.

- *Assuming constant daily doses of RUX:* In the model, we assume that the patients have received constant daily doses of RUX. However, in reality, each patient has most likely received a varying daily dose of RUX dependent on their response to the drug, including side effects, their doctors' recommendations, etc. A varying dosing of RUX will most likely have an impact on the fitted parameter values.
- *Comorbidities and other conditions:* The patients might have been affected by comorbidities and other conditions during the

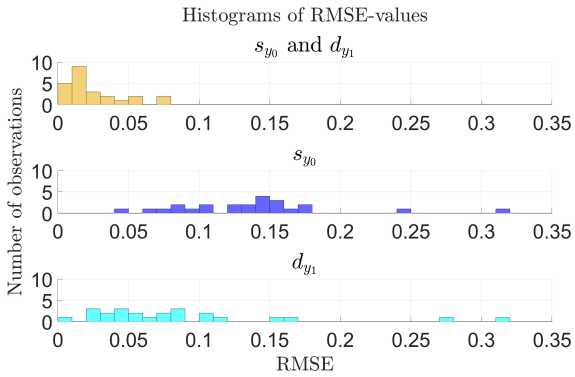

FIGURE 6
Histogram of RMSE-values for the model fitted to the individual patient *JAK2* VAF data as described in sections 2.2-2.3 for all patients (n = 24) as presented in Figures 4, 5 and in sections S6 and S7 of the supplementary. Yellow: Optimal fits allowing RUX treatment to affect both s_{y_0} and d_{y_1}. Blue: Optimal fits allowing only changes in s_{y_0}. Cyan: Optimal fits allowing only changes in d_{y_1}. There are no observations with RMSE-values outside the range shown in the plots.

studies. For example, since it is believed that inflammation affects the development of MPNs (44, 45), inflammatory processes might impact on the treatment response.

- *Modelling precisely one malignant clone:* MPNs are known to be one of the cancers with the lowest number of mutations (14), making these diseases well suited for this type of model with only one malignant clone. However, some patients may have multiple competing malignant clones. To account for different mutations, the model has to be extended accordingly.
- *Resistance to RUX:* The model only implicitly accounts for potential resistance to RUX. One study has shown that 16 out of 39 MF patients were considered to be resistant to RUX, of which 4 were considered to be primary resistant (46). In other studies, the percentage of patients being primary resistant to RUX was estimated to be 2-5% (47). In the COMFORT-II study, approximately 15% of patients discontinued treatment with RUX due to disease progression (11), signifying either primary or secondary resistance. Resistance to RUX will be reflected by low values of $\rho_{s_{y_0}}$ and $\rho_{d_{y_1}}$ in the optimal fit. However, this neglects that resistance can develop over time. Letting $\rho_{s_{y_0}}$ and $\rho_{d_{y_1}}$ be time-dependent would result in a much more complicated model and in a higher risk for overfitting.

Another source of error are the measurement errors, the size of which is unknown to us, but which depends on the equipment and techniques used in the laboratory. In both the COMFORT-II and the RESPONSE studies, the *JAK2* VAF was measured using qPCR methods (11, 15). Though we do not know the exact size of the measurement errors, one study of qPCR methods has shown that for one particular set of equipment and techniques, the standard deviations of the measurements were 0.012 (1.2%) in a reference sample with a *JAK2* VAF of 0.045 (4.5%) and 0.035 (3.5%) in a reference sample with a *JAK2* of 0.13 (13%) (48). These standard deviations are close to the mean RMSE of the model fitted to the available data (0.0249), and thus the deviations between the model and the data are of a reasonable order of magnitude. In the data fitting, we have assumed that the overall errors, i.e. the sum of the model errors and the measurements errors, are normally distributed with 0 mean and some variance, σ^2. This convenient assumption makes the statistical analysis of the results simple (compared to the alternatives, see section S4 of the supplementary for more details), but it is hard to either verify or refute this assumption based on 3-8 data points per patient. The previously mentioned study of different qPCR methods suggests that the size of the measurement errors might depend on the true value of the of the *JAK2* VAF (48). However, simple experiments using weighted least squares fitting gave almost identical results for all patients except patient 15, and therefore we have chosen to use the simpler ordinary least squares approach here. Furthermore, least square fitting approaches can be susceptible to outliers. However, by inspecting the data visually, we have no reason to believe that any one point is an obvious outlier.

In the results presented, we have chosen to fit the data from each patient individually, and thus every patient is completely independent of the other patients. This assumption reduces the computational costs of the fitting procedure. Fitting parameters using the framework of mixed effect models is theoretically possible, however, it increases the computational complexity.

Besides merely testing whether or not specific hypotheses about RUX effects are compatible with clinical data, the model provides a quantitative estimate of the size of a given patient's response to RUX treatment, uncertainty quantification on these estimates, and predictions of the future development of the *JAK2* VAF. The patient-specific parameters, $\rho_{s_{y_0}}$ and $\rho_{d_{y_1}}$, can potentially be used to predict how a given patient will respond to changes in the doses of RUX. For example, it can be used to predict the future development of the *JAK2* VAF if the patient continues or discontinues a specific treatment protocol (for example due to side effects), and it can be used to calculate a critical dose that must be given to the patient to achieve eventual remission. However, such an estimate has to be carefully validated on real world data, and further refinement of the model, e.g., with respect to resistance development, might be required.

Data availability statement

Publicly available datasets were analysed in this study. This data can be found here: In the supplementary of Cervantes et al. (2013), doi.org/10.1182/blood-2013-02-485888 (11), and in the main text of Vannucchi et al. (2017), doi.org/10.1007/s00277-017-2994-x (15).

Ethics statement

Ethical approval was not required for the study involving humans in accordance with the local legislation and institutional requirements. Written informed consent to participate in this study was not required from the participants or the participants' legal guardians/next of kin in accordance with the national legislation and the institutional requirements.

Author contributions

TB: Conceptualization, Formal analysis, Investigation, Methodology, Software, Validation, Visualization, Writing – original draft, Writing – review & editing. JS: Conceptualization, Writing – review & editing. JG-H: Conceptualization, Writing – review & editing. ML: Conceptualization, Writing – review & editing. TK: Conceptualization, Writing – review & editing. CE-D: Conceptualization, Writing – review & editing. VS: Conceptualization, Writing – review & editing. LK: Conceptualization, Writing – review & editing. HH: Conceptualization, Writing – review & editing. MA: Conceptualization, Formal analysis, Investigation, Methodology, Project administration, Supervision, Validation, Visualization, Writing – review & editing. JO: Conceptualization, Formal analysis, Investigation, Methodology, Project administration, Supervision, Validation, Visualization, Writing – review & editing. TS: Conceptualization, Formal analysis, Funding acquisition, Investigation, Methodology, Project administration, Supervision, Validation, Visualization, Writing – review & editing.

Funding

The author(s) declare financial support was received for the research, authorship, and/or publication of this article. This work was supported by the fellowship "Personalized prediction of blood cancer progression using clinical data and mathematical modelling" (R335-2019-2020) from the Lundbeck Foundation (PI: TS).

Conflict of interest

The authors declare that the research was conducted in the absence of any commercial or financial relationships that could be construed as a potential conflict of interest.

Publisher's note

All claims expressed in this article are solely those of the authors and do not necessarily represent those of their affiliated organizations, or those of the publisher, the editors and the reviewers. Any product that may be evaluated in this article, or claim that may be made by its manufacturer, is not guaranteed or endorsed by the publisher.

Supplementary material

The Supplementary Material for this article can be found online at: https://www.frontiersin.org/articles/10.3389/fimmu.2024.1384509/full#supplementary-material

References

1. Tremblay D, Yacoub A, Hoffman R. Overview of myeloproliferative neoplasms: history, pathogenesis, diagnostic criteria, and complications. *Hematology/Oncology Clinics North America*. (2021) 35:159–76. doi: 10.1016/j.hoc.2020.12.001

2. Moliterno AR, Kaizer H, Reeves BN. JAK2V617F allele burden in polycythemia vera: burden of proof. *Blood*. (2023) 141(16):1934–42. doi: 10.1182/blood.2022017697

3. Luque Paz D, Kralovics R, Skoda RC. Genetic basis and molecular profiling in myeloproliferative neoplasms. *Blood*. (2023) 141:1909–21. doi: 10.1182/blood.2022017578

4. How J, Garcia JS, Mullally A. Biology and therapeutic targeting of molecular mechanisms in MPN. *Blood*. (2023) 141:1922–33. doi: 10.1182/blood.2022017416

5. Wilson A, Trumpp A. Bone-marrow haematopoietic-stem-cell niches. *Nat Rev Immunol*. (2006) 6:93–106. doi: 10.1038/nri1779

6. Mullally A, Bruedigam C, Poveromo L, Heidel FH, Purdon A, Vu T, et al. Depletion of Jak2V617F myeloproliferative neoplasm-propagating stem cells by interferon-α in a murine model of polycythemia vera. *Blood*. (2013) 121:3692–702. doi: 10.1182/blood-2012-05-432989

7. Appeldoorn TY, Munnink TH, Morsink LM, Hooge M, Touw DJ. Pharmacokinetics and pharmacodynamics of ruxolitinib: A review. *Clin Pharmacokinet*. (2023) 62:559–71. doi: 10.1007/s40262-023-01225-7

8. Bjørn ME. *Ruxolitinib in the treatment of Myelofibrosis - Studies on Chronic Inflammation in Myelofibrosis and The Impact of JAK1-2 Inhibitor Treatment with Ruxolitinib upon Clinical and Biochemical Parameters with Particular Focus on Markers of Oxidative Stress*. University of Copenhagen (2016).

9. Greenfield G, McPherson S, Mills K, McMullin MF. The ruxolitinib effect: Understanding how molecular pathogenesis and epigenetic dysregulation impact therapeutic efficacy in myeloproliferative neoplasms. *J Trans Med* (2018) 16(1). doi: 10.1186/s12967-018-1729-7

10. Verstovsek S, Mesa RA, Gotlib J, Levy RS, Gupta V, DiPersio JF, et al. A double-blind, placebo-controlled trial of ruxolitinib for myelofibrosis. *New Engl J Med*. (2012) 366:799–807. doi: 10.1056/NEJMoa1110557

11. Cervantes F, Vannucchi AM, Kiladjian JJ, Al-Ali HK, Sirulnik A, Stalbovskaya V, et al. Three-year efficacy, safety, and survival findings from COMFORT-II, a phase 3 study comparing ruxolitinib with best available therapy for myelofibrosis. *Blood*. (2013) 122:4047–53. doi: 10.1182/blood-2013-02-485888

12. Austin RJ, Straube J, Bruedigam C, Pali G, Jacquelin S, Vu T, et al. Distinct effects of ruxolitinib and interferon-alpha on murine JAK2V617F myeloproliferative neoplasm hematopoietic stem cell populations. *Leukemia*. (2020) 34:1075–89. doi: 10.1038/s41375-019-0638-y

13. Wang X, Ye F, Tripodi J, Hu CS, Qiu J, Najfeld V, et al. JAK2 inhibitors do not affect stem cells present in the spleens of patients with myelofibrosis. *Blood*. (2014) 124:2987–95. doi: 10.1182/blood-2014-02-558015

14. Kjær L. Clonal hematopoiesis and mutations of myeloproliferative neoplasms. *Cancers*. (2020) 12:2100. doi: 10.3390/cancers12082100

15. Vannucchi AM, Verstovsek S, Guglielmelli P, Griesshammer M, Burn TC, Naim A, et al. Ruxolitinib reduces JAK2 p.V617F allele burden in patients with polycythemia vera enrolled in the RESPONSE study. *Ann Hematol*. (2017) 96:1113–20. doi: 10.1007/s00277-017-2994-x

16. Mackey M. Unified hypothesis for the origin of aplastic anemia and periodic hematopoiesis. *Blood*. (1978) 51:941–56. doi: 10.1182/blood.V51.5.941.941

17. Roeder I, Loeffler M. A novel dynamic model of hematopoietic stem cell organization based on the concept of within-tissue plasticity. *Exp Hematol*. (2002) 30:853–61. doi: 10.1016/S0301-472X(02)00832-9

18. Rodriguez-Brenes IA, Wodarz D, Komarova NL. Stem cell control, oscillations, and tissue regeneration in spatial and non-spatial models. *Front Oncol*. (2013) 3:82. doi: 10.3389/fonc.2013.00082

19. Ashcroft P, Manz MG, Bonhoeffer S. Clonal dominance and transplantation dynamics in hematopoietic stem cell compartments. *PloS Comput Biol*. (2017) 13: e1005803. doi: 10.1371/journal.pcbi.1005803

20. Pedersen RK, Andersen M, Skov V, Kjær L, Hasselbalch HC, Ottesen JT, et al. HSC niche dynamics in regeneration, pre-malignancy, and cancer: insights from mathematical modeling. *Stem Cells*. (2023) 41:260–70. doi: 10.1093/stmcls/sxac079

21. Dingli D, Michor F. Successful therapy must eradicate cancer stem cells. *Stem Cells*. (2006) 24:2603–10. doi: 10.1634/stemcells.2006-0136

22. Gentry SN, Jackson TL. A mathematical model of cancer stem cell driven tumor initiation: implications of niche size and loss of homeostatic regulatory mechanisms. *PloS One*. (2013) 8:e71128. doi: 10.1371/journal.pone.0071128

23. Hermange G, Rakotonirainy A, Bentriou M, Tisserand A, El-Khoury M, Girodon F, et al. Inferring the initiation and development of myeloproliferative neoplasms. *Proc Natl Acad Sci*. (2022) 119:e2120374119. doi: 10.1073/pnas.2120374119

24. Stiehl T, Baran N, Ho AD, Marciniak-Czochra A. Clonal selection and therapy resistance in acute leukaemias: mathematical modelling explains different proliferation patterns at diagnosis and relapse. *J R Soc Interface*. (2014) 11:20140079. doi: 10.1098/rsif.2014.0079

25. Stiehl T, Lutz C, Marciniak-Czochra A. Emergence of heterogeneity in acute leukemias. *Biol Direct*. (2016) 11. doi: 10.1186/s13062-016-0154-1

26. Andersen M, Sajid Z, Pedersen RK, Gudmand-Hoeyer J, Ellervik C, Skov V, et al. Mathematical modelling as a proof of concept for MPNs as a human inflammation model for cancer development. *PloS One*. (2017) 12:e0183620. doi: 10.1371/journal.pone.0183620

27. Zhang J, Fleischman AG, Wodarz D, Komarova NL. Determining the role of inflammation in the selection of JAK2 mutant cells in myeloproliferative neoplasms. *J Theor Biol*. (2017) 425:43–52. doi: 10.1016/j.jtbi.2017.05.012

28. Ottesen JT, Pedersen RK, Sajid Z, Gudmand-Hoeyer J, Bangsgaard KO, Skov V, et al. Bridging blood cancers and inflammation: The reduced Cancitis model. *J Theor Biol*. (2019) 465:90–108. doi: 10.1016/j.jtbi.2019.01.001

29. Stiehl T, Baran N, Ho AD, Marciniak-Czochra A. Cell division patterns in acute myeloid leukemia stem-like cells determine clinical course: A model to predict patient survival. *Cancer Res*. (2015) 75:940–9. doi: 10.1158/0008-5472.CAN-14-2508

30. Stiehl T, Wang W, Lutz C, Marciniak-Czochra A. Mathematical modeling provides evidence for niche competition in human AML and serves as a tool to improve risk stratification. *Cancer Res*. (2020) 80:3983–92. doi: 10.1158/0008-5472.CAN-20-0283

31. Ottesen JT, Pedersen RK, Dam MJB, Knudsen TA, Skov V, Kjær L, et al. Mathematical modeling of MPNs offers understanding and decision support for personalized treatment. *Cancers*. (2020) 12:2119. doi: 10.3390/cancers12082119

32. Mosca M, Hermange G, Tisserand A, Noble R, Marzac C, Marty C, et al. Inferring the dynamics of mutated hematopoietic stem and progenitor cells induced by IFNα in myeloproliferative neoplasms. *Blood*. (2021) 138:2231–43. doi: 10.1182/blood.2021010986

33. Nanda S, Moore H, Lenhart S. Optimal control of treatment in a mathematical model of chronic myelogenous leukemia. *Math Biosci*. (2007) 210:143–56. doi: 10.1016/j.mbs.2007.05.003

34. Hermange G, Cournède PH, Plo I. Optimizing IFN alpha therapy against Myeloproliferative Neoplasms. *J Pharmacol Exp Ther*. (2023) 386:31–43. doi: 10.1124/jpet.122.001561

35. Sørensen AL, Mikkelsen SU, Knudsen TA, Bjørn ME, Andersen CL, Bjerrum OW, et al. Ruxolitinib and interferon-α2 combination therapy for patients with polycythemia vera or myelofibrosis: a phase II study. *Haematologica*. (2020) 105:2262–72. doi: 10.3324/haematol.2019.235648

36. Cosgrove J, Hustin LS, de Boer RJ, Perié L. Hematopoiesis in numbers. *Trends Immunol*. (2021) 42:1100–12. doi: 10.1016/j.it.2021.10.006

37. Lee-Six H, Øbro NF, Shepherd MS, Grossmann S, Dawson K, Belmonte M, et al. Population dynamics of normal human blood inferred from somatic mutations. *Nature*. (2018) 561:473–8. doi: 10.1038/s41586-018-0497-0

38. Marciniak-Czochra A, Stiehl T, Ho AD, Jäger W, Wagner W. Modeling of asymmetric cell division in hematopoietic stem cells—Regulation of self-renewal is essential for efficient repopulation. *Stem Cells Dev*. (2009) 18:377–86. doi: 10.1089/scd.2008.0143

39. Stiehl T, Marciniak-Czochra A. Stem cell self-renewal in regeneration and cancer: Insights from mathematical modeling. *Curr Opin Syst Biol*. (2017) 5:112–20. doi: 10.1016/j.coisb.2017.09.006

40. Wang W, Stiehl T, Raffel S, Hoang VT, Hoffmann I, Poisa-Beiro L, et al. Reduced hematopoietic stem cell frequency predicts outcome in acute myeloid leukemia. *Haematologica*. (2017) 102:1567–77. doi: 10.3324/haematol.2016.163584

41. Catlin SN, Busque L, Gale RE, Guttorp P, Abkowitz JL. The replication rate of human hematopoietic stem cells *in vivo*. *Blood*. (2011) 117:4460–6. doi: 10.1182/blood-2010-08

42. Harrison C, Kiladjian JJ, Al-Ali HK, Gisslinger H, Waltzman R, Stalbovskaya V, et al. JAK inhibition with ruxolitinib versus best available therapy for myelofibrosis. *New Engl J Med*. (2012) 366:787–98. doi: 10.1056/NEJMoa1110556

43. Vannucchi AM, Kiladjian JJ, Griesshammer M, Masszi T, Durrant S, Passamonti F, et al. Ruxolitinib versus standard therapy for the treatment of polycythemia vera. *New Engl J Med*. (2015) 372:426–35. doi: 10.1056/nejmoa1409002

44. Hasselbalch HC, Bjørn ME. MPNs as inflammatory diseases: the evidence, consequences, and perspectives. *Mediators Inflammation*. (2015) 2015). doi: 10.1155/2015/102476

45. Hasselbalch HC, Silver RT. New perspectives of interferon-alpha2 and inflammation in treating philadelphia-negative chronic myeloproliferative neoplasms. *HemaSphere*. (2021) 5:e645. doi: 10.1097/HS9.0000000000000645

46. Andreoli A, Verger E, Robin M, Raffoux E, Zini JM, Rousselot P, et al. Clinical resistance to ruxolitinib is more frequent in patients without MPN-associated mutations and is rarely due to mutations in the JAK2 kinase drug-binding domain. *Blood*. (2013) 122:1591–1. doi: 10.1182/blood.v122.21.1591.1591

47. Harrison CN, Schaap N, Mesa RA. Management of myelofibrosis after ruxolitinib failure. *Ann Hematol*. (2020) 99:1177–91. doi: 10.1007/s00277-020-04002-9

48. Asp J, Skov V, Bellosillo B, Kristensen T, Lippert E, Dicker F, et al. International external quality assurance of JAK2 V617F quantification. *Ann Hematol*. (2019) 98:1111–8. doi: 10.1007/s00277-018-3570-8

frontiers | Frontiers in Immunology

TYPE Hypothesis and Theory
PUBLISHED 08 May 2024
DOI 10.3389/fimmu.2024.1373738

OPEN ACCESS

EDITED BY
Vladimir A. Kuznetsov,
Upstate Medical University, United States

REVIEWED BY
Subhas Khajanchi,
Presidency University, India
Deni Hardiansyah,
University of Indonesia, Indonesia

*CORRESPONDENCE
Paolo Castorina
paolo.castorina@ct.infn.it

RECEIVED 20 January 2024
ACCEPTED 15 April 2024
PUBLISHED 08 May 2024

CITATION
Castorina P, Castiglione F, Ferini G, Forte S, Martorana E and Giuffrida D (2024) Mathematical modeling of the synergistic interplay of radiotherapy and immunotherapy in anti-cancer treatments.
Front. Immunol. 15:1373738.
doi: 10.3389/fimmu.2024.1373738

Mathematical modeling of the synergistic interplay of radiotherapy and immunotherapy in anti-cancer treatments

Paolo Castorina[1,2,3]*, Filippo Castiglione[4,5], Gianluca Ferini[6,7], Stefano Forte[1], Emanuele Martorana[1] and Dario Giuffrida[1]

[1]Genomics and molecular oncology unit, Istituto Oncologico del Mediterraneo, Viagrande, Italy, [2]Istituto Nazionale di Fisica Nucleare, Sezione di Catania, Catania, Italy, [3]Faculty of Mathematics and Physics, Charles University, Prague, Czechia, [4]Biotech Research Center, Technology Innovation Institute, Abu Dhabi, United Arab Emirates, [5]Institute for Applied Computing, National Research Council of Italy, Rome, Italy, [6]Radiotherapy Unit, REM Radioterapia, Viagrande, Italy, [7]School of Medicine, University Kore of Enna, Enna, Italy

Introduction: While radiotherapy has long been recognized for its ability to directly ablate cancer cells through necrosis or apoptosis, radiotherapy-induced abscopal effect suggests that its impact extends beyond local tumor destruction thanks to immune response. Cellular proliferation and necrosis have been extensively studied using mathematical models that simulate tumor growth, such as Gompertz law, and the radiation effects, such as the linear-quadratic model. However, the effectiveness of radiotherapy-induced immune responses may vary among patients due to individual differences in radiation sensitivity and other factors.

Methods: We present a novel macroscopic approach designed to quantitatively analyze the intricate dynamics governing the interactions among the immune system, radiotherapy, and tumor progression. Building upon previous research demonstrating the synergistic effects of radiotherapy and immunotherapy in cancer treatment, we provide a comprehensive mathematical framework for understanding the underlying mechanisms driving these interactions.

Results: Our method leverages macroscopic observations and mathematical modeling to capture the overarching dynamics of this interplay, offering valuable insights for optimizing cancer treatment strategies. One shows that Gompertz law can describe therapy effects with two effective parameters. This result permits quantitative data analyses, which give useful indications for the disease progression and clinical decisions.

Discussion: Through validation against diverse data sets from the literature, we demonstrate the reliability and versatility of our approach in predicting the time evolution of the disease and assessing the potential efficacy of radiotherapy-immunotherapy combinations. This further supports the promising potential of the abscopal effect, suggesting that in select cases, depending on tumor size, it may confer full efficacy to radiotherapy.

KEYWORDS

mathematical modeling, Gompertz law, radiotherapy, immune response, abscopal effect, immunotherapy

1 Introduction

Immunological experiments during the last two decades have answered many important questions related to the causal relationship between chronic inflammation and carcinogenesis. The presence of inflammatory cells in the cancer milieu raises the question of the tumor progression despite a likely immune system reaction to tumor antigens. This aspect is particularly important since untreated tumors grow according to non-linear, macroscopic, laws as the Gompertz law (GL) Gompertz (1); Norton (2); Vaghi et al. (3) or the logistic one (LL) Verhulst (4); Vaghi et al. (3). Therefore those growth patterns emerge, at a larger level of magnification, from many microscopic biological factors, which turn out to be summarized by simple mathematical descriptions.

Since prolonged inflammation is a hallmark of cancer Hiam-Galvez et al. (5), initiating tumor genesis or supporting tumor growth, and the global immune response is significantly altered during tumor progression, immunotherapy is becoming a valid option in cancer treatment. However, the immune response can be detrimental rather than helpful [see, for example, Lin et al. (6)]: individual auto-antibodies play an antagonist role in cancer, but the agonist auto-antibody in some cancer patients turned out to be deleterious and harmful.

Some preclinical and clinical evidence confirm the synergistic action of radiotherapy (RT) and immunotherapy against the tumor cells Zhao and Shao (7). Although The intrinsic sensitivity to radiation is patient-specific Puglisi et al. (8); Puglisi et al. (9) and may depend on different factors, RT is able to ablate cancer cells not only by directly induced necrosis or apoptosis but also by triggering an immune response that actively recruits immune cells within the tumor microenvironment. For example, RT promotes the release of tumor-associated antigens, which, once processed by antigen-presenting cells (APCs), prime $CD8^+$ and $CD4^+$ T cells in the draining lymph nodes. These lymphocytes attack both primary tumor and metastatic sites, posing the biological basis of the *in situ* vaccination driving the so-called abscopal effect Ngwa et al. (10); Mole (11); Demaria et al. (12): RT induces a systemic behavior that can activate the immune response against metastasis, i.e., in locations that are far from the RT-treated primary tumor.

The involvement of the immune system has been demonstrated in different experimental models such as melanoma Twyman-Saint Victor et al. (13), colorectal Dovedi et al. (14) and breast cancers Demaria et al. (15), but the clinical presentation where considered anecdotal or at least rare.

Its rarity in clinical practice is likely due to the simultaneous engagement of immune escape mechanisms, such as the recruitment of regulatory $CD4^+$ (Treg) and myeloid-derived suppressor cells counterbalancing the anti-tumor $CD8^+$ T cell-mediated effects, and the tumor release of hypoxia-inducible factors with pro-survival activity Ji et al. (16).

More generally, susceptibility to the abscopal effect has been associated with several biological factors, such as tumor size or oxygen levels in tumor tissues. Indeed, the presence of hypoxic regions results in both increased resistance to the lethal effect of radiation mediated by reactive oxygen species (ROS) production and an immune suppressive tumor landscape ruled by Treg-recruiting chemokines and impaired APC function McNamee et al. (17); Castorina et al. (18)

Mathematical modeling approaches have become increasingly abundant in describing immunotherapy and its synergy with RT Dewan et al. (19) Agur and Vuk-PavlovićCheck that all equations and special characters are displayed correctly. (20) Walker and Enderling (21); Ng and Dai (22); Serre et al. (23) Gong et al. (24) Marconi et al. (25); Vanpouille-Box et al. (26); Chakwizira et al. (27); Kosinsky et al. (28); Liu et al. (29); Valentinuzzi et al. (30); Friedrich et al. (31); Malinzi et al. (32); Bekker et al. (33). Indeed, the complexity of cancer provides challenges and opportunities for new developments, and mathematical formulations contribute by helping to elucidate mechanisms and by quantitative predictions that can be validated experimentally Agur and Vuk-Pavlović (20); Altrock et al. (34); Brady and Enderling (35) .

A large part of mathematical models on tumor growth and therapies are based on sets of coupled differential equations. The number of equations increases together with the details of the biological description and this implies a large number of parameters and initial conditions to be specified. The detailed analyses are often so complex to require surrogate models for a reliable determination of the parameters Browning and Simpson (36).

On the other hand, more economical models introduce a macroscopic evolution of tumor growth and therapy with fewer parameters and a coarse-grain dynamical evolution Norton (2); Wheldon (37); Vaghi et al. (3); Guiot et al. (38); Castorina et al. (39); Castorina et al. (40).

This is the key point to obtain an effective quantitative control of the tumor progression. Indeed, microscopic models, which have the advantage of a deep understanding of the biological dynamics, of the physiologically-based pharmacokinetic [see for example Maaß et al. (41)] and of the possible translation to different populations/diseases, require many parameters and, although some of them can be determined by previous analyses, the parametric error propagation will produce a large band of fluctuation in the prediction of the quantitative evolution of the disease. Therefore we prefer to apply macroscopic growth laws of the sigmoid family with two parameters. Our choice of the GL is due to the result that untreated tumor growth has been better described by it (see Vaghi et al. (3) for a recent study). Moreover, in a transplantable rat tumor, it was shown that control and regrowth curves after radiotherapy could be fitted by the same Gompertzian law, provided adjustments for the initial lag and the estimated number of clonogens immediately after irradiation were performed [Jung et al. (42)]. Gompertzian growth has been assumed to describe human tumor repopulation during fractional radiotherapy also in Hansen et al. (43) and by O'Donoghue (44).

The main motivation of the proposed approach is, in our opinion, its complementary role in the clinical evaluation of disease progression, often based on macroscopic variables, and the better parameter identification, thus increasing model verifiability Braakman et al. (45).

Finally, this method offers a clear description of the complex interplay between radiotherapy, immunotherapy, and tumor progression, providing insights for advancing cancer treatment strategies that harness the abscopal effect.

The paper is structured as follows: the mathematical model, based on the GL and on the definition of the effective GL parameters, is recalled in the next section (Appendices A, B and C contain the corresponding calculations). Different macroscopic growth laws (as the LL) can be applied, without changing the underlying method. The emerging phenomenological approach, based on the suitable redefinition of the two GL parameters to describe the data, is reported in Section 3. The final sections are devoted to discussion and to the possible clinical use of the phenomenological model.

2 Methods

The proposed method is based on the mathematical model reported in detail in Appendices A, B and C in the Supplementary Materials. In what follows, the assumptions and some exact results are reported. Then, the phenomenological model is discussed.

2.1 Mathematical modeling

A general classification of macroscopic growth laws is reported in Castorina et al. (39) Castorina and Blanchard (46). For a population $N(t)$ they are solutions of a general differential equation that can be written as

$$\frac{1}{N(t)}\frac{dN(t)}{dt} = f[N(t)], \tag{1}$$

where $f(N)$ is the specific growth rate and its N dependence describes the feedback effects during the time evolution. If in Equation 1 $f(N)$ becomes constant, the growth follows an exponential pattern.

The untreated tumor progression is described by the GL Norton (2); Vaghi et al. (3), solution of the previous equation (see Data Sheet 1) with

$$f[N(t)] = a - k\ \ln\frac{N(t)}{N_0} = k\ \ln\frac{N_\infty}{N(t)} \tag{2}$$

where a,k,N_0 are constants that respectively indicate the exponential growth, the limiting factor, the initial cell number and N_∞ is the carrying capacity ($N_\infty = N(0)exp(a/k)$).

For untreated tumors, the GL emerges from microscopic, biological mechanisms where natural/adaptive immunity is taken into account Berendt and North (47); Gonzalez et al. (48); Castorina and Carco' (49) The further effects of immune therapy, $I(t)$, can be described by a modification of the previous Equation 2 as follows (see for example Wheldon (37))

$$\frac{1}{N(t)}\frac{dN(t)}{dt} = k\ln\frac{N\infty}{N(t)} - \gamma \mathrm{I}(t) \tag{3}$$

where γ is a constant.Notice that the sign of γ indicates the agonist or antagonist effect of the immune response: a negative γ increases the specific growth rate. The variable $I(t)$ generically refers to the *passive* immunity resulting from the injection of anti-cancer-specific monoclonal antibodies i.e., the drug effects. However, it is, in general, unknown and requires a specific model. An example is the model of immunotherapeutic drug T11 target structure in the progression of malignant gliomas Khajanchi and Ghosh (50) Khajanchi and Banerjee (51).

The general solution of the previous equation and the IT effects on the tumor progression are discussed in Mathematical Formalism. For illustrative purposes, two specific cases are analyzed: $I(t) = I(0) = constant$ and $I(t) = I(0)exp(-\rho t)$. The role of the therapy can be assimilated to a redefinition of an effective carrying capacity (in the first of the two cases) and, in general, in the introduction of effective, time and therapy dependent, parameters a_{eff}, k_{eff} or N_∞^{eff}, k_{eff}, whose quantitative relation with $I(t)$ is given in Mathematical Formalism. The introduction of an effective carrying capacity is well-known in population dynamics Royama (52). For example, the invention and diffusion of technologies lift the growth limit. Its possible time dependence is usually included by (at least) another differential equation, coupled with the growth equation. This will increase the number of parameters and initial conditions and, therefore, in our computational method the two effective parameters will be determined by data fits, giving a phenomenological indication about the disease progression.

There are different outcomes following an immune response to cancer Lin et al. (6): i) a surveillance role that inhibits the initiation and

progression of the cancer; ii) the possibility that under certain conditions the immune response may nourish rather than curtail tumor growth. In other terms, monoclonal antibodies can exert antagonistic as well as sympathetic effects on tumor growth Lin et al. (6).

This possibility translates into a direct comparison among the parameters that describe the immunotherapy effects in Equation 3 and its solutions and the available data. For example, the determination of the crucial sign of the constant γ.

Let us now consider the combination of immune therapy (IT) and radiotherapy (RT). As a first step, we study the case of independent effects, i.e. no synergy between IT and RT.

The effect of radiotherapy is described by the linear quadratic model (LQM). Denoting by $N(t^-), N(t^+)$ respectively the cell number before and after the single dose d at time t, the RT effect is given by

$$N(t^+) = N(t^-)e^{-D} = N(t^-)e^{-\alpha d-\beta d^2} \tag{4}$$

where α and β are constants (numerically $\beta \simeq \alpha/10$) and d is the dose, Van Leeuwen et al. (53). The result in Equation 4 assumes an instantaneous effect of the RT, which could be, in general, not strictly applicable. Also, In this case, the therapy and immune response effects can be translated in the definition of effective parameters of the GL (see Mathematical Formulation).

The number of tumor cells after n_f treatments at time $t_n, t_{n+1}, t_{n+2}, \ldots t_{nf}$ turns out to be (see Mathematical Formalism)

$$N(t_{n_f}^+) = N(t_0)e^{ln\frac{N_\infty}{N(t_0)}\left[1-e^{-k\left(t_{n_f}-t_0\right)}\right]-\bar{W}(t_{n_f},t_0)-D_{n_f}} \tag{5}$$

with the functions D_{n_f} and $\bar{W}(t_{n_f}, t_0)$ as described in Mathematical Formalism.

According to Equation 5, if

$$ln\frac{N_\infty}{N(t_0)}\left[1-e^{-k\left(t_{n_f}-t_0\right)}\right] - \bar{W}(t_{n_f}, t_0) - D_{n_f} < 0 \tag{6}$$

the tumor cell number decreases and the time evolution of the diseases moves toward complete recovery.

Therefore, although RT and IT are considered independent, if the effects of RT are such that

$$ln\frac{N_\infty}{N(t_0)}\left[1-e^{-k\left(t_{n_f}-t_0\right)}\right] \simeq D_{n_f} \tag{7}$$

then, a small impact of the immunotherapy, $\bar{W}$, can produce a tumor volume regression. Moreover, the critical conditions in Equations (6, 7) depend on the fractioning of the radiotherapy, since different schedules give different values of D_{n_f} and $\bar{W}(t_{n_f}, t_0)$. Therefore, the previous conditions correspond to optimal control of the therapy effects, Khajanchi and Banerjee (54); Khajanchi (55); Khajanchi and Banerjee (56).

2.2 The synergy between immune and radio therapies

In the macroscopic framework, the description of the synergy between RT and IT requires a new term in the specific rate, which takes into account the immune response activated by RT, i.e.

$$\frac{1}{N}\frac{dN}{dt} = kln\left(\frac{N_\infty}{N}\right) - \gamma I(t) - \delta Y(t)F(d,t) \tag{8}$$

where δ is a constant, $F(d,t)$ is a function of the dose d and of the time series of the treatments on the tumor, quantifying the cell-killing effect of the adaptive immune response $Y(t)$, triggered by the RT. $Y(t)$ is different from $I(t)$ as it represents the outcome of the active immunization due to antigenic peptides coming from the disintegration of tissues hit by radiotherapy, and following the inflammation. To be more specific, $Y(t)$ represents the immune response to tumor-associated antigens, promoted by the inflammation context due to the damage perpetrated by RT. Also, it must be specified that this immune response has a chance to exert an effect only before evasion mechanisms are established by the tumor (factors that are not counted in the present model).

If $d = 0$, $F(d,t) = 0$ there is no synergy. The specific form of the function $F(d,t)$ requires a microscopic model, however one expects that the coupling $Y(t)F(d,t)$, i.e. the immune activation due to RT, has a typical time decay, τ, after the single dose radiotherapy described by the LQM. For the primary tumor, the parameter δ is small, i.e., $\delta << 1$ and the synergy is small. The abscopal effect is described by considering a finite value of δ for metastases that are far away from the primary tumor location. The result for the time evolution of the abscopal effect is given in Mathematical Formalism.

3 Results

According to the mathematical approach in the previous section a phenomenological, simplified, method of analysis of the experimental data emerges. Indeed, a large part of the therapy and immune response effects can be assimilated to a redefinition of the GL parameters, with time and treatment dependence, which turns out to be detailed enough to compare with data. This phenomenological, simpler, procedure facilitates the validation of the model [Braakman et al. (45)] with respect to more complex analytical approaches, as discussed later.

Moreover, the function $I(t), W(t), Y(t)$ in the previous differential equations are largely unknown, therefore the data fits of the effective GL parameters (see the general formulas in Mathematical Formalism) give model-independent information about the role of IT and RT.

3.1 Analysis of experimental data - immune therapy

In ref. Lin et al. (6) the different immune responses to cancer have been described. The authors highlight the agonist and antagonist effects of, respectively, AB93 and AB641 autoantibodies for the growth factor receptor TrkB in patients with breast cancer. After injection of MDA-MB-231 cells in immunodeficient mice they show the response to treatment, for different dosages of autoantibodies, measuring tumor growth. In particular, the data on the effects of AB641 and AB93 on tumor

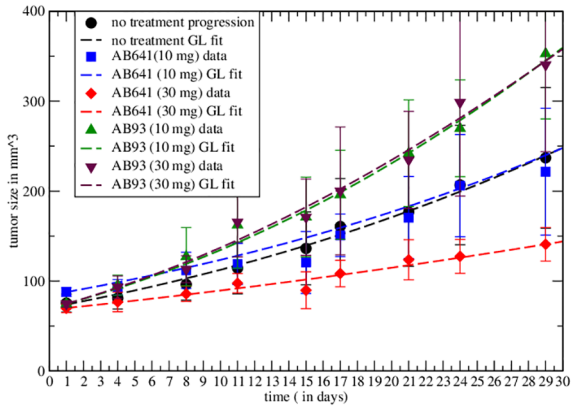

FIGURE 1
Comparison of the effective GL with data from the literature for untreated tumor and immunotherapy results. In the graph the symbols represent real data recorded and the dashed curves represent the Gompertzian fit, the colors are paired for both results. Fitted parameters are reported in Table 1.

progression can be analyzed in the proposed macroscopic approach by Equation 3, by redefining GL parameters. Initially, one has to fit the untreated tumor progression data by GL to determine the corresponding parameters. Then, one repeats the analysis with immunotherapy. The results are shown in Figure 1, which clearly reveal the agonist or antagonist role of the different antibodies.

The experimental result in the case of therapy can be fitted by redefining the GL parameters with respect to the untreated ones (see Equation S2, Equation S23 and Mathematical Formalism in Supplementary Material). The values are reported in Table 1. The agonist effects increase both parameters, producing faster growth, corresponding to a negative γ in Equation 3, whereas the antagonistic effect induces tumor depletion. Notice that the change in the GL parameters, i.e. of the therapy, implies a modification of the exponential rate and the carrying capacity with respect to the untreated tumor.

Non-linear curve fitting was made using Grace (version 5.1.25) Dataset Grace (57), data fitted by GL effective parameters are promising. The correlation coefficients and the root mean squared relative errors are respectively given by (0.982,0.062),(0.977,0.052), (0.995,0.051),(0.992,0.058),(0.996,0.04) for AB641/30 (red curve in Figure 1), AB641/10 (blue), AB93/10 (green), AB93/30 (black triangle) and untreated case.

TABLE 1 GL effective parameters of the comparison in Figure 1 (see Equation S23 in Supplementary Material.

Monoclonal antibody	a_{eff}	k_{eff}
AB641 (10 mg)	0.0285 ± 0.0037	0.0096 ± 0.0012
AB641 (30 mg)	0.034 ± 0.0054	$4.7 * 10^{-5} \pm 1.1 * 10^{-6}$
Untreated	0.049 ± 0.0008	0.011 ± 0.00016
AB93 (10 mg)	0.0714 ± 0.0069	0.02 ± 0.0016
AB93 (30 mg)	0.075 ± 0.0085	0.024 ± 0.002

Statistical error based on χ^2 per degree of freedom.
Parameters in day^{-1}.

3.2 Analysis of experimental data - RT and abscopal effect

The abscopal effect has been experimentally studied in Nesseler et al. (58) by inoculation of undifferentiated fibrosarcoma cells (FSA1) into immunocompetent mice to simulate primary and metastatic conditions, successively divided in four treatment groups: no treatment, anti-PD-1 monoclonal antibody alone, RT alone, and combination of anti-PD-1 with RT.

Initially, only the effect of RT on the primary has been detected, showing a critical dose administration for tumor regression [Figure 2A of ref. Nesseler et al. (58)]. The limited role of anti-PD-1 on the untreated primary tumor has been observed [Figure 2B of ref. Nesseler et al. (58)] and it has been checked that the RT on the primary has no direct effect on the implanted secondary. Finally, the synergy between IT and RT has been verified by the regression of the metastasis.

Let us first consider the data on the primary tumor, treated by RT only, with three treatments of 8 Gy on days 9,10 and 11 after the injection of the cancer cells. The qualitative analysis [Figure 2A of ref. Nesseler et al. (58)] clearly indicates that the LQM with instantaneous cell killing effect is not able to reproduce the observed effect, due to a delay between the treatments (on days 9,10 and 11) and the regression behavior (i.e., a negative specific rate), starting on day 15, Lim et al. (59); McMahon (60). Therefore, more complex dynamics are in place, which, however, can still be described by a GL pattern. As discussed, the effective parameters can be time-dependent (see Equation S23-S30 in Mathematical Formalism) due to the therapy and the results are reported in Figures 2, 3 respectively for the lower and upper data sets of Figure 2A of ref. Nesseler et al. (58). The corresponding fitted effective parameter values are given in Tables 2, 3. The (∗) indicates that the fitted parameter a_{eff} has a linear time dependence $a_{eff} \rightarrow a_{eff}$ $(t - t_0)$. This time dependence and the sign change of k_{eff}, compared

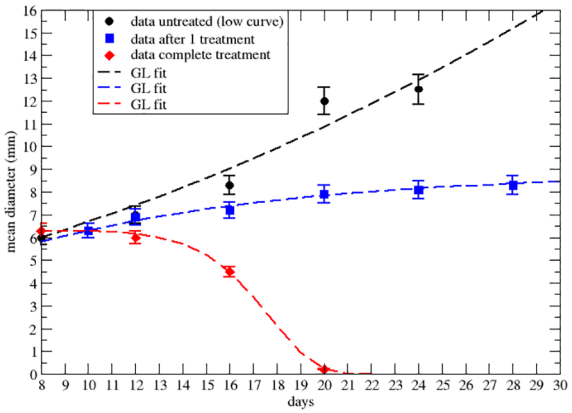

FIGURE 2
Effective GL fit of literature data with effective parameters of the lower data set of Figure 2A of ref.Nesseler et al. (58). Black point and the dashed line represent respectively real data and Gompertzian fitting. Blue squares and curve are data and GL fit after the first 8Gy RT treatment. The red rhombus and curve are data and GL after three treatments of 8Gy each. Parameters reported in Table 2.

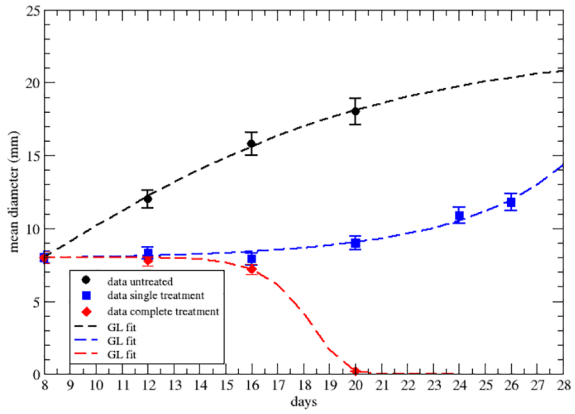

FIGURE 3
GL fit of literature data with effective parameters of the upper data set of Figure 2A of ref.Nesseler et al. (58), where the untreated data are in black, blue for one shot of 8Gy of irradiation and red for three 8Gy shots. Parameter reported in Table 3.

to the untreated case, signal that the therapy produces a complete depletion of the tumor size, analogously to the extinction in population dynamics.

The strong signal of the change of sign in the effective parameters can also be summarized by plotting the specific rate ($1/NdN/dt$), in Figures 4, 5, where its negative value indicates the complete tumor regression trend.

It should be stressed that the approach with GL effective parameters, suggested by the more rigorous previous mathematical model (see Mathematical Formalism), is a phenomenological one with the aim of a simplified clinical, but quantitative, understanding of the tumor progression at a more personalized level (see next discussion section).

The final analysis concerns the abscopal effect, according to Equation 8 with $\gamma = 0$. Let us assume: a) an exponential decay of the immune response with a time delay τ between the RT on the primary and the immunological effect on the secondary; b) the activated immune system continues its effect on the secondary with an exponential rate corresponding to the specific rate obtained at the end of the RT.

In other words, if t_{in} is the starting day of RT on the primary, for $t < t_{in}$ the metastatic site evolves according to the GL progression with the untreated parameters. At t_{in} the RT starts and the immune system targets the secondary (see Equation 8 and its solution reported in Mathematical Formalism). At the end of the RT, the immunity response continues to reduce the metastasis with an exponential behavior if the specific rate turns out to be negative.

In Figure 6 the result is depicted, i.e., the abscopal effect, according to the previous approach, for different values of the parameter $I(0)$, determining the response of the immune system on the secondary induced by RT (see Mathematical Formalism).

4 Discussion

The phenomenological approach, based on the previous mathematical formulation, consists in fitting the specific rate data

TABLE 2 GL effective parameters of the comparison in Figure 2 (see Equation S23 in Supplementary Material).

Tumor size	a_{eff}	k_{eff}
untreated	0.054 ± 0.0031	0.0164 ± 0.0015
after first dose	0.036 ± 0.0058	0.11 ± 0.017
end of therapy (∗)	$-5.06 * 10^{-4} \pm 2 * 10^{-6}$	−0.464 ± 0.003

Parameters in day^{-1}. Statistical error based on χ^2 per degree of freedom.

by GL with effective parameters. Let us recall that the specific rate is much more reliable than the volume tumor variation, in determining its progression and the phase of growth or decrease.

We are aware that the coarse-grain proposed approach misses the detailed dynamics and can be considered an oversimplified description since the underlying pathways, Ng and Dai (22); Serre et al. (23); Marconi et al. (25); Liu et al. (29); Valentinuzzi et al. (30); Friedrich et al. (31); Bekker et al. (33) are summarized by the macroscopic Equation 8. However, one has to recall that, independently of the microscopic conditions, a large part of untreated tumors follow the GL (see Vaghi et al. (3) for a recent review) and that with a small number of parameters, one gets quantitative clinical indications for personalized treatments. If, for example, a patient gets a small specific rate by RT on the primary tumor, then a small contribution of IT might be able to result in a complete recovery.

The abscopal effect has been described by a macroscopic coupling between RT and immune system response, where the initial progression of the metastasis follows the GL with untreated primary tumor parameters. This is a reasonable assumption although the in-situ conditions can produce different results.

According to the specific conditions recalled in the introduction, choosing the best dose fractionation and timing with respect to immunotherapy is difficult. Notoriously, the use of protracted RT schedules (standard fractionation or slight hypofractionation) is discouraged since radiosensitive lymphocytes are cleared out from tumor tissues at each fraction delivery, thus preventing their anti-tumor function, Filatenkov et al. (61). Conversely, large doses per fraction are effectively immunogenic, Muraro et al. (62). In particular, doses below 12 Gy are the most suitable for enhancing the anti-tumor immune response as over such a threshold there is the degradation of immunogenic cytosolic DNA by an exonuclease, Trex, whose expression, as evaluated in preclinical experiments, is cell line-dependent and increases with increasing radiation dose Dewan et al. (19); Vanpouille-Box et al. (26). On the other side, even very low doses per fraction (< 1 Gy) seem to activate macrophages against cancer cells and stimulate T-cell immunity Klug et al. (63). Doses over

TABLE 3 GL effective parameters of the comparison in Figure 3 (see Equation S23 in Supplementary Material.

Tumor diameter (mm)	a_{eff}	k_{eff}
untreated	0.135 ± 0.011	0.131 ± 0.11
after first dose	$2.82 * 10^{-3} \pm 2 * 10^{-4}$	−0.184 ± 0.015
end of therapy (∗)	$-1.99 * 10^{-5} \pm 6 * 10^{-7}$	−0.783 ± 0.002

Parameters in day^{-1}. Statistical error based on χ^2 per degree of freedom.

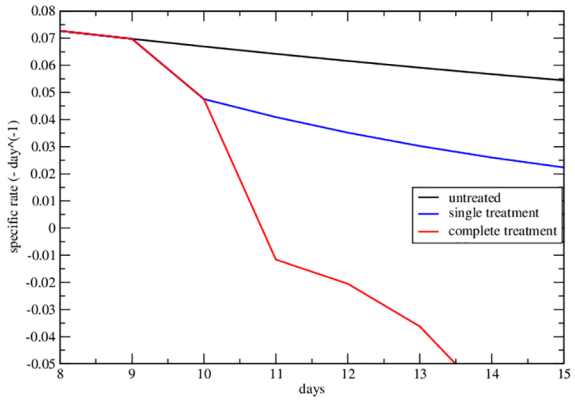

FIGURE 4
Specific rate of the lower data set of Figure 2A of ref. Nesseler et al. (58). The curves represent the specific growth rate day by day, the response to therapy is highlighted by a negative trend.

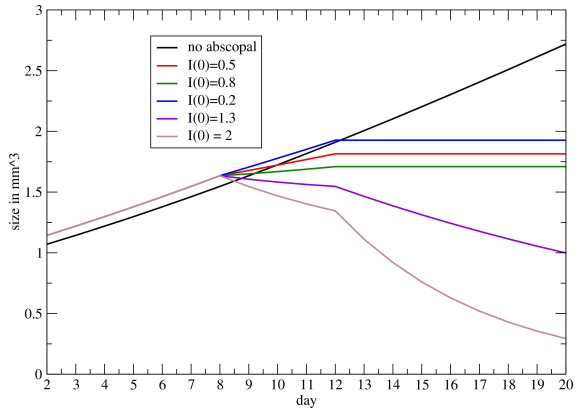

FIGURE 6
Progression on the metastatic volume, triggered by RT on the primary, for different values of the coupling between the immune system and RT (see Mathematical Formalism).

12 Gy are involved in the damage of tumor vasculature by activation of acid sphingomyelinase and production of ceramides, which culminate in vessel obliteration with subsequent tumor regression for insufficient nutrient and oxygen supply Song et al. (64). Therefore, the entire dose range used in clinical practice may be useful to control tumors and all RT fractionations combined with immunotherapy deserve clinical investigations.

Recently, old RT techniques simultaneously combining very different doses within the tumor, namely spatially fractionated radiation therapy (SFRT), are gaining new interest because of the assumption that tumor tissues spanning a wide dose range may benefit from multiple immune activation mechanisms, which eventually could be further boosted by ICI administration Ferini et al. (65); Tubin et al. (66). Given the ability of new instrumental exams to "map" tumor areas with different metabolisms, there is the possibility of modulating the dose distribution according to the oxygenation patterns inside the tumor to maximize both direct and indirect (immune-mediated) lethal effects of radiation Ferini et al. (67); Ferini et al. (68). With the latter approach, complete responses have been documented earlier than with classic homogeneously-delivered stereotactic RT doses and before ICI administration, likely implying rapid immune intervention enhanced and maintained by the addition of IT Ferini et al. (69).

All of the above considerations require the modeling of tumor response to RT and IT to help predict the best combination strategy, also given the inadequacy of current radiobiological mathematical models to comprehensively explain the results deriving from this association Ferini et al. (69).

In the proposed mathematical and computational approach, the fractionization effects are taken into account by the functions D_{n_f} and $\bar{W}(t_{n_f}, t_0)$ and a spatially non-homogeneous behavior can be easily implemented. However, a complete discussion requires a forthcoming devoted analysis.

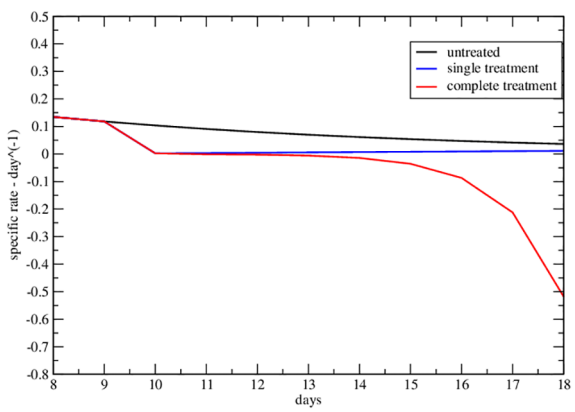

FIGURE 5
Specific rate of the upper data set of Figure 2A of ref. Nesseler et al. (58). The curves represent the specific growth rate day by day, the response to therapy is highlighted by a negative trend.

5 Conclusions

A comprehensive scope of the combined impact of radiotherapy and immunotherapy is vital for clinical decision-making. Yet, numerous mathematical models in existing literature prove overly complex, characterized by an abundance of differential equations, parameters, and initial conditions, rendering their practical implementation quite challenging.

In this study, we use a macroscopic mathematical approach that does not rely on the underlying microscopic dynamics. Instead, we propose a simplified model of the tumor progression using a Gompertz law, which involves just two parameters. Moreover, utilizing numerical solvers of the equations provided in the appendices is a straightforward process.

Examining how control influences system dynamics under radiation and/or drug therapy sheds light on the disease's temporal progression. This approach holds promise in assisting clinicians to make informed decisions by providing a clearer understanding of treatment outcomes, namely, assessing whether the therapy administered results in full recovery.

Besides its clinical relevance, our approach shows potential for additional experimental validation of the synergistic impact of the abscopal phenomenon on treatment outcomes.

We recognize the importance of conducting rigorous experimental investigations to solidify the theoretical basis of our approach. By performing targeted studies and gathering more empirical data, we aim to validate the approach in different conditions and the significance of the abscopal effect in influencing therapy outcomes. This experimental validation will provide a deeper understanding of the interplay between the administered treatment, tumor response, and the abscopal effect.

Moreover, our future research endeavors will focus on elucidating the mechanisms underlying the abscopal effect and quantifying its impact on treatment efficacy. By combining computational modeling with comprehensive experimental studies, we strive to enhance our understanding of this phenomenon and optimize therapeutic strategies accordingly. Ultimately, we aim to improve patient-oriented outcomes by harnessing the full potential of the abscopal effect in cancer therapy.

Data availability statement

Publicly available datasets were analyzed in this study. This data can be found here: https://figshare.com/articles/dataset/autoantibody_discovery/10302227; data on AB93 and AB641, platform figshare.

Author contributions

PC: Conceptualization, Formal analysis, Methodology, Writing – original draft. FC: Conceptualization, Data curation, Investigation, Validation, Writing – review & editing. GF: Methodology, Validation, Writing – original draft. SF: Funding acquisition, Methodology, Resources, Validation, Writing – review & editing. EM: Data curation, Investigation, Software, Validation, Writing – review & editing. DG: Funding acquisition, Resources, Supervision, Writing – review & editing.

Funding

The author(s) declare financial support was received for the research, authorship, and/or publication of this article. This research was totally funded by the department for productive activities of the Sicilian Region, project title: "DiOncoGen Diagnostica innovativa", PO FESR (grant number: G89J18000700007). This work is partially funded by the Italian Ministry of University and Research (MUR, grant "Heal Italia (Health Extended Alliance for Innovative Therapies, Advanced Lab-research, and Integrated Approaches of Precision Medicine, grant n. B83D22001050004).

Conflict of interest

The authors declare that the research was conducted in the absence of any commercial or financial relationships that could be construed as a potential conflict of interest.

The author(s) declared that they were an editorial board member of Frontiers, at the time of submission. This had no impact on the peer review process and the final decision.

Publisher's note

Supplementary material

The Supplementary Material for this article can be found online at: https://www.frontiersin.org/articles/10.3389/fimmu.2024.1373738/full#supplementary-material

MATHEMATICAL FORMALISM
Mathematical model for untreated tumor growth with GL, immune therapy, immune and radiotherapies, critical behavior, and abscopal effect.

References

1. Gompertz B. Xxiv. on the nature of the function expressive of the law of human mortality, and on a new mode of determining the value of life contingencies. in a letter to francis baily, esq. frs &c. *Philos Trans R Soc London*. (1825) 115:513–83. doi: 10.1098/rstl.1825.0026

2. Norton L. A gompertzian model of human breast cancer growth. *Cancer Res*. (1988) 48:7067–71.

3. Vaghi C, Rodallec A, Fanciullino R, Ciccolini J, Mochel JP, Mastri M, et al. Population modeling of tumor growth curves and the reduced gompertz model improve prediction of the age of experimental tumors. *PLoS Comput Biol*. (2020) 16: e1007178. doi: 10.1371/journal.pcbi.1007178

4. Verhulst P-F. Notice sur la loi que la population poursuit dans son accroissement. *Correspondance Mathématique Physique*. (1838) 10:113–21. doi: 10.4000/msh.2893

5. Hiam-Galvez KJ, Allen BM, Spitzer MH. Systemic immunity in cancer. *Nat Rev Cancer*. (2021) 21:345–59. doi: 10.1038/s41568-021-00347-z

6. Lin C-W, Xie J, Zhang D, Han KH, Grande G, Wu NC, et al. Immunity against cancer cells may promote their proliferation and metastasis. *Proc Natl Acad Sci*. (2020) 117:426–31. doi: 10.1073/pnas.1916833117

7. Zhao X, Shao C. Radiotherapy-mediated immunomodulation and anti-tumor abscopal effect combining immune checkpoint blockade. *Cancers (Basel)*. (2020) 12:2762. doi: 10.3390/cancers12102762

8. Puglisi C, Giuffrida R, Borzì G, Di Mattia P, Costa A, Colarossi C, et al. Radiosensitivity of cancer stem cells has potential predictive value for individual responses to radiotherapy in locally advanced rectal cancer. *Cancers (Basel)*. (2020) 12:2072–6694. doi: 10.3390/cancers12123672

9. Puglisi C, Giuffrida R, Borzì G, Illari S, Caronia F, Di Mattia P, et al. Ex vivo irradiation of lung cancer stem cells identifies the lowest therapeutic dose needed for tumor growth arrest and mass reduction in *vivo*. *Front Oncol*. (2022) 12:837400. doi: 10.3389/fonc.2022.837400

10. Ngwa W, Irabor O, Schoenfeld J, Hesser J, Demaria S, Formenti S. Using immunotherapy to boost the abscopal effect. *Nat Rev Cancer*. (2018) 18:313–22. doi: 10.1038/nrc.2018.6

11. Mole R. Whole body irradiation; radiobiology or medicine? *Br J Radiol*. (1953) 26:234–41. doi: 10.1259/0007-1285-26-305-234

12. Demaria S, Ng B, Devitt M, Babb J, Kawashima N, Liebes L, et al. Ionizing radiation inhibition of distant untreated tumors (abscopal effect) is immune mediated. *Int J Radiat Oncology Biology Phys*. (2004) 58:862–70. doi: 10.1016/j.ijrobp.2003.09.012

13. Twyman-Saint Victor C, Rech A, Maity A, Rengan R, Pauken K, Stelekati E, et al. Radiation and dual checkpoint blockade activate non-redundant immune mechanisms in cancer. *Nature*. (2015) 520:373–7. doi: 10.1038/nature14292

14. Dovedi S, Cheadle E, Popple A, Poon E, Morrow M, Stewart R, et al. Fractionated radiation therapy stimulates anti-tumor immunity mediated by both resident and infiltrating polyclonal t-cell populations when combined with pd1 blockade. *Clin Cancer Res*. (2017) 23:5514–26. doi: 10.1158/1078-0432.CCR-16-1673

15. Demaria S, Kawashima N, Yang A, Devitt M, Babb J, Allison J, et al. Immune-mediated inhibition of metastases after treatment with local radiation and ctla-4 blockade in a mouse model of breast cancer. *Clin Cancer Res*. (2005) 11:728–34. doi: 10.1158/1078-0432.728.11.2

16. Ji D, Song C, Li Y, Xia J, Wu Y, Jia J, et al. Combination of radiotherapy and suppression of tregs enhances abscopal antitumor effect and inhibits metastasis in rectal cancer. *J ImmunoTherapy Cancer*. (2018) 8:313–22. doi: 10.1136/jitc-2020-000826

17. McNamee E, Korns Johnson D, Homann D, Clambey E. Hypoxia and hypoxia-inducible factors as regulators of t cell development, differentiation, and function. *Immunol Res*. (2013) 55:58–70. doi: 10.1007/s12026-012-8349-8

18. Castorina P, Castorina L, Ferini G. Non-homogeneous tumor growth and its implications for radiotherapy: A phenomenological approach. *J Personalized Med*. (2021) 11:527. doi: 10.3390/jpm11060527

19. Dewan MZ, Galloway AE, Kawashima N, Dewyngaert JK, Babb JS, Formenti SC, et al. Fractionated but not single-dose radiotherapy induces an immune-mediated abscopal effect when combined with anti–ctla-4 antibodyfractionated radiation synergizes with immunotherapy. *Clin Cancer Res*. (2009) 15:5379–88. doi: 10.1158/1078-0432.CCR-09-0265

20. Agur Z, Vuk-Pavlović S. Mathematical modeling in immunotherapy of cancer: personalizing clinical trials. *Mol Ther*. (2012) 20:1–2. doi: 10.1038/mt.2011.272

21. Walker R, Enderling H. From concept to clinic: Mathematically informed immunotherapy. *Curr Probl Cancer*. (2016) 40(1):68–83. doi: 10.1016/j.currproblcancer.2015.10.004

22. Ng J, Dai T. Radiation therapy and the abscopal effect: a concept comes of age. *Ann Transl Med*. (2016) 4(6):118–20. doi: 10.21037/atm.2016.01.32

23. Serre R, Benzekry S, Padovani L, Meille C, André N, Ciccolini J, et al. Mathematical modeling of cancer immunotherapy and its synergy with radiotherapymodeling of radioimmunotherapy. *Cancer Res*. (2016) 76:4931–40. doi: 10.1158/0008-5472.CAN-15-3567

24. Gong C, Milberg O, Wang B, Vicini P, Narwal R, Roskos L, et al. A computational multiscale agent-based model for simulating spatio-temporal tumour immune response to pd1 and pdl1 inhibition. *J R Soc Interface*. (2017) 14:20170320. doi: 10.1098/rsif.2017.0320

25. Marconi R, Strolin S, Bossi G, Strigari L. A meta-analysis of the abscopal effect in preclinical models: Is the biologically effective dose a relevant physical trigger? *PLoS One*. (2017) 12:e0171559. doi: 10.1371/journal.pone.0171559

26. Vanpouille-Box C, Alard A, Aryankalayil MJ, Sarfraz Y, Diamond JM, Schneider RJ, et al. Dna exonuclease trex1 regulates radiotherapy-induced tumour immunogenicity. *Nat Commun*. (2017) 8:15618. doi: 10.1038/ncomms15618

27. Chakwizira A, Ahlstedt J, Nittby Redebrandt H, Ceberg C. Mathematical modelling of the synergistic combination of radiotherapy and indoleamine-2, 3-dioxygenase (ido) inhibitory immunotherapy against glioblastoma. *Br J Radiol*. (2018) 91:20170857. doi: 10.1259/bjr.20170857

28. Kosinsky Y, Dovedi SJ, Peskov K, Voronova V, Chu L, Tomkinson H, et al. Radiation and pd-(l) 1 treatment combinations: immune response and dose optimization via a predictive systems model. *J immunotherapy Cancer*. (2018) 6:1–15. doi: 10.1186/s40425-018-0327-9

29. Liu Y, Dong Y, Kong L, Shi F, Zhu H, Yu J. Abscopal effect of radiotherapy combined with immune checkpoint inhibitors. *J Hematol Oncol*. (2018) 11:1–15. doi: 10.1186/s13045-018-0647-8

30. Valentinuzzi D, Simončič U, Uršič K, Vrankar M, Turk M, Jeraj R. Predicting tumour response to anti-pd-1 immunotherapy with computational modelling. *Phys Med Biol*. (2019) 64:025017. doi: 10.1088/1361-6560/aaf96c

31. Friedrich T, Henthorn N, Durante M. Modeling radioimmune response—current status and perspectives. *Front Oncol*. (2021) 11:647272. doi: 10.3389/fonc.2021.647272

32. Malinzi J, Basita KB, Padidar S, Adeola HA. Prospect for application of mathematical models in combination cancer treatments. *Inf Med Unlocked*. (2021) 23:100534. doi: 10.1016/j.imu.2021.100534

33. Bekker RA, Kim S, Pilon-Thomas S, Enderling H. Mathematical modeling of radiotherapy and its impact on tumor interactions with the immune system. *Neoplasia*. (2022) 28:100796. doi: 10.1016/j.neo.2022.100796

34. Altrock PM, Liu LL, Michor F. The mathematics of cancer: integrating quantitative models. *Nat Rev Cancer*. (2015) 15:730–45. doi: 10.1038/nrc4029

35. Brady R, Enderling H. Mathematical models of cancer: when to predict novel therapies, and when not to. *Bull Math Biol*. (2019) 81:3722–31. doi: 10.1007/s11538-019-00640-x

36. Browning AP, Simpson MJ. Geometric analysis enables biological insight from complex non-identifiable models using simple surrogates. *PLoS Comput Biol*. (2023) 19:e1010844. doi: 10.1371/journal.pcbi.1010844

37. Wheldon TE. Mathematical models in cancer research. *Adam Hilger Publisher*. (1988).

38. Guiot C, Degiorgis PG, Delsanto PP, Gabriele P, Deisboeck TS. Does tumor growth follow a "universal law"? *J Theor Biol*. (2003) 225:147–51. doi: 10.1016/S0022-5193(03)00221-2

39. Castorina P, Delsanto P, Guiot C. Classification scheme for phenomenological universalities in growth problems in physics and other sciences. *Phys Rev Lett*. (2006) 96:188701. doi: 10.1103/PhysRevLett.96.188701

40. Castorina P, Carcò D, Guiot C, Deisboeck TS. Tumor growth instability and its implications for chemotherapy. *Cancer Res*. (2009) 69:8507–15. doi: 10.1158/0008-5472.CAN-09-0653

41. Maaß C, Sachs JP, Hardiansyah D, Mottaghy FM, Kletting P, Glatting G. Dependence of treatment planning accuracy in peptide receptor radionuclide therapy on the sampling schedule. *EJNMMI Res*. (2016) 6:1–9. doi: 10.1186/s13550-016-0185-8

42. Jung H, Krüger H-J, Brammer I, Zywietz F, Beck-Bornholdt H-P. Cell population kinetics of the rhabdomyosarcoma r1h of the rat after single doses of x-rays. *Int J Radiat Biol*. (1990) 57:567–89. doi: 10.1080/09553009014552701

43. Hansen O, Grau C, Bentzen SM, Overgaard J. Repopulation in the sccvii squamous cell carcinoma assessed by an in *vivo-in vitro* excision assay. *Radiotherapy Oncol*. (1996) 39:137–44. doi: 10.1016/0167-8140(96)01728-8

44. O'Donoghue JA. The response of tumours with gompertzian growth characteristics to fractionated radiotherapy. *Int J Radiat Biol*. (1997) 72:325–39. doi: 10.1080/095530097143329

45. Braakman S, Pathmanathan P, Moore H. Evaluation framework for systems models. *CPT Pharmacometrics Syst Pharmacol*. (2022) 11:264–289. doi: 10.1002/psp4.12755

46. Castorina P, Blanchard P. Unified approach to growth and aging in biological, technical and biotechnical systems. *SpringerPlus*. (2012) 1:1–5. doi: 10.1186/2193-1801-1-7

47. Berendt MJ, North RJ. T-cell-mediated suppression of anti-tumor immunity. an explanation for progressive growth of an immunogenic tumor. *J Exp Med*. (1980) 151:69–80. doi: 10.1084/jem.151.1.69

48. Gonzalez H, Hagerling C, Werb Z. Roles of the immune system in cancer: from tumor initiation to metastatic progression. *Genes Dev*. (2018) 32:1267–84. doi: 10.1101/gad.314617.118

49. Castorina P, Carco' D. Nutrient supply, cell spatial correlation and gompertzian tumor growth. *Theory Biosci*. (2021) 140:197–203. doi: 10.1007/s12064-021-00344-8

50. Khajanchi S, Ghosh D. The combined effects of optimal control in cancer remission. *Appl Mathematics Comput*. (2015) 271:375–88. doi: 10.1016/j.amc.2015.09.012

51. Khajanchi S, Banerjee S. Quantifying the role of immunotherapeutic drug t11 target structure in progression of Malignant gliomas: Mathematical modeling and dynamical perspective. *Math Biosci*. (2017) 289:69–77. doi: 10.1016/j.mbs.2017.04.006

52. Royama T. *Analytical population dynamics* Vol. 10. UK: Springer Science & Business Media (2012).

53. Van Leeuwen C, Oei A, Crezee J, Bel A, Franken N, Stalpers L, et al. The alfa and beta of tumours: a review of parameters of the linear-quadratic model, derived from clinical radiotherapy studies. *Radiat Oncol*. (2018) 13:1–11. doi: 10.1186/s13014-018-1040-z

54. Khajanchi S, Banerjee S. Influence of multiple delays in brain tumor and immune system interaction with t11 target structure as a potent stimulator. *Math Biosci*. (2018) 302:116–30. doi: 10.1016/j.mbs.2018.06.001

55. Khajanchi S. Stability analysis of a mathematical model for glioma-immune interaction under optimal therapy. *Int J Nonlinear Sci Numerical Simulation*. (2019) 20:269–85. doi: 10.1515/ijnsns-2017-0206

56. Khajanchi S, Banerjee S. A strategy of optimal efficacy of t11 target structure in the treatment of brain tumor. *J Biol Syst*. (2019) 27:225–55. doi: 10.1142/S0218339019500104

57. Dataset Grace. (2008). Available at: https://plasma-gate.weizmann.ac.il/Grace/.

58. Nesseler JP, Lee M-H, Nguyen C, Kalbasi A, Sayre JW, Romero T, et al. Tumor size matters—understanding concomitant tumor immunity in the context of hypofractionated radiotherapy with immunotherapy. *Cancers*. (2020) 12:714. doi: 10.3390/cancers12030714

59. Lim K, Chan P, Dinniwell R, Fyles A, Haider M, Cho Y-B, et al. Cervical cancer regression measured using weekly magnetic resonance imaging during fractionated radiotherapy: radiobiologic modeling and correlation with tumor hypoxia. *Int J Radiat Oncol Biol Phys*. (2008) 70:126–33. doi: 10.1016/j.ijrobp.2007.06.033

60. McMahon SJ. The linear quadratic model: usage, interpretation and challenges. *Phys Med Biol*. (2018) 64:01TR01. doi: 10.1088/1361-6560/aaf26a

61. Filatenkov A, Baker J, Mueller A, Kenkel J, Ahn G, Dutt S, et al. Ablative tumor radiation can change the tumor immune cell microenvironment to induce durable complete remissions. *Clin Cancer Res*. (2015) 21:3727. doi: 10.1158/1078-0432.CCR-14-2824

62. Muraro E, Furlan C, Avanzo M, Martorelli D, Comaro E, Rizzo A, et al. Local highdose radiotherapy induces systemic immunomodulating effects of potential therapeutic relevance in oligometastatic breast cancer. *Front Immunol*. (2017) 8:1476. doi: 10.3389/fimmu.2017.01476

63. Klug F, Prakash H, Huber P, Seibel T, Bender N, Halama N, et al. Low-dose irradiation programs macrophage differentiation to an inos+/m1 phenotype that orchestrates effective t cell immunotherapy. *Cancer Cell*. (2013) 24:589. doi: 10.1016/j.ccr.2013.09.014

64. Song C, Glatstein E, Marks L, Emami B, Grimm J, Sperduto P, et al. Biological principles of stereotactic body radiation therapy (sbrt) and stereotactic radiation surgery (srs): Indirect cell death. *Int J Radiat Oncology Biology Phys*. (2021) 110:21. doi: 10.1016/j.ijrobp.2019.02.047

65. Ferini G, Valenti V, Tripoli A, Illari S, Molino L, Parisi S, et al. Lattice or oxygen-guided radiotherapy: What if they converge? possible future directions in the era of immunotherapy. *Cancers (Basel)*. (2021) 13:3290. doi: 10.3390/cancers13133290

66. Tubin S, Vozenin M, Prezado Y, Durante M, Prise K, Lara P, et al. Novel unconventional radiotherapy techniques: Current status and future perspectives - report from the 2nd international radiation oncology online seminar. *Clin Trans Radiat Oncol*. (2023) 40:100605. doi: 10.1016/j.ctro.2023.100605

67. Ferini G, Parisi S, Lillo S, Viola A, Minutoli F, Critelli P, et al. Impressive results after "metabolism-guided" lattice irradiation in patients submitted to palliative radiation therapy: Preliminary results of lattice$_{01}$ multicenter study. *Cancers (Basel)*. (2022) 14:3909. doi: 10.3390/cancers14163909

68. Ferini G, Valenti V, Viola A, Umana G, Illari S, Parisi S, et al. First-ever clinical experience with magnetic resonance-based lattice radiotherapy for treating bulky gynecological tumors. *Anticancer Res*. (2022) 42:4641. doi: 10.21873/anticanres.15968

69. Ferini G, Castorina P, Valenti V, Illari S, Sachpazidis I, Castorina L, et al. A novel radiotherapeutic approach to treat bulky metastases even from cutaneous squamous cell carcinoma: Its rationale and a look at the reliability of the linear-quadratic model to explain its radiobiological effects. *Front Oncol*. (2022) 12:809279. doi: 10.3389/fonc.2022.809279

frontiers | Frontiers in Oncology

TYPE Original Research
PUBLISHED 31 May 2024
DOI 10.3389/fonc.2024.1352065

OPEN ACCESS

EDITED BY
Heiko Enderling,
University of Texas MD Anderson Cancer Center, United States

REVIEWED BY
Shixiang Wang,
Sun Yat-sen University Cancer Center (SYSUCC), China
Pirmin Schlicke,
Technical University of Munich, Germany

*CORRESPONDENCE
Svetlana Bunimovich-Mendrazitsky
svetlanabu@ariel.ac.il

RECEIVED 07 December 2023
ACCEPTED 02 April 2024
PUBLISHED 31 May 2024

CITATION
Yosef M and Bunimovich-Mendrazitsky S (2024) Mathematical model of MMC chemotherapy for non-invasive bladder cancer treatment.
Front. Oncol. 14:1352065.
doi: 10.3389/fonc.2024.1352065

Mathematical model of MMC chemotherapy for non-invasive bladder cancer treatment

Marom Yosef and Svetlana Bunimovich-Mendrazitsky*

Department of Mathematics, Ariel University, Ariel, Israel

Mitomycin-C (MMC) chemotherapy is a well-established anti-cancer treatment for non-muscle-invasive bladder cancer (NMIBC). However, despite comprehensive biological research, the complete mechanism of action and an ideal regimen of MMC have not been elucidated. In this study, we present a theoretical investigation of NMIBC growth and its treatment by continuous administration of MMC chemotherapy. Using temporal ordinary differential equations (ODEs) to describe cell populations and drug molecules, we formulated the first mathematical model of tumor-immune interactions in the treatment of MMC for NMIBC, based on biological sources. Several hypothetical scenarios for NMIBC under the assumption that tumor size correlates with cell count are presented, depicting the evolution of tumors classified as small, medium, and large. These scenarios align qualitatively with clinical observations of lower recurrence rates for tumor size $\leq$ 30[mm] with MMC treatment, demonstrating that cure appears up to a theoretical x[mm] tumor size threshold, given specific parameters within a feasible biological range. The unique use of mole units allows to introduce a new method for theoretical pre-treatment assessments by determining MMC drug doses required for a cure. In this way, our approach provides initial steps toward personalized MMC chemotherapy for NMIBC patients, offering the possibility of new insights and potentially holding the key to unlocking some of its mysteries.

KEYWORDS

mathematical oncology, tumor-immune interactions, individual-based model, drug dose determination, non-linear dynamics

1 Introduction

Cancer diseases rank as a leading cause of death and a major health concern in modern society (1). In particular, bladder cancer (BC) is among the most prevalent cancer types in the world, with approximately 573,000 new cases and 213,000 deaths annually (1). The highest incidence rates are observed in Europe, North Africa, West Asia, and North America (2). BC's high burden on both patients and health-care systems is mainly

attributed to its intensive treatment and monitoring requirements, making it one of the most economically costly cancers (3).

Research into the development of cancer cures continues to be a highly challenging process despite tremendous scientific, pharmaceutical, and technological progress in recent decades (4–6). Various studies suggest confronting medical decision-making challenges via collaboration between healthcare professionals monitoring and interpreting data to help diagnose or treat patients, and mathematicians developing new models and computational simulations to characterize tumors and to pave the road to personalized medical treatments (7–12). Taken jointly, these contributions represent a step toward the development of quantitative methods in the complex and nonlinear biology of tumors, in particularly, using differential equations (13, 14).

MMC, epirubicin, and gemcitabine are anti-tumor chemotherapeutic drugs used for non-invasive BC (15, 16). MMC is an anti-tumor antibiotic discovered in the 1950s from *Streptomyces caespitosus* cultures, which selectively inhibits DNA synthesis by cross-linking complementary strands of the double helix, leading to cell death (17). Its large molecular weight limits physiologically systemic uptake in NMIBC, making this drug generally well tolerated (18).

To mathematically analyze BC's growth under the treatment of MMC chemotherapy, we studied the biological phenomenon of bladder tumor evolution and the current treatment protocols. Over the past decades, the creation of mathematical models for BC treatments has been driven by the need to address shortcomings in existing treatment protocols, such as their limited efficacy and lack of personalization (19–23). Among these, one study conducted by Burgos Simón et al. (19) involved the use of two distinct systems of difference equations. One system models the interactions between tumor cells and inflammatory cells, while the other addresses the subsequent phase involving tumor removal surgery, followed by Bacillus Calmette-Guérin (BCG) immunotherapy treatment. Their model analyzes hospital-sourced data to describe and predict fluctuations in tumor size and immune responses. In Shaikhet and Bunimovich-Mendrazitsky (21), the authors dealt with BC under BCG immunotherapy treatments, and highlighted the importance of the interplay of multiple parameters on the success of immunotherapy. The model in Nave et al. (22) deals with improvement of BCG immunotherapy for BC by adding interleukin 2 (IL-2). By following the complex biological processes of tumor, immune system, and BCG interactions, they provided a reliable platform for *in silico* testing of alternative protocols for BCG instillations and combinations with *IL-2*. While certain aspects of the models mentioned earlier (19–23), such as the law of mass action, form the foundation for our model concerning bladder tumors and immune cells, it's noteworthy that these models primarily focus on immunotherapy. As a result, our approach to model chemotherapy treatment draws inspiration from the works of de Pillis et al. (24) and Rodrigues et al. (25) who have specifically constructed models addressing chemotherapy treatments.

The work of de Pillis et al. (24) models cancer growth on a cell population level to investigate tumor dynamics. By merging clinical data from both laboratory mice and human trials together with established mathematical terms of cell–cell interactions and Michaelis–Menten, they started from the observation of biologists that cancer growth is controlled by a healthy immune system. Accordingly, they developed an ODEs system (Equation (0)) that follows the stimulation of the immune response by tumor cells under a combination of immune, vaccine, and chemotherapy treatments:

$$\begin{cases} \frac{dT}{dt} = aT(1-bT) - cNT - DT - K_T(1-e^{-M})T, \\ \frac{dN}{dt} = eC - fN + g\frac{T^2}{h+T^2}N - pNT - K_N(1-e^{-M})N, \\ \frac{dL}{dt} = -mL + j\frac{D^2T^2}{k+D^2T^2}L - qLT + (r_1N + r_2C)T \\ -uNL^2 - K_L(1-e^{-M})L + \frac{p_1LI}{g_1+I} + \nu_L(t), \\ \frac{dC}{dt} = \alpha - \beta C - K_C(1-e^{-M})C, \\ \frac{dM}{dt} = -\gamma M + \nu_M(t), \\ \frac{dI}{dt} = -\mu_I I + \nu_I(t), \\ D = d\frac{(L/T)^l}{s+(L/T)^l}. \end{cases} \tag{0}$$

At time t, the populations are represented by $T(t)$ for tumor cell population, $N(t)$ for total NK cell population, $L(t)$ for total $CD8^+T$ cell population, $C(t)$ for number of circulating lymphocytes, $M(t)$ for chemotherapy drug concentration in the bloodstream, and $I(t)$ for immunotherapy drug concentration in the bloodstream. The characterization of the biological phenomenon was captured through stability analysis and simulations, revealing cases where disease progression is very sensitive to the initial tumor size or levels of specific immune cells. This model provides new insights into tumor dynamics, especially regarding the desirable tumor-free state.

Rodrigues et al. (25) proposed an ODEs-based model to study the chronic lymphocytic leukemia (CLL)-immune dynamics under chemoimmunotherapy. Similar to the approach of de Pillis et al. (24), they highlighted the role of the immune system in eliminating cancer cells. This model provides functional structures for chemotherapy terms with saturating behavior, allowing to model constant and periodic drug instillation, that can be applied to every drug that is given periodically. A critical factor in the success of chemotherapy, as shown in their model and observed by clinicians (26, 27), is the intensity with which the tumor cells stimulate immune cell production. This study serves as the foundation for the formulation of chemotherapy terms in our model.

Realistic and physical modeling of the bladder has been studied thoroughly in the context of hyperthermia of MMC treatment for NMIBC, which is a targeted heating of the tumor area (28–31). For example, the authors in Schooneveldt et al. (28) utilized a convective thermophysical fluid model, based on the Boussinesq approximation to the Navier–Stokes equations, to assess the benefits of physically accurate fluid modeling in NMIBC patients undergoing hyperthermia treatment. Their analysis, based on Computed Tomography (CT) scans from 14 BC patients, demonstrated a significant improvement in temperature prediction accuracy within the urinary bladder compared to previous model (29). Additionally, Sadée and Kashdan (31) developed a mathematical model using conductive Maxwell's equations to simulate therapy administration and the Convection-Diffusion equation for incompressible fluid to study heat propagation through bladder tissue. However, despite the

progress made by biological and mathematical studies of MMC chemotherapy for BC treatment, the optimal dose and mechanism of this drug are yet to be determined (18, 32). To the best of our knowledge, the fundamental oncological aspects of tumor-immune dynamics for this purpose are absent in the existing studies.

In the current work, we recapitulate the state of the art of mathematical modeling by presenting in this research a novel mathematical model describing the dynamics of BC considering MMC chemotherapy. The proposed model is based on the solution of a system of three nonlinear ODEs that describes the tumor-immune dynamics under the assumption that MMC chemotherapy is administered continuously at a low dose. Notably, in a biologically feasible parameter regime, a stable tumor-free equilibrium with a non-trivial structure exists. Moreover, we utilized this stability condition of this equilibrium for the creation of a new method of personalized drug dosage determination. There are obvious practical implications for chemotherapy treatment associated with the ability to calculate MMC dose. To evaluate our work, we compared the model simulations with clinical data. In addition, a sensitivity analysis was conducted to observe how variations in the estimated parameters affect the count of tumor cells. Ultimately, we discuss some more general aspects of the therapeutic process.

The rest of the paper is organized as follows: Section 2 introduces the underlying biological processes of BC dynamics under MMC chemotherapy treatment, that the model aims to describe. Section 3 is devoted for the mathematical model formulation. Section 4 presents the model analysis, including the model's steady states and their clinical impact. The results are discussed in Section 5- where necessary conditions for homeostasis and tumor elimination are presented, and a new method is proposed for determining a theoretically patient-specific upper bound of MMC dose. Finally, Section 6 concludes the biological and mathematical features of the model, including its clinical potential.

2 Biological background

NMIBC is defined as a growth of malignant tumor cells in the urinary bladder, superficially developing on the inner surface and confined to the mucosa or submucosa layers of the bladder wall (33). The major risk factors are tobacco smoking and specific chemical exposures in the occupational and general environments (34).

The treatment of BC comprises two phases, transurethral resection (TUR) and adjuvant therapy. TUR is the standard initial treatment involving an endoscopic procedure to remove the visible tumor (35). Although TUR alone is capable of eradicating tumors completely in some cases, these tumors tend to recur and may progress to muscle-invasive BC (MIBC) (16, 36). In an attempt to extend the recurrence-free interval, TUR is followed by the administration of adjuvant therapy, in the form of intravesical treatment with immunotherapy or chemotherapy, which is given via the catheter (16, 36). The focus of our model is on the chemotherapeutic drug MMC. MMC is instilled in the bladder via the catheter and is generally safe due to its limited effects on the bladder (18, 37). After instillation, MMC acts by inhibiting DNA synthesis and subsequent death of tumor cells (38).

Despite improved management for decreasing the recurrence rate and prolonging the progression-free interval, the clinical effectiveness of MMC is often limited, as the estimated 5-year recurrence rate varied between 49% to 75%, with a risk of progression to the muscle-invasive stage (38–43). Moreover, for this treatment modality, the length and frequency of repeat chemotherapy instillations are still controversial (38–43). Clinicians emphasize that the inability to define drug dosage, treatment frequency, and duration plays a significant role in the failure of MMC treatment, highlighting the absence of an ideal MMC regimen as a key issue (18, 44). One way that has shown enhanced efficacy of MMC is treatment via microwave-induced hyperthermia of MMC, but the success of this treatment is also limited (45, 46). Therefore, new strategies are needed to improve treatment protocols. As the initial step in working towards a new strategy, we establish the first mathematical model to encompass both immunological aspects and MMC chemotherapy for BC treatment, conducting analytical investigations incorporating various model assumptions. In this preliminary phase, we will describe BC elimination under MMC chemotherapy.

The cascade of events leading to BC eradication after MMC treatment can be summarized as follows (see Figure 1): BC tumor cells, termed here as (T) undergo proliferation (47–51), and effector cells (E), are produced at a constant rate due to healthy body homeostasis, i.e., bladder functions are kept within a normal range (step 0, Figure 1) (52, 53).

MMC (M) instillation (step 1, Figure 1) results in a cascade effects of tumor elimination:

1. **The direct effect:** The MMC-DNA interaction leads to the inhibition of DNA synthesis and the subsequent influences on the process of cell division. Consequently, a fraction of urothelial tumor cells (T) undergo arrest of the cell cycle and apoptosis (step 2, Figure 1) (54–57).
2. **The indirect effect:** effector cells (E) are activated by apoptotic tumor cells (T) (step 3, Figure 1) and eliminate the latter via DCs' phagocytosis and Cytotoxic T cells' (CTLs) cytotoxicity (step 4, Figure 1) (55, 58). This suppression of tumor cells (T) leads to the destruction of the entire tumor (54, 55).

3 Materials and methods

3.1 Formulation of model equations

Our mathematical model consists of a system of ODEs that describes interactions between tumor cells and the immune system under MMC chemotherapy. Specifically, we track the temporal dynamics of the following three populations: MMC chemotherapy drug dose, $M(t)$; bladder tumor cells population, $T(t)$; and effector cells population, $E(t)$. The formulation of the equations was done by bringing together the specific forms of cell growth, cell-cell interactions, and drug-cell interactions (see Figure 1):

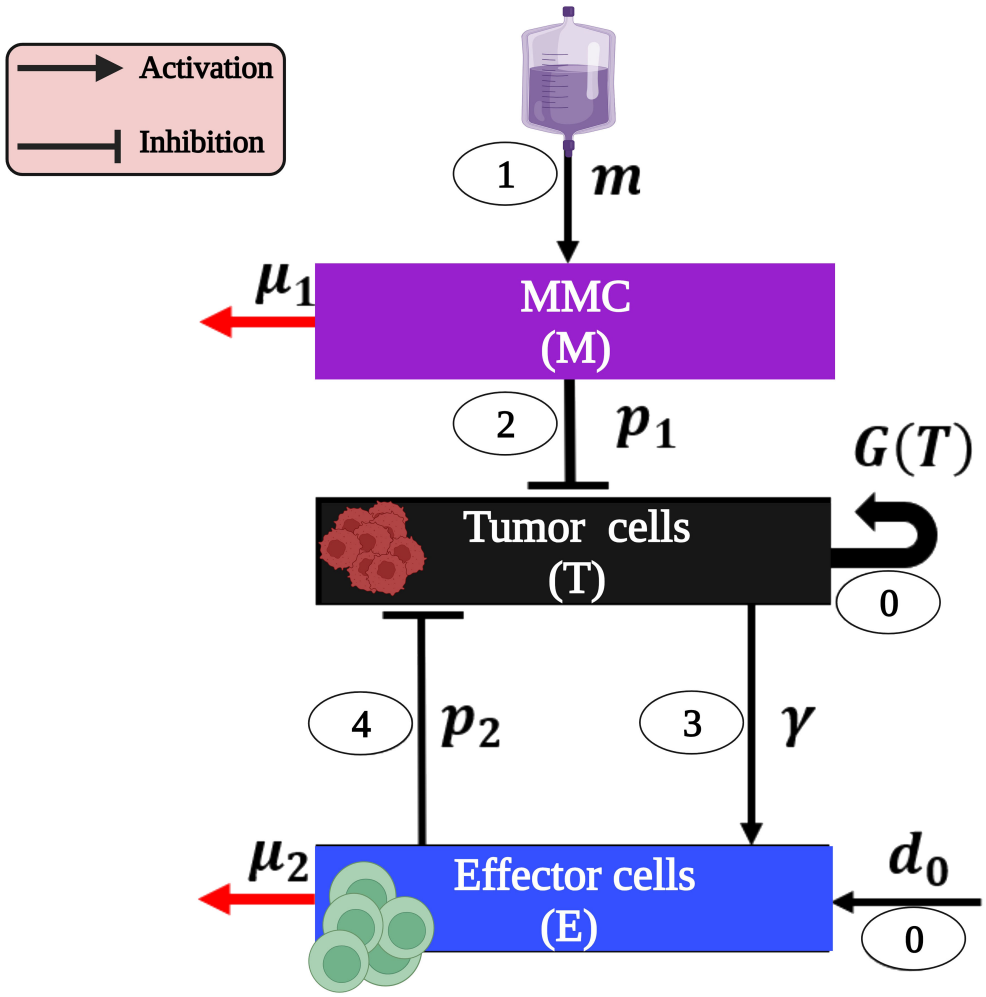

FIGURE 1
The model interactions of BC cells and immune system as a result of MMC chemotherapy (presented with parameters and the cascade steps are numbered inside ovals as outlined in the text). Note that parameters without a direct influence from one cell type to another (p_3) or those defined solely by detailed mathematical terms in system (1) (r,k,a) are exclusively present in system (1). This image was created with BioRender.com.

Equation for the chemotherapeutic agent MMC (M). MMC (M) is delivered into the bladder cavity for 1-2 hours by once-a-week instillations over a 6-week to 8-week period and then once monthly for 1-year (32, 59–61). Processes of this type introduce time-dependent discontinuities into the model. The resultant non-autonomous system may present analytical complexity. Therefore, at the present stage, we have chosen to simplify and model constant administration of MMC to the bladder; $m \geq 0$ is a constant parameter of the MMC instillation rate. We obtain Equation (1a):

$$\frac{dM}{dt} = -\underbrace{\mu_1 M}_{\text{washout}} + \underbrace{m}_{\text{source}}, \tag{1a}$$

where μ_1 is the washout rate of MMC (M).

Equation for the tumor cells (T). Bladder tumor cells (T), known for their heterogeneity (62), are assumed here to be entirely identical for simplification. These cells undergo apoptosis due to direct cytotoxicity of MMC (M) by inhibiting DNA synthesis (38, 54, 56, 57). Hence, tumor cells,(T), must decrease at an intensity that is proportional to their encounter with MMC (M). By assuming these dynamics have a Michaelis-Menten form with p_1 as a rate constant, and a half-saturation parameter a, we get the term $\frac{p_1 TM}{M+a}$. Upon activation by tumor cells' (T) apoptosis, effector cells (E) begin with the subsequent engulfment and destruction of the tumor cells (T) (54, 55, 58), at a constant rate p_2. Based on these processes, the tumor dynamics can be formulated as follows in Equation (1b):

$$\frac{dT}{dt} = -\underbrace{\frac{p_1 MT}{M+a}}_{\text{killed by MMC}} - \underbrace{p_2 ET}_{\text{killed by immune cells}} + \underbrace{r\,T\left(1-\frac{T}{k}\right)}_{\text{growth}}, \tag{1b}$$

Here, the number of tumor cells (T) increases due to natural growth, as indicated by the third term following the logistic growth law; r is the tumor growth rate and k represents the tumor's carrying capacity. In this context, we suggest that the carrying capacity k represents a state of no-cure or even death within the biological context. Hence, our focus is only on the range $0 \leq T \leq k$.

Equation for the effector cells (E). CTLs and dendritic cells (DCs) are immune cells represented by the term effector cells (E). DCs reside in the bladder (63), so we assume that effector cells (E)

proliferate at a constant rate d_0, in alignment with previous mathematical models that describe antigen-presenting cells (APCs) (64, 65). Apoptotic urothelial tumor cells (T), given by the term $\frac{p_1 TM}{M+a}$, induce the activation of effector cells (E) at a constant rate γ (54, 55, 58). The Michaelis-Menten form of this term accounts for the limited nature of this recruitment (66). In addition, the term $p_3 TE$ describes the effector cells' (E) deactivation via an encounter with tumor cells (T) (54, 55). The natural mortality rate of effector cells is μ_2. Hence, effector cells (E) satisfy the following Equation (1c):

$$\frac{dE}{dt} = \underbrace{d_0}_{\text{source}} - \underbrace{p_3 ET}_{\text{deactivation}} - \underbrace{\mu_2 E}_{\text{death}} + \underbrace{\gamma \frac{p_1 TM}{M+a}}_{\text{activation}}. \tag{1c}$$

Thus, the tumor-immune interactions of NMIBC under MMC chemotherapy are modeled by the following system of ODEs:

$$\begin{cases} \frac{dM}{dt} = -\mu_1 M + m, \\ \frac{dT}{dt} = -T\left(\frac{p_1 M}{M+a} + p_2 E\right) + G(T), \\ \frac{dE}{dt} = d_0 + \gamma \frac{p_1 TM}{M+a} - E(p_3 T + \mu_2). \end{cases} \tag{1}$$

Where:

$$G(T) = rT\left(1 - \frac{T}{k}\right)$$

With initial conditions:

$$M(0) \geq 0, \qquad T(0) \geq 0, \qquad E(0) \geq 0.$$

Note that the requirement above that for all $t \in [0,\infty)$,$0 \leq T(t) \leq k$, is just a biological constraint of the model. Without assigning a specific value to bound the tumor cell count, k and, consequently, $T(t)$ can theoretically represent any number of tumor cells.

3.2 Estimation of parameters

For the model to be complete, we carefully estimated parameter ranges so that they are realistic and correspond to values found in biological studies, while some were determined by the model to yield meaningful results in simulations, consistent with reported phenomena in the literature (see Table 1). The parameters, drawn from animal models, cell lines, and human tumor samples, are utilized for exploratory model analysis. Therefore, it is important to note that it is unsafe to use them in clinical settings with human cancer patients, as refinement through separate work based on clinical research findings is mandatory before further utilization. The interpretation of all parameters below should be considered within the context of their respective roles in the ODEs system (Equation 1).

- **The decay rate of MMC - μ_1:**

Removal by metabolism, tissue binding and minimal absorption across the bladder epithelium are the primary factors for MMC (M) decay in urine (16, 67, 71). MMC (M) elimination rate $\mu_1 = 21.05$ $[day^{-1}]$ is derived from the mean constant rate of absorption and degradation, reported by Dalton et al. (67). From the assumption of exponential decay, the biological half-life of MMC (M) is $t_{1/2} = \frac{\ln 2}{21.05[day^{-1}]} = 47.4$ minutes. There have been numerous studies that support this result (37, 72, 73). One of them, the work of Gao et al. (37), confirms that approximately 6% – 16% of the MMC dose was present in the bladder tissue at the end of the 2 hours treatment period [see Table 1 in (37)]. Even when using the same sources, MMC half-life can vary, because there is a substantial intra and inter-patient variability in degradation and absorption constant rates based on various factors, such as incomplete bladder emptying during treatment, urine acidity and hydration status (72, 73).

TABLE 1 List of the model variables and parameters descriptions

Variable	Description	Unit	
M(t)	MMC chemotherapy drug amount at time t	[μM]	
T(t)	Bladder tumor cells population at time t	Cells	
E(t)	Effector cells population at time t	Cells	
Parameter	**Description**	**Estimate**	**Source**
μ_1	Decay rate of MMC	$21.05[day^{-1}]$	(67)
m	Instillation rate of MMC	6.561 [$\mu M/day$]	(32, 59), Calculated
r	proliferation rate of tumor cells (T)	(0.01-0.045) $[day^{-1}]$	(20)
k	Carrying capacity of tumor cells (T)	(0.09-1)$\times 10^9[cells]$	(20, 68)
p_1	Inhibition rate of (T) by MMC	(0.12-0.2) $[day^{-1}]$	(56)
a	Half-saturation constant	$1\times 10^2[\mu M]$	Estimated
p_2	(T) cells inhibition rate by (E) cells	(3.7-5.5)$\times 10^{-6}$ $[cells^{-1}day^{-1}]$	(22, 69)
d_0	Constant production rate of effector cells	1.032×10^5 $[cells\times day^{-1}]$	(52)
γ	Effector cells' (E) activation rate	$9.12[day^{-1}]$	(70)
μ_2	Effector cells' (E) death rate	$9.12[day^{-1}]$	(24)
p_3	Effector cells' (E) deactivation rate	(1.1-1.59)$\times 10^{-6}$ $[cells^{-1}day^{-1}]$	(24)

All parameters used are strictly positive.

- **The MMC instillation rate - *m*:**

A widely accepted protocol for a single MMC treatment session is 40 mg in 50 ml sterile water administered intravesically for 2 hours (74–77). Therefore, we considered the corresponding drug dose, m_0, that was calculated as follows (the molecular weight of MMC is 334 g/mol (78)): m_0 = (Protocol dose)×(Mw of MMC) $= \left(\frac{40\text{ mg}}{50\text{ ml}}\right)\left(\frac{\text{g}}{10^3\text{ mg}}\right)\left(\frac{1\text{mol}}{334\text{ g}}\right)\left(\frac{10^6\mu\text{mol}}{1\text{ mol}}\right) = 2.395[\mu mol/ml] = 2,395[\mu M]$. Given the hypothetical nature of continuous drug administration for hundreds of days, we used a relatively small amount of drug to preserve a total amount similar to that given in a single treatment.

This strategy aims to simplify the real two-hour treatment, which is generally considered safe for the local administration area (18, 37), and may reduce the risk of theoretical over-toxicity. Over-toxicity is indirectly addressed in this work through the consideration of drug doses below the highest recommended values in the literature, as discussed in the results section. Therefore, we chose to scale by $\tau = 365$ days which is close to the number of simulated days, to get the drug instillation rate: $m = \frac{m_0}{\tau} = \frac{2{,}395[\mu M]}{365\ days} = 6.561[\mu M/day]$. We chose to use these units because they are compatible with *in vitro* experiments that were done by Ojha et al. (56, 79). While practical pulsed therapy will be discussed in future work, the rationale for assuming and supporting the validity of our approach in scaling the drug instillation rate, including simulations comparing the effects of this administration on large and low MMC doses, is provided in Subsection 4.2 of the Supplementary Information.

• **The inhibition rate of urothelial tumor cells by MMC- p_1:**

According to Ojha et al. (56), a 24 hours exposure to 5μM of MMC (M) induced 12-20% apoptotic cell death in non-invasive tumor tissue samples from patients. Hence, a reasonable first estimate is the range:

$$p_1 = (0.12 - 0.20)\ [day^{-1}].$$

• **The saturation of the killing effect on urothelial tumor cells *by MMC - a*:**

The half saturation constant was calculated from model simulations, to be $100[\mu M]$. This theoretical value facilitates scenarios representing tumor persistence and elimination with treatment, and the observed activation of effector cells' anti-tumor activity through modulation of anti-tumor immunity compared to the no-treatment case (55, 58).

• **The constant production rate of *Effector cells - d_0*:**

We use the information that during homeostasis, DCs are the only subset of effector cells (E) which is capable of continuous replacement with new cells (53). DCs undergo a limited number of divisions in the spleen or lymph nodes, and are replenished at a rate of nearly 4.3×10^3 cells per hour (52). Hence, $d_0 = 4.3 \times 10^3[cells \times hour^{-1}] = 1.032 \times 10^5[cells \times day^{-1}]$. The explanation for assuming constant effector cell production and the rationale behind choosing this value are provided in Subsection 4.1 of the Supplementary Information.

4 Model analysis

We establish the biological validity of the model through positive invariance property, i.e., every solution of the system (Equation (1)) with positive initial conditions remains in the positive orthant $\mathbb{R}^3_+$. The invariance of positive orthant is quite useful for us to formally verify the safety properties of our dynamical system. Since the model variables describe biological and chemical elements represented by nonnegative values in real processes, it is important that we do not obtain negative values. Thus, we first prove the positivity of the solutions (see proof in the Supplementary Information). Next, the use of positive invariance property allows us to explore the model's equilibrium points from a biological perspective, including their stability analysis and an oncological interpretation to formulate the desired mathematical conditions for cure.

4.1 Steady states and stability analysis

The model [system (1)] is characterized by four nonnegative equilibria (see Supplementary Information for details on the steady-state derivation). In the absence of a straightforward biological interpretation for the parametric form of the cancer equilibria, we decided to analyze their stability numerically in the Supplementary Information, and to focus solely on disease-free equilibrium points which are summarized in Table 2. The stability analysis is performed for the model with and without chemotherapy. For convenience, I_1 and I_2 denote the terms $\frac{p_2 d_0}{\mu_2}, \frac{p_1 \frac{m}{\mu_1}}{(\frac{m}{\mu_1}+a)}$, respectively, when appeared in the text.

With the formulation described in the Supplementary Information, we can now investigate the local stability of the linearized model by studying the Jacobian matrix J of the system, given by Equation (2):

$$J = \begin{bmatrix} \frac{\partial F_1}{\partial M} & \frac{\partial F_1}{\partial T} & \frac{\partial F_1}{\partial E} \\ \frac{\partial F_2}{\partial M} & \frac{\partial F_2}{\partial T} & \frac{\partial F_2}{\partial E} \\ \frac{\partial F_3}{\partial M} & \frac{\partial F_3}{\partial T} & \frac{\partial F_3}{\partial E} \end{bmatrix} = \begin{bmatrix} -\mu_1 & 0 & 0 \\ -\frac{p_1 T}{M+a} + \frac{p_1 TM}{(M+a)^2} & r - \frac{2r}{k}T - p_2 E - \frac{p_1 M}{M+a} & -p_2 T \\ \frac{\gamma p_1 T}{M+a} - \frac{\gamma p_1 TM}{(M+a)^2} & -p_3 E + \frac{\gamma p_1 M}{M+a} & -p_3 T - \mu_2 \end{bmatrix}. \quad (2)$$

The following subsections present a stability analysis of the nonnegative equilibria: first, in the absence of chemotherapy (4.1.1), and second, under continuous therapy (4.1.2).

4.1.1 Homeostasis equilibrium (without treatment)

$$EB_1 = (M^*, T^*, E^*) = \left(0,\ 0,\ \frac{d_0}{\mu_2}\right),$$

TABLE 2 Summary of the stability characteristics for the nonnegative equilibria solutions of system (1), in the absence of chemotherapy ($m = 0$) and with therapy ($m > 0$).

Treatment	Equilibriua	M*	T*	E*	Stability
$m = 0$	EB_1	0	0	$\frac{d_0}{\mu_2}$	$r < I_1$ locally stable
$m > 0$	EB_2	$\frac{m}{\mu_1}$	0	$\frac{d_0}{\mu_2}$	$r < I_1 + I_2$ locally stable

No point is shared by both cases.

At this equilibrium, there are no tumor cells, and the immune cells exhibit a homeostatic net production value dictated by the ratio between constant production and natural mortality of these cells, E^*. This value, regardless of stability condition to be discussed separately, reflects the equilibrium itself as a non-adverse event, as the killing rate of tumor by immune cells, p_2, is not a factor in EB_1. Therefore, we conclude that the bladder maintains homeostasis.

The eigenvalues of the Jacobian evaluated at equilibrium are: $\bar{\lambda} = [-\mu_1; -\frac{d_0 p_2}{\mu_2} + r; -\mu_2]$.

Thus, all eigenvalues are negative if:

$$-\frac{d_0 p_2}{\mu_2} + r < 0, \Rightarrow r < \frac{d_0 p_2}{\mu_2}. \quad (3)$$

Hence, if the condition in Equation (3) is satisfied, then every solution of the original system (1) that starts near EB_1 converges to EB_1 as $t \to \infty$. That is, the homeostasis equilibrium EB_1 equilibrium is locally asymptotically stable when $r < I_1$ and unstable when $r > I_1$. Simulations in Supplementary Figure S1 illustrate that the tumor rapidly disappears for parameters that satisfy the stability criterion.

From an oncological perspective, the term I_1 can be interpreted as the intensity of tumor killing by the immune system [more specifically, effector cells (E)]:

1. The numerator, $d_0 p_2$, is the product of the daily production rate of effector cells (E), and the daily killing rate of tumor cells (T) by effector cells (E), respectively. Therefore, this term reflects the potential daily killing rate of tumor cells (T).
2. The net daily rate of this killing process is obtained as $d_0 p_2$ is divided by the mortality rate of effector cells (E), μ_2.

Accordingly, stability condition (3) characterizes the range of the tumor growth rate r, for which immune activity I_1 is capable of killing tumor cells, to a stage where the immune system is in homeostasis. For smaller values of I_1, the tumor's growth rate dominates and the tumor-free equilibrium destabilizes.

4.1.2 Tumor-free equilibrium (under treatment)

$$EB_2 = (M^*, T^*, E^*) = \left(\frac{m}{\mu_1},\ 0,\ \frac{d_0}{\mu_2}\right).$$

At this point, no tumor cells are present, and the immune system is in homeostasis, as outlined for EB_1. One might wonder, however, how an equilibrium in which chemotherapy is present in the system can indicate a cure for a disease. We resolve this issue by referring back to the model's structure. The term $\frac{m}{\mu_1}$ reflects a very small amount of MMC. Recall that the instillation rate, m, is obtained by division of the drug dose m_0, by τ, which is close to the number of simulated days. Moreover, in EB_2, m is divided by MMC washout rate, μ_1. Using the estimated parameters of the model, this value is of $0.311[\mu M]$, implying that beyond 99.99% of the drug dose m_0 was cleared, i.e., without side effects or toxicity. In other words, we suggest that this equilibrium point indicates cure only under the assumption that there remains a small amount, M^*, of MMC in the bladder (under continuous therapy for a prolonged period of time).

Stability: The eigenvalues of the Jacobian at this equilibrium are: $\bar{\lambda} = \left[-\mu_1, r - \frac{p_2 d_0}{\mu_2} - \frac{p_1 \frac{m}{\mu_1}}{\left(\frac{m}{\mu_1} + a\right)}, -\mu_2\right]$. Therefore, all eigenvalues are negative, if:

$$r < \frac{p_2 d_0}{\mu_2} + \frac{p_1 \frac{m}{\mu_1}}{\left(\frac{m}{\mu_1} + a\right)}. \quad (4)$$

The tumor-free (cure) equilibrium EB_2 is locally asymptotically stable when $r < I_1 + I_2$ and unstable when $r > I_1 + I_2$.

A biological understanding of this criterion may be introduced as follows. At equilibrium, the first term on the right hand, I_1, is the net daily killing rate of tumor by immune cells, as highlighted in condition (3). In the same way, the second term, I_2, is the net daily killing rate of tumor by MMC chemotherapy:

1. I_2 involves the MMC source, m molecules of drug that are introduced daily, multiplied by the killing rate of tumor cells via MMC effects, p_1, to give the daily MMC efficacy.
2. This efficacy, $p_1 m$, is limited by MMC decay, at a daily rate μ_1, and the saturation effect given by the Michaelis-Menten form, with a half-saturation parameter, a.

Therefore, the right hand of (4) reflects the sum of all the killing effects of the tumor, by both the immune system and chemotherapy treatment. When this total killing rate is greater than the tumor growth rate r, the tumor-free equilibrium is stable (numerical simulation appears in Supplementary Figure S4). Should the tumor growth rate, r, be larger, the tumor's strength governs the process and the equilibrium loses stability. The criterion shows the ranges for r, within which constant MMC treatment, together with effector cells (E), can clear the tumor to a state where, similar to EB_1, the immune system is in homeostasis, free from side effects.

5 Results

We begin with formulating conditions for disease-free states through stability analysis. Subsequently, we compare the behavior of model simulations to clinical data, and conduct a numerical parameter sensitivity analysis on estimated parameters. Furthermore, we present an application in MMC dosage determination.

5.1 Mathematical conditions for tumor extinction

It is a main interest to identify the criteria for which tumor is cleared. Two equilibrium points in the current model exhibit the desired result of a healthy bladder, i.e., $T = 0$:

1. **Homeostasis:** When tumor is untreated, the body relies solely on its immune cells for defense. With respect to EB_1, the homeostasis equilibrium, the stability criterion (4), to maintain the state of no tumor cells:

$$r < \frac{p_2 d_0}{\mu_2}. \quad (3)$$

2. **Tumor-free equilibrium:** A similar stability-criterion was found for EB_2, the tumor-free equilibrium:

$$r < \frac{p_2 d_0}{\mu_2} + \frac{p_1 \frac{m}{\mu_1}}{\left(\frac{m}{\mu_1} + a\right)}. \quad (4)$$

The competition of immune cells alone or in combination with chemotherapy against tumor cells is reflected in each criterion here by tumor killing and tumor forming activities, respectively. That is, as outlined in criterion (3), the destructive mechanisms of the immune system alone against tumor cells are strong enough to eliminate tumor cells only up to a certain threshold, I_1, which is the upper bound for the tumor growth rate, r. This theoretical threshold increases in the criterion outlined by Equation (4), as MMC's killing ability, I_2, is added to the immune killing ability I_1. As a result, the synchronization of all tumor killing effects enables to eliminate even more rapidly growing tumors, i.e., $r \in (I_1, I_1 + I_2)$. For smaller destruction rates in each criterion, the tumor's proliferation capacity dominates, resulting in the destabilization of EB_1 and EB_2.

5.2 Model examination

We are now interested in comparing the above model [system (1)] with data obtained from biological studies as well as previous mathematical models, as described below and in Table 1 and Supplementary Table S2. Computer simulations were performed using fifth-order adaptive step Runge-Kutta integration, as implemented in the ode45 subroutine of MATLAB, to visualize approximations to the solution for the model ODEs. We also tested ode23s for systems with varying time scales involving cells and molecules. However, results showed no observable difference compared to the ode45 solver, indicating both are suitable for simulations. We start by illustrating distinct case scenarios of the disease as captured by our model. Then, we study the behavior of our model when confronted with oncological research.

Since no geometrical considerations are being taken in this paper, we used the term tumor size in the meaning of the number of tumor cells. To incorporate oncological terminology into the model, we followed the methodology outlined in (20) to translate the prognostic factor 'tumor size' for recurrence in BC (80) into tumor cell count. The tumor surface area was calculated assuming a circular shape and a 3-cells depth to determine the volume using the length of cell being approximately 10μm. Given that $1\text{mm}^3 \sim 10^6$ cells (81), the formula of the number of tumor cells is:

$$\begin{aligned} \#\text{Cells} &= \pi(\text{radius})^2 h \times 10^6 \\ &\approx \pi \times (\text{radius[mm]})^2 \times 3 \times (10^{-2}[\text{mm}]) \times \frac{10^6\ [\text{cells}]}{1\ [\text{mm}^3]}. \end{aligned} \quad (5)$$

The presence of recurring or residual tumors after TUR has been documented in the literature (39, 82). Therefore, we use the reasonable assumption that the diameter of each residual tumor is not more than the length of resection. Utilizing the formula given in Equation (5) we derive the corresponding initial tumor cells count, $T(0)$, with regard to the initial clinical tumor sizes.

5.2.1 Theoretical simulations

We simulated three types of scenarios according to the initial tumor cell count. The choices for tumor sizes based on the information that small BC tumors typically range from less than 20[mm] in diameter (83), with the lower limit of sensitivity for detecting BC tumors ranging from 5 to 10[mm] (84). Medium tumors are defined within the range of 20-50[mm], while large tumors are classified as > 50[mm] in the study of Loloi et al. (83):

1. The initial tumor cell count for a tumor of "small" size $T(0) = 5.3 \times 10^6$, corresponding to a size of 15[mm].
2. The initial tumor cell count for a tumor of "medium" size $T(0) = 1 \times 10^7$, corresponding to a size of 20.6[mm].
3. The initial tumor cell count for a "large" tumor $T(0) = 6.62 \times 10^7$, corresponding to a size of 26.5[mm]. This value is below the highest reported value of 75[mm], where successful tumor resections were performed, as noted in (85).

In each numerical simulation, we showed the evolution of tumor in time with and without treatment. The simulated "small" tumors can be eliminated by the immune system (effector cells) only for initial tumor size of $T(0) < 7.36 \times 10^6$ (see Figure 2A), and if untreated, tumors with greater $T(0)$ grow until they reach the carrying capacity. With the killing effects of MMC, as specified above, all treatment simulations resulted in decreased tumor cell counts (T), compared to the no-treatment scenario (see Figures 2A-C). However, MMC could eliminate "small" tumors for initial tumor size which is $T(0) \leq 2.93 \times 10^7$. This suggests that MMC has a curative effect within a certain range of initial tumor cell numbers, which, for the results in Figures 2A–C, falls within $7.36 \times 10^6 \leq T(0) \leq 2.93 \times 10^7$. If the number of cells exceeds a theoretical threshold for "large" tumors, the treatment will not be sufficient to cure BC (see Figure 2C). It is noteworthy that even when initial tumor sizes fall below this theoretical threshold, variations in model parameters, such as increased tumor growth rate r or decreased immune production rate d_0, can result in a rise in tumor cell count, manifesting as tumor cell count beyond the theoretical threshold. To demonstrate this influence on tumor cell count, we conducted simulations with parameter variations (see Subsection 4.3 of the Supplementary Information).

The next step is to investigate the behavior of effector cells (E). In all simulations (Figures 2A-C), MMC treatment resulted in a higher effector cell counts compared to the untreated scenario. This is particularly evident in simulations with larger initial tumor sizes (Figures 2B, C), and subtly visible in Figure 2A due to the logarithmic scale of the y-axis; a zoom plot revealed a gap between treated and untreated scenarios, declining from about 1,700 cells after 1 day of simulation to approximately 50 cells only after 250 days. Studies of Hori et al. (54, 55) indeed suggest that immunosuppressive cells called regulatory T-cells (Tregs) which regulate effector cells counts, are reduced by MMC.

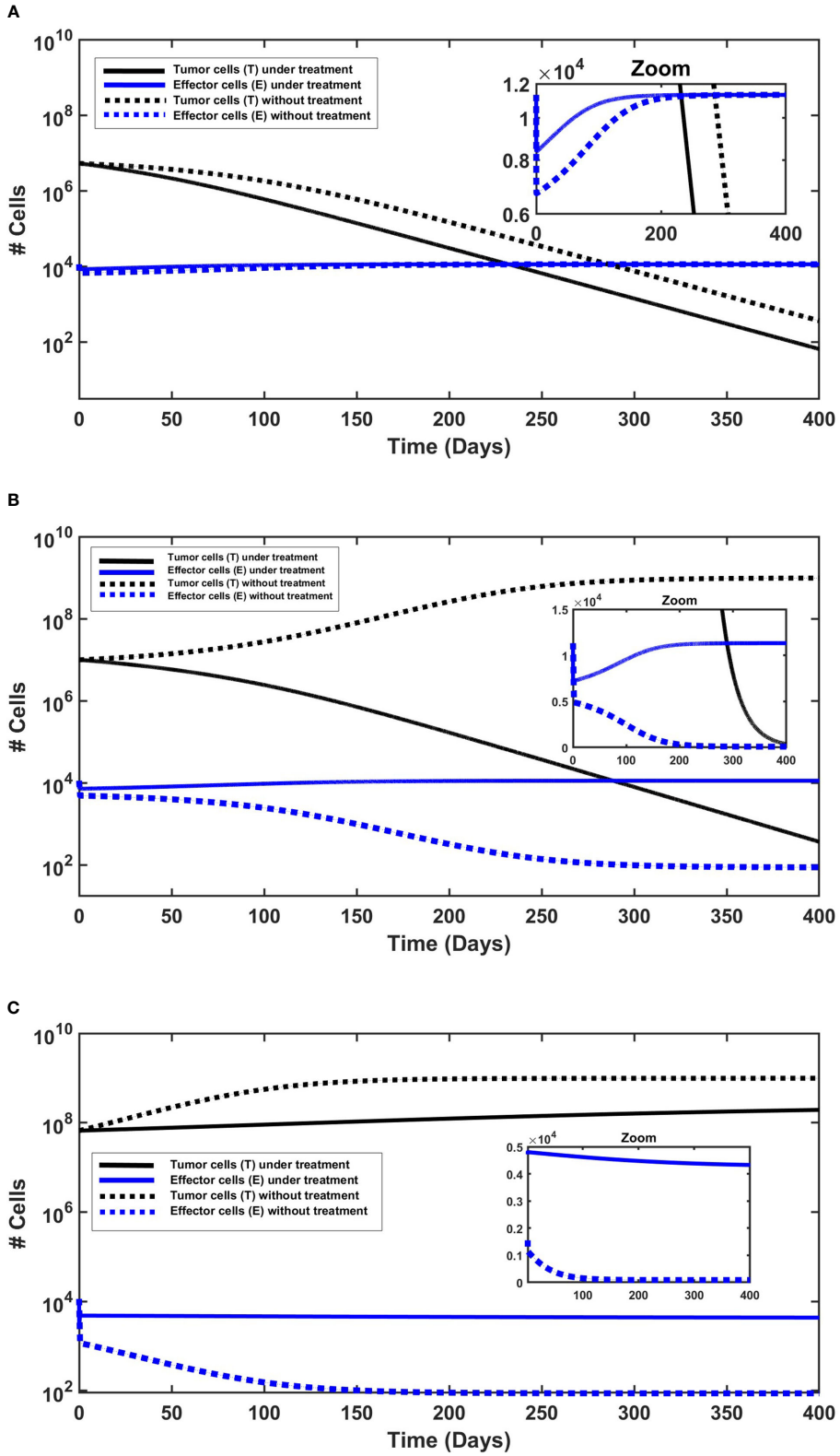

FIGURE 2
The behavior of urothelial tumor cells (black lines) and effector cells (blue lines), with (solid lines) and without (dashed lines) continued application of MMC. Initial conditions are found in the Supplementary Information. **(A)** Tumor elimination with and without chemotherapy. The elimination is slightly faster under continued application of MMC chemotherapy. **(B)** Cure only under chemotherapy. Without treatment there is a logistic growth of tumor cells (*T*), so there is no cure. **(C)** Tumor persistence with and without chemotherapy. Effector cells decrease, but more significantly without treatment.

Regarding treatment outcomes, in cases where a cure is achieved, effector cell counts consistently increased throughout the entire simulated time (Figures 2A, B), approximately starting from the end of day 1 after the initial reduction. The initial reduction during the first day in all simulations (Figures 2B, C) reflects tumor burden (p_3ET) in Equation (1c), which, for given parameters and initial conditions, determines the sign of the term $\frac{dE}{dt}$. Subsequently, a possible interpretation is that the dynamics are determined by the treatment outcome: an increase in effector cells over time if treatment is successful (T declines), or a decrease if tumor persistence occurs (T increases). Distinct behavior is shown in treatment failure (Figure 2C), showcasing an interesting case with a slight decrease in effector cell count from 1 day after treatment to the end point of the 400-day simulation. This can be explained by the larger initial tumor size, as all other initial conditions were identical to those in the other simulations. In other words, beyond Tregs regulation, tumor cells may indirectly induce a slight decrease in effector cells by triggering Tregs elevation beyond a specific threshold. Hori et al. (54, 55) do emphasize that cancer cells induce activation of Tregs, which play a role in controlling immune escape in cancer. The combined effects of MMC and the immune system's killing effects appear insufficient for the complete eradication of tumor cells in this case.

5.2.2 Qualitative comparison to oncological studies

The model is designed to find generic qualitative insights intrinsic to its structure. Accordingly, simulations should not be interpreted as predictions. In the absence of specific observed clinical data, we refer to our approach as 'qualitative agreement', based on the available observations and a comparison with literature consistency. We first confronted the model output to studies of NMIBC without MMC chemotherapy. In two studies (80, 83) that focused solely on TUR, larger-sized tumors were associated with a higher likelihood of developing postoperative complications and death. The model simulations without treatment show that indeed increasing the initial tumor size changed tumor dynamics from tumor elimination to tumor persistence (see Figures 2A-C). Under the model assumption of tumor size, our simulations demonstrate similar behavior: tumors that exhibit a cell count below 7.36×10^6[cells] (< 17.68[mm]) are eliminated by the immune system, and for values above this threshold, no cure is evident.

In the assessment of treatment success, a step toward validation involves addressing the following inverse problem: given the prescribed dose of MMC in the reported protocol, what is the maximum threshold of initial tumor size, under the model for achieving a tumor-free state? To solve this problem, we varied the initial condition of tumor cell count, $T(0)$, while keeping all other parameters and initial conditions unchanged (see calculations and simulations in the Supplementary Information). We used clinical research studies that analyzed the impact of a single MMC instillation post TUR surgery in patients with low-risk BC (tumor size of 30[mm] or less):

1. In the study by Solsona et al. (86), a 24-month follow-up revealed a significant increase in the recurrence-free interval, along with reduced recurrence and tumor rates per year in the MMC group compared to the control group. Our simulations, utilizing the study dosage, establish a threshold of 1.21×10^7[cells], corresponding to a tumor diameter of 22.67[mm] (see Supplementary Figure S7).
2. The prospective study of Ersoy et al. (87), showed no recurrence of patients during the follow-up period of five years. Utilizing their dosage plan, the model attained a threshold of 2.14×10^7[cells], corresponding to a diameter of 30.14[mm] (see Supplementary Figure S8).

Given that no tumor-immune specific parameters can be extracted from these studies, the model simulations can only hypothesize that a curative effect may extend to tumors up to a certain $x[mm]$ size. That is, the resulting values only allow us to demonstrate the technical ability to calculate thresholds. However, simulations with treatment do demonstrate curative effects up to a diameter that exceeds those without treatment, thereby underscoring the positive impact of MMC compared to the control group.

In (86), recurrence was observed in some patients of study. This can be modeled by the inter-patient variability on the biological level- such as different tumor growth rate, different immune cells production rate, as shown in Subsection 4.3 of the Supplementary Information. We conclude that the obtained threshold values for cure state are dependent on the specific choice of the parameters which reflects a specific tumor-immune condition of the patient. This way we can resolve the slight changes in values from the range in these clinical studies.

5.3 Sensitivity analysis

We conducted sensitivity analysis on all model parameters (see Figure 3). The analysis was performed with respect to the tumor cells count (T) at day 365 in the treatment case, which implies that at this specific time point, the total drug dosage administered to the hypothetical patient equals the dose of a single chemotherapy treatment (recall scaling of MMC dosage in Section 3). Following the methodology outlined by (88), we employed Latin hypercube sampling to generate 1000 samples, and chose the range of each parameter from 1/2 to twice its values in Table 1, adopting the strategy described in (89). These samples were then used to calculate the partial rank correlation coefficients (PRCC) and the p-values with respect to the tumor cells count (T) at day 365. We observe that parameters promoting anti-tumor dynamics, including the sources (input) parameters of chemotherapy and the immune system (m, d_0), along with the killing and activation rates of the tumor by these elements (p_1, p_2, γ), demonstrate negative correlations with tumor size. Conversely, parameters that promote tumor growth and anti-tumor dynamics—the growth rate of the tumor (r), deactivation of immune cells (p_3), mortality rate of immune cells (μ_2), and chemotherapy washout rate

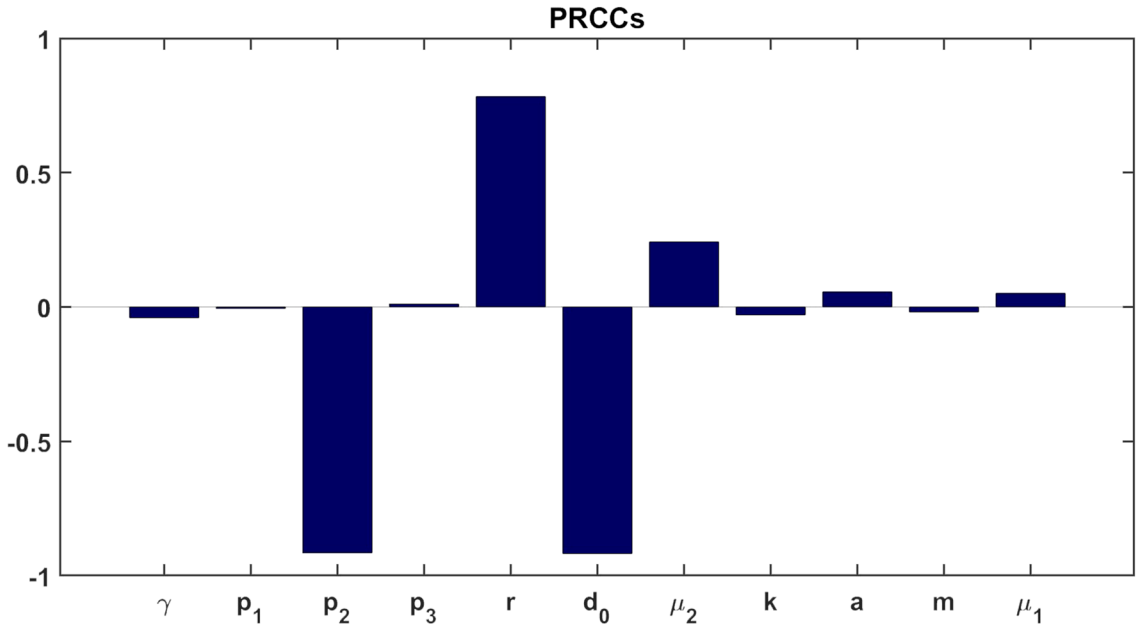

FIGURE 3
Statistically significant PRCC values (p-value< 0.01) for $T(t)$ at day 365.

(μ_1)—exhibit positive correlations with tumor size. Overall, Figure 3 reveals that the parameters p_2, r, and d_0 have the greatest influence on tumor growth. In the quest for a deeper understanding of the influence of two parameters, μ_1 and a, which can be estimated in various ways in the absence of empirical or consensus data, we conducted uncertainty analysis (see Section 6 in the Supplementary Information).

5.4 Application for MMC dose determination

Clinicians often consider 'dosage determination' as a critical aspect in improving MMC delivery and optimizing patient outcomes (39, 44). While variety of MMC chemotherapy treatment programs are available (90), new auxiliary tools are yet necessary to precisely determine the amount of MMC required to cure a specific BC patient.

To facilitate the process of personalized dose determination, we propose a new bio-mathematical algorithm of MMC for the treatment of BC patients. We use the following assumptions regarding the initial conditions of system (1), to describe patient state after MMC treatment:

- The completeness of tumor resection- during the TUR procedure almost all of tumor cells are removed, i.e., $T(0) \approx 0$. Support for this assumption is found in the biological literature (16, 36, 91).
- The vast majority of MMC is cleared (92, 93), so that $M(0) \approx 0$. Therefore, we can choose $\varepsilon = \frac{m}{\mu_1}$ which is negligible, such that $M(0) = \varepsilon$.
- There is a homeostatic production of immune cells, i.e., $E(0) \approx \frac{d_0}{\mu_2}$. This assumption is reasonable since MMC is generally safe due to its limited effects to the local area of administration (18, 37).

This way, system (1) introduces small perturbations from the entries of the tumor-free equilibrium, EB_2. As a next step, we will manipulate the expressions for stability criterion (4) of EB_2:

$$m < \frac{\mu_1 a \left(\frac{p_2 d_0}{\mu_2} - r\right)}{r - \frac{p_2 d_0}{\mu_2} - \frac{p_1}{\mu_1}}. \tag{6}$$

To ensure that the condition in Equation (6) is biologically valid for MMC instillation rate, m, it is essential to verify that the right hand of (6) is positive. We obtain the condition given by Equation (7):

$$\frac{p_2 d_0}{\mu_2} < r < \frac{p_2 d_0}{\mu_2} + \frac{p_1}{\mu_1}. \tag{7}$$

Note that the range for r is valid only if both the numerator and denominator of the right-hand side of criterion (6) are negative. Utilizing local stability condition for EB_2, the dynamical system suggests cure. The obtained criterion (6) enables the calculation of an upper bound for the MMC dose at which treatment is successful, based on theoretically patient-specific parameters. A step-by-step description of the algorithm can be found in Figure 4. The algorithm categorizes patients into two groups; One group for theoretical patients eligible for dose calculation—where the model facilitates determining a dose below the clinically recommended maximum. This indicates that the model identifies a dosage interval within which a cure, according to the model's criteria, is achieved.

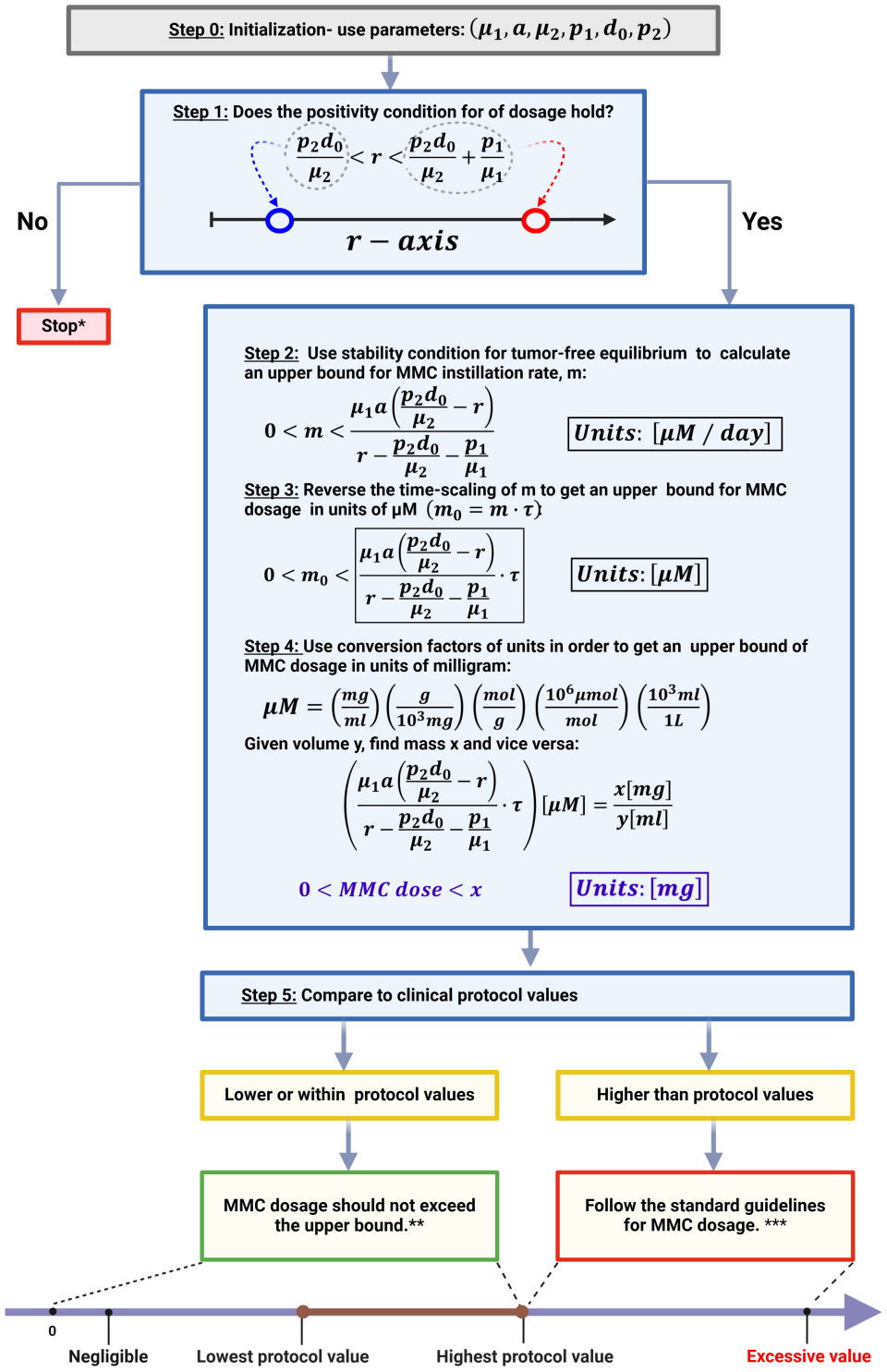

* For this case the model does not predict cure for the case of MMC treatments.
** The amount of chemotherapy dosage that is considered negligible should be defined by the doctors. If the upper bound represents a negligible amount of MMC, the current algorithm is not applicable.
*** For this case the model predicts cure for 0<m<b where b is the upper bound which is above clinicians recommendations. The model does not distinguish between a negligible or excess amount of drug. Therefore , standard dose should be given.

FIGURE 4
Algorithm for MMC drug dose determination in treating BC patients. This image was created with BioRender.com.

Should the upper bound surpass the recommended maximum, we interpret this as over-toxicity, emphasizing the significance of considering the recommended range. It is important to note that, in this particular case, the recommended range is within the curative range. Yet, for enhancing the specificity of the curative range, future efforts will require a focus on determining a lower bound for the curative range, in addition to restricting it by the upper bound. The second group, labeled as 'theoretical non-responders', consists of patients excluded due to theoretically specific parameters not meeting the cure conditions (6) – (7) or receiving an insignificantly small calculated dose.

To demonstrate the robustness of the method for a large number of patients in a 3-D plot, we adopted a systematic approach through virtual experiments with variations of all parameters except r which is determined by the algorithm. The algorithm was used for 2,000 different hypothetical patients to understand how parameters affect the performance of the method (see Figure 5). Variations of parameters from Table 1 were performed, but such that $I_1 < r$ holds. This choice enabled us to exclude instances where parameter sets do not provide positivity of MMC dosage. Thus, the focus was on cases for which a feasible MMC dosage could be calculated; excluded cases are viewed as theoretical non-responders, i.e., further investigation is required beyond the scope of this paper. For each patient, criteria (6)–(7) provided a range of growth rates r for which MMC dosage is positive. For each one of the calculated intervals of r values, one value was chosen randomly by the Matlab rand function, and for this value an upper bound for therapeutic MMC dosage was calculated in units of *mg*. It is noteworthy to observe that intervals of r with higher values are observed alongside higher values of d_0 and p_2.

6 Discussion

Arguments regarding MMC's role in curing NMIBC have been made in many articles (56, 58, 75). This study adds a quantitative basis to these considerations, by showing that under the model assumptions, the complex biological processes of NMIBC, the immune system, and MMC interactions can be captured by a relatively simple 3-dimensional system. The model exhibits four non-negative equilibrium points, which depend on chemical and biological related parameters. The nontrivial dependence of the dynamics on tumor growth (r) is emphasized as oncologically relevant. Particularly, the model analysis in biological context suggested the following distinct dynamical patterns, which are explicitly dependent upon the appropriate range of r (see Supplementary Figures S1-S4). Under no treatment, $m = 0$, homeostatic phase of a healthy bladder is conserved for low tumor formation rates $r < I_1$, meaning that the immune system alone is capable of clearing bladder tumor cells. The tumor is eradicated exponentially fast as immune activity I_1 increases. Violation of this condition results in a logistic expansion of the tumor. When MMC is administered, $m > 0$, it is important to note that stability of tumor-free equilibrium, means that as soon as MMC chemotherapy is added, the killing effects of chemotherapy are added to the process, enabling the elimination of tumors with a faster growth rate than the homeostatic phase, $r < I_1 + I_2$. For high tumor formation rates $r > I_1 + I_2$, in view of the limited killing effects of the immune system and MMC, it is impossible to cure tumors that proliferate very rapidly.

In light of the increasing prominence of mathematical models in cancer research (7), our model did add new elements into the current discussion on treating BC patients, as well as detecting hypothetical properties that are not evident in experimental studies. Chemotherapy protocol investigation is one of these features. Based on a distinctive viewpoint of local stability, we designed a new method to calculate an upper bound to the drug dose, m_0, for which chemotherapy is successful. At its current stage, this method remains theoretical, offering valuable insights into the structural dynamics of the model and its capacity to accommodate unit conversion factors relevant to drug measurements via stability analysis. The analytical procedure allows to classify patients into two groups given a theoretically specific set of patient's parameters:

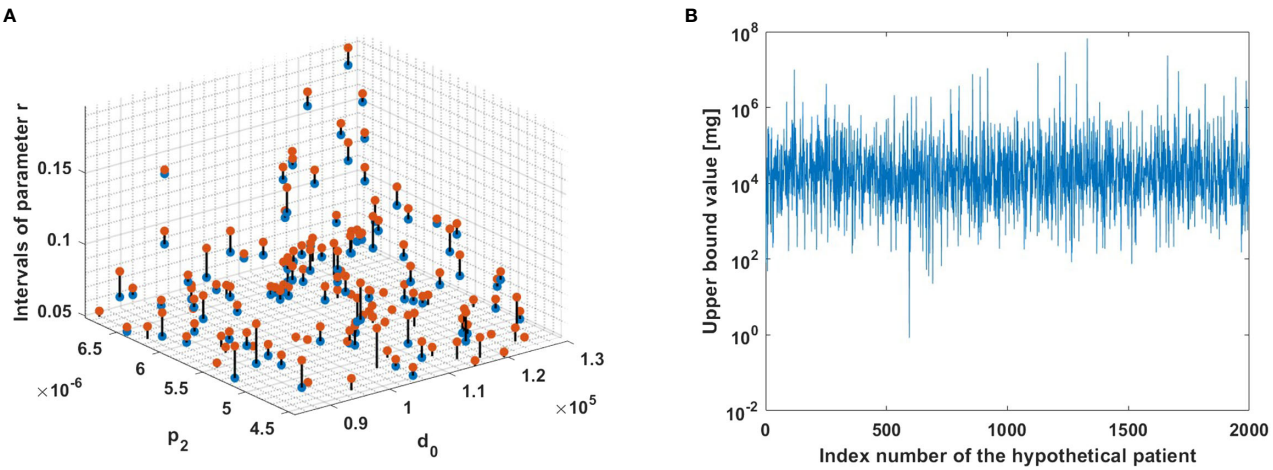

FIGURE 5
The model algorithm applied for 2,000 hypothetical patients. **(A)** Ranges for parameters r, such that m is positive. The blue and red dots correspond to the left and right interval endpoints in (7), respectively. The observed intervals are depicted in the figure using a zoom-in view to enhance visualization. **(B)** Upper bounds for MMC dosage. The upper bound for each hypothetical patient was computed using criterion (6).

those who will benefit from the treatment and those who will not. When the upper bound of MMC amount cannot be calculated or is negligible, the model output does not suggest cure. Otherwise, it is possible to determine the individual drug dosage as shown in Figure 4. We concluded that this kind of range is clinically relevant because it may potentially reveal the effectiveness of the treatment protocol in a nontrivial way compared to classic pharmacological studies which are PK/PD-model-based (9). Furthermore, only a limited number of clinical MMC dose comparison studies have been conducted. For example, in (94), the researchers performed a prospective, randomized study to compare 30 mg and 40 mg of MMC dose for BC patients. This approach is realistic since it provides the actual biological results. However, due to the impracticality of testing all possible dosing options in clinical trials, the efficacy of these studies is inherently constrained.

The clinical observation that low-risk bladder cancer (BC) patients form an inhomogeneous group, that can be stratified by tumor size (95), is highlighted in the model through simulations (Figures 2A-C). The simulations suggest that chemotherapy success depends on the initial tumor size, but also on model parameters (see Figure 3). As described in the literature (59), our simulations demonstrate the effectiveness of MMC that in some cases offers a better cure, and even provide a theoretical threshold of tumor cells number that can be eliminated, given a hypothetical specific set of parameters.

To enable the results above to help doctors evaluate the risks of MMC treatment protocols for BC patients individually, it is essential to measure specific clinical parameters for each one of them. In other words, the presented parameter values and ranges are not asserted as the single possible choice; rather, they serve to demonstrate the adaptability of incorporating biological data into modeling. The eventual refinement of all model parameters will be dictated solely by future findings in biological research. To begin with, the assessment of the tumor growth characteristics in patients *in vivo* to calibrate the growth rate, r. Currently, we are not aware of any *in-vivo* method to continuously track the value for this parameter. With regard to the measurement of the MMC's properties in the human bladder, it is necessary to investigate the specific washout rate μ_1 and killing capacities of MMC for calibration of the killing parameter p_1 and the Michaelis-Menten half-saturation constant a. One step in this endeavor involves the establishment of a bio-bank comprising patient-derived BC organoids for the assessment of drug responses (96). Similarly, progress has been made with the examination and count of tumor infiltrating lymphocytes (TIL) in biopsy samples (97). However, immune cells (CTLs and DCs) production and death rates- d_0, μ_2, respectively, are yet to be found in thorough measurements supported by extensive datasets.

Current model was created to formulate explicit mathematical relations, such that a balance between analytical tractability and biological credibility was maintained. However, this study has limitation by its exclusion of the spatial structure of tumors. Existing models recognize the significance of incorporating the spatial structure of tumors for obtaining realistic results (98–100). Another limitation is exclusion of the heterogeneity within tumor and immune cell populations; specific subpopulations like BC stem cells and Tregs are acknowledged in biological literature for their association with resistance to MMC treatments (54, 56). For instance, the autophagy process, known to be involved in BC resistance to MMC, is associated with BC stem cells (56). Furthermore, the lack of characterization of specific behaviors in immune cell subpopulations, such as the regulatory role of Tregs in tumor dynamics (63, 101), may lead to potential misconceptions about immune system mechanisms. This is evident in the assumption of constant effector cell production (d_0). It does not include important aspects of effector cell proliferation, where DCs play a vital role in adaptive immunity by presenting antigens and activating T cells. Activated DCs can migrate to lymph nodes to prime naïve T cells (63), while Tregs regulate these immune responses. These processes significantly influence effector cell dynamics. Toward an in-depth understanding of the underlying biology, future work should address these limitations.

Finally, MMC is currently considered one of the most effective chemotherapy treatments after TUR to prevent NMIBC. In this paper, we propose theoretical explanation for the fact that still, a substantial percentage of patients fail the treatment (38–43). It is possible that treatment failure results from tumor size, as described in the literature (86, 87) and shown in Figure 5, or from an improper selection of the drug dose, m_0, that is implicitly reflected in the drug instillation rate, m, of the model. In this context, improper is defined as a set of parameters that are theoretically patient-specific and do not meet the conditions required by this mathematical method for cure. In particular, as outlined in the sensitivity analysis section, and as evident from the illustrated behavior in Figure 3, for higher values of parameters p_2 and d_0, in some cases yield higher values of growth rate r such that MMC dosage could be calculated. However, this does not guarantee a valid upper bound for dosage. Upon proper extensions and a thorough validation, the model can potentially pave the way for developing predictive tools for BC growth and determining curative drug dosages.

Data availability statement

Data and code to run model simulations and generate all figures are available at https://github.com/MYAUni/MMC-Model. Further inquiries can be directed to the corresponding author.

Author contributions

MY: Visualization, Writing – original draft, Writing – review & editing, Formal analysis, Software, Data curation. SB-M: Conceptualization, Project administration, Supervision, Funding acquisition, Writing – review & editing.

Funding

The author(s) declare financial support was received for the research, authorship, and/or publication of this article. This research was funded by Ariel University.

Acknowledgments

The authors would like to thank Dr. Sarel Halachmi of the Bnai Zion Medical Center in Haifa, for the helpful information and fruitful discussions. We are grateful to Dr. Teddy Lazebnik and Dr. Gili Hochman for helpful comments and suggestions. Graphical figures (Figures 1 and 4) were created using BioRender.com.

Conflict of interest

The authors declare that the research was conducted in the absence of any commercial or financial relationships that could be construed as a potential conflict of interest.

Publisher's note

All claims expressed in this article are solely those of the authors and do not necessarily represent those of their affiliated organizations, or those of the publisher, the editors and the reviewers. Any product that may be evaluated in this article, or claim that may be made by its manufacturer, is not guaranteed or endorsed by the publisher.

Supplementary material

The Supplementary Material for this article can be found online at: https://www.frontiersin.org/articles/10.3389/fonc.2024.1352065/full#supplementary-material

References

1. Sung H, Ferlay J, Siegel R, Laversanne M, Soerjomataram I, Jemal A, et al. Global cancer statistics 2020: GLOBOCAN estimates of incidence and mortality worldwide for 36 cancers in 185 countries. *CA: Cancer J Clin*. (2021) 71:209–12. doi: 10.3322/caac.21660

2. Jubber I, Ong S, Bukavina L, Black PC, Comperat´ E, Kamat AM, et al. Epidemiology of bladder cancer in 2023: A systematic review of risk factors. *Eur Urol*. (2023) 84:176–90. doi: 10.1016/j.eururo.2023.03.029

3. van Hoogstraten LMC, Vrieling A, van der Heijden AG, Kogevinas M, Richters A, Kiemeney LA. Global trends in the epidemiology of bladder cancer: challenges for public health and clinical practice. *Nat Rev Clin Oncol*. (2023) 20:287–8. doi: 10.1038/s41571-023-00744-3

4. Lowengrub J, Frieboes H, Jin F, Chuang YL, Li X, Macklin P, et al. INVITED ARTICLE: Nonlinear modelling of cancer: bridging the gap between cells and tumours. *Nonlinearity*. (2010) 23. doi: 10.1088/0951-7715/23/1/R01

5. Rosenblum D, Joshi N, Tao W, Karp J, Peer D. Progress and challenges towards targeted delivery of cancer therapeutics. *Nat Commun*. (2018) 9. doi: 10.1038/s41467-018-03705-y

6. Zhang Y, Zhang Z. The history and advances in cancer immunotherapy: understanding the characteristics of tumor-infiltrating immune cells and their therapeutic implications. *Cell Mol Immunol*. (2020) 17:1–15. doi: 10.1038/s41423-020-0488-6

7. Rockne RC, Hawkins-Daarud A, Swanson KR, Sluka JP, Glazier JA, Macklin P, et al. The 2019 mathematical oncology roadmap. *Phys Biol*. (2019) 16:041005. doi: 10.1088/1478-3975/ab1a09

8. Altrock P, Liu L, Michor F. The mathematics of cancer: Integrating quantitative models. *Nat Rev Cancer*. (2015) 15:730–45. doi: 10.1038/nrc4029

9. Barbolosi D, Ciccolini J, Lacarelle B, Barlési F, André N. Computational oncology — mathematical modelling of drug regimens for precision medicine. *Nat Rev Clin Oncol*. (2015) 13. doi: 10.1038/nrclinonc.2015.204

10. Jarrett AM, Faghihi D, Hormuth DA, Lima EABF, Virostko J, Biros G, et al. Optimal control theory for personalized therapeutic regimens in oncology: background, history, challenges, and opportunities. *J Clin Med*. (2020) 9. doi: 10.3390/jcm9051314

11. Bull JA, Byrne HM. The hallmarks of mathematical oncology. *Proc IEEE*. (2022) 110:523–40. doi: 10.1109/JPROC.2021.3136715

12. Hormuth DA, Jarrett AM, Lorenzo G, Lima EABF, Wu C, Chung C, et al. Math, magnets, and medicine: enabling personalized oncology. *Expert Rev Precis Med Drug Dev*. (2021) 6:79–81. doi: 10.1080/23808993.2021.1878023

13. Brady R, Enderling H. Mathematical models of cancer: when to predict novel therapies, and when not to. *Bull Math Biol*. (2019) 81:3723–6. doi: 10.1007/s11538-019-00640-x

14. Karev G, Novozhilov A, Koonin E. Mathematical modeling of tumor therapy with oncolytic viruses: Effects of parametric heterogeneity on cell dynamics. *Biol direct*. (2006) 1:30. doi: 10.1186/1745-6150-1-30

15. Griffiths T. Current perspectives in bladder cancer management. *Int J Clin Pract*. (2012) 67:440. doi: 10.1111/ijcp.12075

16. Shen Z, Shen T, Wientjes M, O'Donnell M, Au J. Intravesical treatments of bladder cancer: review. *Pharm Res*. (2008) 25:1500–10. doi: 10.1007/s11095-008-9566-7

17. Tomasz M. Mitomycin c: small, fast and deadly (but very selective). *Chem Biol*. (1995) 2:575–9. doi: 10.1016/1074-5521(95)90120-5

18. Zargar H, Aning J, Ischia J, So A, Black P. Optimizing intravesical mitomycin C therapy in nonmuscle-invasive bladder cancer. *Nat Rev Urol*. (2014) 11:220. doi: 10.1038/nrurol.2014.52

19. Burgos Simón C, García-Medina N, Martínez-Rodríguez D, Villanueva R. Mathematical modeling of the dynamics of the bladder cancer and the immune response applied to a patient: Evolution and short-term prediction. *Math Methods Appl Sci*. (2019) 42:5747. doi: 10.1002/mma.5536

20. Bunimovich-Mendrazitsky S, Shochat E, Stone L. Mathematical model of BCG immunotherapy in superficial bladder cancer. *Bull Math Biol*. (2007) 69:1847–70. doi: 10.1007/s11538-007-9195-z

21. Shaikhet L, Bunimovich-Mendrazitsky S. Stability analysis of delayed immune response BCG infection in bladder cancer treatment model by stochastic perturbations. *Comput Math Methods Med*. (2018) 9653873. doi: 10.1155/2018/9653873

22. Nave O, Hareli S, Elbaz M, Iluz IH, Bunimovich-Mendrazitsky S. BCG and IL 2 model for bladder cancer treatment with fast and slow dynamics based on SPVF method-stability analysis. *Math Biosci Eng. (MBE)*. 16 (2016) –79. doi: 10.3934/mbe.2019267

23. Guzev E, Halachmi S, Bunimovich-Mendrazitsky S. Additional extension of the mathematical model for BCG immunotherapy of bladder cancer and its validation by auxiliary tool. *Int J Nonlinear Sci Numerical Simulation*. (2019) 20:1–2. doi: 10.1515/ijnsns-2018-0181

24. de Pillis L, Gu W, Radunskaya A. Mixed immunotherapy and chemotherapy of tumors: modeling, applications and biological interpretations. *J Theor Biol*. (2006) 238:841–62. doi: 10.1016/j.jtbi.2005.06.037

25. Rodrigues D, Mancera P, Carvalho T. Gonc¸alves L. A mathematical model for chemoimmunotherapy of chronic lymphocytic leukemia. *Appl Mathematics Comput*. (2019) 349:118–33. doi: 10.1016/j.amc.2018.12.008

26. Machiels JPH, Reilly RT, Emens LA, Ercolini AM, Lei RY, Weintraub D, et al. Cyclophosphamide, doxorubicin, and paclitaxel enhance the antitumor immune response of granulocyte/macrophageColony stimulating factor-secreting whole-cell vaccines in HER-2/neu tolerized mice1. *Cancer Res*. (2001) 61:3689–97.

27. Dudley ME, Wunderlich JR, Robbins PF, Yang JC, Hwu P, Schwartzentruber DJ, et al. Cancer regression and autoimmunity in patients after clonal repopulation with antitumor lymphocytes. *Science*. (2002) 298:850–4. doi: 10.1126/science.1076514

28. Schooneveldt G, Kok HP, Bakker A, Geijsen ED, Rasch CRN, de la Rosette JJMCH, et al. Clinical validation of a novel thermophysical bladder model designed to improve the accuracy of hyperthermia treatment planning in the pelvic region. *Int J Hyperthermia*. (2018) 35:383–97. doi: 10.1080/02656736.2018.1506164

29. Yuan Y, Cheng KS, Craciunescu OI, Stauffer PR, Maccarini PF, Arunachalam K, et al. Utility of treatment planning for thermochemotherapy treatment of nonmuscle invasive bladder carcinoma. *Med Phys*. (2012) 39:1170–81. doi: 10.1118/1.3679839

30. Schooneveldt G, Kok HP, Bakker A, Geijsen ED, Hulshof MCCM, de Reijke TM, et al. The effect of air pockets in the urinary bladder on the temperature distribution during loco-regional hyperthermia treatment of bladder cancer patients. *Int J Hyperthermia*. (2018) 35:441–9. doi: 10.1080/02656736.2018.1506890

31. Sadée C, Kashdan E. A model of thermotherapy treatment for bladder cancer. *Math Biosci Eng*. (2016) 13:1169–83. doi: 10.3934/mbe.2016037

32. Racioppi M, Di GianFrancesco L, Ragonese M, Palermo G, Sacco E, Bassi P. Chemoablation with intensive intravesical mitomycin c treatment: A new approach for non–muscle-invasive bladder cancer. *Eur Urol Oncol*. (2019) 2:576–83. doi: 10.1016/j.euo.2018.08.032

33. Pasin E, Josephson D, Mitra A, Cote R, Stein J. Superficial bladder cancer: An update on etiology, molecular development, classification, and natural history. *Rev Urol*. (2008) 10:31–43.

34. Cumberbatch M, Jubber I, Black P, Esperto F, Figueroa J, Kamat A, et al. Epidemiology of bladder cancer: A systematic review and contemporary update of risk factors in 2018. *Eur Urol*. (2018) 74:784. doi: 10.1016/j.eururo.2018.09.001

35. Babjuk M. Transurethral resection of non-muscle-invasive bladder cancer. *Eur Urol Suppl*. (2009) 8:542–3. doi: 10.1016/j.eursup.2009.06.003

36. Lamm DL, McGee WR, Hale K. Bladder cancer: current optimal intravesical treatment. *Urologic Nurs*. (2005) 25:323—6.

37. Gao X, Au J, Badalament R, Wientjes M. Bladder tissue uptake of mitomycin C during intravesical therapy is linear with drug concentration in urine. *Clin Cancer Res*. (1998) 4:139–43.

38. Shariat SF, Chade DC, Karakiewicz PI, Scherr DS, Dalbagni G. Update on intravesical agents for non-muscle-invasive bladder cancer. *Immunotherapy*. (2010) 2:381—392. doi: 10.2217/imt.10.1

39. Babjuk M, Burger M, Zigeuner R, Shariat SF, van Rhijn BW, Compérat E, et al. EAU guidelines on non–muscle-invasive urothelial carcinoma of the bladder: update 2013. *Eur Urol*. (2013) 64:639–53. doi: 10.1016/j.eururo.2013.06.003

40. Lum B. Intravesical chemotherapy of superficial bladder cancer. *Recent results Cancer Res Fortschr der Krebsforschung Progres` dans les recherches sur le Cancer*. (1983) 85:3–36. doi: 10.1007/978-3-642-81994-02

41. Onishi T, Sugino Y, Shibahara T, Masui S, Yabana T, Sasaki T. Randomized controlled study of the efficacy and safety of continuous saline bladder irrigation after transurethral resection for the treatment of non-muscle invasive bladder cancer. *BJU Int*. (2016) 119:276–9. doi: 10.1111/bju.13599

42. Bohle A. An individual patient data meta-analysis of the long-term outcome of randomised studies comparing intravesical mitomycin C versus bacillus Calmette-Guerin´ for non-muscle-invasive bladder cancer. *Int Braz J urol*. (2009) 35:747–8. doi: 10.1590/S1677-55382009000600025

43. Persad R, Lamm D, Brausi M, Soloway M, Palou J, Hle A, et al. Current approaches to the management of non-muscle invasive bladder cancer: comparison of current guidelines and recommendations. *Eur Urol Suppl - Eur UROL Suppl*. (2008) 7:637–43. doi: 10.1016/j.eursup.2008.07.007

44. Liem E, Crezee H, Rosette J, de Reijke T. Chemohyperthermia in non-muscle-invasive bladder cancer: An overview of the literature and recommendations. *Int J Hyperthermia*. (2016) 32:1–11. doi: 10.3109/02656736.2016.1155760

45. Longo TA, Gopalakrishna A, Tsivian M, Noord MV, Rasch CR, Inman BA, et al. A systematic review of regional hyperthermia therapy in bladder cancer. *Int J Hyperthermia*. (2016) 32:381–9. doi: 10.3109/02656736.2016.1157903

46. Babjuk M, Burger M, Compérat EM, Gontero P, Mostafid AH, Palou J, et al. European association of urology guidelines on non-muscle-invasive bladder cancer (TaT1 and carcinoma in situ) - 2019 update. *Eur Urol*. (2019) 76:639–57. doi: 10.1016/j.eururo.2019.08.016

47. Bellmunt J. Stem-like signature predicting disease progression in early stage bladder cancer. *Role E2F3 SOX4 Biomedicines*. (2018) 6:85. doi: 10.3390/biomedicines6030085

48. Volkmer JP, Sahoo D, Chin R, Ho P, Tang C, Kurtova A, et al. Three differentiation states risk-stratify bladder cancer into distinct subtypes. *Proc Natl Acad Sci United States America*. (2012) 109:2078–83. doi: 10.1073/pnas.1120605109

49. Chan K, Espinosa I, Chao M, Wong D, Ailles L, Diehn M, et al. Identification, molecular characterization, clinical prognosis, and therapeutic targeting of human bladder tumor-initiating cells. *Proc Natl Acad Sci United States America*. (2009) 106:14016–21. doi: 10.1073/pnas.0906549106

50. Ho P, Kurtova A, Chan K. Normal and neoplastic urothelial stem cells: Getting to the root of the problem. *Nat Rev Urol*. (2012) 9:583–94. doi: 10.1038/nrurol.2012.142

51. Garg M. Urothelial cancer stem cells and epithelial plasticity: current concepts and therapeutic implications in bladder cancer. *Cancer metastasis Rev*. (2015) 34:693. doi: 10.1007/s10555-015-9589-6

52. Liu K, Waskow C, Liu X, Yao K, Hoh J, Nussenzweig M. Origin of dendritic cells in peripheral lymphoid organs of mice. *Nat Immunol*. (2007) 8:578–83. doi: 10.1038/ni1462

53. Merad M, Manz MG. Dendritic cell homeostasis. *Blood*. (2009) 113:3418–27. doi: 10.1182/blood-2008-12-180646

54. Hori S, Miyake M, Tatsumi Y, Onishi S, Morizawa Y, Nakai Y, et al. Topical and systemic immunoreaction triggered by intravesical chemotherapy in an N-butyl-N-(4-hydroxybutyl) nitorosamine induced bladder cancer mouse model. *PloS One*. (2017) 12:13. doi: 10.1371/journal.pone.0175494

55. Hori S, Miyake M, Tatsumi Y, Morizawa Y, Nakai Y, Onishi S, et al. Intravesical treatment of chemotherapeutic agents sensitizes bacillus Calmette-Guerin by the modulation of the tumor immune environment. *Oncol Rep*. (2019) 41:1869. doi: 10.3892/or.2019.6965

56. Ojha R, Jha V, Singh S. Gemcitabine and mitomycin induced autophagy regulates cancer stem cell pool in urothelial carcinoma cells. *Biochim Biophys Acta (BBA) - Mol Cell Res*. (2015) 1863:347–58. doi: 10.1016/j.bbamcr.2015.12.002

57. Chen SK, Chung CA, Cheng YC, Huang CJ, Ruaan RC, Chen WY, et al. Hydrostatic pressure enhances mitomycin C induced apoptosis in urothelial carcinoma cells. *Urologic Oncol: Semin Original Investigations*. (2014) 32:26.e17–24. doi: 10.1016/j.urolonc.2012.09.004

58. Oresta B, Pozzi C, Hurle R, Lazzeri M, Faccani C, Colombo P, et al. Mitomycin C triggers immunogenic cell death in bladder cancer cells. *Eur Urol Suppl*. (2019) 18: e585–6. doi: 10.1016/S1569-9056(19)30435-X

59. Logan C, Brown M, Hayne D. Intravesical therapies for bladder cancer – indications and limitations. *BJU Int*. (2012) 110:12–21. doi: 10.1111/j.1464-410X.2012.11619.x

60. Okeke A, Probert J, Gillatt D, Schwaibold H. Is intravesical chemotherapy for superficial bladder cancer still justified? *BJU Int*. (2005) 96:763–7. doi: 10.1111/j.1464-410X.2005.05711.x

61. Melekos MD, Moutzouris GD. Intravesical therapy of superficial bladder cancer. *Curr Pharm Des*. (2000) 6(3):345–59. doi: 10.2174/1381612003401019

62. Li Y, Lin K, Yang Z, Han N, Quan X, Guo X, et al. Bladder cancer stem cells: clonal origin and therapeutic perspectives. *Oncotarget*. (2017) 8:66668–79. doi: 10.18632/oncotarget.19112

63. Joseph M, Enting D. Immune responses in bladder cancer-role of immune cell populations, prognostic factors and therapeutic implications. *Front Oncol*. (2019) 9:1270. doi: 10.3389/fonc.2019.01270

64. Bunimovich-Mendrazitsky S, Claude Gluckman J, Chaskalovic J. A mathematical model of combined bacillus calmette-guerin (BCG) and interleukin (IL)-2 immunotherapy of superficial bladder cancer. *J Theor Biol*. (2011) 277:27–40. doi: 10.1016/j.jtbi.2011.02.008

65. Marino S, Kirschner DE. The human immune response to mycobacterium tuberculosis in lung and lymph node. *J Theor Biol*. (2004) 227:463–86. doi: 10.1016/j.jtbi.2003.11.023

66. Nolz J. English (US)Molecular mechanisms of cd8+ t cell trafficking and localization. *Cell Mol Life Sci*. (2015) 72:2461–73. doi: 10.1007/s00018-015-1835-0

67. Dalton J, Wientjes M, Badalament R, Drago J. au J. Pharmacokinetics of intravesical Mitomycin C in superficial bladder cancer patients. *Cancer Res*. (1991) 51:5144–52.

68. Kirschner DE, Panetta JC. Modeling immunotherapy of the tumor – immune interaction. *J Math Biol*. (1998) 37:235–52. doi: 10.1007/s002850050127

69. Kogan Y, Foryś U, Shukron O, Kronik N, Agur Z. Cellular immunotherapy for high grade gliomas: mathematical analysis deriving efficacious infusion rates based on patient requirements. *SIAM J Appl Mathematics*. (2010) 70:1953–76. doi: 10.1137/08073740X

70. Kronik N, Kogan Y, Elishmereni M, Halevi-Tobias K, Vuk-Pavlović S, Agur Z. Predicting outcomes of prostate cancer immunotherapy by personalized mathematical models. *PloS One*. (2010) 5:1–8. doi: 10.1371/journal.pone.0015482

71. Hu L, Wientjes M, Li J. au J. Bladder tissue pharmacokinetics of intravesical mitomycin C and suramin in dogs. *AAPS J*. (2010) 12:586–91. doi: 10.1208/s12248-010-9219-8

72. Au JLS, Jang SH, Wientjes M. Clinical aspects of drug delivery to tumors. *J Controlled Release*. (2002) 78:81–95. doi: 10.1016/S0168-3659(01)00488-6

73. Volpato M, Phillips R. Tailoring targeted therapy to individual patients: Lessons to be learnt from the development of mitomycin c. *Cancer Genomics Proteomics*. (2007) 4:175–86.

74. Maffezzini M, Campodonico F, Manuputty EE, Puntoni M, Martelli A, Marini V, et al. Systemic absorption and pharmacokinetics of single-dose early intravesical mitomycin C after transurethral resection of non-muscle-invasive bladder cancer. *Urology*. (2013) 82:400–4. doi: 10.1016/j.urology.2013.03.036

75. De nunzio C, Carbone A, Albisinni S, Alpi G, Cantiani A, Liberti M, et al. Long-term experience with early single Mitomycin C instillations in patients with low-risk non-muscle-invasive bladder cancer: Prospective, single-centre randomised trial. *World J Urol*. (2011) 29:517–21. doi: 10.1007/s00345-011-0691-2

76. Moskovitz B, Meyer G, Kravtzov A, Gross M, Kastin A, Biton K, et al. Thermo-chemotherapy for intermediate or high-risk recurrent superficial bladder cancer patients. *Ann Oncol*. (2005) 16:585–9. doi: 10.1093/annonc/mdi124

77. Tan WS, Palou J, Kelly J. Safety and tolerability analysis of hyperthermic intravesical mitomycin to mitomycin alone in HIVEC I and HIVEC II: An interim analysis of 307 patients. *Eur Urol Suppl*. (2017) 16:e1150–1. doi: 10.1016/S1569-9056(17)30717-0

78. Vildanova R, Lobov A, Spirikhin L, Kolesov S. Hydrogels on the base of modified chitosan and hyaluronic acid mix as polymer matrices for cytostatics delivery. *Gels*. (2022) 8:7. doi: 10.3390/gels8020104

79. Ojha R, Singh S, Bhattacharyya S, Jha V. Mp34-20 inhibitors of autophagy potentiates the cytotoxic effect of chemotherapeutic agents on urothelial carcinoma of urinary bladder. *J Urol*. (2014) 191:e370–0. doi: 10.1016/j.juro.2014.02.1033

80. Sylvester RJ, van der Meijden AP, Oosterlinck W, Witjes JA, Bouffioux C, Denis L, et al. Predicting recurrence and progression in individual patients with stage ta t1 bladder cancer using eortc risk tables: A combined analysis of 2596 patients from seven eortc trials. *Eur Urol*. (2006) 49:466–77. doi: 10.1016/j.eururo.2005.12.031

81. Spratt JA, von Fournier D, Spratt JS, Weber EE. Decelerating growth and human breast cancer. *Cancer*. (1993) 71:2013–9. doi: 10.1002/(ISSN)1097-0142

82. Babjuk M, Burger M, Capoun O, Cohen D, Compérat EM, Dominguez Escrig JL, et al. European association of urology guidelines on non–muscle-invasive bladder

cancer (Ta, T1, and carcinoma in situ). *Eur Urol*. (2022) 81:75–94. doi: 10.1016/j.eururo.2021.08.010

83. Loloi J, Allen J, Schilling A, Hollenbeak C, Merrill S, Kaag M, et al. In the world of bladder tumors: Size does matter. *Bladder Cancer*. (2020) 6:1–6. doi: 10.3233/BLC-200273

84. Abouelkheir RT, Abdelhamid A, El-Ghar MA, El-Diasty T. Imaging of bladder cancer: Standard applications and future trends. *Medicina*. (2021) 57:3. doi: 10.3390/medicina57030220

85. Kim LHC, Patel MI. Transurethral resection of bladder tumour (turbt). *Trans Androl Urol*. (2019) 9:3065. doi: 10.21037/tau

86. Solsona E, Iborra I, Ricós JV, Monrós JL, Casanova J, Dumont R. Effectiveness of a single immediate mitomycin c instillation in patients with low risk superficial bladder cancer: short and long-term followup. *J Urol*. (1999) 161:1120–3. doi: 10.1016/S0022-5347(01)61606-9

87. Ersoy H, Yaytokgil M, Karakoyunlu AN, Topaloglu H, Sagnak L, Ozok HU. Single early instillation of mitomycin c and urinary alkalinization in low-risk non-muscle-invasive bladder cancer: a preliminary study. *Drug Design Dev Ther*. (2013) 7:1–6. doi: 10.2147/DDDT.S39541

88. Marino S, Hogue IB, Ray CJ, Kirschner DE. A methodology for performing global uncertainty and sensitivity analysis in systems biology. *J Theor Biol*. (2008) 254:178–96. doi: 10.1016/j.jtbi.2008.04.011

89. Friedman A, Xiulan L. Combination therapy for cancer with oncolytic virus and checkpoint inhibitor: A mathematical model. *PloS One*. (2018) 13:e0192449. doi: 10.1371/journal.pone.0192449

90. Bahouth Z, Halachmi S, Moskovitz B, Nativ O. The role of hyperthermia as a treatment for non-muscle invasive bladder cancer. *Expert Rev Anticancer Ther*. (2015) 16. doi: 10.1586/14737140.2016.1126515

91. Adiyat KT, Katkoori D, Soloway CT, De Los Santos R, Manoharan M, Soloway MS. "complete transurethral resection of bladder tumor": Are the guidelines being followed? *Urology*. (2010) 75:365–7. doi: 10.1016/j.urology.2009.08.082

92. Wientjes M, Badalament R, Wang R, Hassan F. au J. Penetration of mytomicin c in human bladder. *Cancer Res*. (1993) 53:3314–20.

93. Joice G, Bivalacqua T, Kates M. Optimizing pharmacokinetics of intravesical chemotherapy for bladder cancer. *Nat Rev Urol*. (2019) 16(10):599–612. doi: 10.1038/s41585-019-0220-4

94. Jeong C, Jeon H, Kwak C, Jeong H, Lee S. Comparison of 30 mg and 40 mg of mitomycin C intravesical instillation in korean superficial bladder cancer patients: Prospective, randomized study. *Cancer Res Treat*. (2005) 37:44–7. doi: 10.4143/crt.2005.37.1.44

95. Gofrit ON, Pode D, Pizov G, Duvdevani M, Landau EH, Hidas G, et al. 'very-low-risk' bladder tumours – a new entity? *BJU Int*. (2018) 121:627–31. doi: 10.1111/bju.14108

96. Lee S, Hu W, Matulay J, Silva M, Owczarek T, Kim K, et al. Tumor evolution and drug response in patient-derived organoid models of bladder cancer. *Cell*. (2018) 173:515–528.e17. doi: 10.1016/j.cell.2018.03.017

97. Krpina K, Babarović E, Dordevic G, Fuckar Z, Jonjić N. The association between the recurrence of solitary non-muscle invasive bladder cancer and tumor infiltrating lymphocytes. *Croatian Med J*. (2012) 53:598–604. doi: 10.3325/cmj.2012.53.598

98. Lazebnik T. Cell-level spatio-temporal model for a bacillus calmettendash; gueacute;rin-based immunotherapy treatment protocol of superficial bladder cancer. *Cells*. (2022) 11:1–15. doi: 10.3390/cells11152372

99. Lazebnik T, Aaroni N, Bunimovich-Mendrazitsky S. PDE based geometry model for BCG immunotherapy of bladder cancer. *Biosystems*. (2021) 200:104319. doi: 10.1016/j.biosystems.2020.104319

100. Lazebnik T, Bunimovich-Mendrazitsky S. Improved geometric configuration for the bladder cancer bcg-based immunotherapy treatment model. In: Bebis G, Gaasterland T, Kato M, Kohandel M, Wilkie K, editors. *Mathematical and Computational Oncology*. Springer International Publishing, Cham (2021). p. 63–7.

101. Kondělková K, Vokurková D, Krejsek J, Borská L, Fiala Z, Ctirad A. Regulatory t cells (treg) and their roles in immune system with respect to immunopathological disorders. *Acta Med (Hradec Kralove)*. (2010) 53:73—77. doi: 10.14712/18059694.2016.63

Frontiers in Immunology

Explores novel approaches and diagnoses to treat immune disorders.

The official journal of the International Union of Immunological Societies (IUIS) and the most cited in its field, leading the way for research across basic, translational and clinical immunology.

Discover the latest Research Topics

See more →

Frontiers

Avenue du Tribunal-Fédéral 34
1005 Lausanne, Switzerland
frontiersin.org

Contact us

+41 (0)21 510 17 00
frontiersin.org/about/contact